

NAVY RESEARCH

MAR 29 1974

Project THEMIS  
Technical Report No. 26  
TURBULENCE INDUCED CHANGES IN VORTEX  
SHEDDING FROM A CIRCULAR CYLINDER

by  
Kenneth M. Barnett  
and  
J. E. Cermak

Prepared under  
Office of Naval Research  
Contract No. N00014-68-A-0493-0001  
Project No. NR 062-4146-6-68 (Code 438)  
U.S. Department of Defense  
Washington, D.C.

"This document has been approved for public  
release and sale; its distribution is  
unlimited."

Fluid Dynamics and Diffusion Laboratory  
College of Engineering  
Colorado State University  
Fort Collins, Colorado

January, 1974

CER73-74KMB-JEC27



U18401 0077449

## ABSTRACT

### TURBULENCE INDUCED CHANGES IN VORTEX SHEDDING FROM A CIRCULAR CYLINDER

Turbulence effects on vortex shedding from a circular cylinder were investigated in a wind tunnel.

Most of the literature on vortex shedding reports investigations in air flows where special efforts had been made to keep the turbulence intensity very low (usually  $<.5\%$ ) in the free stream. Under such conditions, vortex shedding from a circular cylinder can be classified into four regimes with a discontinuity condition between each two succeeding regimes. These regimes are identified by the span of Reynolds numbers,  $Re$ , and Strouhal numbers,  $St$ , by the angle of boundary layer transition,  $\alpha$ , and by the transition point from laminar to turbulent flow in the boundary layer or vortex.

In this study, turbulence intensity, near the center of a wind tunnel, was increased from  $.3\%$  to  $25\%$  by plates of similar geometry (many small holes) with blockage ratios from  $.50$  to  $.97$ . The  $Re$  of all flows was kept near  $4 \times 10^4$ . Vortex shedding frequency,  $f$ , was observed simultaneously by a pressure transducer (with sensors on cylinder surface) and a hot wire anemometer (immediately downstream). Means of 50 to 150 cross-spectra defined  $f$ . Flow visualization, spectra and transducer output voltages with different  $\alpha$  were utilized to estimate transition and separation.

Four concepts were verified that are already in the literature. As the turbulence intensity of the upstream flow is increased: (a) the vortex shedding regimes occur at lower  $Re$ ; (b) discontinuities lose any dominant  $f$  value that they might have had; (c) vortices are

destroyed closer to the cylinder; and (d) the size of cylinders influence turbulence effects on vortex shedding.

Six things were observed that have not been published, to the best of the author's knowledge: (a) analogous changes in vortex shedding processes can be obtained either by increasing the air speed (while holding the turbulence intensity very low) or by increasing the turbulence intensity (while holding the air speed approximately constant); (b) the frequency of the vortex shedding becomes relatively smaller, for the vortex shedding regime, as the turbulence intensity is increased; (c) an estimate of the turbulence induced changes in vortex shedding can be made from  $Re$  of the flow, mean air speed, rms value of longitudinal speed fluctuations, integral scale of turbulence and cylinder diameter; (d) the "super critical" regime, associated with highest  $\alpha$  and  $St$ , can be disrupted by sufficient turbulence intensity; (e) the extent to which turbulence can induce changes in vortex shedding is limited.

A model of vortex shedding is hypothesized which includes the concept that vortex shedding is continuous from  $Re$  near 40 until either the mean air speed and the turbulence intensity, or both, are increased until turbulence destroys individual vortices before they can be shed.

## TABLE OF CONTENTS

<u>Chapter</u>		<u>Page</u>
	LIST OF TABLES . . . . .	v
	LIST OF FIGURES . . . . .	vi
	LIST OF SYMBOLS AND ABBREVIATIONS . . . . .	ix
1	INTRODUCTION . . . . .	1
2	VORTEX SHEDDING . . . . .	6
3	TURBULENCE PARAMETERS . . . . .	11
4	INSTRUMENTATION AND EXPERIMENTAL PROCEDURE . . . . .	14
5	EXPERIMENTAL RESULTS . . . . .	22
6	DISCUSSION . . . . .	38
7	CONCLUSIONS . . . . .	55
	BIBLIOGRAPHY . . . . .	61
	APPENDIX A. THEORETICAL BACKGROUND . . . . .	67
	APPENDIX B. TURBULENCE PARAMETERS . . . . .	114
	APPENDIX C. ACCURACY CONSIDERATIONS . . . . .	129
	TABLES . . . . .	148
	FIGURES . . . . .	165

LIST OF TABLES

<u>Table</u>		<u>Page</u>
1	Turbulence producing plates . . . . .	148
2	Vortex shedding data . . . . .	149
3	Observation of turbulence parameters . . . . .	150
4	Comparison of first derivatives . . . . .	152
5	Programs for Fourier Analyzer System . . . . .	153
6	Relation of turbulence parameters to $Re(E)$ and $Re(E)/Re$ . . . . .	155
7	Digital computer programs . . . . .	157

## LIST OF FIGURES

<u>Figure</u>		<u>Page</u>
1	Vortex shedding flow regimes . . . . .	165
2	Characteristics of the four major vortex shedding regimes . . . . .	166
3	Variation of $l/s$ and $C_d$ as functions of $R$ . . . . .	167
4	Photograph of Fourier Analyzer System . . . . .	168
5	General view of wind tunnel and instrumentation . . . . .	169
6	Diagram of wind tunnel . . . . .	170
7	Picture of plate .500 . . . . .	171
8	Photograph of plate .972 . . . . .	172
9	Picture of "Surry" grid . . . . .	173
10	Pressure transducer inside 4.5" cylinder . . . . .	174
11	End view of 2.75" diameter cylinder . . . . .	175
12	Power spectra of $f$ ; $\alpha = \pm 90^\circ$ , $U \approx 18$ fps . . . . .	176
13	Power spectra of $f$ ; $\alpha = \pm 130^\circ$ , $U \approx 18$ fps . . . . .	177
14	Power spectra of $f$ ; $\alpha = \pm 150^\circ$ , $U \approx 18$ fps . . . . .	178
15	$f$ observed simultaneously, 4.5" cylinder, open tunnel, "A" . . . . .	179
16	$f$ observed simultaneously, 4.5" cylinder, plate .690, "B" . . . . .	180
17	$f$ observed simultaneously, 2.75" cylinder, plate .748, "B'" . . . . .	181
18	$f$ observed simultaneously, 4.5" cylinder, plate .748, "C" . . . . .	182
19	$f$ observed simultaneously, 2.75" cylinder, plate .801, "C'" . . . . .	183
20	$f$ observed simultaneously, 4.5" cylinder, plate .804, "D" . . . . .	184

LIST OF FIGURES (continued)

<u>Figure</u>		<u>Page</u>
21	f observed simultaneously, 2.75" cylinder, plate .861, "D'" . . . . .	185
22	f observed simultaneously, 4.5" cylinder, plate .945, "E" . . . . .	186
23	f observed simultaneously, 2.75" cylinder, plate .945, "E'" . . . . .	187
24	f observed simultaneously, 4.5" cylinder, plate .972, "F" . . . . .	188
25	f observed simultaneously, 4.5" cylinder, plate .972, "F'" . . . . .	189
26	f observed simultaneously, 4.5" cylinder, plate .972, "F'" . . . . .	190
27	f observed simultaneously, 2.75" cylinder, plate .972, "F'" . . . . .	191
28	Flow visualization . . . . .	192
29	Variation of voltage with $\alpha$ . . . . .	193
30	Power spectra of f, plate .804, $U \approx 7$ fps . . . . .	194
31	Power spectra of f, plate .972, $U \approx 16$ fps . . . . .	195
32	Turbulence and speed distributions . . . . .	196
33	Comparison of power spectra . . . . .	197
34	Power spectra of turbulent flow, plate .690, #1, "B" . . . . .	198
35	Power spectra of turbulent flow, plate .690, #1-1 . . . . .	199
36	Power spectra of turbulent flow, plate .748, #2, "B'" . . . . .	200
37	Power spectra of turbulent flow, plate .748, #3, "C" . . . . .	201
38	Power spectra of turbulent flow, plate .801, #4, "C'" . . . . .	202
39	Power spectra of turbulent flow, plate .804, #5, "D" . . . . .	203
40	Power spectra of turbulent flow, plate .861, #6, "D'" . . . . .	204

LIST OF FIGURES (continued)

<u>Figure</u>		<u>Page</u>
41	Power spectra of turbulent flow, plate .945, #7, "E", "E'" . . . . .	205
42	Power spectra of turbulent flow, plate .972, #8, "F", "F'" . . . . .	206
43	$\tau_0$ observations, 4.5" cylinder . . . . .	207
44	$\tau_0$ observations, 2.75" cylinder . . . . .	208
45A	Re(E) vs turbulence parameters, 4.5" cylinder . . . . .	209
45B	Re(E)/Re vs turbulence parameters, 4.5" cylinder . . . . .	210
46A	Re(E) vs turbulence parameters, 2.75" cylinder . . . . .	211
46B	Re(E)/Re vs turbulence parameters, 2.75" cylinder . . . . .	212
47	Turbulent boundary layer representation . . . . .	213
48	Pressure distribution around a cylinder . . . . .	214
49	Change in turbulent fluctuations along stagnation line . . . . .	215
50	Calibration curve of DISA hot wire . . . . .	216
51	Example of calculation of $F(0)$ . . . . .	217
52.	Example of calculation of $\int_0^\infty f^2 F_{xx}(f) df$ . . . . .	218
53.	Calculation of hot wire time constant . . . . .	219
54	Check on hot wire calibration . . . . .	220
55	Least squares calibration of DISA hot wire . . . . .	221
56	Comparison of turbulence intensity by diffusion and hot wire . . . . .	222

## LIST OF SYMBOLS AND ABBREVIATIONS

		<u>Dimensions</u>
A	Constant	
A	Area	$L^2$
AC	Alternating current	
ASL	Atmospheric Sciences Laboratory (US Army, White Sands Missile Range, NM)	
B	Constant; coefficient in King's equation	
Br	Blockage ratio of a turbulence producing screen	
C	Constant; exponent in King's equation; capacitance	
Cd	Drag coefficient = drag force/ $\rho U^2 A$	
COHU	Instrument manufacturer	
Cp	Specific heat of air at constant pressure	$\text{cal M}^{-1}\theta^{-1}$
CSU	Colorado State University	
CTA	Constant temperature anemometer	
c	Same as Cp	
D	Diameter of cylinder	L
DC	Direct current	volts
DFT	Discrete finite transform, $S_x(f)$	
DISA	Instrument manufacturer	
d	Diameter of hole in turbulence producing plates	L
$\overline{de/dt}$	RMS value of $de/dt$	volts $T^{-1}$
E	Mean DC voltage	volts
ENDEVCO	Instrument manufacturer	
e	Fluctuating instantaneous voltage	volts

LIST OF SYMBOLS (continued)

$\bar{e}$	RMS value of e	volts
FAS	Fourier Analyzer System (Hewlett Packard 5451A)	
FM	Frequency modulated	
$f_m$	Maximum frequency used in a FAS	Hz
$F(f)$	Normalized power spectra	T
$F(M)$	$F(f)$ evaluated at $f$ with peak power	T
$F(0)$	Extrapolation of $F(f)$ to $f = 0$	T
$F_x(f)$	Fourier integral transformation	
$F_{xx}(f)$	Normalized power spectra, same as $F(f)$	T
$f$	Frequency of vortex shedding (from one side), or in power spectra	Hz
fps	Feet per second	$LT^{-1}$
$\Delta f$	Frequency increment used in analog to digital conversion	Hz
$G_{xx}(f)$	Power spectra, not normalized	$\text{volts}^2; L^2T^{-2}$
$G_{yx}(f)$	Cross spectra	$\text{volts}^2; L^2T^{-2}$
H	Fourier transform	
H-P	Instrument manufacturer	
HWA	Hot wire anemometer (CTA with hot wire sensor)	
Hz	Hertz - cycles per second	$T^{-1}$
h	Width of a wind tunnel; lateral spacing of vortices	L
h	Inverse Fourier transform	
i	Square root of -1; subscript for variables	
ips	Inches per second	$LT^{-1}$
$J_\epsilon$	Eulerian integral scale of turbulence	T

LIST OF SYMBOLS (continued)

$K_m$	Eddy viscosity, $K_m = \bar{u}L_x$	$L^2T^{-1}$
Kron-Hite	Instrument manufacturer	
$k$	Thermal conductivity	cal $T^{-1}L^{-1}\theta^{-1}$
$k, m, n$	Integers in numerical summations	
$L$	Length	$L$
Lim	Limit	
$L_x$	Integral scale of turbulence, $L_x = J_\epsilon U$ ; $L_x = UF(0)/4$	$L$
$L_x(\tau)$	$L_x$ calculated from autocorrelation, $L_x(\tau) = U\tau_0$	$L$
$L_x(F)$	$L_x$ calculated from normalized spectra, $L_x(F) = UF(0)/4$	$L$
$\ell$	Longitudinal spacing of vortices	$L$
$M$	Number of spectra or correlations used for a mean result. Distance between centers of adjacent squares in turbulence producing grids.	$L$
MRI	Instrument manufacturer	
$N$	Total number of data samples in analog to digital conversion	
$n$	Exponent; number of data set	
$P$	Pressure	$ML^{-1}T^{-2}$
$\Delta P$	Pressure difference for pitot tube	$ML^{-1}T^{-2}$
$p$	Refers to turbulence producing plate	
$Q_{yx}(f)$	Quadrature spectral density function	
$R$	Resistance of hot wire or film when heated	ohms
$R$	Rankine temperature; Correlation coeff.	$\theta$ ; ND
$R$	Radius of pipe; resistance	$L$ ; ohms

LIST OF SYMBOLS (continued)

RA	Resistance of hot wire or film at ambient temperature	ohms
Re	Reynolds number using kinematic viscosity, $UD/\nu$	
Re(C)	Critical Reynolds number, estimated from physical phenomena	
Re(E)	Effective Reynolds number	
Re(Km)	Reynolds number, using eddy viscosity, $UD/Km$	
Re(M)	Mesh Reynolds number, $UM/\nu$	
Re(p)	Reynolds number, for turbulence producing plates, $Ud/(1 - Br)\nu$	
Re( $\lambda$ )	Turbulence Reynolds number, $\bar{u}\lambda/\nu$	
Re( $\nu$ )	Same as Re	
RMS	Root mean square	
R( $\tau$ )	Autocorrelation	volts <sup>2</sup> ; L <sup>2</sup> T <sup>-2</sup>
Rx	Correlation coefficient of speed variations x distance apart	
Rxx( $\tau$ )	Same as R( $\tau$ )	
Ryx( $\tau$ )	Cross correlation	volts <sup>2</sup> ; L <sup>2</sup> T <sup>-2</sup>
S	Separation point of boundary layer from cylinder	
St	Strouhal number, $fD/U$	
Sx(f)	Discrete finite transform, DFT, of analog data to digital	
T	Time; total data time used in analog to digital conversion for one data sample for numerical processing	T
T	Temperature	$\theta$
Tv	Virtual temperature	$\theta$

LIST OF SYMBOLS (continued)

$\Delta T$	Temperature increment	$\theta$
$Ta$	Taylor parameter, $Ti(D/Lx) \cdot^2$	
$Ti$	Turbulence intensity, $\bar{u}/U$	
TSI	Instrument manufacturer	
$t$	Time	$T$
$\Delta t$	Time increment used in analog to digital conversion	$T$
$U, V, W$	Mean air speed parallel to $x, y, z$ axes, respectively	$LT^{-1}$
$U_{\infty}$	Free stream value of $U$	$LT^{-1}$
$u, v, w$	Instantaneous air speed fluctuations parallel to $x, y, z$ axes, respectively	$LT^{-1}$
$u_*$	Friction velocity	$LT^{-1}$
$\overline{uv}$	Turbulent shearing stress	$ML^{-1}T^{-2}$
$\bar{u}, \bar{v}, \bar{w}$	RMS values of $u, v, w$	$LT^{-1}$
VM	Voltmeter	
WSMR	White Sands Missile Range, New Mexico	
$x$	General variable	
$x, y, z$	Cartesian coordinate axes	
$\alpha$	Angle; level of statistical significance	
$\Delta$	Small increment	
$\delta$	Boundary layer thickness	$L$
$\theta$	Temperature	$\theta$
$\lambda$	Microscale of turbulence	$L$
$\mu$	Dynamic viscosity	$ML^{-1}T^{-1}$
$\nu$	Kinematic viscosity ( $1.9 \times 10^{-4} \text{ ft}^2 \text{ sec}^{-1}$ )	$L^2T^{-1}$

LIST OF SYMBOLS (continued)

$\pi$	3.14 . . .	
$\rho$	Density	$ML^{-3}$
$\Sigma$	Summation	
$\tau$	Time delay	$\theta$
$\tau_0$	Time delay for autocorrelation to first reach zero -- same as $J_e$ ; surface stress	$\theta$
$\tau_{yx}$	Shearing stress	$ML^{-1}T^{-2}$

SUBSCRIPTS

$i$	Counter for individual data points
$i, j, k$	Tensor notation

SUPERSCRIPTS

$\bar{\quad}$	Mean value; correlation
$\overline{\quad}$	RMS value
$\ast$	Complex conjugate

## 1. INTRODUCTION

Vortex shedding from a circular cylinder and other bluff bodies has been observed for a long time. In the 15th century, Leonardo da Vinci drew fairly accurate sketches of a vortex street. Strouhal, in 1878, conducted experiments to show that the frequency of vortex shedding depended on the air speed and wire diameter rather than the elastic properties of a wire. In 1879, Rayleigh formulated a Reynolds number,  $Re^*$  ( $Re = UD/\nu$ ), dependence of the shedding frequency. Von Karman made the greatest theoretical contribution to vortex shedding knowledge. Using potential flow theory and an instability analysis in 1911, von Karman established that vortices alternate in being shed from each side of a cylinder and have a fixed geometry. This has become known as the "Karman vortex street." The next page has photographs of several of them.

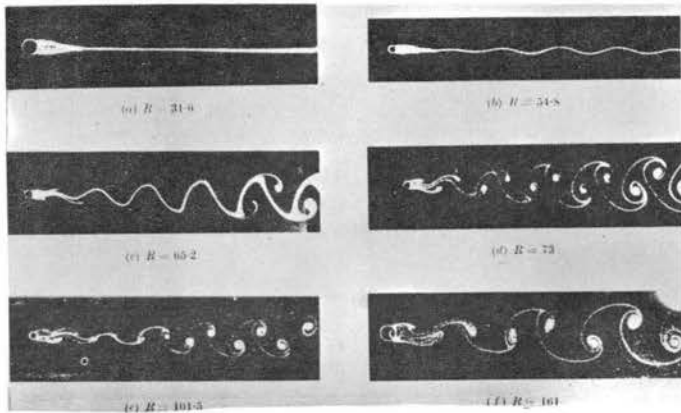
Since von Karman's theoretical analysis, much experimental work has been done. Initially, this was aimed at testing his analysis. Later, and still continuing, the experiments are seeking to extend the theory and understanding of vortex shedding, resulting stresses on structures, and influences on wake development.

Limited theoretical studies beyond von Karman's have been carried out. These include more complicated potential flow approaches, such as free-streamline analysis and hodograph models (Roshko, 1955; Bearman, 1967)\*\* and some analysis of viscous effects (Schafer and

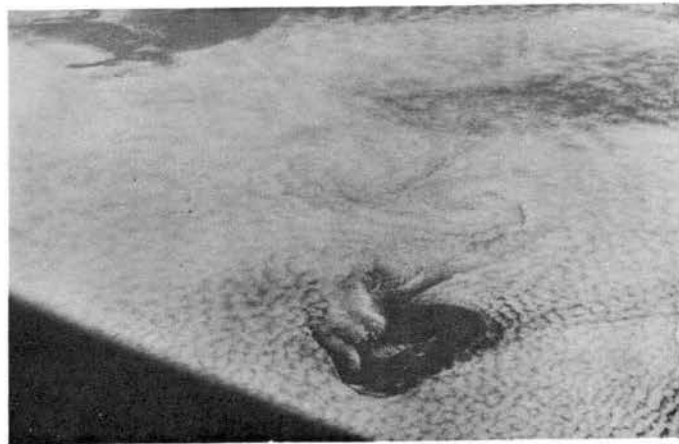
---

\* Definitions are also in "List of Symbols and Abbreviations."

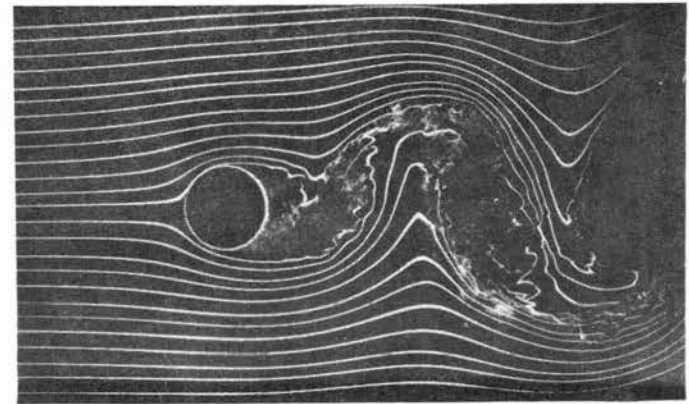
\*\* See "Bibliography" for details of referenced articles.



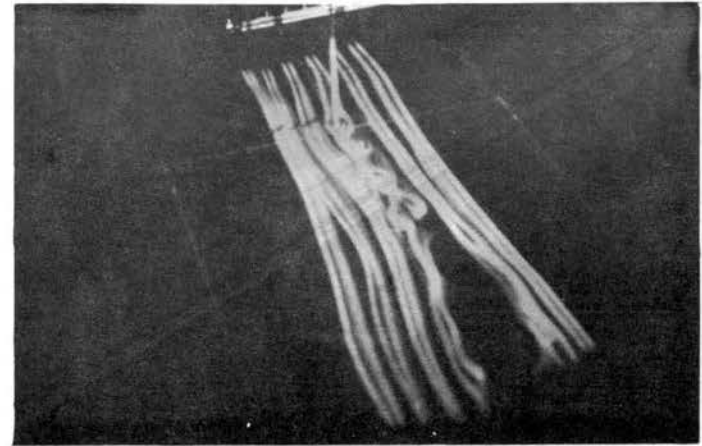
Laminar vortex street, visualized by oil on water. From figure 1.6, Schlichting, 1960; original work by Homann.



Atmospheric vortex street in lee of Guadalupe Island, Mexico. NASA photograph S-65-45697 by Gemini 5 Astronauts, 1965.



Turbulent vortex street, visualized by smoke streams in a wind tunnel. From figure 4.17, Robertson, 1965; original work by Lippisch.



Wind tunnel model of atmospheric vortex street, using smoke streams, by Barnett, 1972.

Examples of vortex shedding as seen in Karman vortex streets.

Eskanazi, 1959). However, most theoretical development beyond von Karman's potential flow model has resulted from experimental observational data.

In the literature, vortex shedding observations usually have been reported for wind tunnel flows where steps had been taken to suppress turbulence in the mean flow passing the cylinder. Turbulence intensities less than .5% are typical. This was no doubt done because free stream turbulence can be a serious obstacle in obtaining good observations of the vortex shedding process. Notable exceptions are recent reports by Simon, et al., (1967), Surry (1969), Mujumdar (1971) and Ko and Graf (1972), who introduced turbulence into their wind tunnel flows; their work is discussed later.

This dissertation has evolved from an interest in studying atmospheric processes by modeling them in a wind tunnel. Cermak (1971) presents a comprehensive review of the modeling theory and practices. The author (Barnett, 1972) simulated several features, in a wind tunnel, of atmospheric vortex streets in the lee of isolated islands. These results are summarized by the two lower photographs on the preceding page. The atmospheric vortex streets display characteristics similar to laminar vortex streets, created in wind tunnels behind circular cylinders, with  $Re$  values near 150, using cylinder diameter, mean air speed, and kinematic viscosity. However, the  $Re$  values in the atmospheric flows, using island diameters, mean air speed, and kinematic viscosity, are of the order of  $10^9$  or  $10^{10}$ .

Considering that nearly all atmospheric flows are turbulent, these differences of  $Re$  values can be reconciled by using eddy

viscosity to calculate  $Re$  in atmospheric flows and retaining kinematic viscosity to determine  $Re$  in simulated wind tunnel flows. Chopra and Hubert (1964, 1965) were among the first to apply this concept to atmospheric vortex streets. This has led to good qualitative results in several other atmospheric simulations, as noted by Cermak (1971). However there are debatable aspects to this concept of  $Re$  equality, as pointed out by Snyder (1972).

Because of the above debatable concept and because nearly all previous laboratory investigations of vortex shedding have been conducted in air flow of very low turbulence intensity, it appeared useful to conduct a study in which the maximum practical amount of turbulence is introduced into wind tunnel flow past a cylinder and observe the changes in vortex shedding. This should contribute new knowledge concerning turbulence effects on vortex shedding processes.

Such new knowledge is the goal of this dissertation. It is hoped that this new knowledge can, in turn, be applied to a better understanding of the atmospheric vortex street as well as to the solution of engineering problems concerning vortex shedding from buildings and structures.

In this dissertation, increasing turbulence was systematically introduced into wind tunnel flows past a cylinder until the highest feasible turbulence intensity was obtained (near 25%) in the center of a tunnel. Vortex shedding from two different sizes of cylinders (4.5" and 2.75" diameters) was observed in various turbulent flow conditions. The tunnel had a test section 2' x 2' x 6'.

The development of turbulence intensities approaching 25% in the middle of a wind tunnel is higher than in any studies known to the author. In addition, this turbulence was produced by plates with many small holes and having very high blockage ratios, as high as .97. This also is different from most previous investigations which generally used square grids with blockage ratios less than 50%.

The approach used in this dissertation is: Step A, observe the effects of increasing turbulence intensity upon vortex shedding, at nearly constant  $Re$ , as displayed by changes in vortex shedding frequency, angle of boundary layer separation, and point of transition; Step B, observe the turbulence conditions (mean air speed, rms of fluctuating air speed, integral scale of turbulence, eddy viscosity, micro scale of turbulence, etc.) of the air flows associated with significant effects observed in the step above; and Step C, analyze the first two steps to provide some predictive relations showing what increased turbulence would do to a vortex shedding condition, as well as an improved model of general turbulence effects on vortex shedding.

The coordinate system is three-dimensional Cartesian, as shown:



The  $x$  axis is horizontal along the main air stream down the wind tunnel;  $y$  is vertical, normal to the mean flow;  $z$  is horizontal, normal to the mean flow. The origin is 48" downstream from the entrance to the wind tunnel test section and 12" from each wall of the tunnel. The cylinder's center coincides with the origin and its axis is along the vertical  $y$  axis.

## 2. VORTEX SHEDDING

### 2.1 GENERAL

The best single review of the entire literature on vortex shedding theory and experimentation is believed to be the article by Marris (1964). Mair and Maull (1971) include later developments. Gerrard (1966b), Bloor (1964) and Bearman (1969) have studied the mechanics of vortex street formation. Robertson (1965) explains the potential flow theory for vortex streets. Following is a summary, and Appendix A gives more detailed information.

### 2.2 CLASSICAL VORTEX SHEDDING REGIMES

Karman vortex streets have been observed from Reynolds number,  $Re$  ( $Re = UD/\nu$ ), values of 40 to  $10^7$ , except for small transition regions from one vortex shedding regime to another.

The periodicity of the vortex shedding is expressed non-dimensionally by the Strouhal number,  $St$  ( $St = fD/U$ ). The frequency of shedding,  $f$ , is from one side only.  $D$  is the cylinder diameter. Empirical information shows that  $St$  has some functional dependence on  $Re$  over most of the entire range  $40 < Re < 10^7$ . The preceding  $Re$  values are for free stream flows with a minimum of turbulence and past smooth cylinders. Consequently,  $Re$  has always been calculated by kinematic viscosity,  $\nu$ , sometimes referred to as  $Re(\nu)$ .

Figure 1 shows the observed relation between  $St$  and  $Re$ . This is a composite of information from several authoris, primarily Roshko (1954, 1961), Bearman (1969) and Achenbach (1968). Their references are further treated in Section A.1. The terminology and limiting

Re values are not consistent in the literature. Consequently, I have used some new terminology which I believe is more descriptive and defines four "classical" vortex shedding regimes which will include most of the data found in the literature.

Figure 2 depicts these four vortex shedding regimes in Re values; St values; cylinder boundary layer  $\pm$  separation angle,  $\alpha$ , from the front stagnation point; and turbulence characteristics in the cylinder boundary layer and in the vortex street. It is emphasized that they apply to air streams with near zero turbulence intensity upstream from the cylinder. Following is a definition of these four classical regimes which will be used throughout this study.

(1) "Laminar" vortex shedding regime (same as Roshko's "regular"):  $40 < Re < 150$ , boundary layer and vortices are laminar;  $\alpha$  near  $\pm 109^\circ$ ;  $.10 < St < .18$ ;  $St = .212 - 4.49/Re$ .

(2) "Sub-critical" vortex shedding regime (similar to Roshko's "irregular"):  $300 < Re < 3.0 \times 10^5$ ; laminar boundary layer and turbulent vortices;  $\alpha \pm 72^\circ$  to  $\pm 95^\circ$ ;  $.18 < St < .21$ .

(3) "Super-critical" vortex shedding regime:  $4.0 \times 10^5 < Re < 1.5 \times 10^6$ ; laminar boundary layer separation near  $\pm 105^\circ$  with immediate transition and reattachment as a turbulent boundary layer; boundary layer separation near  $\pm 140^\circ$ ; turbulent vortices;  $.40 < St < .46$ .

(4) "Turbulent" vortex shedding regime:  $2.5 \times 10^6 < Re < 10^7+$ ; boundary layer and vortices are turbulent;  $\alpha$  between  $\pm 115^\circ$  and  $\pm 120^\circ$ ;  $.24 < St < .29$ .  $10^7$  is the largest Re value at which vortex shedding has been observed.

Three distinct "changes" in flow regimes are indicated: one between "Laminar" and "Sub-critical" regimes; one between "Sub-critical"

and "Super-critical," and between "Super-critical" and "Turbulent." To avoid confusion with "transition," meaning a change from laminar to turbulent flow, the term "discontinuity" will be used for all (three) regions of change between the four vortex shedding regimes. In these discontinuities, the  $St$  and  $\alpha$  values are less distinct; they become chaotic in the discontinuity between "Super-critical" and "Turbulent."

### 2.3 MECHANICS OF VORTEX SHEDDING

As air passes a cylinder (the cylinder is always perpendicular to the mean air flow) it forms two boundary layers on the cylinder, each starting at the stagnation point and extending around the cylinder. If the cylinder diameter is much larger than the boundary layer thickness, the boundary layers are almost identical to the Blasius flat plate boundary layer. This case applies to this study.

For Stokes flow ( $Re < 4$ ) these boundary layers extend completely around the cylinder to the rear stagnation point. The streamlines past the cylinder appear to be the same as for potential flow.

As  $Re$  increases, the boundary layers begin to separate from the cylinder surface before reaching the rear stagnation point. This separation angle works back to about  $\pm 110^\circ$  by the time  $Re$  becomes 40. Simultaneously, the pressure begins to decrease just downstream from the rear stagnation point (base pressure). Also, two small, stationary, symmetrical vortices form just behind the cylinder and enlarge (if  $Re < 40$ ). These are developed by the separated boundary (or shear) layers rolling up into vortices.

At this point, with  $Re$  approaching 40, there are two conditions of flow instability in the lee of the cylinder. First, there is a

sizeable wake in which the mean longitudinal flow is less than the mean free flow, giving a shear condition. Second, the separated laminar boundary layers extend inside the wake as two streams of shear flow and form two stationary vortices. It is generally considered that when  $Re \approx 40$ , the instability in the wake first creates a vortex street some distance downstream. As  $Re$  increases to 95, the vortex street works upstream and a change occurs such that the vortices in the street begin to originate in the separated boundary layers very close to the cylinder (see Tritton, 1959). At all higher  $Re$ , the vortices continue to form in the separated boundary layers, immediately downstream from the cylinder.

In the sub-critical regime, there is little variation in  $St$  over  $Re$  values from 300 to  $3 \times 10^5$ . Gerrard (1966b) explains this by changes in the length and width of the "formation region" between the cylinder and the first organized vortex street. As  $Re$  increases, they change inversely with each other; their product is nearly constant and  $St$  values vary directly with their product.

If there is turbulence in the free stream, it can penetrate into the boundary layer on the cylinder and make transition occur at a lower  $Re$ . The effectiveness of this penetration increases with the turbulence intensity, but it is also influenced by the integral scale of turbulence. If the integral scale of turbulence is much larger than the cylinder diameter,  $D$ , the eddies may pass the cylinder with little effect on the boundary layer; if it is much smaller than  $D$ , the turbulence may be dissipated before affecting the boundary layer. Bearman (1972) and Hunt (1971) treat this. It is related to vortex stretching in stagnating flow, as discussed by Sadeh, et al., (1970).

Bloor (1964) showed that Tollmein-Schlichting waves help cause the laminar vortices to become turbulent. Increased free stream turbulence should enhance this transition.

Roshko (1954) found that, for  $Re > 300$ , the vortex street dissipates and loses its identity at shorter distances downstream. Increased free stream turbulence should cause this dissipation to happen faster (i.e., at lower  $Re$ ).

#### 2.4 RELATION BETWEEN STROUHAL NUMBER AND DRAG COEFFICIENT

The drag coefficient,  $C_d$  ( $C_d = \text{drag force}/\rho U^2 A$ ), depends upon both the fluid friction on a cylinder and the "base pressure" (pressure deficit immediately behind the cylinder relative to the pressure in the undisturbed flow). As  $Re$  increases, the base pressure becomes more important, and for air flows past cylinders with  $Re > 10^4$  (see Goldstein, figure 154),  $C_d$  and the base pressure effects can be considered identical.

The base pressure is directly proportional to the width of the wake immediately behind the cylinder. Hence,  $C_d$  is directly proportional to the width of the wake, at higher  $Re$ . The vortex shedding frequency is faster when the two shear lines (from separated boundary layers) are closer together. Thus the Strouhal number is inversely proportional to the width of the wake.

Figure 3 shows Roshko's (1961) representation of  $C_d$  and  $1/St$  as functions of  $Re$ ; the similarity of the two curves is striking.

From the preceding arguments it follows that, for  $Re > 10^4$ , the product of  $St \times C_d$  should be approximately constant.

### 3. TURBULENCE PARAMETERS

Turbulence was introduced into the wind tunnel test section by placing a series of plates (with different amounts of flow blockage), one at a time, across the entrance to the test section. Changes in the  $St$  values describing the vortex shedding from the cylinder in the tunnel were noted. Changes in  $\alpha$  were observed for certain cases. Turbulence parameters describing the different flows, in which these changes took place, were then needed to make comparisons with these vortex shedding changes and to seek interrelations among the turbulence parameters.

Eight different types of turbulence parameters were measured to describe several turbulent flows. To allow representative comparisons of different flows, the cylinder was removed and the turbulence characteristics measured by a hot wire sensor placed at the point which had been occupied by the center of the cylinder.

The turbulence parameters are:

(1) Turbulence intensity,  $Ti = \bar{u}/U$ . If expressed as a percentage, the ratio has been multiplied by 100. When King's equation is

applied, 
$$Ti = \bar{u} \left[ \frac{2E}{R(R-RA)BCU^c} \right]$$

(2) Spectra and correlation analyses.  $G_{xx}(f)$ , power spectra, was used to identify dominant vortex shedding frequencies or in calculating the integral scale of turbulence, or for determining the micro-scale of turbulence.

$$G_{xx}(f) \equiv \lim_{\Delta f \rightarrow 0} \lim_{T \rightarrow \infty} \frac{1}{(\Delta f)T} \int_0^T x^2(t, f, \Delta f) dt$$

$R_{xx}(\tau)$ , the autocorrelation, was employed as a second method of finding dominant frequencies or in calculating the integral scale of turbulence.

$$R_{xx}(\tau) \equiv \lim_{T \rightarrow \infty} \frac{1}{T} \int_0^T x(t) x(t-\tau) dt$$

In addition, cross spectra,  $G_{yx}(f)$ , and cross correlations,  $R_{yx}(\tau)$ , were utilized to find dominant frequencies when both a pressure transducer and a hot wire sensor were used simultaneously to observe the same vortex shedding. These spectra and correlations were calculated, by numerical methods employing the Fast Fourier Transform, in a Fourier Analyzer (Hewlett-Packard, H-P, Model 5450A) from recorded analog data. Figure 4 is a photograph of the Fourier Analyzer System. The above terms are more fully explained in Appendix B.

(3) Integral scale of turbulence,  $L_x$ .  $L_x = \tau_0 U$ , where  $\tau_0$  is the lag time for  $R_{xx}(\tau)$  to first reach zero. Also,  $L_x = UF(0)/4$  and  $L_x = UF(M)/4$  where  $F(0)$  is the  $F_{xx}(f)$  value extrapolated to  $f = 0$ , and  $F(M)$  is similar to  $F(0)$  but is the  $F_{xx}$  value where a distinct maximum of  $F_{xx}(f)$  exists at a low  $f$  value.

(4) Microscale of turbulence,  $\lambda$ .

By Taylor's method:

$$\frac{1}{\lambda^2} = \frac{4\pi^2}{U^2} \int_0^{\infty} f^2 F_{xx}(f) df$$

Or Townsend's method:

$$\lambda = \sqrt{2} U \bar{u} / \overline{(du/dt)}$$

(5) Eddy viscosity,  $K_m$ .  $K_m = \bar{u} L_x$  is adopted because  $K_m$  values are needed at the center of the tunnel, and  $K_m = -\overline{uv}/(dU/dy)$  would not be appropriate due to a theoretical zero in the denominator.

(6) Taylor parameter,  $T_a$ .  $T_a = T_i \times (D/L_x)^{.2}$  combines both the turbulence intensity and the ratio of cylinder diameter to integral scale. Taylor developed this theoretically while investigating the critical  $Re$ ,  $Re(c)$ , which is the  $Re$  value for the beginning of the super-critical vortex shedding regime, for a sphere.

(7) Special Reynolds numbers. Eddy viscosity [ $Re(K_m) = UD/K_m$ ], using eddy viscosity; plate  $Re$ , [ $Re(p) = Ud/(1 - Br)\nu$ ], for plate effects, where  $Br$  is the area blockage ratio of the turbulence producing plate and  $d$  is a hole diameter; and the classical turbulence  $Re$ , [ $Re(\lambda) = \bar{u} \lambda/\nu$ ].

(8) Fluctuations in  $x$ ,  $y$ ,  $z$  direction. For one flow condition, comparisons of  $\bar{u}$  and  $\bar{w}$  were made by two methods. They are the yawed hot wire and the heat diffusion methods. The heat diffusion method was used for several flow conditions.  $\bar{v}$  and  $\bar{w}$  were assumed to be comparable;  $\bar{u}$  was larger for most flows.

Turbulence parameters are discussed in more detail in Appendix B.

## 4. INSTRUMENTATION AND EXPERIMENTAL PROCEDURE

### 4.1 WIND TUNNELS

Data was gathered in a Meteorology Research, Inc., Model 2035 low speed wind tunnel. Figure 5 is a general view of the tunnel, and figure 6 gives a diagram drawn to scale. It is an open circuit type with a test section 2' x 2' square and 6' long. The overall length is 22 feet. The motor and fan are at the downwind end. The entrance has a honeycomb and a fine mesh screen followed by a 4:1 contraction. The test section can be separated from the entrance section. Both are on rollers so they can be pushed apart for easy insertion of a plate.

The cylinder was placed vertically through the center of the tunnel, putting the center of the cylinder 48" downstream from the entrance to the test section. The center of the cylinder was also 12" from each wall. The center of the cylinder coincided with the origin of the coordinate system.

The turbulence producing plates were placed across the upstream end of the test section and then the entrance portion of the tunnel was pushed against them and clamped tightly. Steps were taken to make the entire wind tunnel secure from air leaks.

For the open tunnel, the turbulence intensity was .3%.

A larger, closed return tunnel, built for WSMR by CSU, with a vortex shedding anemometer and a Prandtl tube, was used for calibration purposes. Due to its rigid construction which prevented the insertion of the plates, it was not practical to utilize it for introducing turbulent flows.

#### 4.2 TURBULENCE PRODUCING PLATES

Table 1 lists the specifications of the turbulence producing plates. All were made by drilling many small holes ( $3/16"$  or  $1/4"$  diameter) in sheets of metal or masonite. They gave blockage ratios from .500 to .972. Figures 7 and 8 show plates .500 and .972, respectively.

A square grid was modeled after one of Surry's (1969) in a closely related study. This gave valuable comparisons that are considered part of the equipment check out and calibration (see Appendix C). A second square grid, with open areas and bars one half the size, was also utilized. Figure 9 is "Surry's" grid, with  $Br = .340$ .

All plates are identified by their blockage ratio values.

#### 4.3 CYLINDERS

Two cylinders, with 4.5" and 2.75" diameters, were employed.

Figure 5 shows the 4.5" cylinder in the wind tunnel. Figure 10 has it "broken" apart at the middle. This was necessary to change the pressure transducer pressure tubes from taps at one  $\pm\alpha$  to another. The taps are brass tubes glued in place through the cylinder wall and extruding about  $1/4"$  inside. Plastic tubing (3.5" long) connected the pressure transducer to the taps. They were changed from one set of taps to another manually. The taps extend from  $\alpha = \pm 70^\circ$  to  $\alpha = \pm 160^\circ$ . On the outside of the cylinder the brass tubes were filled with glue and sanded flush with the cylinder. Then a hole .02" diameter was drilled through the glue to complete the tap. The brass tubes have inner and outer diameters of .063" and .096"; the plastic tubing has inner and outer diameters of .070" and .128", respectively.

Both cylinders were constructed of plastic. Their surfaces were made as smooth as possible and the pressure tap holes gave minimum protuberances on the surface. On the 4.5" cylinder the pressure tap holes were staggered from 1" to 2" below the seam. All holes were 12" to 13" from the tunnel floor.

The 4.5" cylinder was chosen as the smallest one in which the pressure transducer could be fitted and still leave room to change the connections to the pressure taps. The initial observations were made with this cylinder.

As explained in Appendix C, a reduction of 8% was made to the free stream air speed to account for the solid blockage and wake blockage effects of the 4.5" cylinder.

Because the 4.5" cylinder caused a large blockage in the tunnel, a second cylinder, 2.75" in diameter was used to compare the accuracy of the correction for solid blockage and wake blockage, see figure 11. It also offered a method of checking the St values for significant flow conditions. The 2.75" cylinder was the smallest one in which the pressure transducer could be placed. Taps were constructed separately at  $\alpha = \pm 90^\circ$ ,  $\pm 130^\circ$  and  $\pm 150^\circ$ . Taps were exposed ends of the plastic tubing, 5.25" long, trimmed flush with the exterior of the cylinder. A correction of 5% was made to the free stream air speed.

#### 4.4 AIR SPEED

##### 4.4.1 PITOT TUBE

A pitot tube and micromanometer (Mark 5, Airflow Developments Ltd) were utilized to calibrate the constant temperature anemometers, CTA, when there were no plates in the tunnel. The pitot tube entered

from the roof of the tunnel; its leading point was 18.75" upstream from the cylinder stagnation point and 6" down from the ceiling, ( $x = -21"$ ,  $y = 6"$ ,  $z = -1"$ ). The pitot tube was not used for air flow less than 14 fps and most data were taken at 16 to 18 fps.

The pitot tube air speed was calculated by the following equation which was derived from the Ideal Gas Law, Bernoulli's Equation, and a Gas Constant from dry air. This required the use of the virtual temperature,  $T_v$ , to account for water vapor;  $\Delta P$  was observed by the manometer and  $P$  by a barometer.

$$U \text{ (fps)} = 92.35 \times \left[ \frac{\Delta P \text{ (inches water)} \times T_v \text{ (}^\circ\text{R)}}{P \text{ (mbs)}} \right]^{.5}$$

#### 4.4.2 CONSTANT TEMPERATURE ANEMOMETER (CTA) SYSTEMS

This includes hot wire anemometers and hot film anemometers. Both are resistance-temperature transducers and can be used to measure either the mean air speed,  $U$ , or the rapid fluctuations in air speed,  $u$ . For a full discussion, see Sandborn's text (1972).

Two CTA systems were available: a DISA 55A01 hot wire anemometer, and a TSI 1054B hot film anemometer.

The DISA system was equipped with a hot wire, platinum plated tungsten, 5 microns in diameter and 1.25 mm long. It provided all turbulence observations where the fluctuating voltage,  $e$ , was needed for calculating power spectra, autocorrelations, and related items. The DISA was also used for some observations of mean air speed. The overheat ratios were 1.5 or 1.8.

Most mean air speed observations were made by the TSI 1054B system. It had a Model 1330-60 temperature compensated hot film sensor.

This sensor was .15 mm in diameter and 3.0 mm long; it had gold plating on the sensing area over a quartz coated platinum film sensor on a glass rod.

All of the CTA's were calibrated by comparing them with the pitot tube. This gave an  $E$  vs  $U$  curve. This calibration was made in a clear tunnel (no plates) immediately before and after a CTA was used. In most cases, comparisons were made at speeds of 14, 18, 22, and 28 fps.

In addition, the TSI CTA was calibrated by comparison with a vortex shedding anemometer, in the larger WSMR tunnel, using speeds of 2 to 8 fps, and with its Prandtl tube for 10 to 30 fps.

It was found that for both CTA's, the calibrations for 14, 18 and 22 fps could be accurately approximated by straight lines if  $E^2$  vs  $\sqrt{U}$  (or  $E^4$  vs  $U$ ) were used on rectangular coordinates. This, of course, is an application of King's equation,  $E^2/R(R - RA) = A + BU^c$ , using an exponent of  $c = 0.5$ .

The DISA calibration always drifted with time. It was assumed that this drift was linear with time and corresponding corrections were made in converting  $E^2$  to  $\sqrt{U}$ .

The TSI hot film system, with a temperature compensating device built into the sensor circuit, was found to have very little drift in its calibration. Daily changes, when compared with the pitot tube, were less than 1% at 14 to 30 fps. Consequently, the TSI CTA was used as a transfer standard for calibrating the DISA hot wire CTA. A TSI calibration curve was prepared in the larger tunnel for speeds from 2 to 30 fps. This curve was subsequently checked daily by the pitot tube in the smaller tunnel (for speeds of about 14 to 28 fps).

A daily correction for the entire curve was determined by this pitot tube comparison. See Appendix C for more details.

Peterka's (1971) computer program provided least squares solutions of the coefficients and exponents of King's equation. This, in turn, provided a more accurate calibration of the DISA CTA.

The CTA DC voltage was read visually from a H-P digital voltmeter Model 3459A. To obtain a mean DC voltage during a long data recording (e.g., 10 to 15 minutes recording of  $f$  or  $e$ ), successive maximum and minimum DC voltages were tabulated. The voltmeter was adjusted to give a DC voltage every three to five seconds. 20 to 30 maximum and minimum voltmeter readings were chosen for tabulation. These maximum and minimum values were then averaged to give a mean DC voltage,  $E$ , for the entire data recording.  $E$  was converted to mean air speed,  $U$ , by the daily calibration curve, for the entire data collection.

Each CTA had voltmeters which provided useful comparisons.

Several attempts were made to record the DC voltage and then obtain  $E$  from the Fourier Analyzer. This was simple to record and process in the Analyzer. However, the maximum voltage output by the recorder was 2.5 volts while a typical HWA DC voltage was 7 volts. These differences required a delicate setting of the "record" and "reproduce" attenuators so that the reproduced voltage could be multiplied by a factor to give the original HWA voltage. This procedure never provided a "good" HWA calibration curve of  $E$  vs  $U$ . Therefore, recording of DC voltage was not used.

The  $\bar{e}$  voltages from the DISA, used for calculation of  $T_i$ , were obtained by readings of the RMS voltmeter in the DISA system. This voltmeter is built on the thermocouple principle and has a very long

time constant. The voltage selected was the one at which it seemed to settle after slowly reaching a maximum value and then falling back slightly. Usually, this voltage was compared simultaneously with the value from a TSI True RMS Voltmeter, Model 1060, set to a 3 or 10 second time averaging period. Good comparison was consistent.

#### 4.5 VORTEX SHEDDING FREQUENCY

The pressure transducer, Statham Model PM 283 TC  $\pm 0.15-350$ , with pressure ports at  $\alpha = \pm 70^\circ$  to  $\alpha = \pm 160^\circ$  by  $10^\circ$  increments (in the 4.5" cylinder), measured vortex shedding frequency,  $f$ , from the cylinder. The voltage variations from the transducer were amplified and then recorded in a H-P, Model 3690, Instrumentation Recorder. A low pass filter was utilized to keep out higher frequency noise. The recorded data was analyzed by power spectra, and sometimes autocorrelation, to determine the major shedding frequency. Approximately 10 minutes of data was recorded for each plate and for each set of pressure taps. This was done so that a mean of a large number of spectra or correlations (60 to 120) could be made.

For all significant flows, simultaneous measurements, by both the pressure transducer inside the cylinder and a hot wire in the cylinder wake, were recorded to get two independent observations of  $f$ . Cross spectra or cross correlations were employed to analyze them. A separate hot film anemometer was used upstream to observe  $U$ .

#### 4.6 DATA ACCURACY

This is treated in detail in Appendix C and comes to these conclusions concerning the accuracy of data observations;

(1) Air temperature or virtual temperature (to account for water vapor) and atmospheric pressure can be observed to within  $\pm 1\%$ .

(2) The frequency of vortex shedding,  $f$ , can be obtained to  $\pm 2\%$  by power spectra and to  $\pm 1\%$  by correlation when the latter indicates one dominant frequency.

(3) The mean air speed,  $U$ , is accurate to  $\pm 3\%$  at speeds near 18 fps. This accuracy decreases at lower speeds and improves slightly at higher speeds. Corrections for blockage effects add to the error when  $U$  is used in calculating  $St$ ; this error may increase with the  $Ti$ .

(4) The RMS of the longitudinal velocity variations,  $\bar{u}$ , is probably accurate to  $\pm 5\%$  or less at low  $Ti$ , but becomes less accurate as  $Ti$  increases. As a rule of thumb, it is suggested that the error range is quantitatively the same as the  $Ti$ , when both are in percents.

(5) The microscale of turbulence,  $\lambda$ , is accurate to about  $\pm 10\%$ .

(6) The integral scale of turbulence,  $L_x$ , as calculated from  $e$  data by one HWA, is the least accurate of the basic parameters observed. Comparison of the  $\tau_0$  and  $F(0)$  methods, for the same data, suggest  $\pm 100\%$ . However, in comparing  $L_x$  in different flows, but calculated by the same method, it is assumed that the results of these comparisons should be more reliable, estimated at  $\pm 20\%$ .

(7) Eddy viscosity,  $K_m$ ; the Taylor parameter,  $T_a$ ; and the special Reynolds numbers,  $Re(K_m)$ ,  $Re(p)$ , and  $Re(\lambda)$  are derived from one or more of the above. They range from  $\pm 3\%$  for  $Re(p)$  to  $\pm 32\%$  for  $T_a$  or  $Re(K_m)$  with  $25\% Ti$ .

All of the above values are conservative and most data should be much more accurate than these error ranges or uncertainty limits.

## 5. EXPERIMENTAL RESULTS

### 5.1 GENERAL

Data collection started at CSU. It was observed that when a high blockage ratio plate (.958) was inserted across a tunnel, the dominant vortex shedding frequency became much smaller for the same air speed.

The work has been completed at WSMR. A variety of plates and grids were built; a 4.5" cylinder allowed changing values of  $\alpha$  for the pressure transducer; and it was possible to define the dominant shedding frequency by averaging a large number of spectra or correlations.

For an "open" tunnel (no plate across entrance to test section) at WSMR with  $Re = 4 \times 10^4$ ,  $St$  values near .20 were observed. This is the classical "sub-critical regime," and is indicated by "A" in figure 1. The much reduced frequency behind plate .958 (and .972) was observed to give  $St = .10$ .

Experimentation suggested that higher  $St$  values should result in flow conditions somewhere between the extremes of an open tunnel flow and flow behind plate .972.

It was then hypothesized that, while keeping  $Re$  values near  $4 \times 10^4$  and steadily introducing more turbulence into the mean flow, it should be possible to induce changes in vortex shedding conditions ( $St$  and separation angles) that are analogous to the following five classical vortex shedding conditions (see also figures 1 and 2):

- (1) "Top  $Re$  value of the sub-critical regime"
- (2) "Discontinuity between the sub- and super-critical regimes"
- (3) "Super-critical regime"
- (4) "Discontinuity between super-critical and turbulent regimes"
- (5) "Turbulent regime"

The above turbulence induced changes were observed with the 4.5" cylinder. Then a 2.75" diameter cylinder was used to see if changes could be induced in vortex shedding from it. A smaller cylinder was selected because it required a lesser flow blockage correction. In addition, it was fitted with "end plates" (after Bradshaw, p. 180, 1964) to reduce end effects.

Later, associated turbulence conditions of the air flows inducing these ten changes (five for each cylinder) were observed. The effective Reynolds number,  $Re(E)$ , associated with each induced change was used to compare the effects of individual turbulence parameters on vortex shedding.  $Re(E)$  was estimated from figure 1 as the  $Re$  value associated with the corresponding classical vortex shedding regime (in near zero turbulence intensity air flow).

## 5.2 PRELIMINARY INVESTIGATIONS

Several plates were constructed with different  $Br$  values. The 4.5" cylinder provided pressure taps that could be varied from  $\alpha = \pm 70^\circ$  to  $\alpha = \pm 160^\circ$ . Figures 12, 13, and 14 show resulting spectra, for  $\pm 90^\circ$ ,  $\pm 130^\circ$ , and  $\pm 150^\circ$ , for the open tunnel and for several plates with  $Br$  of .500 to .972. At all angles the open tunnel and plate .500 gave sharp spectra with equal  $St$  values. All of the other plates showed completely turbulent spectra for  $\alpha$  of  $150^\circ$  and  $160^\circ$ ; the spectral changes were gradual and consistent for all of the other plates at angles from  $\alpha = \pm 70^\circ$  to  $\alpha = \pm 140^\circ$ .

$Ti$  values increased steadily as the plate  $Br$  increased and  $Ti$  as high as 28% was observed upstream from the cylinder. (Very near to the cylinder much higher  $Ti$  values existed.)

All  $f$  values up to this point had been obtained by pressure transducer observations. The distinct possibility existed that these dominant  $f$  values were a result of the free stream turbulence rather than from vortex shedding. To resolve this question, a hot wire was placed directly behind the cylinder. Cross spectra of the simultaneously recorded signals from both the hot wire and the pressure transducer were utilized to find the dominant  $f$ .

It is believed that one clear maximum  $f$  value in this cross spectra, especially when averaged over 50 to 120 spectra, could only be caused by an organized vortex shedding process. The random, turbulent fluctuations observed by both instruments should be uncorrelated because one senses pressure changes on the cylinder surface and the other observes air speed changes a short distance from the cylinder.

Several figures (16 to 27) depict the results of simultaneous pressure transducer and hot wire measurements of vortex shedding frequencies from each of the cylinders in different induced vortex shedding regimes. Each figure shows four analyses of the same vortex shedding: power spectra of hot wire; power spectra of pressure transducer; cross spectra of the wire and the transducer; and cross correlation between the instruments.

The entire range of  $Re$  values of the air flows, indicated by "R" in figure 1, was  $.9$  to  $5 \times 10^4$ .

The possible influence of cylinder or wind tunnel vibrations on the pressure transducer and hot wire observations was investigated. An accelerometer was attached to the cylinder and a cross spectra made with the pressure transducer signal. The accelerometer was

later attached to the wind tunnel motor and fan support, and a cross spectra was made with the turbulent wind variations,  $u$ , as observed by the hot wire, with the cylinder removed. In all cases, the cross spectra showed no significant relation between vibrations and the  $f$  or  $u$  observations. Consequently, vibration effects can be ignored.

### 5.3 INDUCED CHANGES IN STROUHAL NUMBER

#### 5.3.1 OPEN TUNNEL FLOW (CONDITION A)

Figure 15 presents results in the open tunnel at  $U = 19.4$  fps,  $St = .205$  and  $Re = 3.8 \times 10^4$  for the 4.5" cylinder. The spectra and correlations are all sharp and clean, and give identical  $f$  values. This is the classical "sub-critical" vortex shedding regime. The  $T_i$  of this flow is .3%. This condition is represented by point "A" in figure 1.

With  $U = 30$  fps, ( $Re = 3.6 \times 10^4$ ) the 2.75" cylinder produced  $f = 25.3$  Hz which indicated  $St = .193$  and also is represented by "A." A figure of this is not included because its appearance was very similar to that of figure 15.

#### 5.3.2 INDUCED CONDITIONS FOR THE TOP OF THE SUB-CRITICAL REGIME (CONDITION B)

Figure 16 shows flow behind plate .690 with  $U = 17.4$  fps,  $St = .211$  and  $Re = 3.4 \times 10^4$ . The spectra and correlation are slightly less sharp but still show a clear cut maximum  $f$ . This is induced vortex shedding near the top  $Re$  values of the sub-critical regime.  $Re(E) \approx 2.1 \times 10^5$ . It is indicated by "B" in figure 1.

Figure 17 is the same for the 2.75" cylinder behind plate .748 with  $U = 13.7$  fps,  $St = .206$  and  $Re = 1.7 \times 10^4$ ; it is indicated by "B".  $Re(E) \approx 2.2 \times 10^5$ .

### 5.3.3 INDUCED CONDITIONS FOR THE DISCONTINUITY BETWEEN THE SUB- AND THE SUPER-CRITICAL REGIMES (CONDITION C)

Figure 18 depicts conditions behind plate .748 at  $U = 16.9$  fps,  $St = .249$  and  $Re = 3.3 \times 10^4$ . The spectra have widened considerably and the correlation indicates randomness in the flow. However, the same dominant  $f$  can be seen in all. This is induced vortex shedding similar to the discontinuity condition between the sub- and the super-critical regimes.  $Re(E) = 3.6 \times 10^5$  is estimated. It is shown at point "C" in figure 1.

All discontinuities are considered to consist of a mixture of three things: (1) individual vortices shed at the "lower" regime, sub-critical in this case; (2) individual vortices shed at the "higher" regime, super-critical in this case; and (3) random fluctuations caused by turbulence in the main flow. The changes in shedding from one regime to the other are due to small variations in the mean air speed and direction, slight variations in the cylinder shape and surface, and turbulent fluctuations which happen to enhance an individual vortex as it is shed. By taking the mean of a large number of observations of  $f$ , a dominant  $St$  value can be found where it would not be apparent in individual observations of  $f$ , such as by Lissajous figures or strip chart recordings.

This explanation is compatible with Roshko's (1954) observations of the "lowest" discontinuity, between laminar and sub-critical

regimes, although turbulence in the main stream was negligible. He developed two  $Re$  vs  $St$  relations ( $St = .212 - 4.49/Re$  for the laminar regime and  $St = .212 - 2.69/Re$  for the lower part of the sub-critical regime) both of which approximately described the discontinuity condition.

The turbulence in the mean flow will always tend to spread the spectra of  $f$  because the turbulent fluctuations are more random. As the turbulence increases a point will be reached where the turbulent fluctuations dominate and no single dominant  $f$  can be found. As shown later, this is common in the super-critical/turbulent discontinuity.

This induced discontinuity, sub-critical/super-critical, apparently is in the range where turbulence effects can first overshadow a dominant  $f$  value being observed by both a pressure transducer and a hot wire.

In seeking an example of condition  $C'$  for the smaller cylinder, many combinations of plates,  $\alpha$ ,  $U$  and hot wire position were used. None gave a dominant  $f$  in the cross spectra. Figure 19 presents the best example ( $Br = .801$ ,  $\alpha = \pm 150^\circ$ ,  $U = 16.4$  fps, hot wire at  $x = 2D$ ,  $z = .4D$ ). The pressure transducer showed a dominant  $f$  at 16.3 Hz, giving  $St \approx .23$ . The hot wire spectra was more like the turbulence in the mean flow with a maximum near 8 Hz. The free stream turbulence is apparently strong enough to sufficiently disrupt the vortex shedding so that the hot wire senses no organized vortex street.

#### 5.3.4 INDUCED CONDITIONS COMPARABLE TO THE SUPER-CRITICAL REGIME (CONDITION D)

Figure 20 indicates induced vortex shedding similar to the "super-critical" regime. The spectra all identify a dominant  $f$  but the turbulence has become so large that the cross correlation no longer defines  $f$ .  $U = 8.1$  fps behind plate .804 produced  $St = .329$  and  $Re = 1.6 \times 10^4$ . It is shown by "D" in figure 1.  $Re(E)$  is estimated at  $1 \times 10^6$ .

Figure 21 is the counterpart for the 2.75" cylinder, plate .861,  $U = 7.1$  fps,  $St = .339$   $Re = 8.6 \times 10^3$ , shown by "D'."

These induced conditions were both difficult to find. Many trials of different plates and wind speeds were required. In both cases, air speed was reduced through plates that previously were producing discontinuity conditions between super-critical and turbulent regimes. This suggests that the super-critical regime may be especially sensitive to free stream fluctuations,  $\bar{u}$ ,  $\bar{v}$ , and  $\bar{w}$ .

#### 5.3.5 INDUCED CONDITIONS SIMILAR TO THE DISCONTINUITY BETWEEN THE SUPER-CRITICAL AND THE TURBULENT REGIMES (CONDITION E)

No definition of a dominant  $St$  value was possible in this condition; it existed for a wide range of blockage ratios in the plates.

Figure 22, where  $U = 18.7$  fps,  $Re = 3.7 \times 10^4$ , behind plate .945 is shown, is used to depict the induced vortex shedding condition that is similar to the discontinuity between the super-critical and the turbulent regimes. No  $St$  value can be defined. It is represented by point "E" in figure 1.  $Re(E) = 2 \times 10^6$ .

Figure 23 is the same for the smaller cylinder. Plate .945 was utilized with  $U = 20.9$  fps,  $Re = 2.5 \times 10^4$ .  $Re(E) = 2 \times 10^6$ .

It is interpreted that the turbulent  $\bar{u}$ ,  $\bar{v}$  and  $\bar{w}$  are sufficiently strong to override all organized vortex shedding, especially since it is partially in the super-critical and partially in the turbulent regimes.

The pressure transducer gives a wider spectra in both cases which could be interpreted as a combination of vortices shed by both regimes plus random pressure fluctuations. The hot wire in both cases has the strongest signal near 6 or 8 Hz which is among the frequencies of dominant power in the free stream turbulence (see figure 42). This suggests that some organized vortex shedding may exist at the cylinder surface but it is quickly destroyed by the free stream turbulence and the hot wire, less than one or two diameters downstream, observes mainly the free stream turbulence condition.

#### 5.3.6 INDUCED TURBULENT REGIME (CONDITION F)

Figure 24 presents conditions behind plate .972 at  $U = 23.2$  fps,  $St = .100$ ,  $Re = 4.6 \times 10^4$  and  $Re(E) = 5 \times 10^6$ . The spectra again define a dominant  $f$  but the cross correlation is not. This is induced vortex shedding similar to that in the turbulent regime. It is given by point "F" in figure 1. This condition was relatively easy to induce for both cylinders. This further indicates that the super-critical regime is especially sensitive or unstable to turbulence in the mean flow.

It was found that the location of the hot wire behind the cylinder becomes very sensitive at higher  $Ti$  conditions. At the start, in the open tunnel and plates with lower  $Br$ , the position of  $x = 1.5D$  and  $z = .5D$ , as recommended by Bearman, worked fine. (Some

sensitivity of position was noted for plates .801 and .861.) Behind plate .972, the hot wire had to be placed much closer to the cylinder to pick up the dominant  $f$  recorded by the pressure transducer. Following Gerrard's analysis of vortex formation, this has significant implications in explaining the induced  $St$  values. In figure 24 the hot wire was at  $x = 1.5D$  and  $z = .5D$ . But, as shown in figure 25, the best cross spectra behind the 4.5" cylinder was found when the wire was  $.25D$  downstream from a  $130^\circ$  pressure tap ( $x = .47D$ ,  $z = .38D$ , or wire was  $.13D$  from cylinder surface). At  $x = 1.5D$ ,  $z = .5D$ , a much poorer cross spectra is given, figure 26.

A similar position,  $x = .25D$  downstream from  $90^\circ$ , provided  $St = .128$  for the 2.75" cylinder behind plate .972,  $U = 23.3$  fps,  $Re = 2.8 \times 10^4$ , shown in figure 27, and indicated by "F" in figure 1. The smaller cylinder showed an induced turbulent shedding at  $U \approx 15$  fps, but the  $U = 23.3$  fps was used because it was the same as for the larger cylinder. Also it provided an  $f$  value clearly larger than the frequencies of major power of the main stream turbulence spectra.

## 5.4 INDUCED CHANGES IN BOUNDARY LAYERS

### 5.4.1 FLOW VISUALIZATION

A flow visualization device was prepared, using 256 strands of fine silk thread on a black background and placed over half of the 2.75" cylinder. The end of each strand was partially unraveled to increase its responsiveness to local air flow. This device was wrapped around the smaller cylinder so the threads were free to move with air flow in the boundary layer. Photographs of flows for the

open tunnel (classical sub-critical), induced super-critical, and the induced turbulent regimes are presented in figure 28. The motion of the threads is compatible with the separation and transition points for the sub-critical and turbulent regimes. The super-critical conditions were not well represented, but this may have been because of the lower air speed used.

#### 5.4.2 VARIATION OF VOLTAGE WITH ANGLE OF PRESSURE TRANSDUCER TAPS

The RMS AC voltage output of the pressure transducer at various  $\alpha$  for flows in the open tunnel and for induced super-critical and turbulent regimes (points "A," "D" and "F" in figure 1) were observed. It is assumed that a maximum voltage should be obtained when the vortex shedding is best organized at the two corresponding pressure taps, shortly downstream from the separation point. Figure 29 shows results, for angles of  $\alpha = 70^\circ$  to  $\pm 160^\circ$  by  $10^\circ$  changes, on the 4.5" cylinder. The results show a maximum at  $\alpha = \pm 80^\circ$  in the classical sub-critical regime; the voltage is nearly constant for  $\alpha = \pm 70^\circ$  to  $\pm 120^\circ$  for the super-critical regime; and a more pronounced maximum voltage occurs also at  $\alpha = \pm 80^\circ$  with the induced turbulent regime. These results are compatible with the separation characteristics for each regime as given in figure 2.

#### 5.4.3 CHANGE IN SPECTRA SHAPE WITH ANGLE OF PRESSURE TRANSDUCER TAPS

Figures 30 and 31 show the variations of spectra shapes for different angles behind plates .804 and .972, representing conditions "D" and "F" respectively. The spectra for plate .972 at  $90^\circ$  appear most pronounced and become turbulent at  $150^\circ$ . The spectra for plate

.804 are less definitive but suggest vortex shedding with one maximum frequency can occur at  $\alpha$  up to  $160^\circ$ .

The spectra for the open tunnel showed no change in shape with  $\alpha$ . See figures 12, 13 and 14.

## 5.5 OBSERVATION OF TURBULENCE PARAMETERS

### 5.5.1 FLOWS TO BE INVESTIGATED

The preceding investigations have provided ten different induced vortex shedding conditions, five for each of the two cylinders: conditions "B" to "F" for the 4.5" cylinder and conditions "B'" to "F'" for the 2.75" cylinder. Conditions "A" and "A'" in open tunnel flow are considered "no turbulence" conditions.

Induced Regime	Flow Condition for Induced Vortex Shedding	
	<u>For 4.5" cylinder</u>	<u>For 2.75" cylinder</u>
Top of sub-critical	Plate .690, U = 17.4 (figure 16) "B"	Plate .748, U = 13.7 fps (figure 17) "B'"
Sub- and super-critical discontinuity	Plate .748, U = 16.9 (figure 18) "C"	Plate .801, U = 16.4 fps (figure 19) "C'"
Super-critical	Plate .804, U = 8.1 (figure 20) "D"	Plate .861, U = 7.1 fps (figure 21) "D'"
Super-critical and turbulent discontinuity	Plate .945, U = 18.7 (figure 22) "E"	Plate .945, U = 20.9 fps (figure 23) "E'"
Turbulent	Plate .972, U = 23.2 (figure 24) "F"	Plate .972, U = 23.3 fps (figure 27) "F'"

Table 2 summarizes information concerning the vortex shedding characteristics of these flows; figures 12 to 31 give details.

Ten different flow conditions are implied, but in two cases the same flow condition induced the same vortex shedding regime from both

cylinders, consequently only eight observations of turbulence data were required. One additional observation was taken for comparison purposes

Turbulence Data Observation	Related Flow Condition for Induced Vortex Shedding	
	(No cylinder)	4.5" cylinder
#1: plate .690, U = 17.6 fps	"B"	--
#2: plate .748, U = 12.9	--	"B'"
#3: plate .748, U = 17.2	"C"	--
#4: plate .801, U = 15.9	--	"C'"
#5: plate .804, U = 9.7	"D"	--
#6: plate .861, U = 8.7	--	"D'"
#7: plate .945, U = 20.3	"E"	"E'"
#8: plate .972, U = 20.2	"F"	"F'"

The conditions "B" through "F" and "B'" through "F'" are also marked in figure 1.

#### 5.5.2 BASIC OBSERVATIONS

Because the normalized U and  $T_i$  can vary at different positions near the cylinder in different turbulent flows (as shown in figure 32), it was necessary to remove the cylinder to observe turbulent parameters for comparison between the induced vortex shedding flow conditions.

The cylinder was removed and the DISA hot wire placed at the origin -- the position previously in the center of the cylinder. Different plates and air speeds were used to produce the above flow conditions to be used with the ten induced vortex shedding conditions.

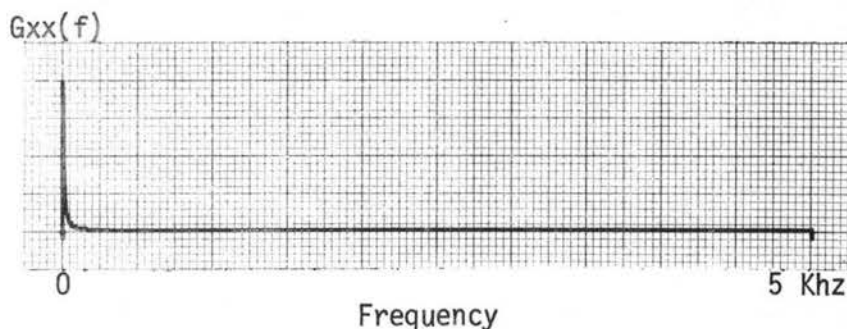
The following turbulence data were taken for each of the turbulence data observations:

- (1) Recording of  $e$
- (2) Readings of  $E$
- (3) Readings of  $\bar{e}$
- (4) Readings of  $\overline{de/dt}$

## 5.6 ANALYSIS OF TURBULENCE DATA

### 5.6.1 GENERAL FORM OF SPECTRA

It became obvious immediately that most of the power in the spectra for all of the eight flows was concentrated at frequencies below 100 Hz. Here is a typical power spectra for frequencies from zero to 5 KHz:



A detailed examination was made of the power spectra behind plate .972 (#8), by: (1) observing the mean square voltage as the frequency range was changed by a low pass filter, and (2) by summation of  $G_{xx}(f)$  calculated by the Fourier Analyzer System. (See figure 33.) Both methods agreed within 4% except for the lower frequencies where it was not possible to read the figure accurately. With  $f$  from 0 to 5 KHz, 89% of the power was below 100 Hz and 96% was below 250 Hz. For lower Br plates, these percentages were less.

Normalized power spectra for all turbulence flow conditions are given in figures 34 to 42. The lowest Br plate (.690;  $U = 17.6$  for vortex shedding condition B, fig 36) has a spectrum with the power spread over a wide range of frequencies and a poorly defined maximum near 25 Hz. For most of the higher Br plates, a distinct maximum of power occurs between 1 and 7 Hz. This low frequency maximum is interpreted as a result of the flow instability due to the high blockage ratios. The most extreme case of this appears to be behind plate .801 (figure 38,  $U = 15.9$  fps) with a strong maximum at 1 Hz. As discussed later, the  $L_x$  value for this was very large.

One extra normalized power spectra is included for special comparisons. Figure 35 (plate .690,  $U = 29.3$  fps) indicates that an increased air speed produces the low frequency maximum power where figure 34 (plate .690,  $U = 17.6$  fps) did not have it. This is interpreted as showing that in the lower speed flow, the flow instabilities had had time to dissipate. Consequently, air speed as well as distance downstream is important for the turbulence conditions.

#### 5.6.2 CALCULATION OF INTEGRAL SCALE, $L_x$

This was the most difficult parameter to observe. It was observed by one hot wire.

$L_x$  was calculated in two ways, by  $F(0)$  or  $F(M)$  from normalized power spectra and by  $\tau_0$  from autocorrelations.  $F(0)$  or  $F(M)$  are marked on the spectra in figures 34 to 42. The  $\tau_0$  value for condition C' (plate .801;  $U = 16$  fps) did not occur until a time lag of .3 sec which is unrealistic. The  $F(M)$  evaluation provided  $L_x = .36$  ft = 4.3" which is large but feasible.

The two methods of calculating  $L_x$  are not specifically related.

The spectrum scale defined in terms of  $F(0)$  is Taylor's length scale, originally defined as

$$L_x = \int_0^{\infty} R(x) dx$$

which leads to  $L_x(F) \equiv U F(0)/4$

The autocorrelation scale, defined by  $\tau_0$ , cannot be related mathematically to Taylor's scale. As mentioned later, the  $L_x(F)$  values were almost exactly one-half of the  $L_x(\tau)$  values.

The spectrum scale defined in terms of  $\tau_0$  should be compared with

$$L_x = U \int_0^{\infty} R(\tau) d\tau$$

but this gives unreasonable results due to the failure of Taylor's space-time hypothesis in highly turbulent flow. Instead the empirical relation was used

$$L_x = U \tau_0 \equiv L_x(\tau)$$

where  $\tau_0$  is the time for the autocorrelation of the turbulent air speed fluctuations, at one point, to first reach zero.

See Section B.3 for further discussion.

The power spectra were made at  $F_m = 100$  Hz,  $N = 1024$  to obtain a small  $\Delta f = .195$  Hz. The autocorrelations were made with  $F_m = 500$  Hz,  $N = 2048$  to obtain a small  $\Delta t = .001$  sec. A low pass filter was used to prevent any significant aliasing. Better definitions of  $F(0)$  or  $F(M)$  and  $\tau_0$  were possible from these  $F_m$  and  $N$  combinations.

The  $L_x$  values by  $\tau_0$ ,  $L_x(\tau)$  and by  $F(0)$  or  $F(M)$ ,  $L_x(F)$ , for the turbulence conditions related to the ten induced vortex shedding

conditions, are tabulated in Table 3. An indicated correction was made for the 60 Hz harmonics in some cases. The harmonics made calculations of  $L_x$  smaller. The corrections were determined by deleting the obvious harmonics in the  $F_{xx}(f)$  results, in the FAS, and inserting values which gave smooth curves; the resulting changes in  $\Sigma F_{xx}(f)$  were noted and used as the basis for corrections for both  $\tau_0$  and  $F(0)$  or  $F(M)$ . However, all data presented in figures 34 to 42 are the original data with the harmonics left in.

The  $L_x(\tau)$  and  $L_x(F)$  values were compared. The  $L_x(F)$  values were almost exactly one-half of the  $L_x(\tau)$  values and  $L_x(F)$  varied from 1" to 3" (except for condition C') which seems to be a reasonable size range for the average sized eddy in the turbulent flow. With the exception of  $L_x$  for condition C', the other seven values of  $L_x(\tau)$  and  $L_x(F)$  had a correlation coefficient,  $r = .989$ , which indicates good consistency in the observations and analyses. The following equation for  $r$  was obtained from Hoel (1958),

$$r = \frac{n \sum x_i y_i - (\sum x_i)(\sum y_i)}{\sqrt{[n \sum x_i^2 - (\sum x_i)^2][n \sum y_i^2 - (\sum y_i)^2]}}$$

### 5.6.3 CALCULATION OF OTHER TURBULENCE PARAMETERS $\bar{u}$ , $T_i$ , $\lambda$ , $K_m$ , $T_a$ , $Re(K_m)$ , $Re(p)$ , $Re(\lambda)$

The methods of calculating these have been defined in Section 3 and discussed in Appendix B. They are tabulated in Table 3. They were relatively easy compared with the  $L_x$  observations and consistent results were obtained.

## 6. DISCUSSION

### 6.1 GENERAL

The results considered in the previous section, presented in figures 12 through 46, and summarized in tables 2 and 3, support three types of conclusions:

(1) Increasing turbulence in wind tunnel flow past a cylinder can induce changes in vortex shedding that are analogous to the changes resulting from increasing the air speed.

(2) Several turbulence parameters, corresponding to each induced change in vortex shedding, have been measured and related to the  $Re(E)$  and  $Re(E)/Re$  values of these changes.

(3) A hypothesis of the general effects of turbulence on vortex shedding from a circular cylinder can be formulated.

In addition, three anomalies need to be considered.

### 6.2 INDUCED CHANGES IN VORTEX SHEDDING

#### 6.2.1 INCREASED TURBULENCE CAN BE ANALOGOUS TO INCREASED AIR SPEED

The first result, at CSU, utilized a 6.2" cylinder in a 6' x 6' wind tunnel with  $Re \approx 2 \times 10^4$ . Insertion of plate .958 across the entrance significantly reduced the  $St$  value of the vortex shedding. This was a change from the classical sub-critical to the induced turbulent regime.

The CSU result was reaffirmed and extended by experiments at WSMR. Two cylinders, 4.5" and 2.75" in diameter, were used in a 2' x 2' wind tunnel with  $Re \approx 4 \times 10^4$ . Spectra and correlation analyses provided a more accurate observation of  $f$  for the  $St$  values.

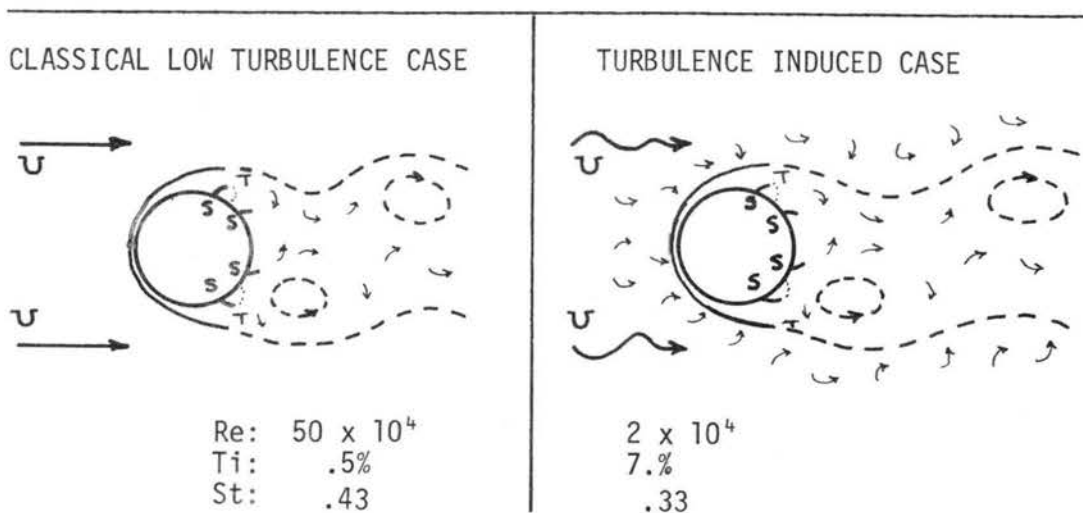
The WSMR experiments also induced the intervening super-critical vortex shedding regime and the two intervening discontinuity conditions.

The major conclusion of this study comes from these experiments.

By increasing the turbulence intensity from .3% to 25% and keeping  $Re$  between  $.9$  and  $5 \times 10^4$ , vortex shedding conditions can be changed from the sub-critical to an induced turbulent vortex shedding regime. Using estimated  $Re(E)$  values from the classical vortex shedding, this increases the  $Re(E)$  by a factor of from 110 to 180.

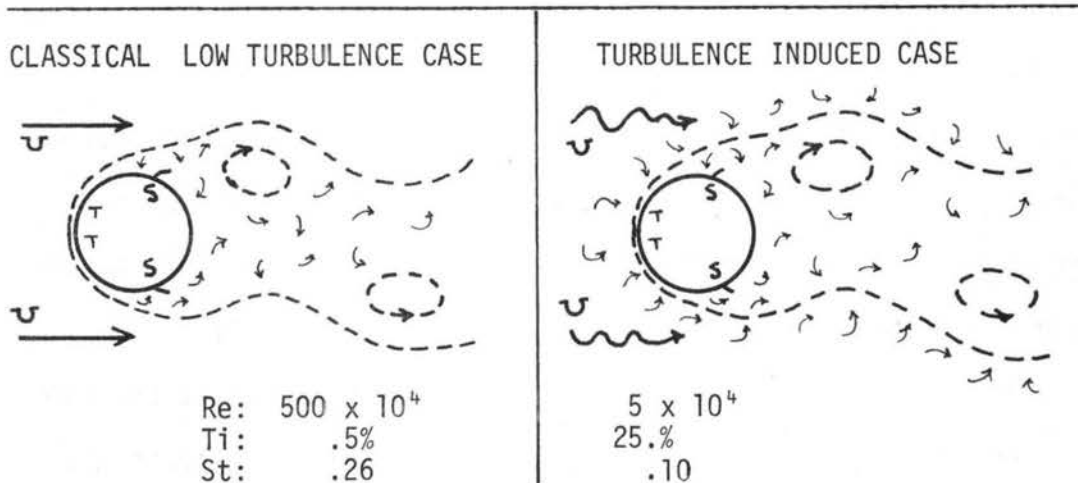
The reason for this is that the free stream turbulence impinges upon the boundary layer on the cylinder and increases vorticity in the boundary layer which causes transition and separation angle changes to occur at lower  $Re$  values. The diagram below compares the super-critical vortex shedding regime as it occurs in classical, low turbulence flow and as it occurs when induced by increased free stream turbulence.

#### SUPER-CRITICAL VORTEX SHEDDING REGIMES



A similar diagram is given for the turbulent vortex shedding regimes. The turbulent eddies and fluctuations are considerably larger in this case.

#### TURBULENT VORTEX SHEDDING REGIMES



#### 6.2.2 RELATIVE DECREASE OF ST WITH INCREASING TURBULENCE

In the induced super-critical regimes (D and D' in figure 1) the St values were .33 and .34 respectively for the 4.5" and the 2.75" cylinders, giving a decrease of 23% and 21% from the classical value of  $St \approx .43$ .

In the induced turbulent regimes (F and F' in figure 1) the St values were .10 and .13 or a decrease of 62% and 50% respectively from the classical  $St \approx .26$ .

This is the first anomaly.

The differences in the St values of the two cylinders in each induced regime approximately fit this empirical equation:

$$St(\text{induced}) = St(\text{classical}) \times 9.99 \times \left[ \frac{Lx}{D} \right]^{.1} \times \left[ \frac{Re}{Re(E)} \right]^{.6} \quad (6.1)$$

where  $D$  is the cylinder diameter in inches;  $Re$  is calculated by mean air flow, by  $D$  and  $v$ ;  $Re(E)$  is the  $Re$  value of the classical vortex shedding process analogous to the turbulence induced process and  $St$  (classical) is the  $St$  value associated with  $Re(E)$ . For the four cases, the following checks are made. The mean of the ratios is 1.00.

For 4" cylinder:

Ratio:

$$D: .329 \approx .46 \times 9.99 \times \left[ \frac{.168}{.375} \right]^{.1} \times \left[ \frac{1.6}{100} \right]^{.6} = .356; \quad \frac{.329}{.356} = .924$$

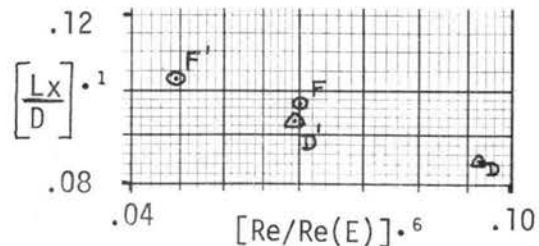
$$F: .100 \approx .26 \times 9.99 \times \left[ \frac{.295}{.375} \right]^{.1} \times \left[ \frac{4.6}{500} \right]^{.6} = .152; \quad \frac{.100}{.152} = .658$$

For 2.75" cylinder:

$$D': .339 \approx .46 \times 9.99 \times \left[ \frac{.113}{.229} \right]^{.1} \times \left[ \frac{.9}{100} \right]^{.6} = .253; \quad \frac{.339}{.253} = 1.340$$

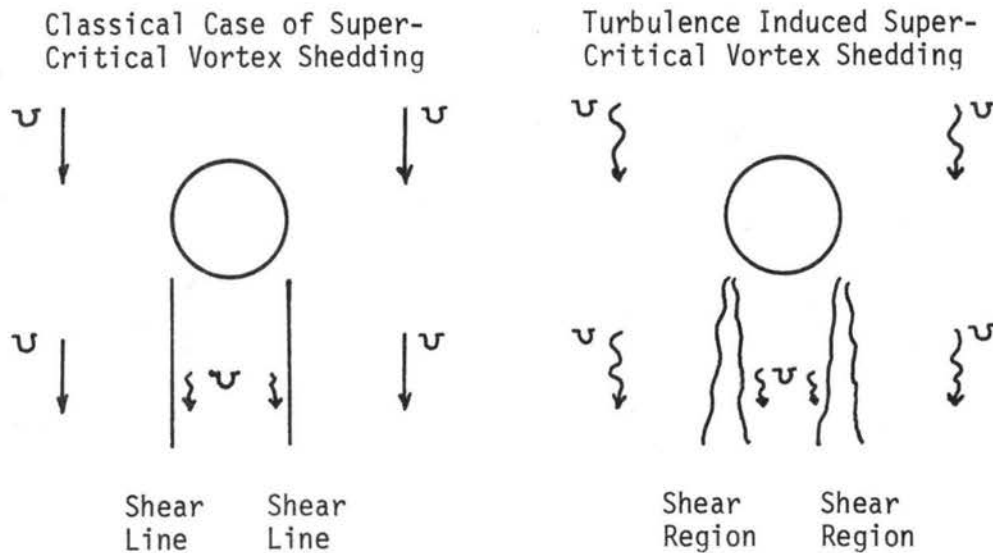
$$F': .128 \approx .26 \times 9.99 \times \left[ \frac{.295}{.229} \right]^{.1} \times \left[ \frac{2.8}{500} \right]^{.6} = .119; \quad \frac{.128}{.119} = 1.076$$

A plot of the data is shown:



The relative decrease of the  $St$  value can be explained by the associated increases in turbulent intensities. All eddies in vortex streets come primarily from the shear line or "vortex sheet", immediately downstream from the cylinder, between the mean flow and the slower flow in the wake of the cylinder. (The shear in the cylinder boundary layer also contributes.) As the turbulence intensity increases in the main flow, eddies mix into this shear line

and weaken its organized vorticity; consequently, the source of vorticity for creating the individual vortices becomes weaker for the same mean air speed. With a weaker source of vorticity, it takes longer to create an individual vortex for shedding, which means a smaller  $f$  and a smaller  $St$ . This concept is illustrated by two sketches:



### 6.2.3 COMPARISON WITH GERRARD'S ANALYSIS

These  $St$  changes are also consistent with Gerrard's analysis that  $St$  depends upon the product of two dimensions (roughly, longitudinal  $\times$  lateral) in the vortex formation region.

For the open tunnel (sub-critical, case A, figure 15) Bearman's recommended position of  $x = 1.5D$  and  $z = .5D$  for the hot wire was utilized and found satisfactory. In several other flows, it was a good position but in higher turbulence flows it was not. For the induced super-critical case with the smaller cylinder ( $D'$ , figure 21), the best hot wire observation of the vortex shedding was at

$x = 2.5D$  and  $z = .4D$ . Both cylinders required the hot wire to be very close,  $x = .36D$  and  $z = .5D$ , or  $x = .47D$  and  $z = .38D$ , for the best cross spectra in the induced turbulent vortex shedding condition ( $F$  and  $F'$ , figures 25 and 27). Then comparing the three:

Sub-critical (both cylinders)  $St \approx .18$ ;  $xz \approx .75D^2$

Induced Super-critical (smaller cylinder)  $St \approx .32$ ;  $xz \approx 1.00D^2$

Induced Turbulent (both cylinders)  $St \approx .10$ ;  $xz \approx .18D^2$

There is a direct relation between  $St$  and the product  $xz$ , compatible with Gerrard's concept.

#### 6.2.4 STABILITY OF INDUCED TURBULENT VORTEX SHEDDING REGIME

The induced turbulent vortex shedding regime was relatively easy to obtain. It was observed several times behind plates .972 and .958. A definite maximum  $f$  was observed from air speeds of 10 fps up to 22 fps. Higher speeds were not attempted because of excessive wind tunnel vibrations. This vortex shedding condition appeared to be stable.

#### 6.2.5 SENSITIVITY OF SUPER-CRITICAL VORTEX SHEDDING REGIME TO INCREASED TURBULENCE

It was found, for both cylinders at WSMR, that the induced super-critical condition could not be obtained with air speeds as high as those in the other induced regimes. In fact, they were found by decreasing the air speed past plates that were inducing the super-critical/turbulent discontinuity.

This is the second anomaly.

The super-critical vortex shedding separates a laminar boundary layer near  $\pm 105^\circ$  which undergoes transition to a turbulent

boundary layer, reattaches to the cylinder and finally separates at  $\pm 140^\circ$ . If there is sufficient free stream turbulence, the  $\partial U/\partial z$  structure or the required  $\partial P/\partial x$  condition for reattachment of the separated boundary layer could be sufficiently changed, between  $105^\circ$  and  $140^\circ$ , to prevent reattachment. Because the first separated boundary layer has not started shedding vortices, this would destroy the vortex street and prevent its observation, even immediately downstream. This concept can explain why the hot wire did not observe vortex shedding in the sub/super-critical discontinuity for the smaller cylinder, but did for the larger cylinder.

A logical extension of this concept is the suggestion that with sufficient turbulence in the main flow, the super-critical vortex shedding regime should cease to exist. A large discontinuity condition would then occur between the induced super-critical and the induced turbulent vortex shedding regimes.

#### 6.2.6 EFFECT OF DIAMETER OF CYLINDER

The diameter of the cylinder has two effects upon how well or how far vortex shedding can be induced.

For the same  $U$ ,  $Re$  varies directly with  $D$ . the 4.5" cylinder is therefore 64% closer to induced changes than is the 2.75" cylinder. This is consistent with the fact that the 4.5" cylinder had a major cross spectra,  $f$ , in the sub-/super-critical discontinuity and the 2.75" did not. If the cylinder is small enough, some induced changes may not be possible because the "Re spread" or the  $Re(E)/Re$  ratio is too great.

The  $D/L_x$  ratio and very small sizes of either  $D$  or  $L_x$  should be a limiting factor for free stream turbulence affecting the cylinder boundary layers. For the 4.5" cylinder in this experiment, the ratio varies from 3.8 to 1.3, and from 2.6 to .64 for the 2.75" cylinder. According to Hunt's data (figure 64), the  $\bar{u}/\bar{u}_{\text{upwind}}$  changes should be between 1.5 and 0.7 when the eddies approach the stagnation region of the cylinders which indicates a mean ratio near unity. Hence, the  $D/L_x$  ratio for this experiment should not greatly affect the efficiency of turbulent eddies entering the cylinder boundary layer.

### 6.3 RELATIONSHIPS BETWEEN TURBULENCE PARAMETERS AND INDUCED CHANGES

Two sets of turbulence parameters are produced. First are the  $Re(E)$  values associated with each of the ten induced vortex shedding conditions ( $B, B', \dots, F, F'$ ) and the associated  $Re(E)/Re$  values. Second, for each flow condition, measurements were made of turbulence parameters  $T_i, L_x, K_m, T_a, Re(K_m), Re(p)$  and  $Re(\lambda)$ . The data are tabulated in table 3 (continued). Various relations between  $Re(E)$ ,  $Re(E)/Re$  and each turbulence parameter can be investigated. This was done initially by plotting the data on linear, log-linear, and log-log charts. Only the log-log plots are shown, figures 45 and 46, because the curves are more nearly linear on those graphs.

#### 6.3.1 $Re(E)$ AS A FUNCTION OF $T_i, L_x, K_m, T_a$ , and $Re(K_m)$

As a first analysis, 28 relations were obtained by a least squares solution to

$$\ln(Y_j) = A + C \ln(X_j), \text{ or } Y_j = BX_j^C$$

The 28 relations are

For 4.5" cylinder:

$$\text{Re}(E) = f(\text{Ti}); f(\text{Lx}); f(\text{Km}); f(\text{Ta}); f[\text{Re}(\text{Km})]; f[\text{Re}(p)]; f[\text{Re}(\lambda)]$$

$$\text{Re}(E)/\text{Re} = f(\text{same seven turbulence parameters})$$

For 2.75" cylinder:

$$\text{Re}(E) = f(\text{same seven turbulence parameters})$$

$$\text{Re}(E)/\text{Re} = f(\text{same seven turbulence parameters})$$

All 28 relations are listed in table 6. Two indicators of "goodness of fit" are included: one is the correlation coefficient,  $r$ , between  $\text{Ln}(X_i)$  and  $\text{Ln}(Y_i)$  and the other is the sum,  $\Sigma$ , of the least squares. The seven "best" relations are listed here ( $r > .95$ ) and are the ones with monotonic data:

$$\text{For 4.5" cylinder: } \text{Re}(E) = f(\text{Lx}); f[\text{Re}(\text{Km})]; f(\text{Ta}); f(\text{Ti}); f(\text{Km})$$

$$\text{For 2.75" cylinder: } \text{Re}(E) = f(\text{Ti}); f(\text{Ta})$$

A more general functional relation would be of the form  $Y = D + EX^f$ , of which the above equations are a special case with  $D = 0$ . The more general form is non-linear and therefore more complicated to solve. A Newton-Raphson iteration was applied to solve for  $D$ ,  $E$  and  $F$  that provided a least squares fit to the  $X$ ,  $Y$  data. See table 7 for details. This requires a first estimate of  $D$ ,  $E$  and  $F$  to start the iteration. An estimate can be provided by a Slope-Intercept numerical solution for three data points, as explained in table 7. A first estimate is also given by the above solutions, letting  $D = 0$ .

Following is a list of the seven best relations as obtained by the above solutions to  $Y_i = BX_i^C$ ; and by the Newton-Raphson iteration, where  $D = 0$ ,  $E = B$  and  $F = C$  were first estimates. The correlation coefficient is for  $Y_i$  vs  $(D + EX_i^F)$  and  $Y_i$  vs  $BX_i^C$ . The sum,  $\Sigma$ , of least squares is for scaled values of  $Re(E)$  (to avoid "ill-conditioned matrices" in the Newton-Raphson solution) and the actual values of the turbulence parameters -- consequently, the numerical values of  $r$  and  $\Sigma$  will be different from those in table 6 where  $\ln X_i$  and  $\ln Y_i$  were utilized with some normalization. However,  $r$  and  $\Sigma$  are significant for comparing their related functions, either in table 6 or in the following "log-log" form of Newton-Raphson, "N-R" form:

For 4.5" cylinder:		$r$	$\Sigma$
$Re(E) \times 10^{-5} =$	$250.0 (Ti)^{1.247}$ (by log-log)	.9787	79.9
$Re(E) \times 10^{-5} = 2.835 =$	$615.9 (Ti)^{1.877}$ (by N-R)	.9916	31.8
$Re(E) \times 10^{-5} =$	$1304. (Lx)^{2.767}$	.9877	49.1
$Re(E) \times 10^{-5} = -.9982 + 1449. (Lx)^{2.787}$		.9880	37.2
$Re(E) \times 10^{-5} =$	$33.10(Km)^{.7790}$	.9682	100.
$Re(E) \times 10^{-5} = 4.786 + 24.27(Km)^{1.665}$		.9898	31.4
$Re(E) \times 10^{-5} =$	$273.4 (Ta)^{1.361}$	.9778	84.2
$Re(E) \times 10^{-5} = 1.364 + 506.4 (Ta)^{1.759}$		.9873	39.1
$Re(E) \times 10^{-5} =$	$176.3 [Re(Km)]^{-.8560}$	.9862	52.9
$Re(E) \times 10^{-5} = 2.782 + 349.4 [Re(Km)]^{-1.260}$		.9950	15.7
For 2.75" cylinder:			
$Re(E) \times 10^{-5}$	$355.6 [ Ti ]^{1.442}$	.9842	49.2
$Re(E) \times 10^{-5} = 2.763 + 756.3 [ Ti ]^{1.982}$		.9918	25.3

$$\begin{aligned} \text{Re}(E) \times 10^{-5} &= 431.0 [ \text{Ta} ]^{1.542} && .9835 \quad 54.7 \\ \text{Re}(E) \times 10^{-5} &= 2.335 + 915.0 [ \text{Ta} ]^{2.057} && .9916 \quad 26.9 \end{aligned}$$

It is seen that the Newton-Raphson analysis improves the correlation coefficients only by about 1%. The simpler  $\text{Re}(E) = B(\text{Turbulence Parameter})^C$  relation is a good approximation. The exponent was found to be very sensitive in the Newton-Raphson calculations.

The Taylor parameter,  $\text{Ta} = \text{Ti}(D/Lx)^{.2}$ , was monotonic with  $\text{Re}(E)$  for both cylinders. This recommends it as a good turbulence parameter to relate to vortex shedding changes.  $\text{Ti}$  also was monotonic with  $\text{Re}(E)$  for both cylinders.

$\text{Re}(K_m) = (1/\text{Ti})(D/Lx)$  is a very similar parameter to  $\text{Ta}$ . Both are functions of  $\bar{u}$ ,  $U$ ,  $D$ , and  $Lx$ , which are important parameters in describing turbulence effects on vortex shedding.

### 6.3.2 PREDICTIVE RELATION BETWEEN TURBULENCE FACTORS AND INDUCED CHANGES IN VORTEX SHEDDING

The preceding discussion shows that  $\text{Re}(E)$  can be satisfactorily used to describe the turbulence induced changes and that  $\text{Ti}$  and  $D/Lx$  are indicators of turbulence effects. The use of  $\text{Re}(E)$  implies that  $\text{Re}$  is another relevant factor because it describes the original state from which turbulence changes start. In the next section it is shown that the ratio  $\text{Re}(E)/\text{Re}$  is not a good factor to describe induced changes. With this information, dimensional analysis considerations immediately suggest the following type of relation as feasible for predicting turbulence induced changes in vortex shedding:

$$\text{Re}(E) = \text{Re} + [C_1 \times (\bar{u}/U)^{C_2} \times (D/Lx)^{C_3}]$$

Using the results of the preceding section and a little experimentation, the following values of  $C_1$ ,  $C_2$ , and  $C_3$  were found to give an approximate relation for all ten cases B - F, and B' - F'.

$$\text{Re}(E) = \text{Re} + [3836 \times 10^4 \times (\bar{u}/U)^{1.5} \times (D/Lx)^{.25}] \quad (6.2)$$

Formula (6.2) is checked for the ten cases as follows.

For 4.5" cylinder:

$$\begin{aligned} \text{B: } 21 \times 10^4 &\approx [3.4 \times 10^4] + [3836 \times 10^4 \times (.021)^{1.5} \times (3.788)^{.25}] \\ &= 19.7 \times 10^4; \quad \text{Ratio} = 21.0/19.7 = 1.066 \end{aligned}$$

$$\begin{aligned} \text{C: } 36 \times 10^4 &\approx [3.3 \times 10^4] + [3836 \times 10^4 \times (.036)^{1.5} \times (3.205)^{.25}] \\ &= 38.4 \times 10^4; \quad .938 \end{aligned}$$

$$\begin{aligned} \text{D: } 100 \times 10^4 &\approx [1.6 \times 10^4] + [3836 \times 10^4 \times (.067)^{1.5} \times (2.232)^{.25}] \\ &= 82.9 \times 10^4; \quad 1.206 \end{aligned}$$

$$\begin{aligned} \text{E: } 200 \times 10^4 &\approx [3.7 \times 10^4] + [3836 \times 10^4 \times (.160)^{1.5} \times (1.582)^{.25}] \\ &= 279 \times 10^4; \quad .717 \end{aligned}$$

$$\begin{aligned} \text{F: } 500 \times 10^4 &\approx [4.6 \times 10^4] + [3836 \times 10^4 \times (.244)^{1.5} \times (1.271)^{.25}] \\ &= 495 \times 10^4; \quad 1.010 \end{aligned}$$

For 2.75" cylinder:

$$\begin{aligned} \text{B': } 22 \times 10^4 &\approx [1.7 \times 10^4] + [3836 \times 10^4 \times (.032)^{1.5} \times (2.575)^{.25}] \\ &= 29.5 \times 10^4; \quad \text{Ratio} = 22.0/29.5 = .746 \end{aligned}$$

$$\begin{aligned} \text{C': } 38 \times 10^4 &\approx [2.0 \times 10^4] + [3836 \times 10^4 \times (.045)^{1.5} \times (.6643)^{.25}] \\ &= 35.1 \times 10^4; \quad 1.086 \end{aligned}$$

$$\begin{aligned} \text{D': } 100 \times 10^4 &\approx [0.9 \times 10^4] + [3836 \times 10^4 \times (.066)^{1.5} \times (2.028)^{.25}] \\ &= 78.5 \times 10^4; \quad 1.247 \end{aligned}$$

$$\begin{aligned} \text{E': } 200 \times 10^4 &\approx [2.5 \times 10^4] + [3836 \times 10^4 \times (.160)^{1.5} \times (.9670)^{.25}] \\ &= 246 \times 10^4; \quad .813 \end{aligned}$$

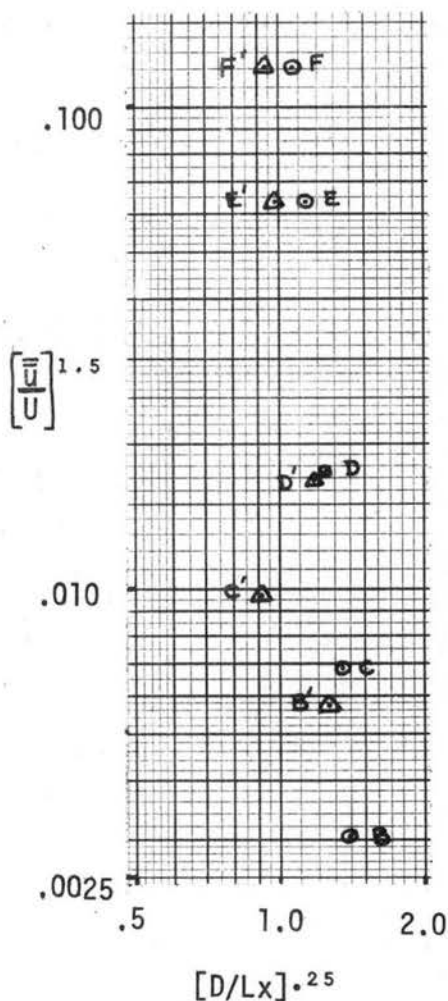
$$\begin{aligned} \text{F': } 500 \times 10^4 &\approx [2.8 \times 10^4] + [3836 \times 10^4 \times (.244)^{1.5} \times (.7769)^{.25}] \\ &= 437 \times 10^4; \quad 1.144 \end{aligned}$$

The predictive relation of equation (6.2) fits all ten data points within  $\pm 28\%$  and the mean of all ten cases is .9995. The ten data points of  $(\bar{u}/U)^{1.5}$  vs  $(D/Lx)^{.25}$  are plotted below.

Equations (6.1) and (6.2) are among the major results of this investigation because they tie together induced changes in vortex shedding,  $Re(E)$  and  $St(\text{induced})$  with  $Re$ ,  $St(\text{classical})$  and turbulence factors  $\bar{u}$ ,  $U$ ,  $D$  and  $Lx$ .

### 6.3.3 NO OTHER MONOTONIC RELATIONS

No further analysis was attempted on the other 21 relations because each had one or two data points that were not monotonic and five data points were insufficient to attempt a higher degree polynomial analysis. One of the non-monotonic points was associated with the low air speed at the induced super-critical regime for both cylinders. Because of this, all  $Re(E)/Re$  relations were not monotonic. The second non-monotonic condition resulted from the very high  $Lx$  value behind plate .801 for the 2.75" cylinder in the induced sub/super-critical discontinuity.



As a result, the  $L_x$ ,  $K_m$  and  $Re(K_m)$  values were abnormally large. The values are shown in table 3 (continued) and referenced to case C'.

The unusually large  $L_x$  value is the third anomaly.

It is possible that this large  $L_x$  value was due to a large DC drift in the hot wire turbulent recording of  $e$ . Mujumdar reported difficulties similar to this and resolved them by offsetting the zero line in the  $R_{xx}$  plots (e.g., figure 44). This is rejected for two reasons. First, a large DC output (10 to 13 volts) was found in the  $e$  output from the DISA hot wire and was "bucked out" by inserting a variable DC power supply until the DC output was less than  $\pm 0.5$  volts. This was necessary to keep from overloading the amplifiers required for good data recording -- a large DC drift would have prevented the data recording. Second, the plates with  $Br$  near .80 actually caused more flow blockage than did the plates with higher or lower  $Br$ . This was first noted by the maximum power required by the wind tunnel fan to obtain 16 fps. At first, it was considered that the eddy sizes interacted with the fan blades to make them inefficient, but this was discarded when non-dimensional measurements of static pressure drop across the plates ( $2\Delta P/\rho U^2$ ) showed a distinct maximum for plate .804.

No satisfactory explanation is apparent, but several factors appear to be relevant to an explanation: (a) the boundary layer inside each hole of the plates may change from laminar to turbulent for  $U=16$  fps and  $Br \approx .80$ , increasing the momentum thickness of the boundary layer and having the effect of considerably reducing the

size of the holes; (b) for higher Br plates, the distance between adjacent holes is much larger, which could reduce the interaction between individual jets and allow air to come through more easily; (c) for the highest Br plates, jets could have speeds of the order of 500 fps which could introduce compression effects which would not appear for the  $Br \approx .80$  plates with a maximum jet speed of near 90 fps. It is suggested that this anomaly could be a new dissertation subject.

Plate .804 had 1/4" diameter holes while plate .801 had 3/16" diameter holes, which may explain why an abnormally large Lx was not observed for the corresponding condition for the 4.5" cylinder.

#### 6.4 COMPARISON WITH CLOSELY RELATED EXPERIMENTS

##### 6.4.1 SIMON

Simon (1968a) prepared an "informal report" for the Martin Marietta Corporation which the author learned about only after this dissertation was being prepared for final printing. Simon and his associates had conducted investigations relative to wind-induced oscillations of Saturn Boosters in the vertical launch position. This included studies on the effect of surface roughness, turbulence and Mach number on the flow regime boundaries for two-dimensional flow around circular cylinders. Simon found that . . . "The effects of surface roughness and turbulence are very large and can therefore be used to obtain any desired flow regime, even at relatively low Reynolds number ( $Re = 10^5$ )."

Simon's investigations parallel and corroborate much of the work reported in this dissertation. My work goes considerably further

into the subject. The details of the approaches and results are quite different. See Simon, Howard, and Peterson (1967) and Simon (1968), as well as section A.5.4 of this dissertation for further information.

#### 6.4.2 SURRY

Surry's (1969, 1972) experiments about the turbulence effects on the aerodynamics of a circular cylinder provided valuable guidance in the early part of this study. A scaled version of one of his grids was used as part of the instrumentation check out. Similar  $St$  and  $Ta$  values were obtained.

#### 6.4.3 KO AND GRAF

It is interesting to note that the  $Ti$  for both of my induced super-critical regimes (maximum  $St$ ) was between 6 and 7%. This is close to the 4% that Ko and Graf (1972) found for the minimum  $Cd$  values. The two should be related because  $St \times Cd$  is approximately a constant for high  $Re$  values. However, it is believed that the numerical value of  $Ti$  associated with such changes should vary with cylinder size and the plate geometry.

#### 6.4.4 MUJUMDAR

The results of Mujumdar (1971) are not easy to explain. He found  $St$  values of  $.205 \pm .005$  for  $.5\% < Ti < 15\%$  and for  $6 \times 10^3 < Re < 1.2 \times 10^4$ . Figure 1 and the results of my studies indicate that Mujumdar's  $St$  values should have varied from .210 to .192 due to  $Re$  changes alone. If his maximum  $Ti$  occurred with this maximum  $Re$ , an induced change of  $St$  to about .185 should be expected. On

the other hand, my observations of  $St$ , with  $Ti = .3\%$  and  $Re = 4 \times 10^4$  were approximately .200 rather than .180 shown in figure 1. Several possible explanations can be considered: one, the  $St$  curve may be flatter in that range of  $Re$  values than is given in figure 1, in which case my results and Mujumdar's would support each other; two, turbulence may have little effect for inducing changes in the  $St$  value because of the smallness of Mujumdar's cylinder; and, three, the rather large blockage of my cylinders may have introduced errors in calculating  $U$  and  $St$ . A good explanation is not obvious.

#### 6.5 GENERAL EFFECTS OF TURBULENCE ON VORTEX SHEDDING

A hypothesis about the general effects of turbulence on vortex shedding can be formulated from the results and discussion. In general, increasing turbulence in the main stream has these effects on vortex shedding: (1) vortex shedding regimes occur at lower  $Re$  values; (2) single dominant  $f$  values in discontinuities begin to disappear; (3) the induced super-critical regime is disrupted by preventing reattachment of the separated laminar boundary layer; (4) the relative size of  $St$  values for each regime decreases; and (5) the vortex street is destroyed closer to the cylinder.

## 7. CONCLUSIONS

### 7.1 GENERAL

Turbulence effects on vortex shedding from a circular cylinder were investigated in a wind tunnel. Turbulence intensity,  $T_i$ , near the middle of the tunnel, was increased from .3% to 25% by using plates with many small holes and having plate blockage ratios from .50 to .97. The Reynolds number,  $Re$ , of all flows was kept near  $4 \times 10^4$ , using mean air speed, cylinder diameter and kinematic viscosity. Investigations of vortex shedding with turbulence as high as 25% and behind plates with plate blockage ratios as large as .97 have not been published before to the best of the author's knowledge.

Most of the literature on vortex shedding are reports of investigations in air flows past smooth cylinders where special efforts have been made to keep  $T_i$  values very low, usually  $< .5\%$ . Under such near zero freestream turbulence conditions, vortex shedding can be classified, by the range of  $Re$  values, into four "classical" vortex regimes with a discontinuity condition between each two successive regimes. Strouhal number,  $St$ , values as well as characteristic angles of boundary layer separation and point of transition to turbulence also characterize each regime. The classical, low turbulence vortex shedding regimes are summarized here with  $Re$  and  $St$  values:

Laminar Regime:  $4. \times 10^3 < Re < 1.5 \times 10^5$ ;  $.10 < St < .18$

Discontinuity:  $1.5 \times 10^5 < Re < 3. \times 10^5$

Sub-critical Regime:  $3. \times 10^5 < Re < 3. \times 10^6$ ;  $.18 < St < .21$

Discontinuity:  $3. \times 10^6 < Re < 4. \times 10^6$

Super-critical Regime:  $4. \times 10^6 < Re < 1.5 \times 10^7$ ;  $.40 < St < .46$

Discontinuity:  $1.5 \times 10^6 < Re < 2.5 \times 10^6$

Turbulent Regime:  $2.5 \times 10^6 < Re < 1. \times 10^7+$ ;  $.24 < St < .29$

## 7.2 PREVIOUS CONCEPTS VERIFIED

Four concepts were verified that are already in the literature. As the  $Ti$  of the free stream past a cylinder is increased: (a) the vortex shedding regimes occur at lower  $Re$  values; (b) discontinuities lose any single dominant  $St$  values they may have had; (c) individual vortices of the downstream Karman vortex street are destroyed closer to the cylinder; and (d) the diameter of the cylinder influences the turbulence effects on vortex shedding.

## 7.3 NEW CONCEPTS DEVELOPED

Several things have been observed or inferred that have not been published previously to the best of the author's knowledge.

### 7.3.1 INCREASED TURBULENCE PRODUCES EFFECTS ON VORTEX SHEDDING THAT ARE ANALOGOUS TO THOSE RESULTING FROM INCREASED AIR SPEED

Starting with  $Re \approx 4 \times 10^4$  and  $Ti < .5\%$ , vortex shedding is operating in the classical sub-critical regime. If the air speed (or  $Re$ ) is steadily increased and the  $Ti$  kept very low, the vortex shedding process will successively go through a discontinuity, operate in the super-critical regime, go through a second discontinuity, and finally operate in the turbulent regime as  $Re \rightarrow 10^7$ .

Starting at the same initial condition but keeping  $Re$  nearly constant and steadily increasing the  $Ti$  from  $.3\%$  to  $25\%$ , an analogous sequence of changes in the vortex shedding processes was observed. In other words, by keeping  $Re \approx 4 \times 10^4$  and increasing the  $Ti$ , the

vortex shedding eventually operated as if  $Re \rightarrow 10^7$  but with minimum  $Ti$ . The turbulence induced changes in vortex shedding are expressed by the equivalent  $Re$ ,  $Re(E)$ , which are numerically the same as the  $Re$  estimated to have analogous vortex shedding characteristics in classical, minimum turbulence flow. Using these  $Re(E)$  values and the actual  $Re$  of the turbulent flow, ratios of  $Re(E)/Re$  as high as 180 were observed. Or, by increasing the  $Ti$  with an approximately constant  $Re$ , vortex shedding changes were induced that are analogous to those occurring with near zero turbulence intensity but with air speeds as much as 180 times faster.

The turbulence induced changes in vortex shedding, as expressed by  $Re(E)$ , can be approximately predicted for both cylinders of this study by this non-dimensional relation:

$$Re(E) \approx Re + [3836 \times 10^4 \times (\bar{u}/U)^{1.5} \times (D/Lx)^{.25}] \quad (7.1)$$

where  $(\bar{u}/U)$  is the turbulence intensity,  $Ti$ ,  $D$  is the cylinder diameter and  $Lx$  is the integral scale of turbulence.

### 7.3.2 VORTEX SHEDDING FREQUENCY IS RELATIVELY DECREASED BY INCREASED TURBULENCE INTENSITY

In the turbulence induced super-critical and turbulent vortex shedding regimes, for both cylinders, the vortex shedding frequencies, expressed by  $St$ , were smaller relative to the  $St$  value in the classical case for the same  $Re$ . The induced  $St$  values, for this study, can be approximately predicted by this non-dimensional relation:

$$St \text{ (Induced)} \approx St \text{ (Classical)} \times 9.99 \times \left[ \frac{Lx}{D} \right]^{.1} \times \left[ \frac{Re}{Re(E)} \right]^{.6} \quad (7.2)$$

where  $Re(E)$  can be obtained from equation (7.1) and  $St$  (classical) is the  $St$  value associated with  $Re(E)$  in classical low turbulence flow.

### 7.3.3 SUPER-CRITICAL REGIME SENSITIVE TO TURBULENCE AND AIR SPEED

The induced super-critical vortex shedding regime is very sensitive to increased  $Ti$ . Apparently, the separated laminar boundary layer can be easily disrupted by free-stream turbulence so that it does not reattach after undergoing transition to turbulent flow. This suggests that this regime could be disrupted by sufficient free-stream  $Ti$  and air speed and would provide a very extensive discontinuity condition between the sub-critical and the induced turbulent vortex shedding regime.

### 7.3.4 LIMIT TO TURBULENCE INDUCED CHANGES

Although this seems intuitively obvious, some quantitative measurements were made which indicate that too much turbulence intensity should result in the destruction of individual vortices before they can be shed.

## 7.4 A HYPOTHESIZED MODEL OF TURBULENCE EFFECTS ON VORTEX SHEDDING FROM A CIRCULAR CYLINDER

Vortex shedding is a result of the basic instability that exists between two shear layers in the separated flow immediately downstream from the cylinder. Vortex shedding is a continuous process from the lowest  $Re$  value ( $\approx 40$ ) at which inertial forces overcome viscous forces up to the  $Re$  and  $Ti$  values at which turbulent effects destroy an individual vortex before it can be shed. The latter

should occur at  $Re > 10^7$  for  $Ti < .5\%$  but at lower  $Re$  values for higher  $Ti$ .

Four vortex shedding regimes can exist over this range of  $Re$ . Each has a stable combination of boundary layer separation angle and laminar to turbulent transition in the boundary layer and/or the vortices. The separation angle greatly influences the frequency of vortex shedding, so typical  $St$  values occur for each regime.

Discontinuity conditions exist between each two successive regimes. In these conditions, individual vortices will shed at one or the other regime so that a mean  $St$  value can vary between the values for the two regimes. Turbulence effects, either from turbulent vortices and/or the main stream will broaden the spectra of the vortex shedding frequency. Then, as turbulence effects increase, the spectra will become random and no longer define a dominant shedding frequency.

As turbulence is increased in the main stream, it affects the vortex shedding regimes in several ways: (1) the regimes occur at lower  $Re$  values; (2) the induced  $St$  becomes smaller relative to the  $St$  value in the classical case for the same  $Re$ ; (3) the separated boundary layer in the induced super-critical regime is disrupted so that this regime should cease to exist with a sufficiently large  $Ti$ ; (4) the vortex street is destroyed closer to the cylinder, and a sufficiently large  $Ti$  should end the vortex shedding process by destroying each individual vortex before it is shed.

## 7.5 SUGGESTED FUTURE RESEARCH

7.5.1 In view of the fact that the upper limit of Re values for vortex streets has not been established, is it possible that vortex streets could exist at Re values of  $10^9$  or  $10^{10}$  as suggested by atmospheric observations of vortices in the lee of isolated islands?

7.5.2 Does the equation of the form

$$\text{Re}(E) = \text{Re} + [C_1 \times (\bar{u}/U)^{C_2} \times (D/Lx)^{C_3}]$$

fit a wide range of vortex shedding conditions? If so, could the terms  $C_1$ ,  $C_2$ , and  $C_3$  be formulated as functions of the cylinder and the turbulence producing factors?

7.5.3 Why did the maximum flow blockage occur in flow through a plate with blockage ratio near .80 rather than at .97?

7.5.4 Using a larger tunnel, with less cylinder blockage and smaller end effects on the cylinder, verify that Strouhal numbers decrease (relative to the St value in the classical case for the same Re) with increasing  $T_i$ . If so, does the equation of the form

$$\text{St}(\text{induced}) = \text{St}(\text{classical}) \times K_1 \times (Lx/D)^{K_2} \times [\text{Re}/\text{Re}(E)]^{K_3}$$

fit a wide range of vortex shedding conditions? If so, could the terms  $K_1$ ,  $K_2$  and  $K_3$  be formulated as functions of the cylinder and the turbulence producing factors?

7.5.5 Would it be possible to protect chimneys and buildings from excessive vibrations (caused by vortex shedding) through generation of higher  $T_i$  in the air flow past them -- by providing suitable surface roughness upstream, such as smaller buildings or terrain?

## BIBLIOGRAPHY\*

- Achenbach, E., 1968, Distribution of local pressure and skin friction around a circular cylinder in cross flow up to  $Re = 5 \times 10^6$ , JFM 34, 625-639
- Allen, H. J., and Vincenti, W. G., 1944, Wall interference in a two-dimensional flow wind tunnel with consideration of the effect of compressibility, NACA Report 782
- Baines, W. D., and Peterson, E. G., 1951. An investigation of flow through screens, ASME Trans. 73, 467
- Barnett, K. M., 1972, A wind-tunnel experiment concerning atmospheric vortex streets, Boundary Layer Meteorology, 2, 427-443
- Batchelor, G. K., 1953, The theory of homogeneous turbulence, 1970 printing, Cambridge Univ. Press
- Batchelor, G. K., and Townsend, A. A., 1948, Decay of isotropic turbulence in the initial period, PRSL, A1035, 539-558
- Bearman, P. W., 1967, On vortex street wakes, JFM 28, 625-641
- Bearman, P. W., 1969, On vortex shedding from a circular cylinder in the critical Reynolds number regime, JFM 37, 577-585
- Bearman, P. W., 1972, Some measurements of the distortion on turbulence approaching a two-dimensional bluff body, JFM 53, 451-467
- Bendat, J. S., and Piersol, A. G., 1966, Measurement and analysis of random data, John Wiley and Sons
- Birkhoff, G., 1953, Formation of vortex streets, Journal of Applied Physics 24, 1, 98-103
- Bloor, M. S., 1964, The transition to turbulence in the wake of a circular cylinder, JFM 19, 290-304
- Bradshaw, P., 1964, Experimental fluid mechanics, Pergamon Press
- Bradshaw, P., 1965, The effect of wind tunnel screens on nominally two-dimensional boundary layers, JFM 22, 679-688
- Cermak, J. E., 1971, Laboratory simulation of the atmospheric boundary layer, AIAA Jour. 9, 9, 1746-1754

---

\*Abbreviations are defined at the end of this list

- Chopra, K. P., and Hubert, L. F., 1964, Karman vortex-streets in the earth's atmosphere, *Nature*, 203, 4952, 1341-1343
- Chopra, K. P., and Hubert, L. F., 1965, Mesoscale eddies in the wake of islands, *JAS*, 22, 6, 652-657
- Corrsin, S., 1944, Investigation of the behavior of parallel two-dimensional air jets, NACA Wartime Report W-90, ACR 4H24
- Corrsin, S., 1963, Turbulence: experimental methods, *Handbuch der Physik*, Band VIII/2, *Stroemungsmechanik*, II, 524-590
- DISA instructional manual for hot wire anemometer system 55A01, DISA Corp., 779 Susquehanna Ave., Franklin Lakes, NJ 07417
- Drew, T. B., 1931, Mathematical attacks on forced convection problems: a review, *Trans Am Inst Chem Engr*, 26, 30-31
- Dryden, H. L., Schubauer, G. B. Mock, E. C. Jr., and Skramstad, H. K. 1936, Measurements of intensity and scale of wind tunnel turbulence and their relation to the critical Reynolds number of spheres, NACA Report 581
- Fage, A., 1929, The airflow around a circular cylinder in the region where the boundary separates from the surface, *Philosophical Mag* 7, 253-273
- Fage, A., and Johansen, F. C. 1928, The structure of vortex streets, *Philosophical Mag* 7, 417-441
- Friedlander, S. K., and Topper, L. (Editors), 1961, *Turbulence, classic papers on statistical theory*, Interscience Publishers
- Gaster, M., 1969, Vortex shedding from slender cones at low Reynolds numbers, *JFM* 38, 565-576
- Gerrard, J. H., 1965, A disturbance sensitive Reynolds number range of the flow past a circular cylinder, *JFM* 22, 187-196
- Gerrard, J. H., 1966a, The three-dimensional structure of the wake of a circular cylinder, *JFM* 25, 143-164
- Gerrard, J. H., 1966b, The mechanics of the formation region of vortices behind bluff bodies, *JFM* 25, 401-413
- Goldstein, S., (Editor) 1965, *Modern developments in fluid dynamics*, two vols, Dover Publications (first published in 1938)
- Hagist, W., July 1968, Measurement of turbulence by a diffusion method, Unpublished report for course CE 795AX, CSU

Hewlett-Packard Corp., 5301 Stevens Creek Blvd, Santa Clara,  
California 95050

- a. Kiss, A. A., June 1970, A calibrated computer-based analyzer, Hewlett-Packard Journal, 10-19
- b. Rex, R. L., and Roberts, G. T., Nov 1969, Correlation, signal averaging and probability analysis, Hewlett-Packard Journal, 2-8
- c. Roth, P. R., June 1970, Digital Fourier Analysis, Hewlett-Packard Journal, 2-9
- d. Systems Operating Manual, Sept 1970, Fourier Analyzer System 5450A/5452A

Hinze, J. O., 1959, Turbulence, McGraw Hill

Hoel, P. G., 1954, Introduction to mathematical statistics, Second Edition, John Wiley and Sons

Humphreys, J. S., 1960, On a circular cylinder in a steady wind at transition Reynolds numbers, JFM 9, 603

Hunt, J. C. R., 1971, The effect of single buildings and structures, PTRSL, A269, 457-467

King, L. V., 1914, On the convection of heat from small cylinders in a stream of fluid; determination of the convective constants of small platinum wires with application to hot wire anemometry, PTRSL A214, 373-432

Kline, S., and McClintok, F., 1953, Describing uncertainties in single-sample experiments, Mechanical Engineering, 3-8

Ko, S. C., and Graf, W. H., 1972, Drag coefficient of cylinders in turbulent flow, J. of Hydraulics Div., Proc ASCE, 8920, HY5, 897

Kovaszny, L. S. G., 1949, Hot wire investigation of the wake behind cylinders at low Reynolds numbers, PRSL, A198, 174-190

Kuethe, A. M. and Schetzer, J.D., 1961, Foundations of aerodynamics, Second Ed, John Wiley and Sons

Laurance, J. C. and Landus, L. G., 1952, Auxiliary equipment and techniques for adapting the constant temperature hot wire anemometer to specific problems in air flow measurements NACA TN 2843

- Lumley, J. L., and Panofsky, H. A., 1964, The structure of atmospheric turbulence, Interscience
- Mair, W. A., and Maull, D. J., 1971, Bluff bodies and vortex shedding - a report on Euromech 17, JFM 45, 290-324
- Marris, A. W., June 1964, A review of vortex streets, periodic wakes, and induced vibration phenomena, Journal of Basic Engineering, ASME, 185-196
- Morgan, P. G., 1960, The stability of flow through porous screens, Journal of Royal Aeronautics Society 64, 359
- Mujumdar, A. S., 1971, Effect of free-stream turbulence parameters on heat transfer from cylinders in cross flow, Ph.D thesis, McGill Univ., Montreal Canada, National Library, Ottawa, No. 9430
- Peterka, J. A., 1971, Computer program to obtain least squares solution to King's equation, Private communication, CSU
- Pope, A., and Harper, J. J., 1966, Low-speed wind tunnel testing, John Wiley and Sons
- Robertson, J. M., 1965, Hydrodynamics in theory and application, Prentice-Hall, Chapter 4, Vortex Dynamics, 103-146
- Rosenhead, L., 1931, The formation of vortices from a surface of a discontinuity, PRSL A134, 170-192
- Rosenhead, L., 1953, Vortex streets in wakes, Advances in Applied Mechanics 3, 185-195
- Roshko, A., 1954, On the development of turbulent wakes from vortex streets, NACA Report 1191
- Roshko, A., 1955, On the wake and drag of bluff bodies, Journal of Aeronautical Science 22, 124-132
- Roshko, A., 1961, Experiments on the flow past a circular cylinder at very high Reynolds numbers, JFM 10, 345
- Rotta, J. C., 1962, Turbulent boundary layers in incompressible flow, Section 1, Progress in Aeronautical Sciences, 2, edited by Ferri, Juechemann, and Sterne, Pergamon Press
- Sadeh, W. Z., Suter, S. P., and Maeder, P. F., 1970, Analysis of vorticity amplification in the flow approaching a two-dimensional stagnation point, Zeitschrift fuer angewandte Mathematik und Physik, vol 21, Fasc 5, 699-716

- Sandborn, V. A., 1970, Boundary Layer notes, Civil Engr Dept, CSU
- Sandborn, V. A., 1972, Resistance temperature transducers, Metrology Press, Fort Collins, Colorado
- Sandborn, V. A., and Slogar, R.J., 1955, Longitudinal turbulent spectrum survey of boundary layers in adverse pressure gradients, NACA TN 3453
- Schafer, J. W., and Eskanazi, S., An analysis of the vortex street generated in a viscous fluid, JFM 6, 241-260
- Scheid, F., 1968, Theory and problems of numerical analysis, Schaum Outline Series, McGraw-Hill
- Schlichting, H., 1960, Boundary layer theory, 4th ed., McGraw Hill
- Schubauer, G. B., 1935, A turbulence indicator utilizing the diffusion of heat, NACA TR 524
- Schubauer, G. B., and Skranstad, H. K., 1948, Laminar boundary-layer oscillations and transition on a flat plate, NACA Report 909
- Schubauer, G. B., Spangenberg, W. G., and Klebanoff, P. S., 1950, Aerodynamic characteristics of damping screens, NACA TN 2001
- Shepard, C. E., 1955, A self-excited, alternating current, constant temperature hot wire anemometer, NACA TN 3406
- Simon, W. E., Howard, C. R., and Peterson, H. C., 1967, Annual report; investigations relative to wind-induced oscillations of Saturn booster in the vertical launch position, MCR-67-33, Martin Marietta Corp, PO Box 179, Denver, Colo, 80201, for NASA contract NAS8-5322
- Simon, W. E., 1968, Effect of surface roughness, turbulence and Mach number on flow regime boundaries for tunnel-spanning cylinders, Informal report no. 20, Martin Marietta, as above
- Snyder, W. A., 1972, Similarity criteria for the application of fluid models to the study of air pollution meteorology, Boundary layer meteorology 3, 113-134
- Stanton, R. G., 1964, Numerical methods for science and engineering, Prentice-Hall
- Surry, D., 1969, The effect of high intensity turbulence on the aerodynamics of a rigid circular cylinder at sub-critical Reynolds numbers, UTIAS Report 142, University of Toronto

- Surry, D., 1972, Some effects of intense turbulence on the aerodynamics of a circular cylinder at subcritical Reynolds numbers, JFM 52, 543-563
- Sutton, O. G., 1953, Micrometeorology, McGraw Hill
- Taylor, G. I., 1935, 1936, Statistical theory of turbulence, Parts I-V, PRSL, A151, 421-478; A156, 307-317
- Taylor, G. I., 1938, The spectrum of turbulence. PRSL. A164, 476-490
- Townsend, A. A., 1947, The measurement of double and triple correlation derivatives in isotropic turbulence, PRCPS 43, 560-570
- Townsend, A. A., 1951, The passage of turbulence through wire gauzes, Q J Mech and Appl Math IV, 308
- Tritton, D. J., 1959, Experiments on the flow past a circular cylinder at low Reynolds numbers, JFM 6, 547
- Tritton, D. J., 1971, A note on vortex streets behind circular cylinders at low Reynolds numbers, JFM 45, 203-208
- von Bohl, J. G. Edler, 1940, Das verhalten paralleler luftstrahlen, Ing.-Arch, II, 5, 295-314

Abbreviations used in this Bibliography:

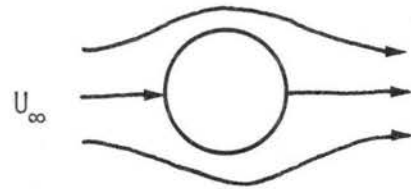
- ASCE: American Society of Civil Engineers
- ASME: American Society of Mechanical Engineers
- CSU: Colorado State University, Fort Collins, Colorado
- JAS: Journal of Atmospheric Sciences
- JFM: Journal of Fluid Mechanics
- NACA: National Advisory Committee for Aeronautics
- PRCPS: Proceedings of Cambridge Philosophical Society
- PRSL: Proceedings of the Royal Society of London
- PTRSL: Philosophical Transactions, Royal Society of London

## APPENDIX A. THEORETICAL BACKGROUND

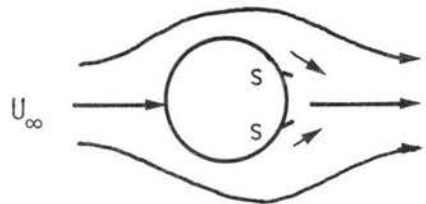
### A.1 VORTEX SHEDDING FROM A CIRCULAR CYLINDER

Figure 11.5 of Schlichting (1960) shows several stages in the development of a Karman vortex street in flow past a cylinder. This figure has photographs of flow past a cylinder as it is accelerated through a standing liquid. It is useful to consider several of the photographs as similar to that of air flow past a cylinder at different values of the Reynolds number,  $Re$ .

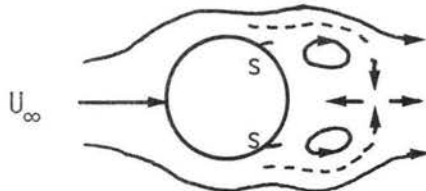
(1) Stokes flow: When  $Re$  is very low, unity or less, the flow has streamlines very much like potential flow. A boundary layer on the cylinder starts at



the forward stagnation point and continues to the rear stagnation point. As  $Re$  increases to about 4, the streamlines behind the cylinder begin to separate near the rear stagnation point, indicating boundary layer separation before the rear stagnation point is reached at the two "S" points.



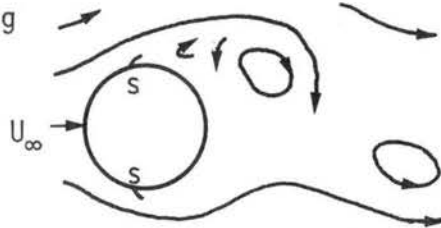
(2) Foepfel flow: As  $Re \approx 10$  to 15 the separation point of the boundary layer has moved further back and two, symmetrical "Foepfel" vortices form just behind



the "shoulders" of the cylinder. This fixed vortex pair is separated from the main flow of the fluid by the vortex layers (dashed lines) which are continuations of the laminar boundary layers after their separation. Their vorticity comes from the shear between the main flow

and the stagnated flow behind the cylinder. As  $Re$  increases towards 40, the two Foepfel vortices remain in place but increase in size and vorticity strength.

(3) Stable vortex flow ( $40 < Re < 150$ ): When  $Re$  is approximately 40, the Foepfel vortices start breaking away alternately with new ones replacing them. A Karman vortex street is established. The vortices move downstream at a speed less than  $U_\infty$ . The reasons for the vortices breaking away are discussed in Section A.3.1.



This is an entirely laminar, viscous process. Roshko calls this the "regular" vortex shedding regime. The instability of the two symmetrical Foepfel vortices immediately behind the cylinder is transformed into a different kind of laminar flow. The individual vortices shed alternately, keep their laminar individuality, and can exist as far as 100 diameters downstream. The vortex geometry is originally very close to Karman's idealized value of  $h/\ell = .28$ , but is not constant because the lateral spacing,  $h$ , increases downstream ( $\ell$  is longitudinal spacing). Vortices must have cores of finite radius; they grow downstream, so they diffuse into each other and decrease their circulation. The relation between  $St$  and  $Re$  is rather accurately stated by Roshko's (1954) empirical formula:

$$St = .212 - 4.49/Re \quad (A-1)$$

This indicates that  $St$  increases rapidly, from .100 for  $Re = 40$ , to .182 for  $Re = 150$ . This relation is generally used for vortex shedding anemometers.

The next stages are based on Roshko's work (1954, 1961) and it is assumed that the undisturbed upstream flow has near zero turbulent intensity.

(4) Laminar transition ( $150 < Re < 300$ ): At  $Re \approx 150$ , some of the vortices become turbulent after they break away from the cylinder. The undisturbed flow is still laminar. By the time  $Re$  reaches 300, most or all of the vortices become turbulent soon after shedding. Equations (A-1) and (A-2) both apply with approximate accuracy in this region. In this range there are irregular bursts of velocity in the wake, the bursts becoming stronger as  $Re$  increases. The shedding frequency is more difficult to determine.

(5) Irregular vortex flow ( $300 < Re < 3 \times 10^5$ ): The vortices become increasingly turbulent and lose their identity more rapidly downstream as  $Re$  increases. By the time  $Re$  approaches the transition value near  $3 \times 10^5$ , turbulent conditions in the wake have moved upstream and transition has started in the cylinder boundary layer. The following formula is fairly accurate for the lower  $Re$  numbers but is not applicable for the higher values:

$$St = .212 - 2.69/Re \quad (A-2)$$

Roshko (1954) used data only up to  $Re$  of  $10^4$  but stated that vortex shedding continues up to at least  $10^5$ . (As shown later, this vortex shedding regime has been reported for values as high as  $5.5 \times 10^5$  but is very sensitive to transition, free stream turbulence, or cylinder smoothness, and has a three-dimensional structure.)

(6) Critical transition range ( $3 \times 10^5 < Re < 5 \times 10^5$ ): In this range the boundary layer of the cylinder has a transition to a

turbulent boundary layer and the boundary layer separation points move considerably forward (downwind) on the cylinder. Vortex shedding has usually not been observed.

(7) Super-critical range ( $5 \times 10^5 < Re < 1 \times 10^6$ ): There is some question as to whether or not vortex shedding occurs in this range. Roshko investigated this by applying a "universal"  $St$  based on a free-streamline model; he obtained accurate results for the trans-critical range discussed later. The following is quoted from his 1961 paper:

"Attempts to make similar calculations in the supercritical regime are unsuccessful . . . calculated values of  $St$  vary from 0.15 to 0.7. We must conclude that either the experimental data in this region is inaccurate . . . or the free-streamline model is inapplicable here."

(8) Upper transition range ( $1 \times 10^6 < Re < 3.5 \times 10^6$ ): Roshko observed no vortex shedding in this region, although Delaney and Sorenson reported shedding at  $1$  to  $2 \times 10^6$ ; the associated  $St$  values were from .42 to .46.

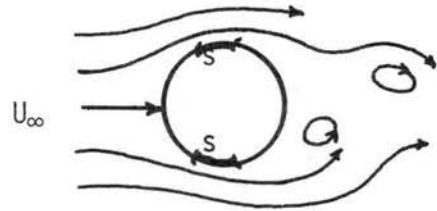
(9) Trans-critical range ( $3.5 \times 10^6 < Re < 10^7+$ ): Roshko observed vortex shedding here with  $St$  of .27. This is consistent with drag coefficient measurements made (by Dryden and Hill) with pressure observations 80 feet up on a 120 foot smoke stack. No observations for  $Re$  above  $10^7$  are known, so the upper limit of this regime is uncertain.

So far, this has followed Schlichting's or Roshko's reports. Achenbach's more recent analysis is slightly different for  $Re > 3 \times 10^5$ .

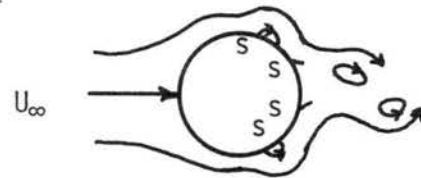
Achenbach (1968) used very precise measurements of skin friction on a circular cylinder to define three regions of  $Re$  regimes for flow, giving some overlap with the above terminology. Furthermore, Achenbach ties in angles of boundary layer separation and pressure distributions with the skin friction data. His observations were in the  $Re$  range

$6 \times 10^4$  to  $5 \times 10^6$ . Separation was defined to take place where the directly observed skin friction became zero. He used a cylinder 6" in diameter and operated in two tunnels; one at atmospheric pressure and the other pressurized to 40 bars.  $T_i$  was .7%, cylinder blockage 16.7%,  $L/D = 3.3$ . His three regimes are defined as:

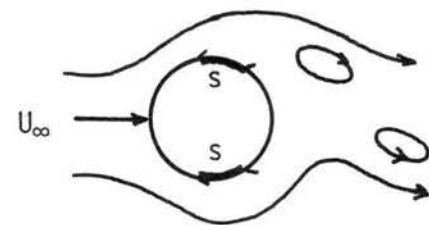
(1) Sub-critical vortex flow ( $Re < 3.0 \times 10^5$ ): The cylinder boundary layer separates lamina-ly at angles from  $72^\circ$  to  $94^\circ$ . This includes the "stable vortex flow," "laminar vortex transition," and "irregular vortex flow" following Roshko's analysis.



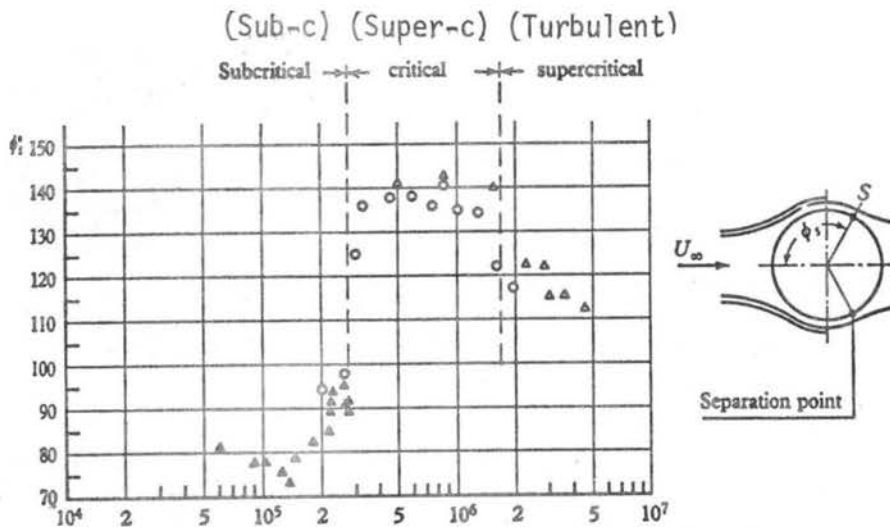
(2) Critical flow ( $3 \times 10^5 < Re < 1.5 \times 10^6$ ): This includes Roshko's "critical transition" and "super-critical" range. A separation bubble occurs as a region between laminar separation (near  $105^\circ$ ), a transition to turbulent flow, a turbulent reattachment and a turbulent separation takes place near  $140^\circ$ . Vortex streets have generally not been observed in this flow.



(3) Super-critical flow ( $Re > 1.5 \times 10^6$ ): This includes Roshko's "upper transition" and "trans-critical" range. Organized vortex shedding is again observed. The separation bubble disappears. The boundary layer is now turbulent before separation and the transition point shifts toward the stagnation point as  $Re$  increases. The separation point is  $85^\circ$  to  $115^\circ$ .

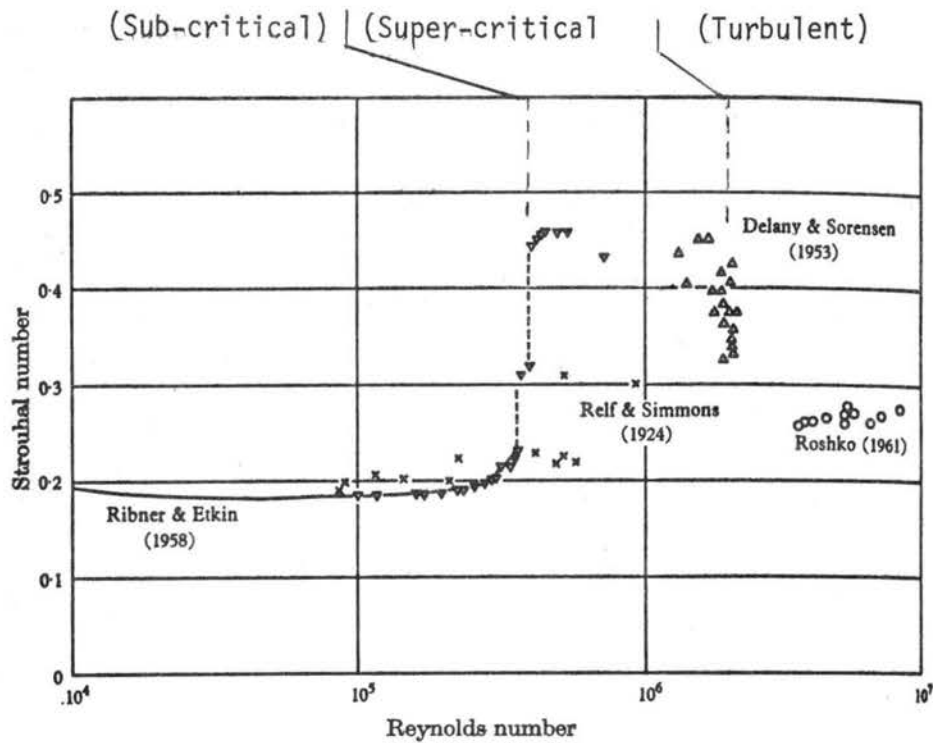


Achenbach compared his results with earlier work by Wieselsberger, Fage and collaborators, Giedt, and Roshko. Compatible results were obtained with variations believed explainable by differences of free stream turbulence and cylinder smoothness. Achenbach's data on the separation angles is reproduced here. My terminology is in parenthesis at the top, above his.



Position of separation angle of boundary layer on a circular cylinder, as a function of Reynolds number. These apply to air flow in wind tunnels with near zero turbulence intensity. (From Achenbach, 1968)

Bearman (1969) obtained more detailed measurements of shedding frequencies throughout the critical  $Re$  ranges. They supplement other measurements by Rolf and Simmons in 1924, Delany and Sorenson in 1953, Ribner and Etkin in 1958 and Roshko in 1961. All of their data are plotted in the following figure from Bearman. Bearman's tunnel was 9' x 7' in cross section with a cylinder of 7" diameter and a free stream turbulence intensity of .7%. This is believed to be the latest information on the subject. My terminology is inserted at the top in parentheses:



Strouhal number versus Reynolds number, for circular cylinders. These apply to air flow in wind tunnels with near zero turbulence intensity. (From Bearman, 1969)

Bearman states a viewpoint about vortex shedding which justifies the underlining I have given it:

"The super-critical regime is characterized by a less regular vortex shedding behavior and it was at one time thought that this flow regime extended to extremely high Reynolds numbers. It was only with the experiments of Roshko (1961) that it was realized that a further narrow-band vortex shedding regime, the trans-critical, existed. Roshko suggested that in the trans-critical regime there was no laminar separation bubble and that separation was purely turbulent. It came as a surprise that regular vortex shedding should recommence, but, since vortex shedding is a result of the basic instability that exists between two shear layers and is inherent in most separated flows behind two-dimensional bodies, it is perhaps more surprising that regular shedding should ever cease."

Bearman measured shedding frequency by a hot wire set  $1.5D$  downstream and  $.5D$  laterally from the cylinder center. He obtained sharp

peaks in power spectra analyses of the recorded voltage. However, he found that the vortex shedding (near the critical  $Re$ , about  $3 \times 10^5$ ) could be spread across a wide frequency band by placing any small protuberance (e.g., a dust particle) on the surface of his smooth, polished cylinder.

The above information has been summarized in figures 1 and 2. Four vortex shedding regimes are defined in figure 2 for use in this study.

## A.2 BOUNDARY LAYER CONSIDERATIONS\*

### A.2.1 LAMINAR BOUNDARY LAYERS

The Navier-Stokes equations and the continuity equation define flow in laminar boundary layers.

$$\begin{aligned} \rho \frac{Dv_i}{Dt} &= -\frac{\partial P}{\partial x_i} + \mu \frac{\partial^2 v_i}{\partial x_j \partial x_j} \\ \frac{\partial v_i}{\partial x_i} &= 0 \end{aligned} \tag{A-3}$$

Prandtl in 1904 derived the two-dimensional, incompressible, laminar boundary layer equation for flow along a flat plate. He simplified the Navier-Stokes equations by discarding terms which were much smaller than the others. The resulting "Prandtl Boundary Layer" equations are

$$\begin{aligned} \frac{\partial v}{\partial t} + u \frac{\partial v}{\partial x} + v \frac{\partial v}{\partial y} &= -\frac{1}{\rho} \frac{\partial P}{\partial x} + \nu \frac{\partial^2 v}{\partial y^2} \\ \frac{\partial v}{\partial x} + \frac{\partial v}{\partial y} &= 0 \end{aligned} \tag{A-4}$$

---

\*Major references are Kuethe & Schetzler (1961), Rotta (1962), Sandborn (1970), and Schlichting (1960).

with boundary conditions:           at  $y = 0$ ;  $U = V = 0$   
   as  $y \rightarrow \infty$ ;  $U = U(x,t)$

where  $U(x,t)$  is the potential flow outside the boundary layer.

Several major assumptions were required to obtain this simplified form, namely:

(1) The boundary layer depth or thickness,  $\delta$ , (in the  $y$  direction) is much less than the length of the plate;

(2) The pressure distribution in the boundary layer is the same as in the potential flow at the top of the boundary layer.

(3) The Reynolds number of the flow is large.

$$(4) \quad \left| \frac{\partial^2 \psi}{\partial y^2} \right| \gg \left| \frac{\partial^2 \psi}{\partial x^2} \right|$$

Tollmein in 1931 showed that these boundary layer equations could be applied to a curved wall also if there are no large variations in the curvature and if the radius of curvature is much larger than the depth of the boundary layer. These conditions should be satisfied in the cases of the 4.5" and 2.75" diameter cylinders with undisturbed (open tunnel) air flows of near 18 fps used in this study.

To solve Prandtl's boundary layer equations, (A-4), the pressure gradient must be specified. Because of the assumptions used in deriving these equations, the pressure gradient in the potential flow outside the boundary can be used. Several methods of specifying this outer flow have been used which lead to a solution (Falkner and Skan, Howarth, Tani, etc.). A general method of solving equation (A-4) in terms of series was given by Goertler. The simplest solution is that by Blasius for a zero pressure gradient.

Another approach is to consider the boundary layer enclosed in a momentum box and to integrate the boundary layer equation terms in the boundary layer. This leads to gross quantities as skin friction, displacement thickness and momentum thickness. This work was done originally by von Karman and results in the "Karman Integral Momentum Equation:"

$$\int_{y=0}^{y=\delta} \left[ u \frac{\partial u}{\partial x} + v \frac{\partial v}{\partial y} - u_{\infty} \frac{\partial u_{\infty}}{\partial x} \right] dy = - \frac{\tau_0}{\rho} \quad (\text{A-5})$$

This equation is valid for both laminar and turbulent flows, on condition that in the latter case  $u$  and  $v$  denote the time averages of the respective velocity components.

Laminar boundary layers can become turbulent ("transition") and they can separate from the boundary or they can do both. Transition from laminar to turbulent flow will be considered next.

#### A.2.2 TRANSITION

Reynolds, late in the 19th century, was the first to regularly observe transition of laminar flow into turbulent flow. He developed the concept of critical flow conditions, now called the "critical Reynolds number,"  $Re(c)$ , at which transition occurs. He recognized that increased disturbances in flows lowered the critical value. He hypothesized that transition was due to a type of instability in the flow.

Subsequent studies showed that changes took place in boundary layer phenomenon when transition occurred: the point of boundary layer separation moved downstream; the boundary layer became thicker; the

velocity profile changed; the shape factor decreased. It was also observed that the pressure gradient and surface roughness influenced transition. It was noted that in laminar flow the longitudinal pressure gradient,  $\partial P/\partial x$ , is proportional to  $U$ , but in turbulent flow is proportional to  $U^2$ .

When turbulence appears in a boundary layer, the momentum from outer, potential flow is transported more effectively downward through the boundary layer to the layers of fluid next to the surface. This explains why a turbulent boundary layer can proceed further downstream on a body before it separates.

During the first four decades of this century, a complex theory of flow instability was developed, mainly by German investigators, known as the "small disturbance stability theory." It was derived by introducing random variations into the mean flow of the Navier-Stokes equation and then imposing a small sinusoidal disturbance into the flow. This results in the Orr-Sommerfeld equation (without viscosity) which asserted that boundary layer velocity profiles which possess a point of inflection are unstable and lead to transition. A point of inflection is directly related to an unfavorable pressure gradient and agrees with observed effects. Rayleigh's result was later proven by Tollmein for conditions that gave full account of viscosity effects.

In 1940, Schubauer and Skramstad (1948) used a new wind tunnel at the National Bureau of Standards that was especially designed for investigating the theory of flow instability over a flat plate. With a contraction ratio of 7.1:1 and six damping screens, they obtained tunnel flow with only .03% turbulence intensity. Small disturbances

were made and controlled by a bar activated by an alternating current. Their resulting experiments brilliantly verified Tollmein's and Schlichting's theory.

The reason that the NBS experiment succeeded when previous ones had not is because of the extremely low turbulence intensity in the NBS tunnel flow. Higher turbulence intensity of earlier tunnels had caused transition before selective amplification of small disturbances could be seen.

The Orr-Sommerfeld equation is based on two-dimensional flow. It would seem obvious that three-dimensional disturbances should be more effective in creating transition and make the above results unrealistic. However, Squire has shown theoretically that the Orr-Sommerfeld expression of instability is more susceptible to two-dimensional disturbances than to three-dimensional ones.

Schubauer and Skramstad could obtain a variety of pressure gradients ( $dP/dx$ ) by placing objects in the tunnel or by altering the tunnel ceiling. They verified the earlier results of Rayleigh. In the strongest favorable gradient (accelerating, or  $dP/dx < 0$ , or  $dU/dx > 0$ ) damping of the oscillations always occurred, and vice versa.

Pretsch applied the results of Tollmein and Schlichting to boundary layer on bodies of revolution and found that the stability solutions were the same. Goertler generalized the stability criterion for profiles with a point of inflection to include the influence of wall curvature. He found that, for convex walls, the influence of wall curvature is very small if the boundary layer thickness is much smaller than the radius. (For concave walls, a different kind of instability exists.)

By laminar boundary layer theory, the pressure gradient in the outside (potential) flow governs the pressure gradient inside the boundary layer. Consequently, the point of lowest pressure on a cylinder corresponds to the highest velocity in the free stream. This also defines the point where  $dP/dx$  becomes zero as it changes from a favorable to an unfavorable gradient. So, the point of beginning instability corresponds to a point of minimum pressure and the point of transition follows shortly downstream.

As the  $Re$  is increased, the points of instability and transition move downstream. At very high  $Re$  [ $> Re(c)$ ] the points of instability and transition may precede the point of minimum pressure.

### A.2.3 TURBULENT BOUNDARY LAYERS

Turbulent, viscous flow is described by the Reynolds equations of motion and the equation of continuity. For steady, incompressible conditions, they are:

$$\begin{aligned} \nu_j \frac{\partial v_i}{\partial x_j} &= -\frac{1}{\rho} \frac{\partial P}{\partial x_i} + \frac{\partial}{\partial x_j} \left[ \nu \frac{\partial v_i}{\partial x_j} - \overline{u_i u_j} \right] \\ \frac{\partial v_i}{\partial x_i} &= 0 \end{aligned} \tag{A-6}$$

New unknown factors in the form of Reynolds stresses have been added but no additional equations are available. Hence no unique mathematical solution is even theoretically possible. Practical approximations to solutions require assumed additional relations as well as simplifications.

It is doubtful that Prandtl's earlier approach in simplifying equations can be used because there is no physical reasoning to

determine the relative magnitude of the turbulent terms. Instead, an empirical approach must be used.

Sandborn and Slogar (1955) experimentally evaluated the relative importance of the terms in Reynolds equations for two-dimensional, incompressible flow over a flat plate. They obtained these equations for a turbulent boundary layer:

$$\begin{aligned} \text{x direction: } & U \frac{\partial U}{\partial x} + V \frac{\partial U}{\partial y} = -\frac{1}{\rho} \frac{\partial P}{\partial x} - \frac{\partial}{\partial y} (\overline{uv}) + \nu \frac{\partial^2 U}{\partial y^2} \\ \text{y direction: } & 0 = \frac{1}{\rho} \frac{\partial P}{\partial y} + \frac{\partial \overline{v^2}}{\partial y} \\ \text{continuity: } & \frac{\partial U}{\partial x} + \frac{\partial V}{\partial y} = 0 \end{aligned} \quad (\text{A-7})$$

Sandborn and Slogar further found that, in adverse pressure gradient flow, the Y direction equation is independent of the X direction equation.

The boundary conditions for the turbulent boundary layer equations are not as straightforward as for the laminar case. The following comments can be made:

- (1) The mean velocities,  $U = V = 0$ , at  $y = 0$  are the same.
- (2) A question can be raised as to whether or not the turbulent velocities are zero at the wall, although some texts specify this.
- (3) Because the  $v$  component in the layer need not be zero or even excessively small, it results that  $\partial P / \partial y$  is not required to be zero. Consequently, the pressure distribution at the base of the layer may not be the same as the outside flow.
- (4) The outer edge of the layer is intermittent so that the depth must be specified by some probability considerations.

(5) The mean value of the total shearing stress, through the layer, is given by:  $\tau_{yx} = \mu \frac{\partial \bar{u}}{\partial y} - \rho \overline{u'v'}$

(6) The concept that  $\frac{\partial}{\partial y} \gg \frac{\partial}{\partial x}$  applies to both laminar and turbulent boundary layers.

The evaluation of the term  $\frac{\partial}{\partial y}(\overline{u'v'})$  is the dominant problem in evaluating the turbulent boundary layer.

#### A.2.4 MODEL OF A TURBULENT BOUNDARY LAYER

Measurements by many investigators have shown that the turbulent boundary layer can be approximately classified into three regions:

- (a) an "inner region" in which the viscous shear stress is dominant;
- (b) an "outer region" where the turbulent shear stresses are much greater than the viscous; and
- (c) the "intermediate region" where the viscous and turbulent shears are of comparable magnitude.

In the inner region, the mean velocity distribution,  $U$ , is determined by  $\tau_0$ ,  $\rho$ ,  $\nu$ , and  $y$ . Dimensional considerations lead to the following expression which is known as Prandtl's "law of the wall."

$$\frac{U}{u_*} = f\left[\frac{yu_*}{\nu}\right]; \quad \text{where } u_* \equiv \text{friction velocity} \equiv \sqrt{\tau_0/\rho} \quad (\text{A-8})$$

This is valid up to about  $(yu_*/\nu) < 5$ . The term  $yu_*/\nu$  is a dimensionless wall distance and is also a special form of the Reynolds number. It is used as the abscissa in showing the similarity form of the turbulent velocity profile near the surface.

In the outer region, which comprises the great majority of the turbulent boundary layer depth, is a region independent of viscosity but dependent on the friction velocity. This dependence, first

recognized by von Karman, is known as the "velocity defect" law and can be expressed:

$$\frac{u_{\infty} - u}{u_*} = f \left[ \frac{y}{\delta} \right] \quad (\text{A-9})$$

This is valid for approximately  $\frac{yu_*}{\nu} > 70$

In the overlap region, both equations (A-8) and (A-9) must be closely satisfied. Several experimenters (Clauser, Ludweig, Tillman; Hama, Klebanoff and Diehl, Freeman, and Schultz-Grunow) have investigated this. This transition velocity profile is of the form:

$$\frac{u}{u_*} = C_1 \log \left[ \frac{yu_*}{\nu} \right] + C_2 \quad (\text{A-10})$$

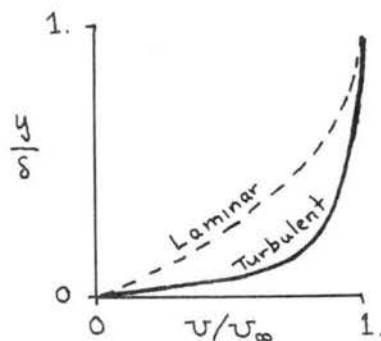
Experimental results give values of  $C_1$  of 5.6 and 5.75, and values of  $C_2$  of 4.9, 5.2 and 5.5. As implied above this is valid for

$$5 < \left[ \frac{yu_*}{\nu} \right] < 70$$

The inner and transition region are shown as function of the non-dimensional parameters  $\left( \frac{yu_*}{\nu} \right)$  and  $\left( \frac{y}{\delta} \right)$  in figure 47 from Kuethe and Schetzer.

It is apparent from figure 47 that the turbulent boundary layer cannot be expressed as a function of a single parameter (as is possible for the laminar boundary layer) but must be treated piecemeal with the parameters  $(yu_*/\nu)$  and  $(y/\delta)$ . In general, the turbulent velocity profile has a much sharper curvature at a small distance from the wall as is shown in the following diagram:

The depth of the turbulent boundary layer, although it increases with downstream distance, fluctuates in a turbulent manner.



It is noteworthy that equation (A-10) was first derived using the mixing length hypothesis and the two additional assumptions: (a) mixing length is proportional to the distance from the wall; and (b) the shear stress through that part of the turbulent boundary layer is constant and equal to the wall shearing stress. A somewhat similar result can be found by applying von Karman's similarity hypothesis. The goal of this application is to determine the dependence of the mixing length upon the space coordinates within a turbulent boundary layer. His hypothesis is that the turbulent fluctuations are "similar" at all points of the field of flow and they differ from point to point only by time and length (or velocity) scales. See Section XIX f of Schlichting.

It should be noted that all of the above are satisfied only at large Reynolds numbers. This is not a limitation since large Reynolds numbers are needed to insure turbulent flow.

Nikuradse carried out thorough investigations of velocity profiles in smooth pipes for  $4 \times 10^3 < Re < 3.2 \times 10^6$ . The results can be represented by the empirical equation:

$$\frac{u}{u_\infty} = \left[ \frac{y}{R} \right]^{1/n} \quad (\text{A-11})$$

where  $n = 6$  for  $Re \approx 4 \times 10^3$ ;  $n = 7$  for  $Re \approx 110 \times 10^3$ ; and  $n = 10$  for  $Re \approx 3240 \times 10^3$ .

### A.2.5 SEPARATION

Separation of fluid flow, from a solid surface, occurs when the limiting streamline, close to and parallel to the surface, suddenly increases its distance from the surface by a large amount. The boundary layer then thickens and has significant vertical ( $y$ ) motion so that the boundary layer theory is no longer applicable. Back flow usually starts near the surface just downstream from the separation point.

In a boundary layer, either laminar or turbulent, viscosity acts through skin friction to remove momentum from the main flow and transfers it to the surface as heat. If a sufficient supply of momentum is not fed into the region near the surface, there will soon be a finite layer next to the surface in which there is no momentum. At this time boundary layer separation commences. More precisely, separation commences when the surface shear stress becomes zero, or:

$$\tau_0 = \mu \frac{\partial U}{\partial y} \Big|_{y=0} = 0$$

The mathematical condition for separation can be further defined by considering the laminar boundary layer equation (A-4) at the surface, Here,  $U = V = 0$ , and the equation becomes:

$$\frac{\partial P}{\partial x} = \mu \frac{\partial^2 U}{\partial y^2} \Big|_{y=0} \quad (A-12)$$

This equation states that in the immediate neighborhood of the surface, the curvature of the velocity profile depends only on pressure gradient, and the curvature of the velocity profile at the wall changes its sign with the pressure gradient. Because of the pressure gradient in a laminar boundary layer's being imposed on it by gradient in the external potential flow, some further inferences can be

derived from equation (A-12). Consider the example of laminar flow past a cylinder.

In an accelerated flow, such as around the upwind half of a cylinder,  $\partial P/\partial x < 0$  and  $\partial U/\partial x > 0$  so that one has a "favorable" pressure gradient.

When the pressure gradient changes to  $\partial P/\partial x > 0$ , it must first go through the value  $\partial P/\partial x = 0$ . Then by equation (A-12),  $\partial^2 U/\partial y^2 = 0$ . In potential flow this occurs at  $\alpha = \pm 90^\circ$ . Due to the inertia of flow, little change has yet taken place in the  $U(y)$  profile except for the establishment of an inflection point at the surface.

Then as the pressure gradient becomes  $\frac{\partial P}{\partial x} > 0$  and  $\frac{\partial^2 U}{\partial y^2} > 0$

on the downwind side of the cylinder, the point of inflection in  $U(y)$  moves up from the surface into the boundary layer. If this is continued long enough, back-flow will take place in the  $U(y)$  profile near the surface.

It follows that in a region of retarded potential flow, the velocity profile  $U(y)$  in the boundary layer always has a point of inflection. Since the velocity profile at the point of separation and with a zero tangent must have a point of inflection, it follows that separation can only occur when the potential flow is retarded.

Continuing with the example of flow past a cylinder, Blasius calculated the theoretical separation point for laminar viscous flow past a cylinder. He used a power series to represent the pressure gradient with the application of Bernoulli's equation, the equation of continuity and the Navier-Stokes equations. He finally invoked the requirement that the surface shear stress be zero. His solution defined the

separation point at approximately  $109^\circ$ . This is  $19^\circ$  beyond the point where  $\partial P/\partial x = 0$  in the outside flow and is consistent with the effects of inertia which keeps the fluid moving a short distance against the adverse pressure gradient before  $\partial U/\partial y \Big|_{y=0} = 0$  is realized.

Fage (1929) conducted measurements of air speed and pressure distribution in the boundary layer on a cylinder for air flow at and just below the critical  $Re$ . From this, he determined pressure gradients, separation angle and transition points.

Fage used a cylinder 8.9" in diameter in a 4-foot wind tunnel with air speeds from 22 to 71 fps. These conditions were chosen to obtain  $Re$  values from 1.03 to  $3.33 \times 10^5$  to bracket the boundary layer transition from laminar to turbulent flow as evidenced by a sudden drop in the drag coefficient from 0.6 to 0.2. He used a small steel hypodermic needle to measure total head pressure.

Fage's data is reproduced in figure 48 where a pressure coefficient is plotted versus the angle from stagnation point, and for the highest and lowest air speeds. The following conclusions from that data are quoted:

" . . . the coefficient of the maximum negative pressure increases with the wind speed, and also there is a progressive displacement of the point at which this pressure occurs towards the back of the cylinder . . . An important trait exhibited in each of the curves is the pronounced inflexion (marked BC) between the point of maximum negative pressure (marked A) and the region where the pressure is almost constant. The principal purpose of the subsequent analysis will be to show that the change from the laminar to a turbulent state of flow in the boundary layer probably occurs in this region BC, and that the layer has completely separated from the surface at the point C."

In the case of a turbulent boundary layer, the important requirement that  $\tau_0 = 0$  is needed for separation and the same general

relations to pressure gradients are valid. It is well known that, in the same external pressure gradient, a turbulent boundary layer will experience separation further downstream than for a laminar boundary layer. However, the additional turbulent terms make it difficult to obtain solutions or to even rigorously define all boundary conditions. Turbulence intensity and eddy size can influence the separation process. See Chapter XIII of Sandborn (1970) or Section 16 of Rotta (1962) for a discussion.

Achenbach's observations of separation angles in section A.1 include some from turbulent boundary layers.

When the mean flow outside the boundary layer has a high degree of turbulence, this should tend to cause transition earlier in the boundary layer. This is a result of vorticity entering the boundary layer from the outside.

### A.3 MECHANICS OF VORTEX SHEDDING

This section makes major use of Marris' paper (1964), three reports by Roshko (1954, 1955, 1961), several sections from Goldstein (1965), papers by Gerrard (1965, 1966a, 1966b) and others as mentioned.

#### A.3.1 GENERAL

In von Karman's famous theoretical development of vortex street geometry, he assumed that two parallel rows of vortices already existed for an infinite distance. Unfortunately, there is still disagreement on the details of exactly how the vortices are formed.

In general terms, the individual vortices are formed from the shear between the free stream flow and the stagnant flow immediately behind a cylinder.

The idea is that the two vortex layers, comprised by the laminar boundary layer after its separation from each side of the cylinder, are disturbed as a result of some downstream effect. Rosenhead (1931) showed numerically that for an ideal fluid the vortex layers are unstable against such disturbance and will roll up into local periodic concentrations of vorticity.

Kovaszny (1949) and Tritton (1959) proposed that the appearance of a vortex street ( $Re \approx 40$ ) is not due to shedding but to the instability in the "early wake." Tritton then stated that at a  $Re$  between 90 to 100 this instability moves upstream and starts close to the cylinder but the instability develops further as the vortex goes downstream. All of this takes place in "regular" vortex flow. In the "irregular" vortex flow, and higher  $Re$  flows, a fully developed vortex street exists right from the start close to the cylinder.

One approach has been to couple the vortex street to the free vortex layer by correlating von Karman's results for the potential flow vortex street to the "early wake" results based on a modified Helmholtz-Kirchhoff free streamline theory. An account of this approach is given by Roshko (1955) and by Birkhoff (1953). The basic Kirchhoff theory requires that the separated boundary layers be idealized as surfaces of velocity discontinuity separating the wake from the outer potential flow.

The previous classifications of vortex flow regimes are believed to be associated with different mechanics of vortex formation. An

interaction of velocity shear, boundary layer, separation, transition, roll up into vortices, and pressure differences must be reviewed in attempting to explain the mechanics. The mechanics of vortex street formation at higher  $Re$  will be considered primarily.

#### A.3.2 FORMATION REGION BEHIND CYLINDER

Gerrard (1965) stated that as long ago as 1933, Schiller and Linke discovered that large changes took place in the flow close behind a circular cylinder in the  $Re$  range of approximately  $10^3$  to  $10^4$ . They found that what is now called the formation region of the wake is considerably reduced in size as  $Re$  increases through this range. They were also able to demonstrate that the change was attended by a movement, of the position of the flow transition to turbulence, towards the cylinder.

Bloor (1964) made a careful investigation of the transition to turbulence in the wake of a circular cylinder. She used a hot wire anemometer in flow conditions of  $Re$  ranging from  $2 \times 10^2$  to  $5 \times 10^4$ . Cylinders were 1" or less in diameter. Two tunnels were used, a return-circuit with a turbulence intensity less than .03%, and an open circuit one with about 1.0%. The aim of her study was to consider the manner and position of transition as  $Re$  changes over the range in which turbulent motion develops after the fluid has separated from the cylinder.

The "vortex formation region" is the region of flow inside the wake between the separation point on the cylinder and the first appearance of the periodic vortex street. The edge of the wake is generally thought of as the boundary between the rotational flow of the wake and

the irrotational flow in the free stream. Bloor found a more practical definition for use with a hot wire; the boundary (of the formation region) is where a sudden jump is noticed in the RMS AC voltage as the sensor enters the wake from the free stream. The downstream beginning of the wake is marked by the sudden reduction of low frequency irregularities always observed in the formation region; this agrees well with the appearance of "typical" turbulent vortices.

The length of the formation region, measured from the center of the cylinder, appears to increase from  $2D$  at the beginning of the "laminar transition range" ( $Re \approx 150$ ) to  $2.5D$  at about  $Re \approx 1.3 \times 10^3$ . At  $Re$  above this, there is a steady decrease in the length of the formation region with increasing  $Re$ . There is some dependence on cylinder diameter. It seems likely that the length of the formation region will affect the pressure at the rear of the cylinder.

In the laminar transition range ( $150 < Re < 300$ ), the downstream development of turbulence is thought to be due to three-dimensional distortions. Above  $Re \approx 300$ , transition occurs before the separated layer rolls up. The vortices once formed are turbulent. Regular sinusoidal waves similar to Tollmein-Schlichting two-dimensional waves appear to be a phenomenon connected with transition when it occurs within the vortex formation region. These waves are observed at all  $Re > 1300$ , in the sub-critical regime.

Gerrard (1966b) theorized on the mechanics of the formation region of shedding vortices. He was particularly interested in explaining why the Strouhal number is nearly constant from  $Re \approx 300$  up to near transition at  $3 \times 10^5$ ; he also required that the theory explain the observed effects of splitter plates. He concluded that two different length

scales within the formation region explained the frequency of shedding and that these two scales interacted so that their product was nearly constant.

Gerrard concluded that the entrainment of air into vortices from the interior of the formation region and its replenishment by reversed flow is fundamental to the "length of the formation region" which is one of the lengths that determines the frequency of vortex shedding. The second is the "diffusion length." This is the thickness of the shear layer at the end of the formation region where a shear layer is first drawn across the wake.

Gerrard postulated that a growing vortex continues to increase in strength as it is fed by circulation from the shear layer on its side of the wake. When the vortex becomes strong enough to draw the other shear layer across the center of the wake, this brings in oppositely-signed vorticity so that the vortex ceases to increase in strength. At this stage, the vortex is shed from the cylinder. The shedding frequency increases if the scale of the formation region is reduced. This is because when the shear layers are brought closer together, their interaction is facilitated and the periodic time is shortened.

The significance of Gerrard's diffusion length concept was implied by Fage and Johansen in 1927 and by Berger in 1964. An increase in the turbulence in the shear layers will result in their being more diffuse in the region of interaction. When the layer is diffused it will take longer for a sufficient concentration of vorticity to be carried across the wake and initiate shedding. So one should expect the shedding frequency to decrease as the "diffusion length" increases.

The following is quoted from Gerrard (1966b) with my underline:

"It appears that one may explain the effect of increasing the free stream turbulence from very small values in the same way. (Gerrard means the product of the two characteristic lengths.) . . . On increasing the turbulence level, the scale of the formation region shrinks and one may hypothesize that the diffusion length will increase. Opposing tendencies of frequency variation could cancel out, and hence the Strouhal number be little affected. This explanation has an unsatisfying facet."

As stated in "Discussion," it is my belief that the Strouhal number is significantly affected if the free stream turbulence is sufficiently increased.

Both of the lengths which determine the frequency of vortex shedding change with splitter plate size and position to conform with observed changes in shedding frequency.

### A.3.3 SPLITTER PLATES

Roshko (1954, 1955) experimented with splitter plates to illustrate the dependence of the periodic shedding on interaction between the two free vortex layers in the flow field directly behind the cylinder. Gerrard calls this the "formation region." A thin plate (as tall as the cylinder) was mounted directly behind the cylinder in the center plane of the wake. If the plate touches the rear of the cylinder and extends about  $5D$  downstream, it is completely effective in stopping the periodic shedding. It appears that if the two shear layers from either side of the wake can't "see" each other in the region where they tend to roll up, there is no stabilizing mechanism to fix a definite, periodic, alternating, vortex formation. Then the shear layers will break down in some other manner, independently of each other. The

presence of the splitter plate also greatly reduces the pressure deficit behind the cylinder and thereby greatly reduces the drag on the cylinder.

If a shorter plate is used, about  $1D$  in downstream length, periodic shedding will continue but at a lower frequency. As this plate is moved downstream, the shedding decreases even more and reaches a minimum when the gap between the cylinder and the plate is about  $1.5D$ . Then, when the plate is moved just beyond this critical position, the shedding frequency abruptly increases, almost to its undisturbed value, corresponding to the flow without interference.

What is clear from these experiments is that in every case the flow in the first few diameters downstream is critical for the determination of the vortex shedding and base pressure.

#### A.3.4 THREE-DIMENSIONAL WAKE

At  $Re > 90$ , all workers (with the exception of Hama) found three-dimensional effects in the structure of the wake of circular cylinders. Gerrard (1966a) gave a summary. Roshko and Phillips investigated the wake at two points separated in the spanwise direction. They found a phase shift between the oscillations at the two points. Roshko reported a wave length in the direction of the cylinder axis of  $18D$  at  $Re \approx 80$ , while Phillips found 15 to  $20D$  for  $100 < Re < 150$ .

Hama's highest  $Re$  number photograph is for  $Re \approx 313$ , in which one can see the  $10D$  wave length still persisting but accompanied by waves of much shorter length. Between  $Re$  of  $3 \times 10^3$  and  $10^5$ , Mattingly observed a periodicity in the direction of the axis on the cylinder surface. The spanwise structure became chaotic as the critical  $Re$  is

approached. Roshko gave the correlation length, in the spanwise direction, as  $10D$  at  $Re \approx 220$  and  $3D$  at  $Re \approx 500$ . Phillips found a correlation length of about  $3D$  at  $Re \approx 5 \times 10^3$ . Prendergast and el Baroudi observed that between  $Re$  of  $10^4$  and  $10^5$  the correlation length is about  $4D$ . Using silk threads attached to the cylinder to visualize flow, Humphreys (1960) reported a stationary pattern of wave length  $1.4$  to  $1.7D$  at the critical  $Re$ .

#### A.4 FREE STREAM TURBULENCE EFFECTS

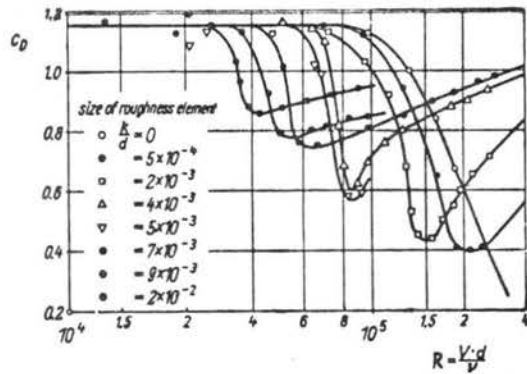
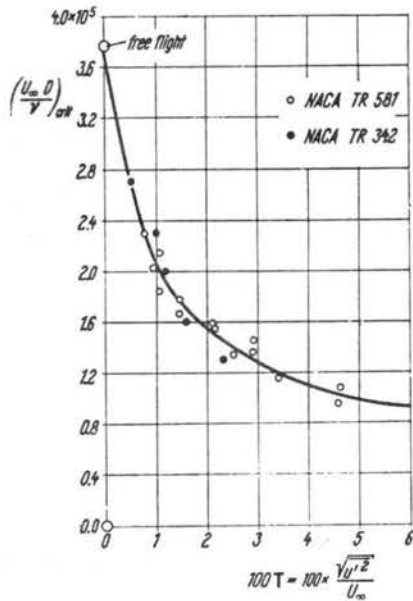
##### A.4.1 CRITICAL REYNOLDS NUMBER, $Re(c)$

For both spheres and cylinders,  $C_d$  suddenly decreases as  $Re$  increases to a value near  $3 \times 10^5$ . This is associated with transition of the boundary layer, a quick narrowing of the wake and a sharp reduction in the "form" drag, caused by the base pressure behind the body being lower than free stream pressure. This value is the "critical Reynolds number,"  $Re(c)$ .

Taylor (1936) makes the following statement:

". . . A drag coefficient of  $C_d = .3$  has been chosen arbitrarily in the middle of the range of Reynolds numbers over which the change from one type of flow to the other is taking place and defined as the drag coefficient corresponding with a critical Reynolds number . . . . The value . . . has been used as a convenient arbitrary measure of turbulence in wind tunnels, for it has been found to depend very much on the amount of turbulence in the wind stream."

$Re(c)$  is sensitive to both the turbulence intensity and the roughness of the sphere or cylinder surface. Two figures from Schlichting show these effects:



Relation between the critical Reynolds number of a sphere and the intensity of turbulence of the tunnel, after H. L. Dryden and A. M. Kuethé (from Schlichting).

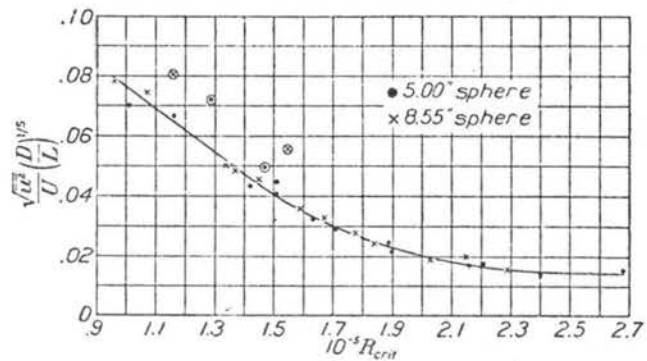
Drag on circular cylinders at varying roughness, after Fage and Warsap (from Schlichting).

Taylor (1936) developed a theory that related  $Re(c)$  to the  $Ti$  and  $L_x$  of the free stream and the sphere diameter. This is given by the "Taylor Parameter,"  $Ta$ :

$$Ta \equiv \frac{\bar{u}}{U} \left[ \frac{D}{L_x} \right]^{1/5}$$

Dryden, et al., (1936) experimentally verified that a functional relation existed between  $Ta$  and  $Re(c)$ . The following diagram is taken from Dryden's report.

It is assumed that  $Ta$  applies approximately for flow past cylinders, although Taylor's theoretical development was limited to spheres.



Critical Reynolds number of spheres as a function of the Taylor Parameter (from Dryden).

#### A.4.2 TURBULENCE PRODUCTION BY WIND TUNNEL GRIDS

Much literature exists on the effects of square grids and fine mesh screens on the turbulence conditions of wind tunnel flow. There are four major sources: (1) the US National Bureau of Standards (Dryden, Schubauer, etc.); (2) the US National Advisory Committee for Aeronautics (Corrsin, etc.); (3) the National Physics Laboratory, England (Taylor, Batchelor, Townsend, Bradshaw, Bearman, etc.); and (4) the "Goettingen School" in Germany (Prandtl, Schlichting, etc.). Most of the Goettingen work is summarized either in Schlichting's, Hinze's, or Batchelor's texts. Two problems seem uppermost in the work of all four groups; one is a study of the decay of turbulence (transformation of kinetic energy to heat), and the other is forcing the reduction of the turbulence intensity in a wind tunnel flow before air enters the test chamber.

Two factors are important when considering the earlier published wind tunnel results. First, it seems that all of the earlier work was done with square grids across the entrance to the test section, and second, nearly all of these grids had blockage ratios less than .50.

In my experiments small holes were drilled in square arrays, giving "plates" with blockage ratios from .50 to .97 except for a model of Surry's "grid" with blockage ratio of .34. Thus, the geometry of my plates is different and can be expected to produce flow instabilities due to high blockage ratios.

It is common to find a mesh Reynolds number,  $Re(M) = UM/\nu$ , used to describe a grid, where  $M$  is the distance between the center lines of adjacent bars or wires forming an individual square open area. A more appropriate form for my experiment is a plate  $Re$ ,  $Re(p) = Ud/(1 - Br)\nu$ , where  $Br$  is the area blockage ratio of the plate and  $d$  is the diameter of an individual hole. The portion,  $U/(1 - Br)$ , is a speed term that gives the approximate air speed through each hole.

The air leaves a plate in the form of individual jets from each hole. Some vortex shedding action takes place behind the solid parts of the plate. The jets are dominant because of their high speed. However, the jets and wakes enlarge in size and interact very quickly so that any intense speed is rapidly reduced by entrainment of air with very low speed. Chapter 23 of Schlichting (1960) treated this subject. Figures 1.6, 1.7, and 1.8 of Hinze (1959) illustrated the turbulence and spreading. Taylor called this region the grid "shadow."

Reports have been made of air flow coming past square grids and interacting so quickly that the effects of individual grids were lost within 10 to 40 grid lengths ( $M$ ) downstream. This is a minimum distance and this distance should increase as the value of  $Br$  increases, especially above .5.

In my experiment, the cylinders are  $256d$  downstream from the plates, where  $d = 3/16"$ ;  $192d$  for  $d = 1/4"$ .

Several investigators have reported that a flow instability sets in downstream from plates or screens with Br values greater than about .50. Because all plates used in this experiment have Br values of .50 to .95, this flow instability will be an ever present factor for consideration, except for Surry's grid.

The first complete theoretical and experimental investigation of the stability of flow behind a grid of rods in a closed duct was by von Bohl (1940). By varying the Br of the grid, he obtained both stable and unstable types of flow. His theoretical analysis used a sinusoidal velocity distribution in the main flow, and a small super-imposed sinusoidal distribution of wave length considerably longer than the original. With this small perturbation approach, he obtained the correct qualitative result that the degree of instability decreases with increasing values of Br. He found that Br values of .37 and .46 corresponded to stable and unstable flows, respectively.

Corrsin (1944) observed strong lateral  $\pm$  variations of total head pressure in a wind tunnel flow a few inches downstream from a lattice with Br of .83.

Schubauer, et al., (1950), using a wire screen with Br value of .79, obtained random variations so much larger than those upstream that the screen was "much better as a turbulence producer than as a damper." Far downstream the random variations gave way to a region of high velocity in the central portion of the air flow.

Baines and Peterson (1951) report that for Br values less than about .50 they found quite satisfactory agreement with the Taylor Batchelor theory of damping screens, but for higher values of Br the deviation between theory and experiment became large.

Bradshaw (1965) observed spanwise variations of surface shear stress amounting to 10% or more in nominally two-dimensional turbulent boundary layers. He found the way to avoid this was to keep Br values below .43. This is the most precise critical value of Br between stable and unstable flows that I have found. His report has a striking photograph of smoke flow showing the random coalescence of individual jets.

The reasons for these instability effects of high Br is that minute variations in the hole sizes, spacing or roundness lead to sufficient variations in velocity and pressure from one jet to the next to cause neighboring jets either to diverge or coalesce. The flow thus becomes unstable with individual jets combining to form local zones of high and low velocities at random locations.

Because these instabilities are random, they should be considered as a superposition of large scale turbulence over and above that turbulence produced directly by the plate. The only feasible way known to analyze such data is to take a long enough sample to insure that a sufficient degree of statistical stationarity of turbulence characteristics can be established. Then the spectra, correlations, turbulence intensities, etc. can satisfy the assumptions upon which their calculations depend. With  $U \approx 18$  fps, observations for this study showed that the mean and mean square values of the hot wire AC voltage satisfied both a Run and a Trend test for stationarity at the  $\alpha = .05$  level of significance. Approximately 10 minutes of recorded data were used.

The decay region is the region downstream from the grid where isotropic turbulence is first approximated and beyond which a steady decay of turbulence takes place. Most of the literature of the past two or

three decades treats this region; it is the one in which the inertial subrange, for example, eventually occurs.

Because of the high values of  $Br$ , and the restriction to observations at 48" downstream from my turbulence producing plates, it is believed that no observations in this study took place in the decay region. The large variations in the hot wire DC voltage observed in most of the flows support this. Flow behind plate .50 may be an exception. The  $Ti$  was much lower behind this plate and flow instabilities were not obvious.

#### A.4.3 MODIFICATION OF CYLINDER BOUNDARY LAYER

Bearman (1972) experimentally studied the passage of grid generated turbulence, in a wind tunnel, approaching the stagnation point of a two-dimensional body, such as a cylinder. (His grids had blockage ratios near 35%.) When  $L_x$  is much smaller than  $D$ , the turbulence is distorted by the mean flow field and  $v$  and  $w$  will amplify owing to vortex stretching. Measurements of the pressure fluctuations at the stagnation point show that for smaller eddies the effect of the cylinder is to reduce the level of pressure fluctuations. On the other hand, when  $L_x$  is much larger than  $D$ , or when the eddies are larger,  $u$  will attenuate like the mean flow and the pressure fluctuations can be predicted by a direct application of Bernoulli's equation.

Bearman referenced recent work by Sadeh, et al., (1970) who have investigated the strong sensitivity of stagnation point heat transfer on cylinders to relatively small  $Ti$  values in the free stream. Large amplification of  $Ti$  can result from vorticity stretching. However, this amplification requires that the wave length or scale of the added

vorticity be greater than a certain neutral wave length. The right scales of vorticity can enter the boundary layer and bring about the generation of strong three-dimensional effects inside the cylinder boundary layer.

From these two results, it appears there is a sort of band pass procedure so that only certain sizes of eddies ( $L_x$ ) will be amplified as they approach the stagnation line of a cylinder.

Hunt (1971), with interest aimed at architectural applications, outlined the various physical effects involved in the flow of the wind around a building. He considered first, uniform flow around a bluff body, and then the added effects of turbulence in the incident flow. There are two basic effects of turbulence on the steady flow: first, to force the wake to start nearer to the rear of the body; and second, to thicken the shear layers which bound the wake region. (Note that this almost identical to some of Gerrard's conclusions which appear to have been developed separately.)

Hunt applied a theory (originally used by Batchelor and Proudman for calculating the effects of wind tunnel contractions on the turbulence) to flow around a long, circular cylinder. He found that the RMS values of turbulent components,  $u$ ,  $v$ ,  $w$  remain more or less constant near the front of a body if the integral scale,  $L_x$ , is about equal to the width of the body. However, if  $L_x$  is much larger than the width, then  $u$  decreases,  $w$  increases and  $v$  remains about the same. He mentioned experiments by Petty on a cylinder which confirm his theoretical results. Hunt's theoretical curves and Petty's experimental data are given in figure 49.

This figure shows that for  $D/L_x = 0.26$ , the RMS value of  $u$  decreased as the flow approached the cylinder; for  $D/L_x = 1.06$ , there was almost no change; and for  $D/L_x = 3.62$ , it increased until the flow was almost up to the cylinder.

## A.5 CLOSELY RELATED EXPERIMENTS

### A.5.1 SURRY

Surry (1969, 1972) experimentally studied the interaction of high intensity turbulence with the aerodynamics of flow past a rigid circular cylinder at  $Re$  near  $4 \times 10^4$ . His interest was to find more realistic design criteria for aircraft and buildings to withstand turbulence due to wind near the ground.

Surry used a cylinder 1.24" in diameter in an octagonal, closed return, wind tunnel with a test section, 48" x 32" in cross section and 4' long. The cylinder blockage was 4% or less. He used square biplanar grids to create turbulence intensities of 8 to 15%; typical air speeds were 54 to 70 fps.  $Br$  values were .27 to .55.

Surry measured the drag and lift of the horizontal cylinder, as well as the simultaneous pressures at any two points, on the cylinder surface. He also measured  $St$  of vortex shedding and several turbulence parameters of the flow:  $T_i$ ,  $L_x$ , and  $T_a$ .

Surry used four simultaneous and independently linearized hot wire channels for single wire probes and an X wire probe. This allowed a variety of measurements including two point longitudinal and lateral velocity component correlations.

An analog frequency analyzer was used. It provided a choice of six different band width filters, whose center frequencies were

continuously tunable from 20 to 20,000 Hz. By using changes in recorder speed, it was possible to compress the data so that the lowest frequency analyzable was 2.5 Hz.

His turbulent fields were produced by placing grids across the entrance to the test section. Immediately behind (downstream from) the grid, the flow is highly inhomogeneous with a strong memory of the particular grid geometry. The flow becomes more homogeneous and the turbulence intensity decreases downstream. Typically, the flow approaches homogeneity about 5 to 10 mesh lengths downstream, and approaches isotropy after about 20 mesh lengths. Whereas  $T_i$  decreases rapidly downstream,  $L_x$  increases slowly due to the dissipation of the high frequency turbulence components.

Surry used results of Batchelor and Townsend (1948), and Baines and Peterson (1951) to relate grid geometry to downstream turbulence intensity. His goal was two-fold: (a) to obtain homogeneous turbulence with the largest practical integral scales of turbulence; and (b) to obtain turbulence intensities between 10 to 20%. (This would give conditions comparable to lower atmospheric turbulence on aircraft and buildings.)

Surry settled on these steps in designing his grids: (a) the grid mesh was taken as 2.5 times the required longitudinal integral turbulence scale, with an upper scale limit of 13% of tunnel width; (b) homogeneity was established in the turbulence field at 9 or 10 mesh lengths downstream; (c) he noted that flow behind grids of blockage ratio greater than .50 becomes unstable.

Surry found the flow to be very sensitive to grid construction tolerances, especially for large blockage ratios. This problem was

solved to a great extent by minor empirical changes in the geometry of individual grids. He verified homogeneity of flow by measurement of some turbulence properties at various spanwise locations.

The final outcome of Surry's turbulence field development was four grids producing  $L_x$  between .45" and 5.5" (up to 9% of local tunnel width) and  $T_i$  of 10 to 20% at the intended cylinder position (cylinder removed).

Surry's grid #4 was modeled for use in my experimentation. The geometry and  $Br$  were made the same. This provided a link for comparison of his and my results. This was useful as a rough check on the accuracy of some of my measurements. These comparisons were considered part of the calibration and checkout procedures. Good comparisons were obtained.

Surry found anisotropy present in all cases but most severe for the highest  $T_i$ .

To obtain power spectra, Surry used best fit to two spectral estimates resulting from high and low frequency "cuts" for each case. (The data was analyzed separately for two frequency bandwidths - every 2 Hz for 0 to 250 Hz, and every 20 Hz for 0 to 2 kHz).

The wake of the cylinder was defined to be behind  $\alpha = \pm 140^\circ$ .

$T_a$  was calculated for all of Surry's flows. Although none of the flows reached the critical  $Re$  (defined after Bearman where  $C_d = .8$ ),  $T_a$  did correctly order the results in terms of decreasing  $C_d$ , decreasing base pressure, and  $St$ . It is believed that the flow behavior is consistent with  $Re(E)$  values up to  $2 \times 10^5$  (Surry's basic flows were all near  $Re(v) = 4 \times 10^4$ ). Thus, Surry's free stream turbulence increased  $Re(E)$  by a factor of 5.

The peak of the RMS pressure is associated with the neighborhood of the mean separation point.

He found the effect of turbulence on vortex shedding was to broaden and lower the pressure peak. Large scale turbulence tends to spread the vortex shedding, hence reducing the peak energy. However, none of the results indicate that the turbulence significantly interferes with the vortex shedding phenomena.

It is evident that  $L_x$  is more effective in modifying vortex shedding than is  $T_i$ . This suggests that high frequency turbulence is not "seen" by the Strouhal phenomenon.

In all cases of two point fluctuating surface pressure measurements, even when subjected to turbulence intensities of 15%, the vortex shedding still dominated the fluctuating surface pressures.

Even in this maximum turbulence, it appears evident that vortex shedding is still the primary cause of the fluctuating lift.

Surry had temperature changes of 50°F during tests while using a DISA 55A01 CTA. He had to obtain a high degree of temperature compensation. The hot wire probe calibration was compensated for the temperature changes by putting a nickel resistor in parallel with the resistor on one arm of the CTA bridge. The nickel resistor was placed in the wind tunnel to change resistance with temperature.

Surry found the uncompensated calibration drift of the order of .5% per 1°F.

He used analog computers to linearize output by King's equation. He found the exponent to be .45.

## A.5.2 MUJUMDAR

In a Ph.D. dissertation at McGill University, Mujumdar (1971) investigated the "Effect of Free-Stream Turbulence on Heat Transfer from Cylinders in Cross-Flow." Turbulent streams of varying characteristics were generated in a wind tunnel using screens of ten different configurations. Hot wire measurements of  $T_i$ ,  $G_{xx}(f)$ , and  $R_{xx}(\tau)$  were made both in the near wake and in the vicinity of the forward stagnation region.

Cylinders of .49" to 1.25" diameters were used with air speeds near 14 to 20 fps giving  $Re$  of  $6 \times 10^3$  to  $1.2 \times 10^4$ . The  $T_i$  values ranged from .5% to 15%.  $L_x$  varied from .7 to 4 cm. The tunnel test section was 11" x 11". His cylinder blockages varied from .04 to .11.

The vortex shedding frequency was determined by autocorrelating the turbulence signal from a hot wire located at  $x = 2D$ ,  $z = D$ . The Strouhal number was found to be constant at  $.205 \pm .005$  for all turbulence intensities and all Reynolds numbers. This result is so different from my results that I wrote to Dr. Mujumdar.

As stated in Mujumdar's reply (1971), a possible explanation of our differences is that my drop in Strouhal number could be real and due to the scale parameter  $L_x/D$ . This is resolved in my "Discussion."

Following is a summary of other items in Mujumdar's dissertation that are significant to mine.

The energy spectra showed greatest divergence in the low frequency region which is controlled by the mechanism of turbulence generation, and hence by the geometry of the plate. The frequency band 1 to 10 Hz showed the greatest spread of the relative energy content, 10 to 23%;

the band 10 to 100 Hz contained an almost constant fraction (60%) of the total energy, while an appreciable variation in the turbulence energy was noted in the band 100 to 1000 Hz. Two kHz was the highest frequency measured. I also found most of the energy below 100 Hz.

Detailed turbulence measurements in the vicinity of the cylinder supported, at least qualitatively, the theory of "vorticity amplification by stretching." This was concluded by the implication that in a stagnation flow, vorticity of a scale larger than a certain scale is amplified while the smaller scale vorticity is viscously attenuated.

Turbulence intensity is an important but insufficient criterion for correlating the effect of turbulence on heat transfer changes.

Sadeh, et al., in 1968 showed that velocity boundary layer is less sensitive to induced effects, from free stream turbulence, than is the thermal boundary layer.

Smith and Kuethé in 1966, in proposing a theory for the analysis of stagnation flow on a cylinder, assumed  $K_m$  to be proportional to  $T_i$  of the free stream. Mujumdar concluded that this leads to the best available correlation between free stream turbulence and heat transfer changes.

The wake interacts with turbulence in the free flow to increase the wake turbulence.

Mujumdar used a DISA 55A01 constant temperature hot wire anemometer whose response was linearized with a DISA type 55D10 linearizer. The hot wire probe was platinum plated tungsten wire, 5 microns in diameter and 1 mm long (DISA 55A25). All data were taken with a 5 kHz low pass filter. The wire was calibrated using a DISA 55A60 calibration unit (a sort of miniature wind tunnel). The wire was operated at

an overheat resistance ratio of 1.8. No corrections were deemed necessary for small variations in ambient temperature. The RMS AC voltage corresponding to the velocity fluctuations were read on the true RMS meter built in the CTA. Real time analog computation of the auto-correlation function was done using a Princeton Applied Research Model 100 Correlator. He found a large DC bias in the turbulence output signal from the DISA CTA.

The turbulent, AC voltage signal from the DISA anemometer, was recorded for later spectral analyses. The DC level of this signal was removed with a capacitor. (I found this to be 10 to 13 volts DC and removed it by inserting a DC source.)

Achenbach in 1968 is quoted as indicating that for small values of the ratio (cylinder length)/(cylinder diameter) less than 3, the flow at the tunnel mid section is influenced by the tunnel walls.

He defined the integral scale of turbulence,  $L_x$ , as:

$$L_x = U \int_0^{\tau_0} R_{xx}(\tau) d\tau$$

where  $\tau_0$  is the time at which  $R_{xx}(\tau)$  first reaches the value of zero. The integral scale can also be computed from the zero intercept of the spectrum,  $F(0)$ . Since it is difficult to obtain accurate spectra at low frequencies, Mujumdar obtained  $L_x$  by integration of the normalized autocorrelograms (the above equation). I simply used  $\tau_0$  as the Eulerian Integral Time Scale.

Mujumdar obtained his turbulence data by measuring the air flow with the cylinder removed. I did the same.

Mean velocity measurements were made using a calibrated hot wire and checked by a vortex shedding anemometer. He obtained a  $\pm 2\%$  accuracy of the vortex shedding anemometer.

Although  $T_i$  generally meant only the intensity in the  $x$  direction ( $\bar{u}/U$ ), some estimates were made of the intensity in the other directions. Thus a  $45^\circ$  slant hot wire was used only to obtain estimates of  $\bar{v}$  and  $\bar{w}$ . For most plates,  $\bar{v}$  and  $\bar{w}$  were generally 10 to 20% smaller than  $\bar{u}$ . Thus, the turbulence was not isotropic. I found  $\bar{u}$  about two times larger than  $\bar{w}$  in the highest turbulence.

The turbulence intensity,  $\bar{u}/U$ , was measured at several stations downstream of the plates for mean velocities of 14.5 to 19.8 fps. The  $T_i$  was found to be independent of  $U$ .

$L_x$  varied with the size of the individual open space in the turbulence producing plate. In certain cases the  $R_{xx}(\tau)$  curve levelled off at a finite positive value parallel to the zero axis. This was attributed to a shift in the DC bias of the recorder. In these cases, the integration was performed by displacing the  $R_{xx}$  axis so that  $R_{xx}(\tau) = 0$  at the value of  $\tau$  where  $R_{xx}(\tau)/U$  became constant.

The magnitude of  $L_x$  increased with distance downstream.

Spectra analyses were made in the low frequency region using a 1 Hz bandwidth filter with the averaging time constant ( $T$ ) set at 100 seconds.

At 25 cm downstream from the plates, Mujumdar found some difficulties in measuring  $L_x$ , both by the integration of the autocorrelation function and by finding  $F(0)$  by von Karman's method of fitting a parabola to the low frequency range of the spectra.

He found the spectra remarkably similar in the intermediate region of decay from 30 to 60 cm downstream from the plates.  $Re(\lambda)$  values were generally greater than 30, with the highest values above 100.

He found that  $U(\text{wake})/U \approx .80$ .

### A.5.3 KO AND GRAF

Ko and Graf (1972) experimentally investigated the effects of turbulence on the  $C_d$  of circular cylinders. They point out that the text book plots of  $C_d$  vs  $Re$  are an accumulation of data which were obtained under almost turbulence free conditions.

They used a circular wind tunnel, interior diameter 5" with cylinders of 1/4" and 1/2" diameter. Their cylinder area blockages were .065 and .13. An X probe hot film anemometer was used for air speed measurements. They operated in the range  $1.4 \times 10^3 < Re < 8 \times 10^3$ . In text book charts (such as figure 1.4 of Schlichting, 1960),  $C_d$  varied from .96 to 1.20 in that range, with a direct relationship between  $C_d$  and  $Re$ .

They conducted a dimensional analysis to specify the relation of turbulence on the drag coefficient. This lead to the result:

$$C_d = f [Ti, (Lx/D)^m, Re]$$

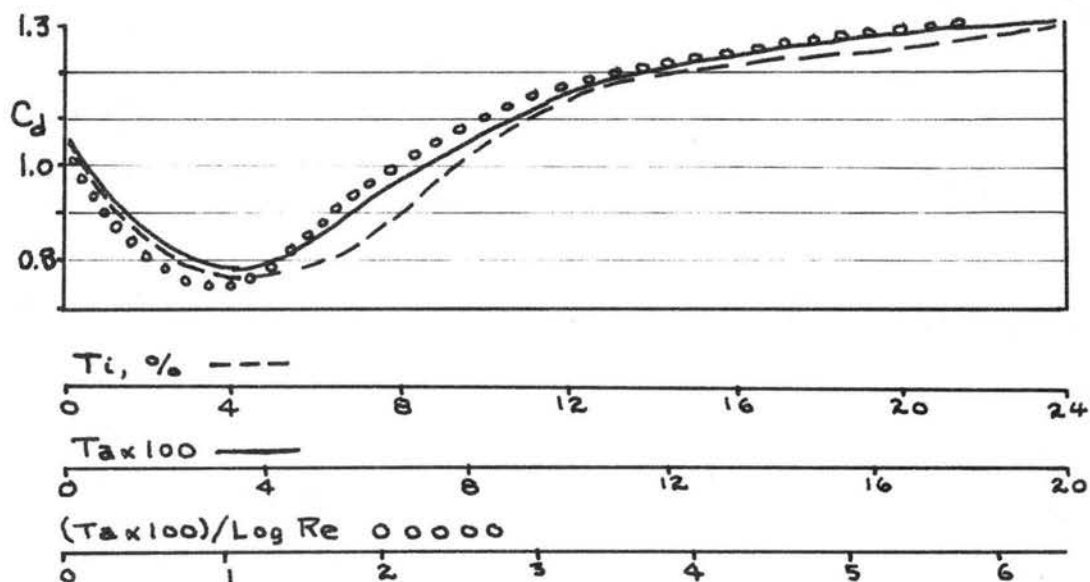
Several measurements of drag force were made on the cylinder, using strain gages, for different  $Re$  and for two different turbulence producing grids. Their data was presented in three forms, each of which showed a similar functional relation:

$$(1) \quad C_d \text{ vs } Ti'; \quad Ti' = (\bar{u}/U_\infty) \times 100$$

$$(2) \quad C_d \text{ vs } Ta'; \quad Ta' = (\bar{u}/U_\infty)(D/Lx)^{1/5} \times 100$$

$$(3) \quad C_d \text{ vs } \frac{Ta'}{\text{Log } Re}$$

In each case the mean  $C_d$  was at 1.05 for zero values of the abscissa [ $Ti'$ ,  $Ta'$  or  $Ta'/(Log Re)$ ]. As the abscissa increased, the value of  $C_d$  declined rapidly to a minimum and then increased in a roughly parabolic manner and exceeded the value of 1.05 at about two times the value of the abscissa at the minimum values.  $C_d$  appeared to still be increasing, with a value of 1.3, at the maximum values of the abscissa. This is presented in the following diagram:



These results show an important point, namely that  $C_d$  responds to turbulence effects in the free stream and, more importantly, the responses are functionally similar for  $Ti$ ,  $Ta$ , and  $Ta/\log Re$ .

It is hypothesized that a plot of  $1/St$  vs  $Ti$ ,  $Ta$ , or  $Ta/\log Re$  should show a similar relation to that in the above diagram, although the numerical values would change with the geometry of the turbulence producing plates and the wind tunnel.

#### A.5.4 SIMON

In a report which did not become available to the author until this dissertation was being typed in final form, Simon (1968) discusses the "Effect of surface roughness, turbulence and Mach number on flow regime boundaries for tunnel-spanning cylinders." This is the result of work carried out by the Martin Marietta Corporation of Denver, Colorado to investigate wind induced oscillations of the Saturn Booster Missile in the vertical launch position, under a NASA contract. He also references Simon, Howard and Peterson (1967).

Simon developed an empirical modified potential flow equation representing a relationship between the steady pressure distribution and the Strouhal frequency for two-dimensional flow around a circular cylinder. Pressures were measured at the cylinder surface. The separation point was then defined by the intersection of the modified potential flow pressure distribution with the base pressure. The square root of the second derivative of the modified potential flow pressure distribution, evaluated at the separation point, was used as the primary factor in the equation for the Strouhal frequency.

The ratio of the dynamic pressures at the separation point and the maximum dynamic pressure could be used as an indicator of the presence or absence of a Strouhal frequency (this is interpreted to mean whether a vortex shedding regime existed or a discontinuity condition existed).

Simon found that flow can be made "subcritical," "supercritical," or "transcritical" (those terms are apparently defined in the

the same way that Roshko uses them, not as used in this dissertation), even at relatively low Reynolds numbers (apparently  $1 \times 10^5$ ), by the use of free stream turbulence and surface roughness. The effects of (cylinder) blockage, although less dramatic, can be observed.

He found that Mach number effects were generally relatively small (he used Mach numbers .28 or less) except in the neighborhood of a flow regime boundary.

## APPENDIX B. TURBULENCE PARAMETERS

A recording of the turbulent voltage output,  $e$ , from a HWA, RMS values of the same voltage,  $\bar{e}$ , and mean values of the DC voltage output of a HWA are all needed to calculate the following turbulence parameters:

- (1) Turbulence intensity,  $T_i$
- (2) Spectra and correlation analyses
- (3) Integral scale of turbulence,  $L_x$
- (4) Microscale of turbulence,  $\lambda$
- (5) Eddy viscosity,  $K_m$
- (6) Taylor parameter,  $T_a$
- (7) Special Reynolds numbers
- (8)  $\bar{u}$ ,  $\bar{v}$ ,  $\bar{w}$  fluctuations

### B.1 TURBULENCE INTENSITY, $T_i$

The turbulence intensity,  $T_i$ , of an air flow is the nondimensional ratio of the RMS value of the turbulent air speed fluctuations,  $\bar{u}$ , divided by the mean air speed,  $U$ . Two general methods of calculation are possible: one using HWA data, which is most commonly used, and a second method using the turbulent diffusion of heat.

#### B.1.1 HOT WIRE ANEMOMETER METHODS

Sandborn's text (1972) develops the HWA method which can be divided into three sub-methods:

- (1) Graphical method. A calibration curve of  $E$  vs  $U$  for the HWA can be used graphically to convert  $\bar{e}$  to  $\bar{u}$ .  $\bar{e}$  is the RMS value of the

fluctuating voltage, and  $E$  is the DC voltage (see figure 7.7 in Sandborn's text). Figure 50 is a sample of such a calibration curve used in this experiment.

(2) Application of King's equation

$$T_i = \frac{\bar{u}}{U} = \bar{e} \left[ \frac{2E}{R(R-RA)BCU^c} \right] \quad (B-1)$$

where  $R$  is the resistance of the wire when heated,  $RA$  is the resistance at room temperature, and  $B$  and  $C$  are constants used in King's equation,

$$E^2/R(R-RA) = A + BU^c \quad (B-2)$$

See equation 7.14 of Sandborn's text. In this experimentation,  $A$ ,  $B$  and  $C$  are determined by a least squares solution of the hot wire calibration. Peterka's (1971) digital computer program is used for this calculation. In some limited cases,  $E^2$  vs  $\sqrt{U}$  plots as a straight line and the above equation is simplified by using  $c = .5$ .

Then

$$T_i = \bar{e} \left[ \frac{4E}{R(R-RA)B\sqrt{U}} \right] \quad (B-3)$$

(3) Intercept method. An easier and less theoretically valid method is to use the Intercept method. It is simplified by two additional assumptions: (1)  $E$  for no flow is sufficient to define the calibration curve intercept for  $U = 0$ ; (2) the intercept rather than a slope of the calibration curve can be used. The resulting relation is:

$$T_i = \bar{e} \left[ \frac{4E}{E^2 - E_0^2} \right] \quad (B-4)$$

A derivation is given in Laurence and Landis (1952) and in the DISA instruction manual for their Model 55A01 system.

### B.1.2 HEAT DIFFUSION METHOD

The heat diffusion method was developed by Schubauer (1935) and was used in my experiment to provide a comparison for the hot wire method using King's equation. This comparison is given in section C.9.

### B.2 SPECTRA AND CORRELATION ANALYSES

The major references for this section are Hewlett-Packard documents. See list in Bibliography.

A Hewlett-Packard Fourier Analyzer System (FAS) analysed the analog tape recording of turbulent data. The FAS employs the "Fast Fourier Transform" concept. It is assumed that all air flow is incompressible, and that the turbulence conditions are random, stationary and ergodic.

#### B.2.1 FAST FOURIER TRANSFORM

To proceed with Fourier analyses by digital methods, the recorded analog data,  $x(t)$ , is then digitized at increments of  $\Delta t$ ,  $\Delta f$ , for a maximum frequency  $F_m$ , and a total of  $N$  data points. The data points are used to develop a "linear spectrum,"  $S_x(m\Delta f)$ , by a "Discrete Finite Transform," (DFT); the DFT is defined as follows:

$$S_x(f) \equiv S_x(m\Delta f) \equiv \frac{1}{N} \sum_{k=0}^{k=(N-1)} x(k\Delta t) \exp\left(-\frac{2\pi i}{N} m k\right) \quad (B-5)$$

where  $m$  is the (integer) counter of  $\Delta f$  over the interval of summation such that  $m\Delta f = f$ , and  $k$  is the counter for summation over  $\Delta t$  intervals such that  $k\Delta t = t$ . These combine to give  $\frac{mk}{N} = tf$ , using the relation  $\Delta f = 1/(N\Delta t)$ , defined later.

The DFT, equation (B-5), is a digital approximation of the Fourier integral transformation:

$$K_x(f) \equiv \int_{-\infty}^{+\infty} x(t) \exp(-2\pi i f t) dt = \int_{-\infty}^{+\infty} x(t) [\cos 2\pi f t - i \sin 2\pi f t] dt \quad (B-6)$$

The use of the DFT is subject to several conditions and relations: (a) the time function,  $x(t)$ , to be transformed must be sampled at discrete time intervals,  $\Delta t$ ; (b) only a finite number,  $N$ , of such samples can be taken and stored; (c) the length of the data record is  $T$  and  $T = N\Delta t$ ; (d) the effect of a finite  $\Delta t$  limits the maximum frequency,  $F_m$ , that can be sampled without aliasing errors (this is given by the Nyquist criterion:  $F_m = 1/2\Delta t$ ); and (e) the effect of a finite time interval  $T$ . The DFT assumes that the voltage input is periodic in the interval  $T$  and has a spectral resolution of  $\Delta f = 1/T$ .

### B.2.3 APPLICATIONS OF THE FAST FOURIER TRANSFORM

The autocorrelation,  $R_{xx}(\tau)$ , is obtained by multiplying  $x(t)$  by itself but with a time lag of  $\tau$  in the second  $x(t)$  factor. These products are made for each  $\Delta t$  sampling interval and summed over the total time interval  $T$ .

$$R_{xx}(\tau) \equiv \lim_{T \rightarrow \infty} \frac{1}{T} \int_0^T x(t) x(t-\tau) dt$$

The power spectra,  $G_{xx}(f)$ , is formed by multiplying the value of the linear spectrum,  $S_x(f)$ , by its own complex conjugate,  $S_x^*(f)$ . The power spectrum is the magnitude squared of the linear spectrum; it has no imaginary part.

$$G_{xx}(f) \equiv \lim_{\Delta f \rightarrow 0} \lim_{T \rightarrow \infty} \frac{1}{(\Delta f)T} \int_0^T x^2(t, f, \Delta f) dt$$

When two sets of data are used, the cross spectra,  $G_{yx}(f)$ , is formed by multiplying the linear spectrum of  $y(t)$ ,  $S_y(f)$ , by a complex

conjugate of the linear spectrum of  $x(t)$ ,  $S_x^*(f)$ , measured at the same time. The cross spectra will then have both a real (cospectra) and an imaginary (quadrature spectral) part. Only the real part is used here. The cross correlation  $R_{yx}(\tau)$  is obtained by multiplying  $y(t)$  by  $x(t)$  but with a time lag of  $\tau$  in the  $x(t)$  factor.

The Fourier Transform  $H$  and the Inverse Fourier Transform  $H^{-1}$  have the same coefficient.  $G_{xx}(f)$  and  $R_{xx}(\tau)$  can be converted by either transform into the other. The major features appear to be maintained accurately.

Following are the numerical equations used by FAS.

$$R_{xx}(\tau) \approx \frac{1}{N} \sum_{k=1}^{k=N} x(k\Delta t) x(k\Delta t - \tau) \quad \text{See program A, Table 5.}$$

$$G_{xx}(f) \approx S_x(f) S_x^*(f) \quad \text{See program B, Table 5.}$$

$$R_{yx}(\tau) \approx \frac{1}{N} \sum_{k=1}^{k=N} y(k\Delta t) x(k\Delta t - \tau) \quad \text{See program C, Table 5.}$$

$$G_{yx}(f) \approx S_y(f) S_x^*(f); \text{ but only the magnitude is used.}$$

See program D, Table 5.

$$H \approx \frac{1}{N} \sum_{n=0}^{n=(N-1)} h(n\Delta t) \exp\left(-\frac{2\pi i}{N} mn\right) = H(m\Delta f)$$

$$H^{-1} \approx \frac{1}{N} \sum_{m=0}^{m=(N-1)} H(m\Delta f) \exp\left(+\frac{2\pi i}{N} mn\right) = h(n\Delta t)$$

Programs for  $H$  and  $H^{-1}$  are built into the FAS.

Steps were taken to avoid aliasing of spectra and "wrap-around" errors in autocorrelations.

Appendix C gives details of how the accuracy and reliability of the Fourier Analyzer System were verified.

#### B.2.4 NORMALIZED POWER SPECTRA $F_{xx}(f)$ , or $F(f)$

This is defined as  $\frac{G_{xx}(f)}{\sum_{K=1}^{K=N/2} G_{xx}(K\Delta f)}$  and has the property that

$$\int_0^{\delta} F_{xx}(f) df = 1 \approx \sum_{K=1}^{K=N/2} F_{xx}(K\Delta f)$$

This normalization assists in the comparison of different spectra and is used for one method of calculating  $\lambda$  and one method of calculating  $L_x$ .

The value of  $\sum_{K=1}^{K=N/2} G_{xx}(K\Delta f)$  is important because it is

proportional to the total turbulent energy and is also equal to  $\bar{e}$  and to  $R_{xx}(0)$  from the FAS calculations.

#### B.3 INTEGRAL SCALE OF TURBULENCE, $L_x$

The integral scale of turbulence can be interpreted as the average diameter of the eddies in a turbulent flow. If only one HWA is used, there are two methods to calculate  $L_x$ : (1)  $L_x = \tau_0 U$ ; and (2)  $L_x = UF(0)/4$ . These two lengths are not specifically related, although results here show one is roughly one-half of the other.

B.3.1  $L_x = U\tau_0$ 

" $J_\epsilon$ " is a time interval called the "Eulerian integral scale." This requires "Taylor's hypothesis" to convert a distance concept into a time measurement [see sections 1-6 to 1-8 in Hinze (1959)].

At first consideration,  $J_\epsilon$  should be defined

$$J_\epsilon = \frac{\sum_{k=0}^{k=N} R_{xx}(k\Delta t)}{R_{xx}(0)}$$

However, experience shows that this leads to unreasonable results. Probably this is because some of the assumptions in Taylor's hypothesis and the Eulerian integral scale are not adequately met in highly turbulent flow. Instead, an empirical definition of  $L_x$  is used, employing  $\tau_0$ , which is the time the autocorrelation curve first reaches the zero value. Then

$$L_x = U\tau_0 \equiv L_x(\tau) \quad (\text{B-9})$$

Figures 43 and 44 give examples of  $\tau_0$  observations.

B.3.2  $L_x = UF(0)/4$ 

$F(0)$  is the extrapolated power spectra value to zero frequency for a normalized spectra. This is credited to von Karman. The following discussion is from Sandborn and Slogar (1955).

Start with  $R_x$  which is the correlation coefficient of speed fluctuations between simultaneous values of  $u$  at two points,  $x'$  distance apart, along the direction of an  $x$  coordinate. Then by Taylor's method, the average size of the eddies is given by the integral scale of turbulence:

$$L_x = \int_0^{\infty} R_x dx$$

A "spectral density function," or "normalized spectra,"  $F_{xx}(f)$ , is defined such that  $\int_0^{\infty} F_{xx}(f) df = 1$ , and then the power spectra is given by  $\int_0^{\infty} u^2 F_{xx}(f) df$ . Using the FAS, one can say  $F_{xx}(f) = G_{xx}(f)/\Sigma G_{xx}(k\Delta f)$  as stated above. It has units of time.

$R_x$  can be evaluated from  $F_{xx}(f)$  because  $R_x$  and  $[U/(2\sqrt{2\pi})]F_{xx}(f)$  are Fourier transforms of each other. Therefore,

$$F_{xx}(f) = \frac{4}{U} \int_0^{\infty} R_x \cos \frac{2\pi fx}{U} dx$$

and 
$$F_{xx}(0) = \frac{4}{U} \int_0^{\infty} R_x dx$$

Hence, 
$$L_x = \frac{U}{4} F_{xx}(0) \equiv L_x(F) \quad (B-10)$$

To determine the value of  $F_{xx}(0)$ , a method of extrapolation must be used. Sandborn and Slogar used band pass filters to obtain spectral data between frequencies of approximately 20 and 100 hz. However, the FAS can calculate  $F_{xx}(f)$  for smaller frequency intervals.

From equation (B-10), it can be seen that the slope of the curve  $F_{xx}(f)$  vs  $f$  has a slope of zero at  $f = 0$ . The simplest logical approximation to such a curve would be parabola of the form,  $F_{xx}(f) = A + Bf^2$ . The value of  $F_{xx}(0)$  can be found by determining the coefficients  $A$  and  $B$ , through a least squares approximation, using several observed values of  $F_{xx}(f)$  for  $f$  from near zero to about 50 Hz.

The least squares is derived by apply section 3-6 of Stanton (1964) as follows, using three data points, and letting  $x = f$ , and  $y = F_{xx}$ .

$$\text{Sum of squared deviations} = S = \sum_{i=1}^{i=3} [y - A + Bx_i^2]^2$$

$$\frac{\partial S}{\partial A} = 0 = -2 \sum_{i=1}^{i=3} [y_i - A + Bx_i^2]; \quad \text{or, } A = \frac{\sum y_i + B \sum x_i^2}{\sum}$$

$$\frac{\partial S}{\partial B} = 0 = 2 \sum_{i=1}^{i=3} [y_i - A + Bx_i^2] x_i^2; \quad \text{or, } B = \frac{A \sum x_i^2 - \sum x_i^2 y_i}{\sum x_i^4}$$

Because  $F_{xx}(0) = A$ , one needs only to solve for  $A$ . The above two equations can be combined to give

$$F_{xx}(0) = \frac{\sum y_i \sum x_i^4 - \sum x_i^2 \sum x_i^2 y_i}{3 \sum x_i^4 - \sum x_i^2 \sum x_i^2} \quad (\text{B-11})$$

Data points of  $x_i$  and  $y_i$  can be obtained by knowing  $\Delta f$  used in the power spectra analysis and by teletype printouts of normalized power spectra  $F_{xx}(f)$ . See figures 40 and 48.

Because the power spectra of the flows in this study have a distinct maximum power well below 100 Hz, the value of  $F_{xx}(f)$  at maximum is roughly proportional to  $F_{xx}(0)$  and will be called " $F_{xx}(M)$ ." So, two versions of the above equation will be used:

$$L_x = UF(0)/4; \quad L_x = UF(M)/4 \quad (\text{B-12})$$

Figure 51 is an example.

#### B.4 MICROSCALE OF TURBULENCE $\lambda_f$

The microscale of turbulent eddies,  $\lambda_f$ , is a measure of the dimension of eddies which, at the same intensity, produce the same dissipation as the turbulence considered. Consequently, they are smaller than the integral scale. Two practical methods are available:

(1) Taylor's (1938) method

$$\frac{1}{\lambda_f^2} = \frac{4\pi^2}{U^2} \int_0^{\infty} f^2 F(f) df \quad (B-13)$$

(2) Townsend's (1947) method

$$\lambda_f = \frac{U \bar{u} \sqrt{2}}{(du/dt)} \quad (B-14)$$

A comparison was made of the Taylor and Townsend methods in two different turbulence flows. Each was in the wind tunnel with a mean air speed near 18 fps. One was behind the Surry grid and one was behind plate .958. Both produced high turbulence intensities. Two values of  $\lambda_f$  were obtained for each of the two flows.

The turbulent voltage,  $e$ , from a hot wire using the DISA CTA, was recorded, after amplification to get an RMS voltage near 15 volts, to obtain optimum performance of the recorder. A recording of several minutes was made for each turbulence flow. A low pass filter of 5 kHz was used in the CTA and the recorder was operated at 15 ips so that it could accurately record from 0 to 5 kHz.

Taylor's method was used by approximating the integration on the FAS. The major steps are shown in figure 52 for one of the cases. The abscissa of all curves is frequency, 0 to 5 kHz. The bottom diagram in the figure is the normalized power spectra  $F_{xx}(f)$  with  $F_m = 5$  kHz,  $\Delta f = 4.88$  Hz,  $\Delta t = 10^{-4}$  sec,  $T = .2048$  sec and a mean of 100 spectra was used. Its area was summed and checked to see that it equaled 1. The next figure up,  $f^2$ , was put into the FAS manually and was checked (by teletype readout) to see that the largest value was  $\approx (5 \text{ kHz})^2$ . The next figure up,  $f^2 F_{xx}(f)$ , is a product of the first two, where the value at each corresponding  $\Delta f$  is multiplied. This gives a much

greater weighting to the power of the higher frequencies of the spectra. Note that the curve is flat and near zero at the higher frequencies -- this indicates that all fluctuations of importance to calculating the microscale have been included. The top figure is the sum of  $f^2 F_{xx}(f)$  so that the right hand value is a numerical approximation of the integral used in Taylor's equation. This value was printed out, by teletype, to four significant figures in units of  $(\text{sec})^{-2}$ .

Townsend's method was applied to the same taped data. It can also use data directly from the CTA. Townsend's equation was converted from  $u$  to  $e$  units because the constants of conversion, by hot wire anemometry are the same for these two equations:

$$\bar{e} = c \bar{u} ; \quad \text{and,} \quad \overline{(de/dt)} = c \overline{(du/dt)}$$

Then, Townsend's equation can be expressed by

$$\lambda_f = \frac{\sqrt{2} \nu \bar{u}}{\overline{(du/dt)}} = \frac{\sqrt{2} \nu \bar{e}}{\overline{(de/dt)}}$$

The value of  $\bar{e}$  was measured by an RMS voltmeter on the recorder reproduction of  $e$ . The value of  $\overline{(de/dt)}$  required that  $e$  be taken through a differentiating amplifier before the RMS AC voltage was read. A Flow Corporation 900-6 differentiating amplifier was used with a time interval setting of 1 millisecond. All RMS AC voltages were made by a TSI model 1060 true RMS AC voltmeter, using a time averaging constant of 30 sec. The RMS voltage was checked by a Ballantine true RMS AC voltmeter.

Following is a comparison of the four calculated values of the microscale  $\lambda_f$ :

1. For flow behind plate .958:

$$\text{Taylor: } \lambda_f = \frac{17.4 \text{ fps}}{2 \pi} \times \frac{1}{(1.923 \times 10^5 \text{ sec}^{-2})^{1/2}} = .076''$$

$$\text{Townsend: } \lambda_f = 17.4 \text{ fps} \times \frac{1.06 \text{ v.} \times \sqrt{2}}{2.61 \times 10^3 \text{ v. sec}^{-1}} = .112''$$

The difference is 47% with the Townsend method giving a larger value.

2. For flow behind the Surry grid (.34):

$$\text{Taylor: } \lambda_f = \frac{18.8 \text{ fps}}{2 \pi} \times \frac{1}{(1.551 \times 10^5 \text{ sec}^{-2})^{1/2}} = .091''$$

$$\text{Townsend: } \lambda_f = 18.8 \text{ fps} \times \frac{\sqrt{2} .852 \text{ v.}}{1.98 \times 10^3 \text{ v. sec}^{-1}} = .137''$$

The difference is 50% with the Townsend method giving a larger value.

These values are smaller than the integral scales of turbulence for similar flows, consistent with each other, and compare well with reports from the literature.

Taylor (in part IV, 1935) states:

"For turbulent air behind a square-mesh honeycomb of  $M = 0.9$  inch, it was found that for  $U = 20$  fps;  $\lambda$  defined by extending the parabola from  $R_{xx}(0)$  gave a microscale of 0.08 inch (.203 cm).

For the same honeycomb at  $U = 25$  fps it was shown that direct observation and calculation from the observed energy dissipation agree in giving  $\lambda = 0.143$  inch."

The Townsend method is much simpler to use because only two RMS voltage readings are required.

Specific observed values are given in the section on "Experimental Results."

### B.5 EDDY VISCOSITY, $K_m$

Major references are Sutton (1953) and Hinze (1959).

Viscosity is the property of the air that allows it to transport information on momentum (heat or mass) of the air particles from one point in the air to another. "Information" is used in a broad sense that includes a shear stress condition between points of different momentum or a fluctuating change of momentum from one point to another. Viscosity can also be defined as the coefficient of momentum diffusion in air flow. It is similar in theory to the coefficients of heat or mass diffusion.

The diffusion capabilities of turbulent flow are so much larger than those of laminar flow (molecular viscosity) that, in turbulent flow, molecular viscosity effects are usually negligible. At laboratory conditions, kinematic viscosity,  $\nu = .16 \text{ cm}^2 \text{ sec}^{-1}$  (or  $1.7 \times 10^{-4} \text{ ft}^2 \text{ sec}^{-1}$ ).

Taylor, in 1915, used the Ekman spiral and assumed a constant  $K_m$  in the entire planetary boundary layer (lowest 3000 feet) to calculate that  $K_m$  had to be of the order of  $10^4 \text{ cm}^2 \text{ sec}^{-1}$  or more.

In the laboratory,  $K_m$  is usually measured with an "X" or "yawed" hot wire sensor, which measures the turbulent shearing stress  $\overline{uv}$ .

Then: 
$$K_m = - \frac{\overline{uv}}{dv/dy}$$

This method limits itself to flows with a mean shear condition, otherwise we have a zero in the denominator. For such a case, a different method of calculating  $K_m$  must be used. Because dimensions of  $K_m$  are ( $L^2 T^{-1}$ ), it is dimensionally correct to obtain  $K_m$  by multiplying a velocity times length. If it is assumed that  $L_x$  is descriptive of the

turbulent exchange process and if it is assumed that  $\bar{u}$  is also descriptive of the same process, then

$$K_m \propto Lx \bar{u} \quad (B-15)$$

The definition will be followed that  $K_m \equiv (Lx \bar{u})$  for turbulent flow near the center of a wind tunnel. There is a precedent for this in equation 7.29 of Sutton (1953). It is also referred to as the Prandtl-Kolmogorov model.

#### B.6 TAYLOR PARAMETER, $Ta$

The Taylor parameter,  $Ta = Ti \left[ \frac{D}{Lx} \right]^{.2}$ , was developed to predict a critical value of the Reynolds number for flow past a sphere. It has been found useful to correlate other turbulence effects. It has been discussed in section A.4.1.

#### B.7 SPECIAL REYNOLDS NUMBERS

Special Reynolds numbers have been discussed in section A.4.2.

The three used, in addition to the basic  $Re = UD/\nu$ , are

(1) Eddy viscosity Reynolds number,  $Re(K_m) = UD/K_m$

(2) Turbulence Reynolds number,  $Re(\lambda) = \bar{u}\lambda/\nu$

(3) Plate Reynolds number,  $Re(p) = Ud/(1 - Br)\nu$ . This is a modification of the earlier "grid Reynolds number"  $UM/\nu$ .

#### B.8 $\bar{u}$ , $\bar{v}$ , $\bar{w}$ FLUCTUATIONS

These are a measure of the RMS value of the air speed fluctuations parallel to the x, y, z axes respectively. They are normally measured by an "X" or a "yawed" hot wire. In an experiment, one wire was yawed at  $\pm 45^\circ$  from a position normal to the mean flow. This was done in the

yz plane to compare  $\bar{u}$  and  $\bar{w}$  -- which, in turn, were found separately by the Schubauer heat diffusion method (see section C.9).

The formulas for calculating  $\bar{w}$  (and  $\bar{v}$ ) are developed in Sandborn's text, section 7.3.1(b). The value of  $\bar{u}$  can be found from the same equations as used for turbulence intensities, equation (B-1). This results in three equations in the three unknowns. The subscripts are used to denote the rotated positions,

$$\bar{u}^2 = \frac{4 E^2 U^2 \bar{e}^2}{R^2 (R-RA)^2 C^2 B^2 U^{2C}} \quad (B-23)$$

$$\begin{aligned} \bar{v}^2 &= U^2 K^2 \left[ \bar{e}_{xya}^2 + \bar{e}_{xyb}^2 \right] - \bar{u}^2; \text{ and} \\ \bar{w}^2 &= U^2 K^2 \left[ \bar{e}_{yza}^2 + \bar{e}_{yzb}^2 \right] - \bar{u}^2 \end{aligned} \quad (B-24)$$

where  $K^2$  has the same value when one wire under one calibration is used throughout.  $K^2$  is given by:

$$K^2 = \frac{4 E^2}{R^2 (R-RA)^2 C^2 B^2 U^{2C} (\sin 45^\circ)^{2(C-1)}} \quad (B-25)$$

$E$  is observed mean DC voltage of the hot wire;  $R$ ,  $R_a$ ,  $B$  and  $C$  are hot wire calibration constants. The subscripts "xy" and "yz" indicate the planes in which the wire is rotated and the subscripts "a" and "b" indicate a rotation of  $+45^\circ$  or  $-45^\circ$ , respectively.

## C. ACCURACY CONSIDERATIONS

### C.1 GENERAL

Because this is primarily an experimental study, emphasis must be given to data accuracy. As a first estimate of the accuracies that should be reasonable, a quotation from Corrsin (1963) is appropriate.

"As in other areas of science, the goals of experiment are, loosely, of two kinds: (a) exploratory; and (b) to confirm or disprove theories . . . . In exploratory measurements . . . 20% accuracy is sometimes satisfactory. The more permanent crucial data . . . are taken with perhaps 2 to 10% uncertainty." (See page 524.)

There are five primary parameters observed for use in the final data ( $f$ ,  $U$ ,  $\bar{u}$ ,  $Lx$ ,  $\lambda$ ) and some of them use air temperature  $T$ , virtual temperature  $T_v$ , air pressure  $P$ , and kinematic viscosity  $\nu$ . Because the accuracy of observing  $T$ ,  $T_v$ ,  $P$  and  $\nu$  are so much better ( $\pm 1\%$ ) than for the primary parameters, the errors of  $T$ ,  $T_v$ ,  $P$  and  $\nu$  can be ignored.

The five primary parameters are used to derive eight others presented in the discussion and conclusions; they are  $Re$ ,  $St$ ,  $Ti$ ,  $Km$ ,  $Ta$ ,  $Re(Km)$ ,  $Re(\lambda)$  and  $Re(p)$ .

The approach used here is to make the best possible estimates of the accuracy of the five primary parameters by good calibration procedures, feeding known data into a system, observing the same data by two instruments, calculating results by two methods, duplicating relevant data from the literature, and reducing disturbing outside influences.

Then, when the accuracy of the five basic parameters is found, a combination of their accuracies can be used to estimate the accuracy of the derived parameters.

## C.2 CHECKOUT OF INSTRUMENTATION RECORDER AND FOURIER ANALYZER SYSTEM

Figure 4 is a photograph of the H-P Model 3960 recorder and the H-P Model 5451A Fourier Analyzer System (FAS).

### C.2.1 POWER SPECTRA AND AUTOCORRELATION

An instrumentation tape recording was made of sine functions at 2, 8, 20, 80, 200, 800, 2000, and 8000 Hz. The recordings were prepared at the WSMR Calibration Laboratory with two different instruments that indicated an accuracy of the original sine function frequency to be within  $\pm 0.05\%$ . The recorded tape was then played into the FAS and analyzed by a power spectra program. Each gave a clean sharp peak within 2% or closer of the recorded frequency. This readout was by XY plotter which requires a manual setting at two calibration points on the chart. Most of the 2% error can be attributed to inaccuracies of the manual setting.

Although it was not done, autocorrelations should have provided a more accurate frequency of these sine waves because a large number of time intervals could have been counted and averaged.

This checkout also tested the performance of the recorder. At maximum record speed, 15 ips, in the FM mode, manufacturer's specifications call for only a 5 KHz maximum performance. It actually reproduced an 8 KHz signal but a greatly reduced magnitude. Therefore, the 5 KHz reproduction is considered valid.

AC voltage from the hot wire in a highly turbulent flow was recorded. The power spectra,  $G_{xx}(f)$  was calculated on the FAS and a summation of the area under the curve  $G_{xx}(f)$  vs  $f$  was made on the FAS. This should also be equal to the autocorrelation at zero time lag. By

theory (see Bendat and Piersol, 1966), this value, which is in volts<sup>2</sup>, should be identical to the mean square of the AC voltage,  $\overline{e^2}$ , from the recordings. The latter was measured by an RMS AC voltmeter. Comparison of results show:

$$\Sigma G_{xx}(f): \overline{e^2} = .0851 \text{ volts}^2$$

$$R_{xx}(0): \overline{e^2} = .0849 \text{ volts}^2$$

$$\text{RMS VM: } \overline{e^2} = .0915 \text{ volts}^2$$

The greatest difference is 7.5%.

A combination of recordings from a sine wave, a hot wire in an air jet, and from a noisy amplifier were used to reproduce Bendat and Piersol's figures 1.15 and 1.16. Their figure 1.15 shows four autocorrelation plots and their figure 1.16 shows four power spectral density plots, each for: (a) sine wave; (b) sine wave plus random noise; (c) narrow band random noise; and (d) wide band random noise.

The results from the FAS were very similar to the Bendat and Piersol figures.

The Fourier transform relation was used repeatedly to first calculate a power spectra and then convert it to an autocorrelation and vice versa. The Fourier transform and the inverse Fourier transform on the FAS appear to be identical in major items such as maximum  $f$ ,  $\Delta\tau$ , spectra shape and  $\overline{e^2}$ . This has been checked by oscillograph displays and teletype printouts of data points.

In using a single sine wave recording, for example, the frequency,  $f$ , given by the power spectra is identical to the reciprocal of time lag,  $\tau$ , between successive peaks of maximum or minimum correlations given by the autocorrelation. This was done in a variety of cases,

using direct calculations of each and using a Fourier transform. In each case, the value of  $f$  and the reciprocal of  $\tau$  were the same, within 1% or less.

### C.2.3 STATIONARITY OF DATA

This discussion follows Section 5.6.1 of Bendat and Piersol (1966) closely.

The use of many analyses, such as power spectra and autocorrelations, requires the assumption that the random data,  $x(t)$ , etc., being analyzed has the quality of "stationarity." For practical purposes, this means that the "statistical properties" of  $x(t)$ , computed by time averaging over each of a sequence of short intervals from a single sample record, will not vary "significantly" from one interval to the next. The two words in quotations can be defined rigorously in mathematical terminology but are almost impossible to satisfy in laboratory work. "Statistical properties" here are limited to mean voltages and the mean square voltages, or the first and second statistical moments. "Significantly" is used in the sense that the variations between sample records are no greater than would be expected due to statistical sampling variations.

The fluctuating voltage signal,  $e$ , from a hot wire anemometer in turbulent flow was tested for stationarity. Twenty samples of mean square voltages,  $\overline{e^2}$ , were obtained by using Program E, Table 5 on the Fourier Analyzer System (FAS). Each sample used 3.28 seconds of recorded  $e$  data. The values of the samples had a mean of  $5.4 \times 10^{-4}$  with variations of  $\pm 15\%$  from the mean. The twenty samples were then

subjected to a "Run Test" and a "Trend Test." Both tests showed that the data samples were independent at the  $\alpha = .05$  significance level.

Twenty samples of mean voltages,  $\bar{e}$ , were calculated by the FAS from the same turbulent voltage signal, using Program F, Table 5. Each sample utilized 5 seconds of data, with extremes of  $+4.6 \times 10^{-4}$  to  $-8.7 \times 10^{-4}$  volts and a mean of  $-.13 \times 10^{-5}$ . This is a large variation but appears reasonable for a turbulent signal. These twenty samples were subjected to the same Run test and Trend test. The results were the same as for the tests of mean square voltages; twenty samples of mean voltage were independent at the  $\alpha = .05$  level of significance.

In view of the above tests, it is concluded that the DISA e data can be considered stationary at the  $\alpha = .05$  level of significance for analyses of mean square, spectra and correlations, if at least ten minutes of recorded e voltages are used.

### C.3 VIBRATION OF CYLINDER AND TUNNEL FAN

The influence of vibrations on the pressure transducer and hot wire observations were investigated. An accelerometer was bolted to the cylinder and cross-spectra were made between the transducer and the accelerometer during highly turbulent air flow. Later, with the cylinder removed, an accelerometer was clamped to the motor and fan housing and cross-spectra made with the hot wire in highly turbulent flow. The spectra of the accelerometer showed major energy far above the vortex shedding frequency or the frequency of major power in the hot wire spectra. The two different types of cross-spectra showed no significant correlation.

#### C.4 CONSTANCY OF WIND TUNNEL AIR FLOW

The constancy of the mean air speed in the wind tunnel, with a steady power setting to the air fans, was tested. Separately, for a clear tunnel and for eight plates or grids, the tunnel air speed was set near 18 fps and left to operate for ten minutes. No changes were made to the power setting after the desired air speed was indicated by the DC voltage of a CTA. Then the DC voltage of both a DISA hot wire and a TSI hot film were recorded. The recordings were analyzed for mean DC voltages of both on the FAS. These results indicated that the tunnel mean air speed was steady within  $\pm 0.5\%$ .

#### C.5 HOT WIRE TIME RESPONSE CHARACTERISTICS

The DISA CTA model 55A01, using a 5 micron platinum plated tungsten wire, was tested for time response characteristics using built-in square wave test procedure. According to this method, the wire should adequately respond to a frequency up to 11 KHz in an air speed of about 18 fps and at an overheat ratio of 1.8. It is known that a square wave method does not fully measure the wire response time but more truly indicates the bridge balance reaction time.

An air pulse method by Shepard (NACA TN 3406, 1955) can provide a better measure of the hot wire time response characteristics. Such an apparatus has been built and a test completed. It indicated that the wire should respond up to 9.05 KHz.

Both approaches assume that the hot wire responds to a step input as a "first order" electrical circuit and that the voltage change can be represented by

$$\text{Transient voltage, } E_t = E_s - e^{-t/\tau} \quad (C-1)$$

where  $E_s$  is the steady state voltage at the increased air speed and  $\tau$  the "time constant" of the wire. ( $\tau = RC$  in electrical terms.)

The air pulse method was conducted in a plexiglass tube device, 4" in diameter and 5' long, but otherwise similar to Shepard's. A sheet of plastic ("Saran Wrap" was found best) sealed off one half of the tube that was slowly filled by compressed air. A hot wire was exposed inside the other half of the tube where the air speed was essentially zero. As the compressed air was increased, the plastic sheet burst and a shock wave of air proceeded past the wire with a steady state flow developing soon thereafter.

A Tektronix Type 564 storage oscilloscope was set to trigger as soon as the hot wire AC voltage changed. Voltage changed so rapidly, during the first 40 microseconds after the shock wave, that the scope could not track it. However, the triggering point and points shortly before the steady state are shown in figure 53 which shows a photograph of the scope traced. Also in figure 53 is an idealized trace produced by an actual RC circuit.  $\tau$  was found to be 17 microseconds.

The oscilloscope trace of the hot wire response shows overshoot and damping before reaching a steady state. This could be interpreted as evidence of some second order time response characteristics or some periodic fluctuations in the air speed between the shock wave and the steady state condition.

The time constant  $\tau$  and the maximum frequency are related by  $f(\max) = 1/2\pi\tau$ . The above  $\tau$  transforms to  $f(\max) = 9.05$  Khz.

## C.6 CORRECTIONS FOR CYLINDER BLOCKAGE OF TUNNEL

The cylinder produces two types of blockage, "solid" and "wake." They are discussed in Sections 6.4 and 6.5 of Pope (1966). Presence of a cylinder in a test section reduces the area through which air can flow, and hence increases the speed of the air past the cylinder. This increase is called "solid blocking" effect. Solid blocking speed increment near the cylinder surface is less than the increment one would obtain from direct area reduction, due to boundary layer effects.

The cylinder wake has a mean velocity lower than the free stream. The velocity outside the wake must be correspondingly higher. The higher velocity in the mainstream produces, by Bernoulli's principle, a lowered pressure, and this lowered pressure puts the cylinder in a pressure gradient and results in a second speed increment near the cylinder. This is the "wake blockage" effect.

A method by Roshko (adapted from Allen and Vincetti) is used to calculate the solid blockage effect as well as the wake blockage effect.

The tunnel is 24" in width. One cylinder is 4.5" in diameter and the other is 2.75". They block 18.75% and 11.46% of tunnel cross section, respectively. The hot wire sensor and stand contribute some small additional blockage. In many of the classic experiments, wires were used instead of cylinders so that blockage was negligible, on the order of 1%. However, in Roshko's later (1961) experiment his cylinder was 18" in diameter in a tunnel 132" wide -- a blockage of 13.6%. Roshko applied the formulas of Allen and Vincetti(1944), which give corrected values of velocity  $U'$  and drag coefficient  $C'd$ , in terms

of measured values  $U$  and  $C_d$ :

$$\begin{aligned} \frac{U'}{U} &= 1 + \frac{1}{4} C_d \left[ \frac{D}{h} \right] + 0.82 \left[ \frac{D}{h} \right]^2; \quad D \text{ diameter of cylinder.} \\ \frac{C'd}{C_d} &= 1 - \frac{1}{2} C_d \left[ \frac{D}{h} \right] - 2.5 \left[ \frac{D}{h} \right]^2; \quad h \text{ width of tunnel} \end{aligned} \quad (C-2)$$

Roshko's application of Allen and Vincetti has been followed.

From Roshko's results for his cylinder,  $C_d$  is estimated to be increased by 10% over the value of about 1.2 from Schlichting's figure 1.4 for  $Re \approx 4 \times 10^4$ , giving  $C_d \approx 1.3$ . Then with  $D/h \approx .19$  and  $.12$ :

$$\begin{aligned} \frac{U'}{U} &= 1 + \frac{1.3}{4} [.19] + 0.82 [.19]^2 = 1.09; \text{ and} \\ &= 1 + \frac{1.3}{4} [.12] + 0.82 [.12]^2 = 1.051. \end{aligned}$$

This means that the solid blockage effect increases the air speed near the cylinder surface. Hence, observed Strouhal numbers or vortex shedding frequencies should be corrected by reducing them by  $1/1.09$  and  $1/1.05$ .

All reported vortex shedding frequencies have been corrected by multiplying  $fD/U$  by  $.92$  or  $.95$ , respectively, for the  $4.5''$  and  $2.75''$  diameter cylinders.

These corrections give  $St$  values slightly high for these cylinders in minimum turbulence flow, with the reference Strouhal numbers in figure 1, for the same  $Re$ . However, the  $St$  vs  $Re$  curve is fairly flat, so this is not a precise test.

It is assumed that these same corrections can be used for turbulent flows.

There are "end effects" at the top and bottom of the cylinder, inside the tunnel. Roper's (1967) Master's Thesis at Colorado State

University describes these. Longitudinally (x axis) oriented vortices exist on each side of the cylinder at its base and top which interact with the shedding vortices which rotate about axes parallel to the y axis. Quoting Mujumdar, Morsbach has shown that in the sub-critical flow region there is no influence of the length-to-diameter ratio,  $L/D$ , on the flow at the middle section of the cylinder for  $L/D > 5$ . (In my experiment  $L/D \approx 5.3$  and  $8.7$ .) Achenbach indicated that for sufficiently large values of  $L/D$  (greater than 3), in the critical range especially, the flow at the middle section is not significantly influenced by the walls.

In addition to this, "end plates" were used on the 2.75" cylinder. As suggested by Bradshaw (1964), the plates were  $1.3D$  in diameter. They were placed at the top and bottom of the cylinder 2.5" from the ceiling and floor of the tunnel. This 2.5" was selected by measuring the depth of the boundary layer in the most turbulent flow and finding it to be about 2".

### C.7 MEASUREMENTS OF FREQUENCY, $f$

The frequency,  $f$ , of vortex shedding from one side of a cylinder, was observed by both a pressure transducer and a hot wire sensor. Both produced a continuous analog voltage which was analyzed by spectra or correlation analyses to find a dominant frequency. Upon repeated occasions, even in turbulent flows, they produced apparently identical results when operated simultaneously. As discussed in Section C.2, a spectra analysis of  $f$  is accurate to better than  $\pm 2\%$ . If only one clearly dominant frequency exists, correlation analyses can give  $f$  to  $\pm 1\%$  or closer.

### C.8 MEAN AIR SPEED, $U$

A graphical plot of  $E$  vs  $U$ , found in the CTA calibration, can be used. This curve became nearly a straight line if  $E^4$  vs  $U$  (or  $E^2$  vs  $\sqrt{U}$ ) was used. The most accurate method was to apply Peterka's least square program to use calibration data to obtain  $A$ ,  $B$  and  $C$  in King's equation (B-2). Then

$$U = \left[ \frac{E^2 - R(R - RA)A}{[R(R - RA)]B} \right]^{1/C} \quad (C-4)$$

In general,  $U$  can be measured more accurately as the air speed increases, at least up to the maximum of 30 to 40 fps used here.

Two pitot tubes, one in each WSMR tunnel, and a vortex shedder anemometer (in the larger tunnel) were available as "standards." They were used to calibrate the CTA instruments. The two pitot tubes were compared, along with a "calibrated" whirling cup anemometer, at several speeds from 15 to 45 fps. The two pitot tubes had a mean difference of .8%. The whirling cup was within 1.2% of the pitot tubes.

The following equation was used to obtain U by the pitot tube:

$$U(\text{fps}) = 92.35 \sqrt{\frac{T(^{\circ}\text{R}) \Delta P (\text{inches water})}{P(\text{mb})}} \quad (\text{C-5})$$

The vortex shedder always operated within the range  $40 < Re < 150$ , using the diameters of the shedding wires. Their diameters were checked with a micrometer. The shedding frequency was measured by a Lissajous figure, comparing the hot wire with a variable sine wave. Using Roshko's equation for laminar vortex shedding,  $St = .212 - 4.49/Re$ , and multiplying both sides by  $Re$ , it defines  $U$ :

$$U = \frac{fD}{.212} + 21.179 \left[ \frac{v}{D} \right] \quad (\text{C-6})$$

The TSI CTA had a temperature compensated hot film sensor. Its calibration drift was usually less than 1% from day to day or even week to week. It was calibrated from 2 to 30 fps by comparison with a vortex shedder and a pitot tube. This basic curve was then checked each day by comparison with a pitot tube and correction made. It also compared closely with some low speed standards at CSU. It was used as a "transfer standard" to calibrate the DISA CTA. It is estimated that the TSI values of  $U$  are accurate to  $\pm 2\%$  or closer; except between 2 and 5 fps, the accuracy is estimated at  $\pm 4\%$ . Below 2 fps, the accuracy decreases rapidly.

The accuracy of the DISA calibration was checked several ways. First, the plot of  $E^2/[R(R-RA)]$  vs  $U^C$  should be very nearly a straight line. Figure 54 shows, on a reduced scale, a computer plot of this. This is based upon Peterka's least squares fit of the calibration data to define A, B and C of King's equation. See figure 55 for a computer printout of this. Second, the empirical fit of the mean data must be

accurate to the first derivative. See Sandborn's text, section 7.2.2. Using the same calibration as in figure 50, this was tested by calculating the slope of the tangent at each calibration point of E vs U and then by calculating the derivative  $dE/dU$  from equation (C-7), applied in figure 55. This comparison of the slope and derivative is completed in table 4. The comparison was very close (<2% mean) except on the point for lowest speed. Third, the value of c was found to be between .41 and .45 for several calibrations which agrees closely with several reports in the literature.

The DISA hot wire calibration always drifted with time. 1% or 2% per hour was usual. It was calibrated before and after use and the drift was assumed linear with time between the two. Corrections were made for the drift. The DISA CTA accuracy is estimated at  $\pm 3\%$  at 18 fps, with slight changes inversely with speed, similar to the TSI.

## C.9 FLUCTUATING AIR SPEED $\bar{u}$

### C.9.1 HOT WIRE METHODS

All observations of  $\bar{u}$  used in this report were found by hot wire data. King's modified equation was generally used, where B and C had been found by Peterka's least squares program.

$$\bar{u} = U_e \left[ \frac{2E}{R(R-RA)BCU^c} \right] = T_1 U \quad (C-7)$$

This is a version of equation (B-1).

In some cases, when a sufficient portion of the calibration curve was linear for  $E^2$  vs  $\sqrt{U}$ ,  $C = .5$  was used to simplify the equation and  $R(R - RA)B$  found from the slope of the line. This is the same as equation (B-3).

The less accurate intercept equation (B-4) was used in figure 34 to compare  $T_i$  ( $\bar{u}/U$ ) for several high turbulence flows, as calculated by equation (C-7). At low  $T_i$  values,  $T_i$ 's by the two methods compared within 1% but differed by as much as 21% at high  $T_i$  values ( $\approx 58\%$ ).

Repeated observations of  $\bar{u}$  in similar flows by equation (C-7) show variations of less than 25% for  $T_i \approx 24\%$ .

It is concluded that the accuracy of  $\bar{u}$  varies with its magnitude but was within  $\pm 25\%$  or less for data used in table 3.

#### C.9.2 DETERMINATION OF $\bar{u}$ BY THE DIFFUSION OF HEAT

Schubauer (1935) reported a method of investigating the effect of turbulence upon the diffusion of heat. He found that the relation between a dimension of the wake from a heated wire and the  $z$  component of turbulence intensity,  $\bar{w}/U$ , as measured by a hot wire, was approximately linear. ("Heated wire" and "hot wire" are two different instruments.)

In my investigation, unusually high turbulence intensities,  $\bar{u}/U$ , (up to 25%) have been observed by the hot wire method near the center of a wind tunnel test section with the cylinder removed. Because of these high values, it was advisable to double check the hot wire turbulence intensity measurements by diffusion of heat measurements.

Schubauer's apparatus used an electrically heated wire held vertically (along  $y$  axis) through the origin of the experimental coordinate system. A small copper-constantan thermocouple was fixed 2" behind the wire. The frames holding the wire and the thermocouple could be rotated about the axis  $y$  through the wire. In that way, the heated wire remained in a fixed position and the thermocouple rotated through an arc in the wake of the wire. A reference thermocouple was kept

elsewhere in the air flow at a constant temperature.  $\Delta T$  is temperature difference between the two thermocouples.

The thermocouple should show the highest  $\Delta T$  when it was directly downwind behind the heated wire (rotation angle  $\theta = 0$ ; or both wires intersecting the x axis) and should register a lower  $\Delta T$  (thermocouple near heated wire - reference thermocouple) as the angle  $\theta$  increases.

The theory of the  $\Delta T$  distribution was derived from the temperature distribution behind a line source in laminar flow (Drew, 1931, who applied the Fourier-Poisson equation for thermal conduction in moving fluids).

Schubauer found it convenient to characterize the spread of the heated wake by the angle,  $\alpha$ , subtended at the source by the two positions where  $\Delta T$  was half that in the center of the wake. Schubauer then derived the equation  $\alpha^2 = \alpha_t^2 + \alpha_0^2$ , using Drew's results. Where

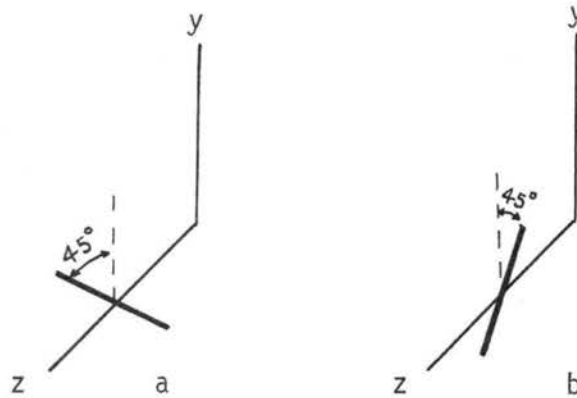
$\alpha_0^2 = 190.8 \sqrt{k/\rho c U x}$  in degrees and is the molecular contribution to diffusion.  $\alpha_0$  can be calculated for laboratory conditions. Then with  $\alpha$  observed,  $\alpha_t$ , or the turbulent contribution can be obtained.

Schubauer plotted  $\alpha_t$  vs  $\bar{w}/U$  obtained by hot wire methods and found a linear relation as shown in figure 56. Hagist (1968) conducted experiments at Colorado State University which verified Schubauer's curve for  $T_i$  ( $\bar{w}/U$ ) values up to 15%, much higher than reported by Schubauer.

Figure 56 also shows my observations of  $\alpha_t$  vs  $T_i$  ( $\bar{u}/U$ ). It is obvious that the  $\bar{u}/U$  values are 2 or 3 times larger than Schubauer's curve indicates for  $\bar{w}/U$ . For plate .972,  $\bar{u}/U$  was 1.72 larger than  $\bar{w}/U$ . This shows a condition of anisotropy in most of my air flows. This was approximately verified by a yawed hot wire determination of  $\bar{w}$ .

C.9.3 OBSERVATION OF  $\bar{u}$ ,  $\bar{v}$ ,  $\bar{w}$  BY YAWED HOT WIRES

With the cylinder removed, a DISA hot wire was put at the origin in air flow behind plate .972. The wire was placed in two different positions in the yz plane with the holder parallel to the x axis. Then it was manually rotated to estimated  $\pm 45^\circ$  from a position normal to the mean flow.



The following data was noted:

$$\overline{e^2} = (.190)^2 = .0361 \text{ volts}^2 \quad (\text{normal position})$$

$$\overline{e_a^2} = (.178)^2 = .031684 \text{ volts}^2 \quad (\text{position a})$$

$$\overline{e_b^2} = (.176)^2 = .030976 \text{ volts}^2 \quad (\text{position b})$$

$$E^2 = (7.04)^2 = 49.5616 \text{ volts}^2 \quad (\text{normal position})$$

$$U^2 = (16.3)^2 = 265.69 \text{ (fps)}^2$$

The above results can be used to calculate  $\bar{u}$  and  $\bar{w}$  by employing equations (B-23), (B-24), and (B-25), which leads to  $\bar{u} = 3.96$  fps, and  $\bar{w} = 1.67$  fps, or  $\bar{u} \approx 2.3 \bar{w}$ , comparable to the results in figure 56. More exactly, 1.7 vs 2.3, or a difference of 35%.

The above indicates that  $\bar{u}$  can be measured to accuracies that vary directly with  $T_i$ . For  $T_i \approx 10\%$ , the accuracy is about  $\pm 10\%$ ; for  $T_i \approx 20\%$ , the accuracy is about  $\pm 20\%$ , etc.

### C.10 MICROSCALE OF TURBULENCE $\lambda$

As stated in Section B.4,  $\lambda$  was calculated from the same data by two different methods, several times. Results indicated an accuracy of  $\pm 10\%$  as reasonable.

### C.11 INTEGRAL SCALE OF TURBULENCE $L_x$

$L_x$  has been the most difficult parameter to measure accurately. No doubt, better accuracy could be obtained if correlations between  $e$  values of two separate hot wires could have been measured as the wires were brought closer together, with both wires parallel to the  $x$  or  $y$  axis. Such equipment was not available, so data from only one hot wire had to be used. This required Taylor's hypothesis to convert from time to space differences. Two formulas are available:

$$L_x(\tau) = \tau_0 U; \text{ and } L_x(F) = \frac{F(0)}{4} U$$

Comparisons of  $L_x$ , computed from the seven sets of the same data, by these two equations, give results consistently different by a factor of two, see section 5.

The correlation coefficient of .99 between the two methods of calculating seven sets of  $L_x$  is very encouraging as far as consistency of data and calculations are concerned.

An error as high as 10% was noted in figure 34 due to 60 Hz harmonics. However, estimates can be made to correct for this.

Although the absolute values of  $L_x$  may be in error by as much as 100%, it is believed that the use of the same type of  $L_x$  measurements for comparison of different flows gives a much less error. It is estimated at  $\pm 20\%$  when used for comparison purposes and when effects of 60 Hz harmonics have been accounted for.

C.12 ACCURACY OF DERIVED PARAMETERS, Re, St, Ti, Km, Ta, Re(Km),  
Re( $\lambda$ ) and Re(p)

It had been planned to use a Kline-McClintock (1953) analysis to define the "uncertainties" of the derived parameters. Their approach is that if parameter P is a function of independent variables  $v_1, \dots, v_n$ , and if  $w_i$  is the uncertainty interval, of measuring each interval, of measuring each variable, then the uncertainty interval, or accuracy, of the total parameter is

$$w_P = \left[ \left( \frac{\partial P}{\partial v_1} w_1 \right)^2 + \dots + \left( \frac{\partial P}{\partial v_n} w_n \right)^2 \right]^{.5}$$

In the preceding sections, the terms  $\left( \frac{\partial P}{\partial v_n} w_n \right)$  have been determined by comparisons or other estimates and all are expressed as  $\pm\%$  figures. Consequently, the above expression for  $w_p$  can be applied directly.

$$(1) \text{ Re} = f(U, D, \nu)$$

$$\text{Accuracy of Re} = [(.03)^2 + (.001)^2 + (.001)^2]^{.5} = \pm.0300$$

This means that  $\text{Re} = 4 \times 10^4$  can be stated as  $\text{Re} = 4 \times 10^4 \pm 1200$ , for example. It is assumed that D,  $\nu$ , and plate dimensions are accurate to  $\pm.001$  or  $\pm.1\%$ . An accuracy of 3% is used for U to include errors in blockage correction.

$$(2) \text{ St} = f(f, D, U)$$

$$\text{Accuracy of St} = [(.02)^2 + (.001)^2 + (.03)^2]^{.5} = \pm.0361$$

$$(3) \text{ Ti} = f(\bar{u}, U)$$

$$\text{Accuracy of Ti}(\approx 1\%) = [(.01)^2 + (.03)^2]^{.5} = \pm.0316$$

$$\text{Accuracy of Ti}(\approx 25\%) = [(.25)^2 + (.03)^2]^{.5} = \pm.2518$$

$$(4) \quad K_m = f(\bar{u}, L_x)$$

$$\text{Accuracy of } K_m(T_i \approx 1\%) = [(.01)^2 + (.2)^2] \cdot .5 = \pm .2002$$

$$\text{Accuracy of } K_m(T_i \approx 25\%) = [(.25)^2 + (.2)^2] \cdot .5 = .3202$$

$$(5) \quad T_a = f(\bar{u}, U, D, L_x)$$

$$\begin{aligned} \text{Accuracy of } T_a(T_i \approx 1\%) &= [(.01)^2 + (.03)^2 + (.001)^2 + (.2)^2] \cdot .5 \\ &= \pm .2025 \end{aligned}$$

$$\begin{aligned} \text{Accuracy of } T_a(T_i \approx 25\%) &= [(.25)^2 + (.03)^2 + (.001)^2 + (.2)^2] \cdot .5 \\ &= \pm .3216 \end{aligned}$$

$$(6) \quad \text{Re}(K_m) = f(U, D, \bar{u}, L_x)$$

$$\begin{aligned} \text{Accuracy of } \text{Re}(K_m)(T_i \approx 1\%) &= [(.03)^2 + (.001)^2 + (.01)^2 + (.2)^2] \cdot .5 \\ &= \pm .2025 \end{aligned}$$

$$\begin{aligned} \text{Accuracy of } \text{Re}(K_m)(T_i \approx 25\%) &= [(.03)^2 + (.001)^2 + (.25)^2 + (.2)^2] \cdot .5 \\ &= \pm .3216 \end{aligned}$$

$$(7) \quad \text{Re}(\lambda) = f(\bar{u}, \lambda, v)$$

$$\begin{aligned} \text{Accuracy of } \text{Re}(\lambda)(T_i \approx 1\%) &= [(.01)^2 + (.1)^2 + (.001)^2] \cdot .5 \\ &= \pm .1005 \end{aligned}$$

$$\begin{aligned} \text{Accuracy of } \text{Re}(\lambda)(T_i \approx 25\%) &= [(.25)^2 + (.1)^2 + (.001)^2] \cdot .5 \\ &= \pm .2693 \end{aligned}$$

$$(8) \quad \text{Re}(p) = f(U, D, d, v)$$

$$\begin{aligned} \text{Accuracy of } \text{Re}(p) &= [(.03)^2 + (.001)^2 + (.001)^2 + (.001)^2] \cdot .5 \\ &= \pm .0300 \end{aligned}$$

It is considered that all of the above accuracy estimates, including those for the primary data ( $f, U, \bar{u}, L_x, \lambda$ ), are very conservative. These estimates should include almost all of the results and the majority of the results should be much more accurate than these estimates indicate.

TABLE 1  
TURBULENCE PRODUCING PLATES

Blockage Ratio "Br"	Open Area Ratio	Hole Diameter "d" ft	Distance Between Centers M ft	M-d ft	Material
.972	.028	.0156	.0825	.0669	Masonite
.958	.042	.0156	.0681	.0525	Masonite
.945	.055	.0156	.0588	.0432	Masonite
.929	.071	.0156	.0514	.0358	Masonite
.902	.098	.0208	.0588	.0380	Masonite
.861	.139	.0156	.0370	.0214	Metal
.804	.196	.0208	.0416	.0208	Masonite
.801	.199	.0156	.0308	.0152	Metal
.748	.252	.0156	.0274	.0118	Metal
.690	.310	.0156	.0250	.0094	Metal
.500	.500	.0156	.0208	.0052	Metal
.340	.660	.511	.635	.124	Square Grid Wooden "Surry"

All plates are identified by their Blockage Ratios.

TABLE 2

## VORTEX SHEDDING DATA (CYLINDER IN TUNNEL)

Ref Fig 1	D In- ches	Plate Br	U fps	f Hz	St	Re $\times 10^4$	Re(E) Est $\times 10^4$	$\frac{Re(E)}{Re}$	Vortex Shedding Regime	Fig	Hot Wire Position		Turbulence Data	
											x	z	Obs	Fig
A	4.5	.000	19.4	10.6	.205	3.8	4.	1.0	Sub-c class	15	1.5D	.5D	--	--
B	4.5	.690	17.4	9.8	.211	3.4	21.	6.2	Top sub-c	16	1.5	.5	#1	34
B'	2.75	.748	13.7	12.3	.206	1.7	22.	13.	Top sub-c	17	1.5	.5	#2	36
C	4.5	.748	16.9	11.2	.249	3.3	36.	11.	Disc SS	18	1.5	.5	#3	37
C'	2.75	.801	16.4	Undef	Undef	2.0	38.	19.	Disc SS	19	2.0	.3	#4	38
D	4.5	.804	8.1	7.1	.329	1.6	100.	62.	Sup-c	20	1.5	.5	#5	39
D'	2.75	.861	7.1	10.5	.339	0.9	100.	109.	Sup-c	21	2.5	.4	#6	40
E	4.5	.945	18.7	Undef	Undef	3.7	200.	54.	Disc ST	22	.25	.5	#7	41
E'	2.75	.945	20.9	Undef	Undef	2.5	200.	80	Disc ST	23	1.5	.5	#7	41
F	4.5	.972	23.2	6.2	.100	4.6	500.	109	Turb	24	1.05	.5	#8	42
F'	2.75	.972	23.3	13.0	.128	2.8	500.	180.	Turb	27	.36	.5	#8	42

TABLE 3

OBSERVATION OF TURBULENCE PARAMETERS  
NO CYLINDER IN TUNNEL. HOT WIRE AT ORIGIN

OBS # Vortex Cond	REF Rxx	FIG Turb Data Fxx	PLATE Br	U fps	$\bar{u}$ fps	Ti	$\lambda$ ft	$\tau_0$ sec	F(0) or F(M) sec	Factor for 60 Hz corr*	Lx( $\tau$ ) ft	Lx(F) ft	Km** $\frac{ft^2}{sec}$
1 B	43	34	.690	17.6	.370	.021	.0040	.0088	.0225	1.10	.155	.099	.037
2 B'	44	36	.748	12.9	.413	.032	.0045	.0145	.0276	1.08	.187	.089	.037
3 C	43	37	.748	17.2	.619	.036	.0064	.0129	.0272	1.06	.222	.117	.072
4 C'	44	38	.801	15.9	.716	.045	.0059	.3000	.0891	1.05	4.77	.345	.247
5 D	43	39	.804	9.7	.650	.067	.0057	.0343	.0693	1.04	.333	.168	.109
6 D'	44	40	.861	8.7	.574	.066	.0054	.0269	.0518	1.01	.234	.113	.065
7 E E'	43 44	41	.945	20.3	3.25	.160	.0072	.0262	.0467	1.00	.532	.237	.770
8 F F'	43 44	42	.972	20.2	4.93	.244	.0080	.0294	.0584	1.00	.594	.295	1.454

\* This correction factor has been used to obtain  $\tau_0$ , F(0), F(M), Lx( $\tau$ ) and Lx(F).\*\* Km  $\equiv \bar{u}Lx(F)$

TABLE 3 (continued)

OBSERVATION OF TURBULENCE PARAMETERS  
NO CYLINDER IN TUNNEL. HOT WIRE AT ORIGIN

DATA RELATED TO 4.5" CYLINDER

DATA RELATED TO 2.75" CYLINDER

Ref	Ti	Lx (F) ft	Km ft <sup>2</sup> sec	Ta	Re (Km)	Re (P) x 10 <sup>4</sup>	Re (λ)	Re(E) Re	Re(E) x 10 <sup>4</sup>	Ref	Ti	Lx (F) ft	Km ft <sup>2</sup> sec	Ta	Re (Km)	Re (P) x 10 <sup>4</sup>	Re (λ)	Re(E) Re	Re(E) x 10 <sup>4</sup>
B # 1	.021	.099	.037	.027	180.	.52	9.	6.2	21	B <sup>-</sup> # 2	.032	.089	.037	.039	80.	.47	11.	13.	22
C # 3	.036	.117	.072	.045	89.	.63	23.	11.	36	C <sup>-</sup> # 4	.045	.345	.247	.041	15.	.79	25.	19.	38.
D # 5	.067	.168	.109	.079	33.	.61	22.	62.	100	D <sup>-</sup> # 6	.066	.113	.065	.076	31.	.57	18.	109.	100.
E # 7	.160	.237	.770	.175	10.	3.4	138.	54.	200	E <sup>-</sup> # 7	.160	.237	.770	.159	6.	3.4	138.	80.	200.
F # 8	.244	.295	1.45	.256	5.	6.6	230.	109.	500	F <sup>-</sup> # 8	.244	.295	1.45	.232	3.	6.6	230.	180.	500.

TABLE 4  
 COMPARISON OF FIRST DERIVATIVES  
 OF  
 HOT WIRE CALIBRATION  
 (DISA, 5 micron, 1 Apr 73)

CALIBRATION		FIRST DERIVATIVE			Analytical See figure 55 $\frac{dE}{dU} = \frac{1.604}{E U^{.5581}}$	COMPARISON $\frac{\text{Graphical}}{\text{Analytical}}$
E volts	U fps	$\Delta E$ volts	$\Delta U$ fps	$\frac{\Delta E}{\Delta U}$		
6.020	2.90	.50	3.0	.167	.147	1.136
6.282	5.00	.50	4.9	.102	.104	.981
6.467	6.90	.50	6.3	.079	.084	.940
6.689	10.00	.50	7.9	.063	.066	.954
6.958	14.70	.50	9.3	.054	.051	1.059
7.132	18.28	.50	11.5	.043	.044	.977
7.267	21.51	.50	12.3	.041	.040	1.025
7.513	28.14	.50	14.4	.035	.033	1.061
					Sum	8.133
					Mean	1.016

Mean comparison of first derivatives is within 2%.

Maximum difference of individual case is 14%.





TABLE 6

APPROXIMATE RELATION OF TURBULENCE PARAMETERS TO  $Re(E)$  AND  $Re(E)/Re$   
 LEAST SQUARES SOLUTION OF  $\ln(Y_i) = A + C \ln(X_i)$ , OR  $Y_i = B(X_i)^C$

## 4.5" Cylinder

<u>Case</u>	<u>Approximate Relation</u>	<u>Correlation Coefficient*</u>	<u>Least Squares Sum**</u>
1	$Re(E) = 2.500 \times 10^7 [Ti]^{1.247}$	.991	$2.53 \times 10^{-11}$
2	$Re(E) = 1.304 \times 10^8 [Lx]^{2.767}$	.996	$2.07 \times 10^{-12}$
3	$Re(E) = 3.307 \times 10^6 [Km]^{.779}$	.965	$3.78 \times 10^{-11}$
4	$Re(E) = 2.734 \times 10^7 [Ta]^{1.361}$	.991	$1.90 \times 10^{-11}$
5	$Re(E) = 1.763 \times 10^7 [Re(Km)]^{-.856}$	-.994	$6.78 \times 10^{-17}$
6	$Re(E) = 7.401 \times 10 [Re(p)]^{.994}$	.912	$3.00 \times 10^{-19}$
7	$Re(E) = 3.424 \times 10^4 [Re(\lambda)]^{.883}$	.943	$1.48 \times 10^{-15}$
8	$Re(E)/Re = 5.444 \times 10^2 [Ti]^{1.127}$	.926	$5.61 \times 10^{-2}$
9	$Re(E)/Re = 2.544 \times 10^3 [Lx]^{2.529}$	.940	$7.28 \times 10^{-3}$
10	$Re(E)/Re = 8.173 \times 10 [Km]^{.662}$	.847	$4.20 \times 10^{-2}$
11	$Re(E)/Re = 5.918 \times 10^2 [Ta]^{1.232}$	.926	$4.01 \times 10^{-2}$
12	$Re(E)/Re = 4.003 \times 10^2 [Re(Km)]^{-.776}$	-.931	$2.14 \times 10^{-7}$
13	$Re(E)/Re = 1.649 \times 10^{-2} [Re(p)]^{.783}$	.741	$2.13 \times 10^{-11}$
14	$Re(E)/Re = 1.788 [Re(\lambda)]^{.734}$	.810	$1.25 \times 10^{-6}$

\* Correlation is between  $\ln(X_i)$  and  $\ln(Y_i)$ .

\*\* Sum is approximately normalized by dividing by  $(X_3)^2(Y_3)^2$ .

TABLE 6 (continued)

## 2.75" Cylinder

<u>Case</u>	<u>Approximate Relation</u>	<u>Correlation Coefficient*</u>	<u>Least Squares Sum**</u>
15	$Re(E) = 3.556 \times 10^7 [Ti]^{1.442}$	.984	$4.62 \times 10^{-11}$
16	$Re(E) = 5.031 \times 10^6 [Lx]^{.992}$	.475	$3.82 \times 10^{-10}$
17	$Re(E) = 2.549 \times 10^6 [Km]^{.664}$	.828	$4.68 \times 10^{-10}$
18	$Re(E) = 4.310 \times 10^7 [Ta]^{1.542}$	.982	$3.85 \times 10^{-11}$
19	$Re(E) = 1.797 \times 10^6 [Re(Km)]^{-.353}$	-.577	$4.37 \times 10^{-11}$
20	$Re(E) = 1.002 \times 10^2 [Re(p)]^{.963}$	.902	$4.00 \times 10^{-20}$
21	$Re(E) = 3.740 \times 10^4 [Re(\lambda)]^{.861}$	.914	$3.21 \times 10^{-15}$
22	$Re(E)/Re = 8.717 \times 10^2 [Ti]^{1.149}$	.854	$2.76 \times 10^{-2}$
23	$Re(E)/Re = 1.086 \times 10^2 [Lx]^{.474}$	.246	$3.28 \times 10^{-2}$
24	$Re(E)/Re = 9.297 \times 10 [Km]^{.434}$	.590	$6.88 \times 10^{-2}$
25	$Re(E)/Re = 1.110 \times 10^3 [Ta]^{1.264}$	.878	$1.77 \times 10^{-2}$
26	$Re(E)/Re = 2.536 \times 10^2 [Re(Km)]^{-.611}$	-.690	$2.43 \times 10^{-7}$
27	$Re(E)/Re = 4.431 \times 10^3 [Re(p)]^{-.431}$	-.395	$1.16 \times 10^{-11}$
28	$Re(E)/Re = 4.979 [Re(\lambda)]^{.607}$	.702	$6.97 \times 10^{-7}$

TABLE 7

DIGITAL COMPUTER PROGRAMS FOR CURVE FITTING OF  $Y = A + BX^C$ 

Equations of the form,  $Y = A + BX^C$ , where  $X$  and  $Y$  are observed data and constants  $A$ ,  $B$ ,  $C$  are determined by a least squares approximation, were defined by two computer programs. A Newton-Raphson iteration was used for the least squares approximation, but a Slope-Intercept procedure was applied first, for three data points, to obtain the first approximations of  $A$ ,  $B$ , and  $C$  needed to start the iteration.

The Slope-Intercept procedure utilized sets 1, 3, and 5 of the  $X, Y$  data:  $Y_1 = A + BX_1^C$ ;  $Y_3 = A + BX_3^C$ ;  $Y_5 = A + BX_5^C$

By algebraically eliminating  $A$  and  $B$ , one equation with only  $C$  could be found: 
$$\frac{X_1^C - X_5^C}{Y_1 - Y_5} = \frac{X_1^C - X_3^C}{Y_1 - Y_3}$$

A difference "R" was defined: 
$$R = \frac{X_1^C - X_5^C}{Y_1 - Y_5} - \frac{X_1^C - X_3^C}{Y_1 - Y_3}$$

when a value of  $c$  ( $c \neq 0$ ) was calculated such that  $R$  was very close to zero (e.g., less than .000001), then  $C$  should be a good approximate solution for the three equations. This value was obtained by using an original estimate of  $C(1)$  and  $C(2)$ .  $R(1)$  and  $R(2)$  are calculated, and  $C(3)$ , for  $R(3) = 0$ , estimated as

$$C(3) = C(2) - R(2) \left[ \frac{C(2) - C(1)}{R(2) - R(1)} \right]$$

$C(4)$  was calculated similarly until  $R$  was small enough. Then, having a value of  $C$ ,  $A$  and  $B$  could be obtained by an algebraic solution.

The Newton-Raphson iteration (Chapt 25, Scheid, 1968) started with these estimates of A, B, and C and proceeded, as follows, to obtain the final approximate values of A, B, and C which fit all the data.

The general form of the Newton-Raphson iteration is

$$X_n = X_{n-1} - \frac{f(X_{n-1})}{f'(X_{n-1})}$$

In this case, the applicable equation was

$$S = \sum_{i=0}^n (Y_i - A - BX_i^c)^2; \text{ then}$$

$$\begin{pmatrix} A_n \\ B_n \\ C_n \end{pmatrix} = \begin{pmatrix} A_{n-1} \\ B_{n-1} \\ C_{n-1} \end{pmatrix} - (\phi)^{-1} \begin{pmatrix} SA \\ SB \\ SC \end{pmatrix}$$

where  $A_n$ ,  $B_n$  and  $C_n$  are first estimates. SA, SB and SC are derivatives evaluated by  $A_n$ ,  $B_n$  and  $C_n$ . The matrices and their elements are specified below. A common factor of "2" was cancelled from each element.

$$SA = \partial S / \partial A = - \sum_{i=1}^n (Y_i - A - BX_i^c)$$

$$SB = \partial S / \partial B = - \sum_{i=1}^n (Y_i - A - BX_i^c)(X_i^c)$$

$$SC = \partial S / \partial C = - \sum_{i=1}^n (Y_i - A - BX_i^c)(BX_i^c \ln X_i)$$

And

$$\phi = \begin{pmatrix} \frac{\partial^2 S}{\partial A^2} & \frac{\partial^2 S}{\partial B \partial A} & \frac{\partial^2 S}{\partial C \partial A} \\ \frac{\partial^2 S}{\partial A \partial B} & \frac{\partial^2 S}{\partial B^2} & \frac{\partial^2 S}{\partial C \partial B} \\ \frac{\partial^2 S}{\partial A \partial C} & \frac{\partial^2 S}{\partial B \partial C} & \frac{\partial^2 S}{\partial C^2} \end{pmatrix} = \begin{pmatrix} S(1,1) & S(1,2) & S(1,3) \\ S(2,1) & S(2,2) & S(2,3) \\ S(3,1) & S(3,2) & S(3,3) \end{pmatrix}$$

$$S(1,1) = \sum_{i=1}^n 1 = n$$

$$S(1,2) = \sum_{i=1}^n X_i^c$$

$$S(1,3) = \sum_{i=1}^n B X_i^c \ln X_i$$

$$S(2,1) = \sum_{i=1}^n X_i^c$$

$$S(2,2) = \sum_{i=1}^n X_i^{2c}$$

$$S(2,3) = \sum_{i=1}^n (A X_i^c \ln X_i + 2AB X_i^{2c} \ln X_i - A Y_i X_i^c \ln X_i)$$

$$S(3,1) = \sum_{i=1}^n B X_i^c \ln X_i$$

$$S(3,2) = \sum_{i=1}^n (A X_i^c \ln X_i + 2AB X_i^{2c} \ln X_i - A Y_i X_i^c \ln X_i)$$

$$S(3,3) = \sum_{i=1}^n (A B X_i^c (\ln X_i)^2 - B Y_i X_i^c (\ln X_i)^2 + 2B^2 X_i^{2c} (\ln X_i)^2)$$

The matrix is symmetric. In this case, five sets of  $(X_i, Y_i)$  data were used, so  $n = 5$ .

The computer program follows. A Gauss-Jordan sub-routine was included to invert the matrix.

```

FOR, IS ,BARNETT, ,LSQABC
C CALCULATE A,B,C IN EQ Y=A+B*X**C BY LEAST SQUARES
C USING NEWTON-RAPHSON ITERATION
    IMPLICIT DOUBLE PRECISION (A-H, O-Z)
    DIMENSION A(9),B(9),C(9),X(5),Y(5),S(3,3),AA(5),
    $ SS(5),H(14),JC(3),V(3),BB(F),CC(F),Z(5)
800 READ(5,801 ,END=504) H, A(1), B(1), C(1)
C H IS HEADING, A B C ARE FIRST ESTIMATES
801 FORMAT(13A6,A2/(5X,3F25.9))
    READ(5,802)(X(I),Y(I),I=1,5)
802 FORMAT(5F15.5)
    WRITE(6,906) H
906 FORMAT(1H1,5X,13A6,A2/20X,'X',20X,'Y')
    DO 101 I=1,5
    WRITE (6,907) X(I),Y(I)
907 FORMAT (5X,2F20.5)
101 CONTINUE
C CALCULATE ELEMENTS FOR MATRIX AND USE TO IMPROVE
C ESTIMATES OF A, B, C
    DO 102 J=2,9
    AA(2)=0.
    BB(2)=0.
    CC(2)=0.
    K=J-1
    A(J)=A(K)-AA(J)
    B(J)=B(K)-BB(J)
    C(J)=C(K)-CC(J)
    A1=A(J)
    B1=B(J)
    C1=C(J)
C CALCULATE LEAST SQUARE, Z7
    Z7=0.
    DO 103 I=1,5
    Z(I)=(Y(I)-A1-B1*(X(I)**C1)**2
    ZZ=ZZ+Z(I)
103 CONTINUE
    WRITE (6,903)
903 FORMAT(1H0,5X,' ITERATION',9X,'A',19X,'B',18X,'C',32X,
    $ 'LEAST SQUARE')
    WRITE (6,904) K,A1,B1,C1,ZZ
904 FORMAT(1H ,5X,I3,3F20.5,1F40.9)
C S(M,N) ARE FLEMENTS OF 3X3 MATRIX
    S(1,1)=5.
    S12=0.
    DO 104 I=1,5
    SS(I)=(X(I)**C1
    S12=S12+SS(I)
104 CONTINUE
    S(1,2)=S12
    S(2,1)=S(1,2)
    S13=0.
    DO 105 I=1,5
    SS(I)=((X(I)**C1)*(DLOG(X(I)))

```

```

S13=S13+SS(I)
105 CONTINUE
S(1,3)=R1*S13
S(3,1)=S(1,3)
S22=0.
DO 106 I=1,5
SS(I)=(X(I))**(2.*C1)
S22=S22+SS(I)
106 CONTINUE
S(2,2)=S22
S231=S13
S232=0.
DO 232 I=1,5
SS(I)=((X(I))**(2.*C1))*(DLOG(X(I)))
S232=S232+SS(I)
232 CONTINUE
S233=0.
DO 108 I=1,5
SS(I)=(Y(I))*((X(I))**C1)*(DLOG(X(I)))
S233=S233+SS(I)
108 CONTINUE
S(2,3)=A1*S231+2.*B1*S232-S233
S(3,2)=S(2,3)
S331=0.
DO 109 I=1,5
SS(I)=((X(I))**(2.*C1))*((DLOG(X(I)))**2)
S331=S331+SS(I)
109 CONTINUE
S332=0.
DO 110 I=1,5
SS(I)=(Y(I))*((X(I))**C1)*((DLOG(X(I)))**2)
S332=S332+SS(I)
110 CONTINUE
S333=0.
DO 115 I=1,5
SS(I)=((X(I))**C1)*((DLOG(X(I)))**2)
S333=S333+SS(I)
115 CONTINUE
S(3,3)=R1*(2.*B1*S331-S332+A1*S333)
WRITE(6,955)
955 FORMAT(1H ,5X, 'ELEMENTS OF MATRIX')
DO 152 M=1,3
WRITE(6,956)(S(M,N),N=1,3)
956 FORMAT(1H ,5X, 'F30.9)
152 CONTINUE
C ALL VALUES OF MATRIX ARE CALCULATED, CALL SUBROUTINE
C TO INVERT MATRIX
V(1)=1.
CALL KMRGJR(S,3,3,3,3,$902,JC,V)
901 CONTINUE
WRITE(6,951)
951 FORMAT(1H ,5X, 'ELEMENTS OF INVERTED MATRIX')
DO 151 M=1,3

```

```

WRITE(6,952)(S(M,N),N=1,3)
952 FORMAT(1H ,5X,3F30.9)
151 CONTINUE
C CALCULATE PARTIAL DERIVATIVES OF S WRT A,B,C =SA,SB,SC
SA=0.
DO 112 I=1,5
SS(I)=(Y(I))-A1-B1*(X(I))**C1
SA=SA+SS(I)
112 CONTINUE
SA=(-1.)*SA
SB1=0.
DO 113 I=1,5
SS(I)=((X(I))**C1)*(Y(I)-A1-B1*(X(I))**C1)
SB1=SB1+SS(I)
113 CONTINUE
SB=(-1.)*SB1
SC=0.
DO 114 I=1,5
SS(I)=(Y(I)-A1-B1*(X(I))**C1)*(((X(I))**C1)
$(DLOG(X(I))))
SC=SC+SS(I)
114 CONTINUE
SC=(-B1)*SC
WRITE(6,957) SA,SB,SC
957 FORMAT(1H ,5X,'SA=',1F20.9,5X,'SB=',
$1F20.9,5X,'SC=',1F20.9)
L=J+1
AA(L)=S(1,1)*SA+S(1,2)*SB+S(1,3)*SC
BB(L)=S(2,1)*SA+S(2,2)*SB+S(2,3)*SC
CC(L)=S(3,1)*SA+S(3,2)*SB+S(3,3)*SC
WRITE(6,953)
953 FORMAT(1H ,5X,'ITERATION',7X,'VALUES OF CORRECTION
$ FACTORS AA, BB, CC')
WRITE(6,954)K,AA(L),BB(L),CC(L)
954 FORMAT(1H ,5X,I3,5X,'AA=',1F25.9,5X,'BB=',1F25.9,
$5X,'CC=',1F25.9)
102 CONTINUE
GO TO 503
902 WRITE (6,905)
905 FORMAT(1H ,5X,'ERROR IN MATRIX INVERSION')
GO TO 504
503 GO TO 800
504 STOP
END
*FOR,IS .KMBGJR
SUBROUTINE KMBGJR(A,NC,NR,N,MC,$,JC,V)
IMPLICIT DOUBLE PRECISION (A-H, O-7)
DIMENSION A(NR,NC),JC(1),V(2)
C JC IS THE PERMUTATION VECTOR
C KD IS OPTION KEY FOR DETERMINANT EVALUATION
C KI IS THE OPTION KEY FOR MATRIX INVERSION
C L IS THE COLUMN CONTROL FOR AX=B
C M IS THE COLUMN CONTROL FOR MATRIX INVERSION

```

```

C              INITIALIZATION
      IW=V(1)
      M=1
      S=1.
      L=N+(MC-N)*(IW/4)
      KD=2-MOD(IW/2,2)
      IF(KD.EQ.1) V(2)=0.
      KI=2-MOD(IW,2)
      GO TO (5,20),KI

C              INITIALIZE JC FOR INVERSION
5      DO 10 I=1,N
10     JC(I)=I

C              SEARCH FOR PIVOT ROW
20     DO 91 I=1,N
        GO TO (22,21),KI
21     M=I
22     IF (I.EQ.N) GO TO 60
        X=-1.
        DO 30 J=I,N
          IF (X.GT.ABS(A(J,I))) GO TO 30
          X=ABS(A(J,I))
        K=J
30     CONTINUE
        IF(K.EQ.I) GO TO 60
        S=-S
        V(1)=-V(1)
        GO TO (35,40),KI
35     MU=JC(I)
        JC(I)=JC(K)
        JC(K)=MU

C              INTERCHANGE ROW I AND ROW K
40     DO 50 J=M,L
        X=A(I,J)
        A(I,J)=A(K,J)
50     A(K,J)=X

C              TEST FOR SINGULARITY
60     IF (ABS(A(I,I)).GT.0.) GO TO 70
C              MATRIX IS SINGULAR
        IF(KD.EQ.1) V(1)=0.
        JC(1)=I-1
        RETURN 6
70     GO TO (71,72),KD

C              COMPUTE THE DETERMINANT
71     IF(A(I,I).LT.0.) S=-S
        V(2)=V(2)+DLOG(ABS(A(I,I)))
72     X=A(I,I)
        A(I,I)=1.

C              REDUCTION OF THE I-TH ROW
      DO 80 J=M,L
        A(I,J)=A(I,J)/X

C              TEST OVERFLOW SWITCH. IF ON
C              RETURN NEGATIVE VALUE OF I IN JC(1)
      CALL OVRFL (IFL)

```

```

      IF(IFL.EQ.1) GO TO 150
80  CONTINUE
C      REDUCTION OF ALL REMAINING ROWS
      DO 91 K=1,N
      IF (K.EQ.I) GO TO 91
      X=A(K,I)
      A(K,I)=0.
      DO 90 J=M,L
      A(K,J)=A(K,J)-X*A(I,J)
C      TEST OVERFLOW SWITCH. IF ON
C      RETURN NEGATIVE VALUE OF I IN JC(1)
      CALL OVERFL (IFL)
      IF(IFL.EQ.1) GO TO 150
90  CONTINUE
91  CONTINUE
C      AX=B AND DET.(A) ARE NOW COMPUTED
      GO TO (95,140),KI
C      PERMUTATION OF COLUMNS FOR MATRIX INVERSION
95  DO 130 J=1,N
      IF (JC(J).EQ.J) GO TO 130
      JJ=J+1
      DO 100 I=JJ,N
      IF (JC(I).EQ.J) GO TO 110
100  CONTINUE
110  JC(I)=JC(J)
      DO 120 K=1,N
      X=A(K,I)
      A(K,I)=A(K,J)
120  A(K,J)=X
130  CONTINUE
140  JC(1)=N
      IF(KD.EQ.1) V(1)=S
      RETURN
150  JC(1)=1-I
      IF(KD.EQ.1) V(1)=S
      RETURN 6
      END
*XQT
C INSERT HEADING AND DATA CARDS HERE
*FIN

```

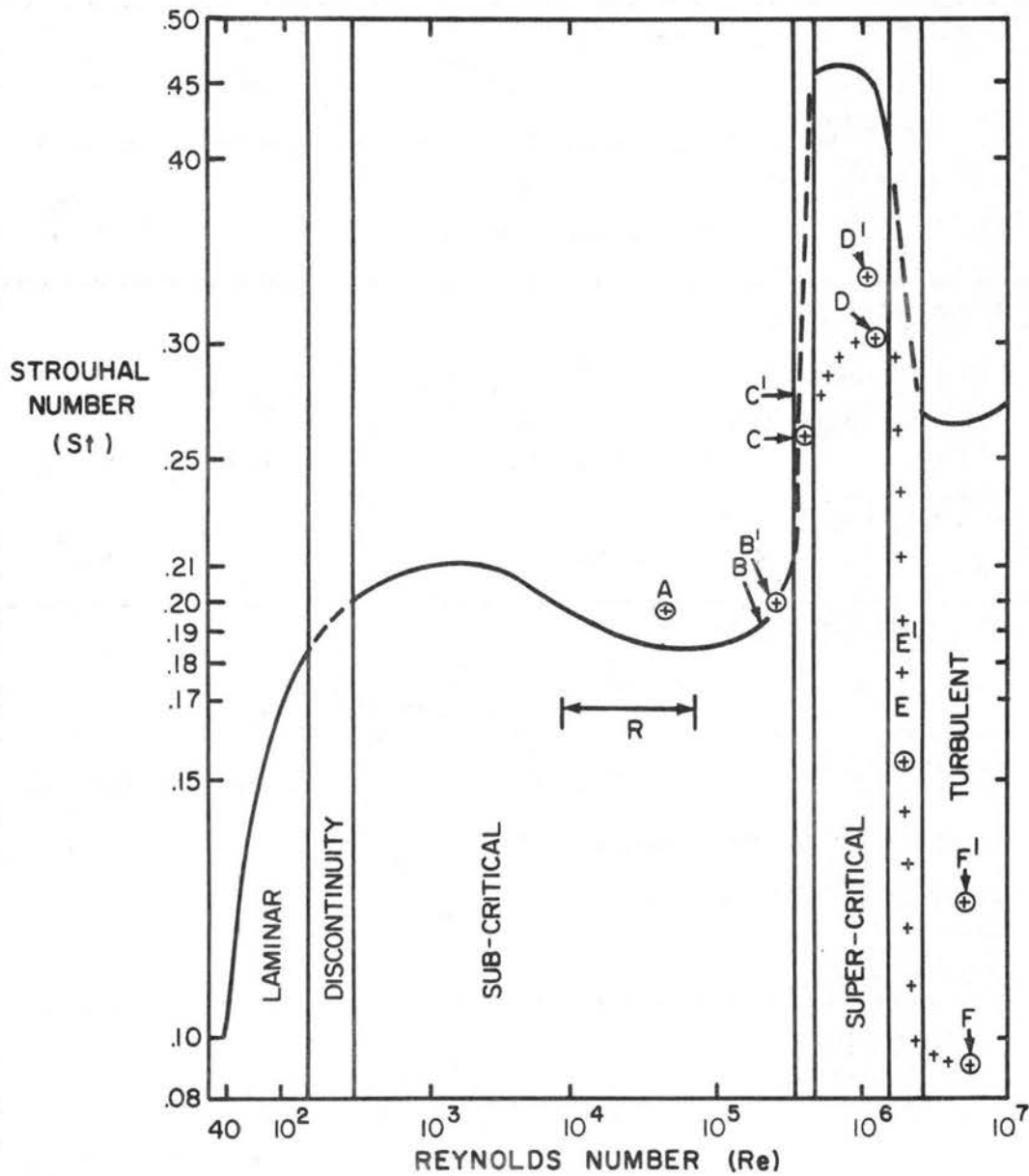


Figure 1. Vortex Shedding Flow Regimes. Four vortex shedding regimes, from a circular cylinder, are shown with relation between Reynolds and Strouhal numbers. All are for wind tunnel flows with minimum turbulence intensity (usually < 0.5%). Regions between regimes are "discontinuity" vortex shedding flow conditions. See text for explanation of letters "A" to "R." The symbol "⊕" indicates changes in vortex shedding induced behind larger cylinder by introducing increasing turbulence into a wind tunnel; B', D' and F' are similar results for smaller cylinder.

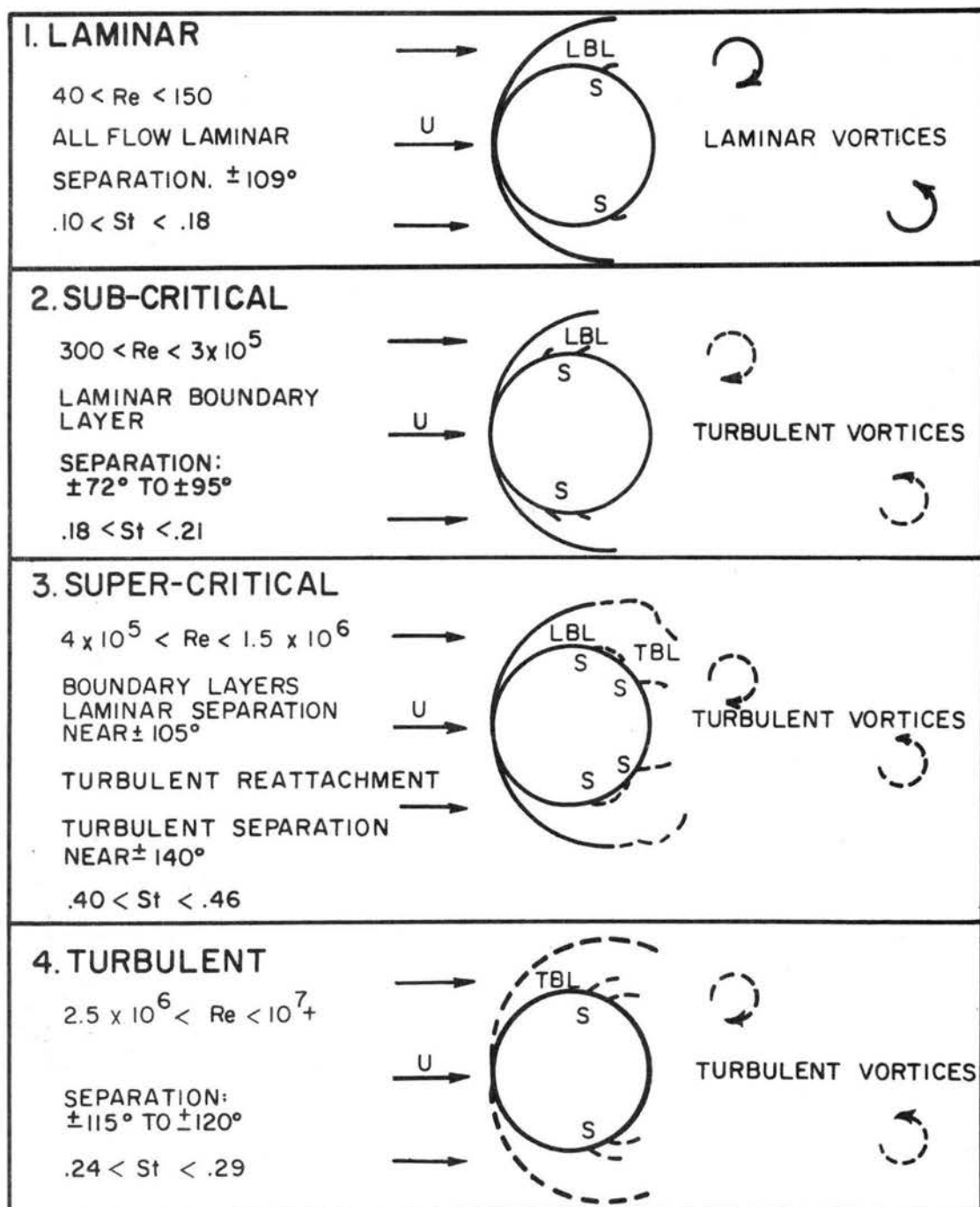


Figure 2. Characteristics of the four major vortex shedding regimes from a smooth cylinder in air flow with near zero turbulence intensity. Turbulent boundary layers and vortices are dashed. "S" means separation point; "LBL" means laminar boundary layer; "TBL" means turbulent boundary layer. Boundary layer depths are exaggerated.

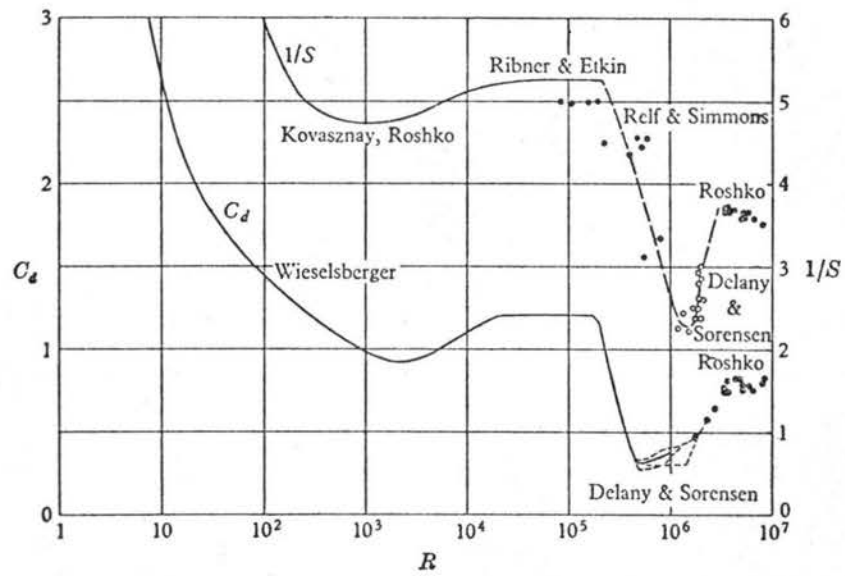


Figure 3. Variation of reciprocal of Strouhal number,  $1/S$ , and drag coefficient,  $C_d$ , both as functions of the Reynolds number,  $R$ . From Roshko (1961)

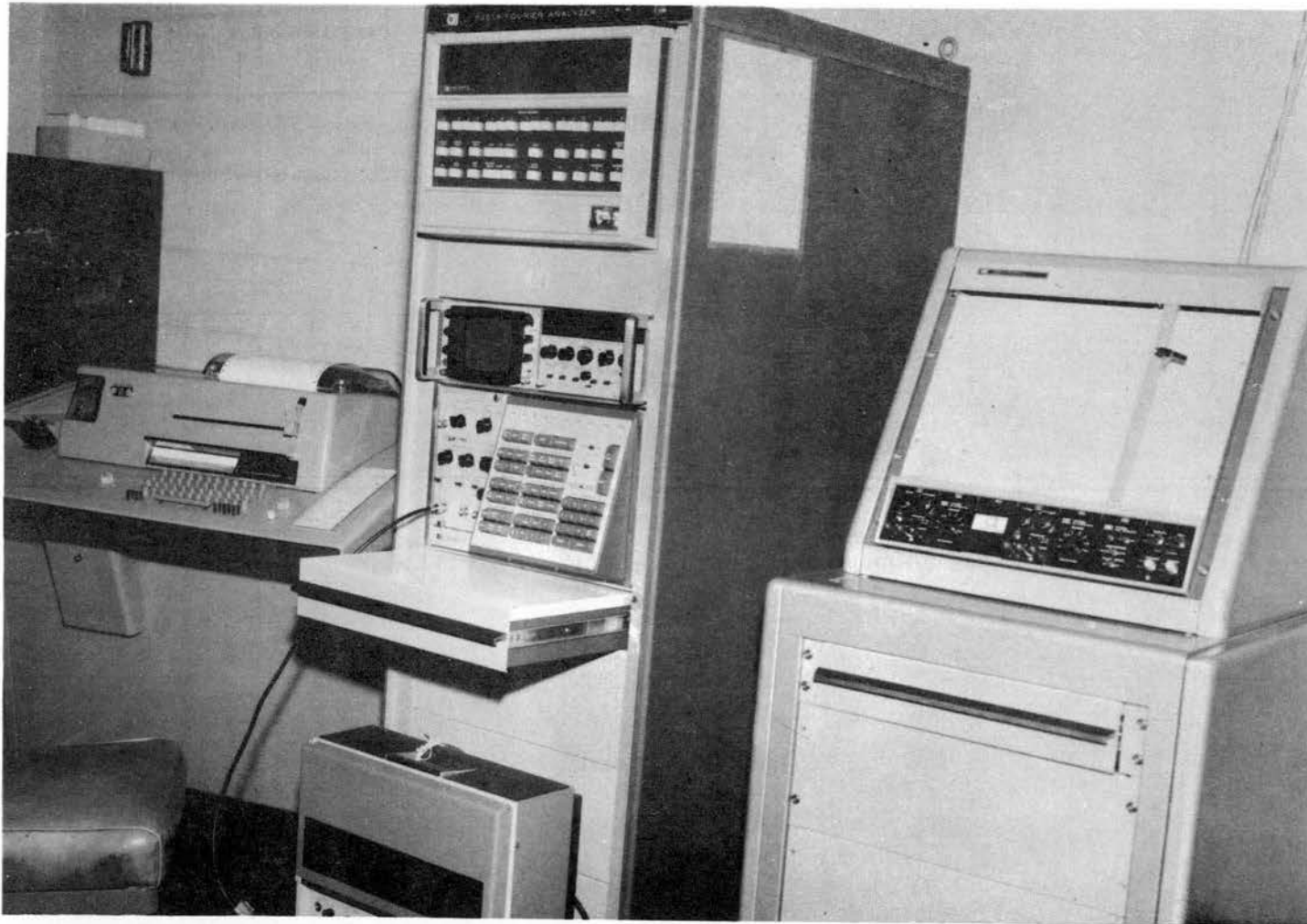


Figure 4. Photograph of Fourier Analyzer System utilized to analyze data. (US Army photograph)

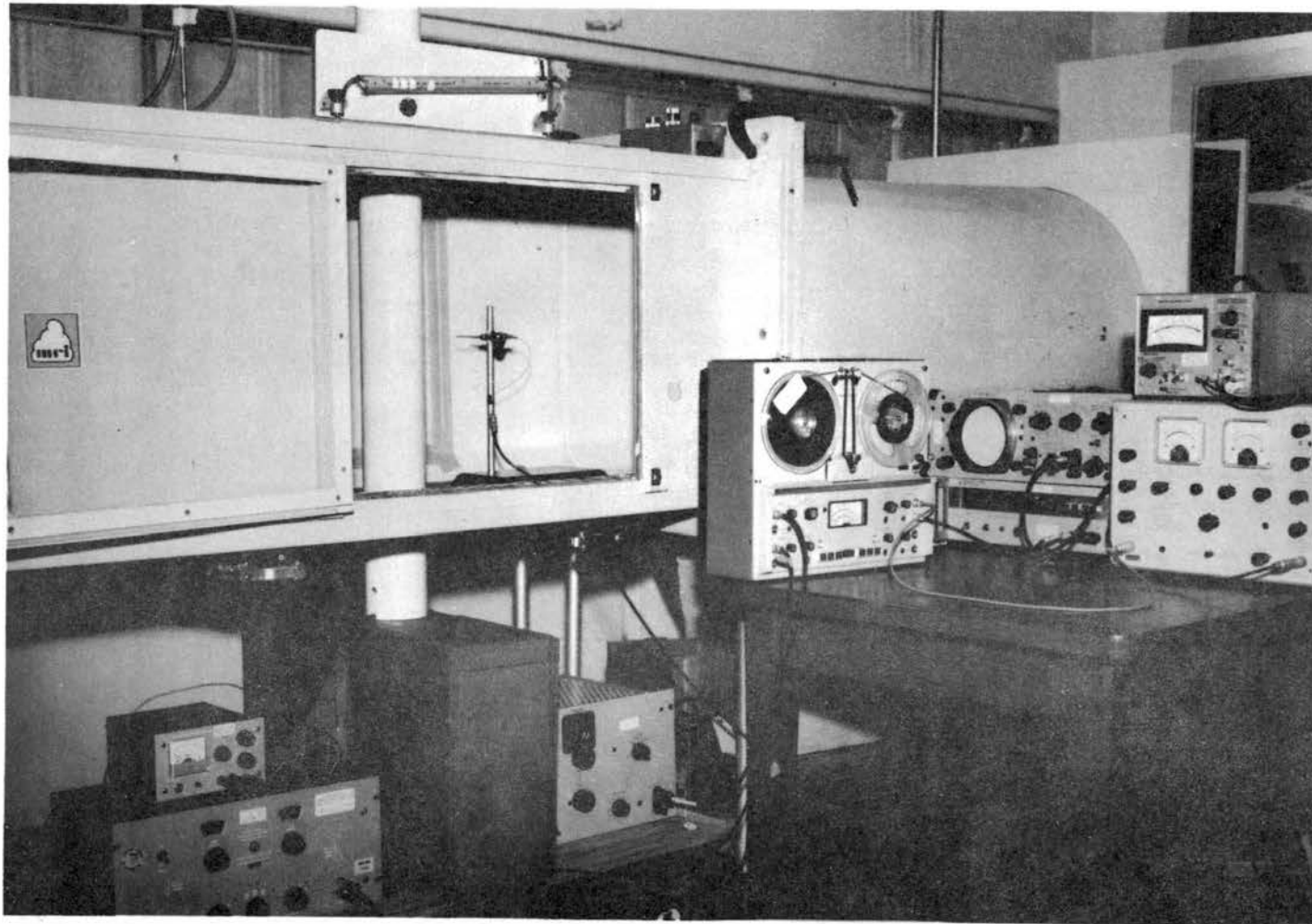


Figure 5. General view of wind tunnel and instrumentation used. The cylinder is in a vertical position with a hot wire sensor immediately downstream. (US Army photograph)

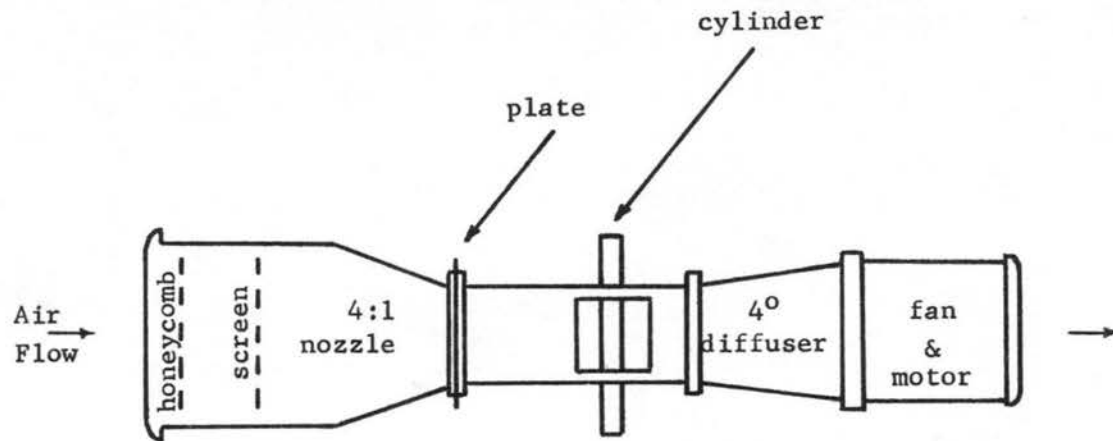


Figure 6. Diagram of Wind Tunnel used at White Sands.

Side view. Scale: 1" = 5'. Test section: 2' x 2' x 6'.  
 Over-all length 22'. Intake: 4' x 4'.

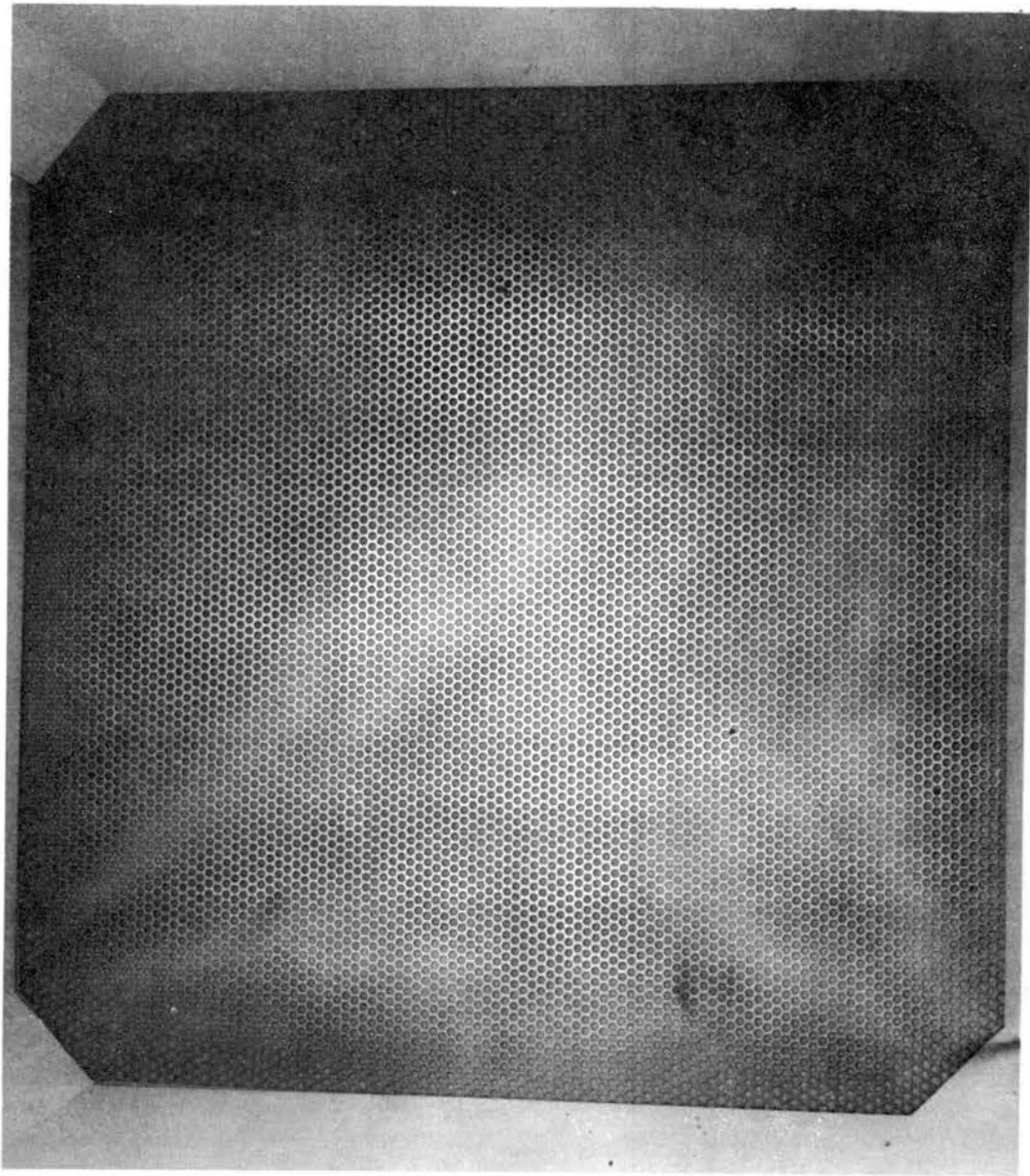


Figure 7. Picture of plate .500. Area covered is 24" x 24".  
3/16" diameter holes are in a commercially obtained  
metal sheet. (US Army photograph)

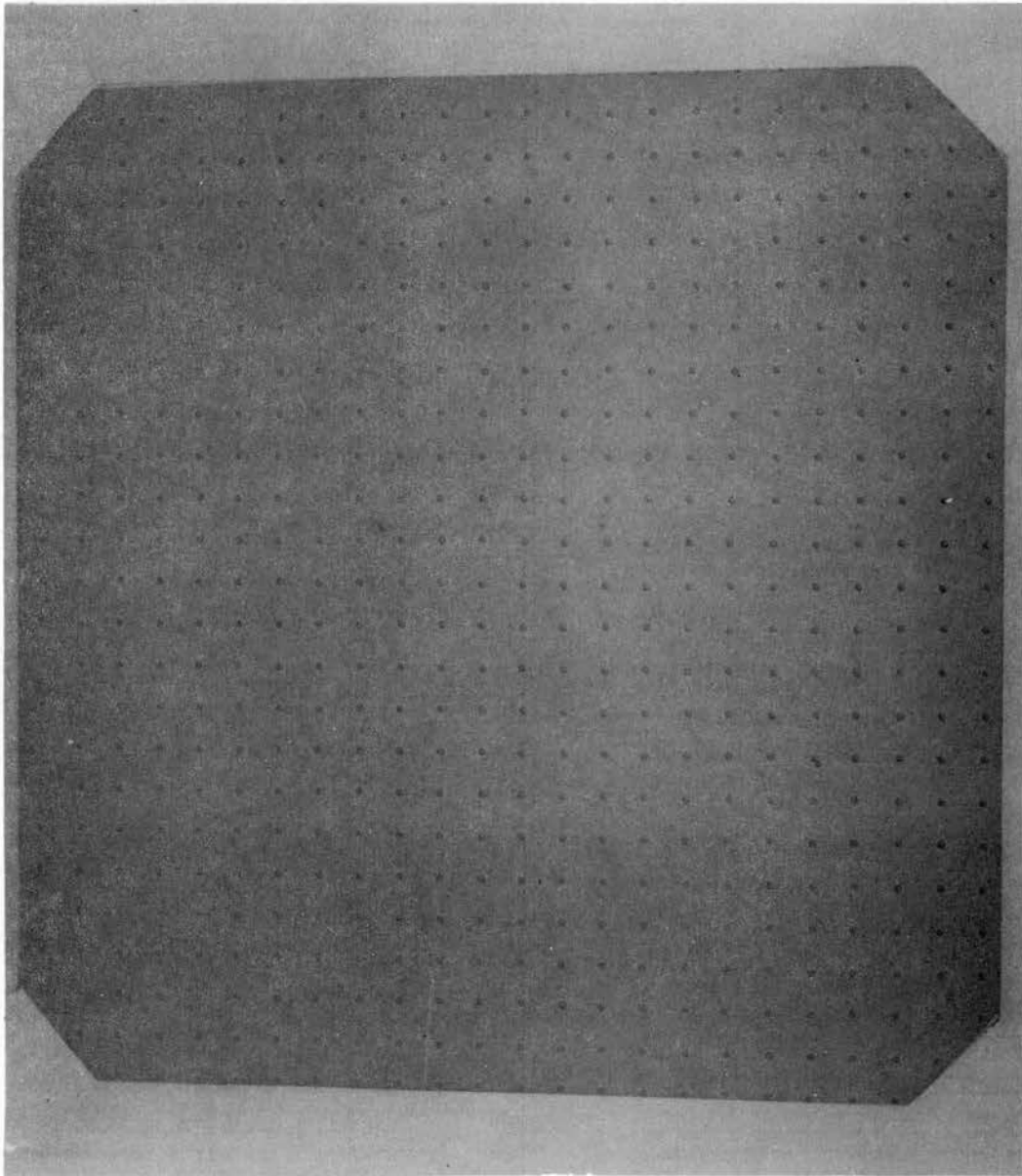


Figure 8. Photograph of plate .972. Area covered is 24" x 24".  
3/16" diameter holes are drilled through masonite.  
(US Army photograph)

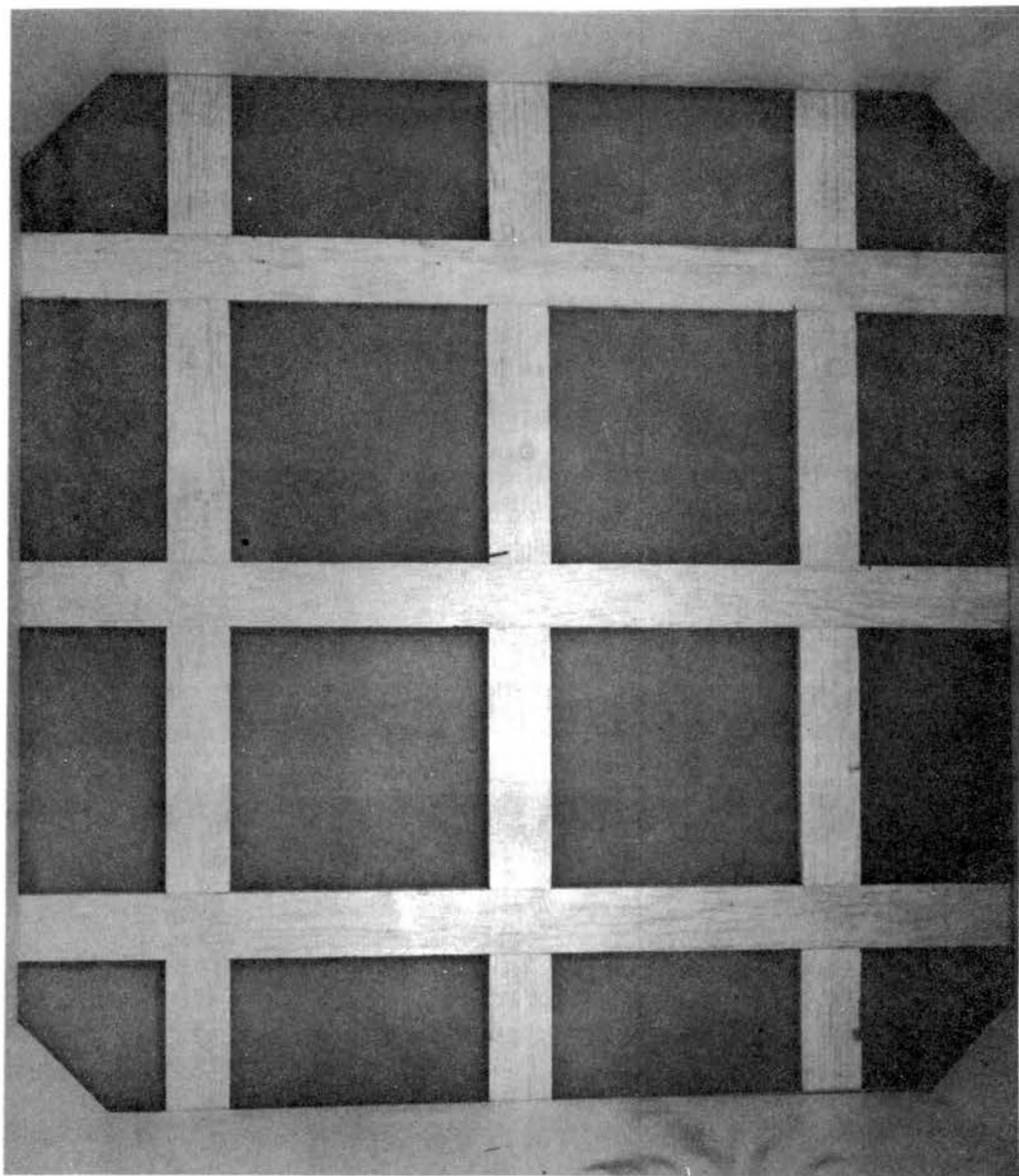


Figure 9. Picture of "Surry" grid, modeled after a larger size grid he used. Open spaces are  $6 \frac{1}{8}$ " x  $6 \frac{1}{8}$ ". Boards are 1.5" wide. Blocking ratio is .34. (US Army photograph)

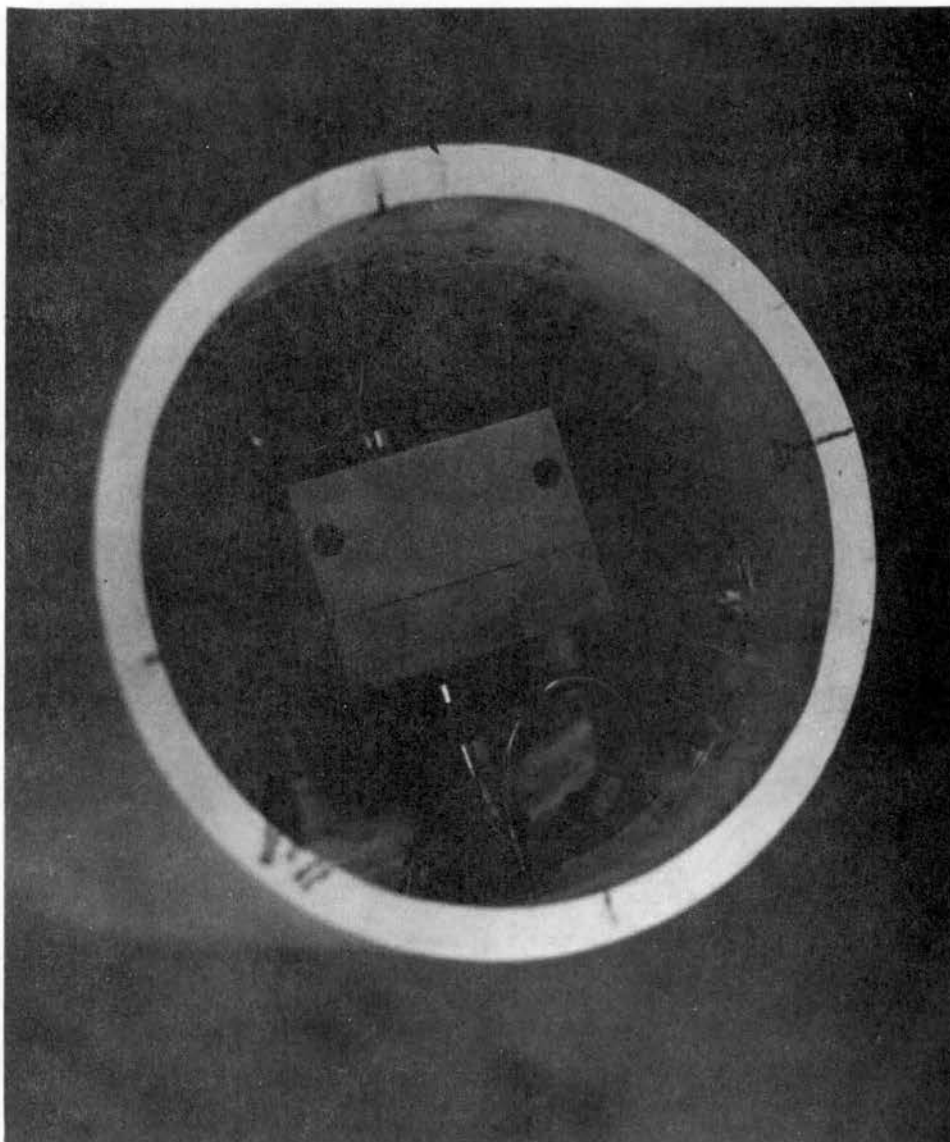


Figure 10. Pressure transducer inside 4.5" diameter cylinder. Plastic tubing can be changed to different pressure taps. (US Army photograph)

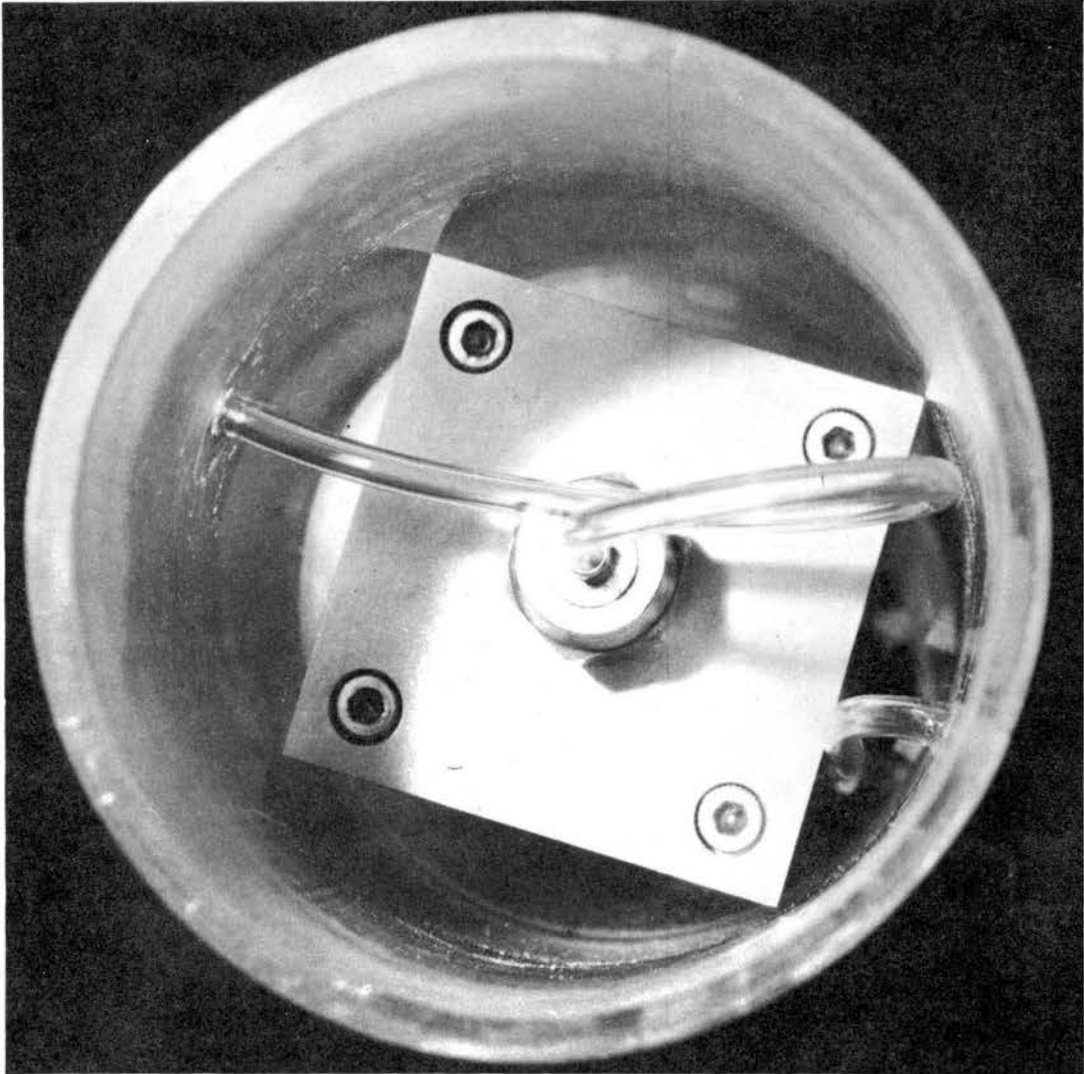


Figure 11. End view of 2.75" diameter cylinder showing pressure transducer with tubes at  $\pm 90^\circ$ .

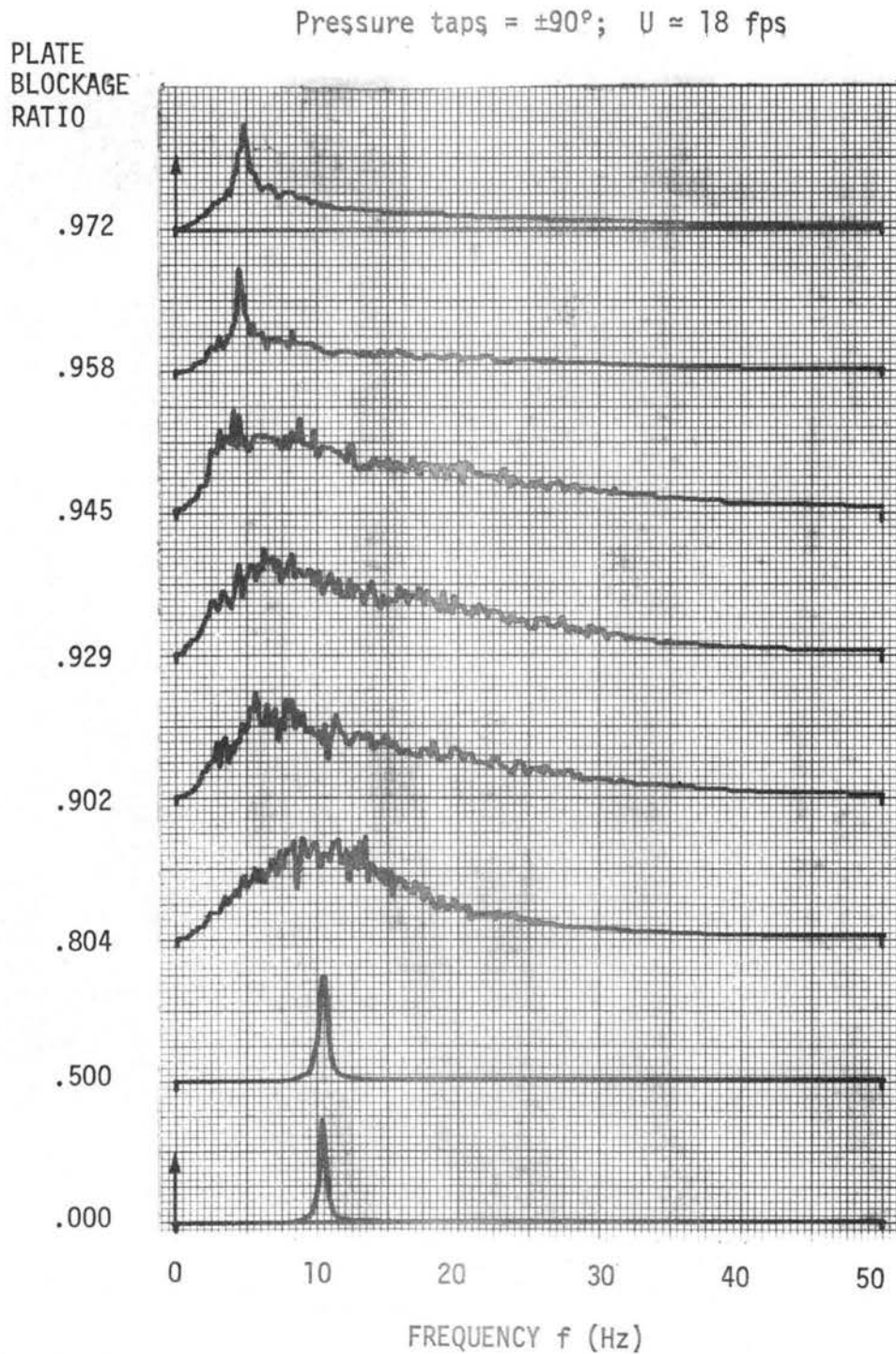


Figure 12. Power spectra of vortex shedding frequencies by pressure transducer. 4.5" diameter cylinder. Mean of 60 spectra.  $N = 512$ .

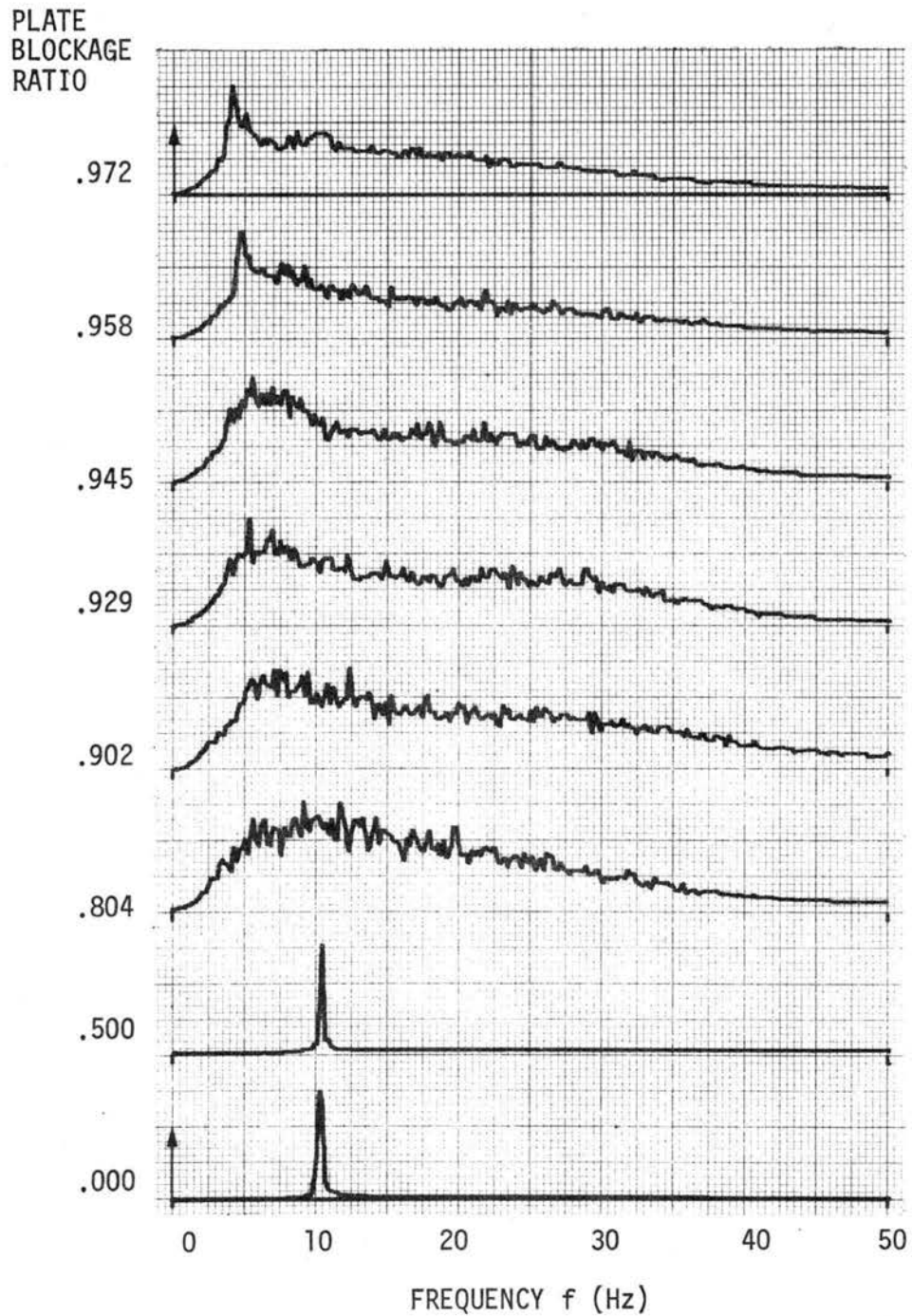
Pressure taps =  $\pm 130^\circ$ ;  $U \approx 18$  fps

Figure 13. Power spectra of vortex shedding frequencies by pressure transducer. 4.5" diameter cylinder. Mean of 60 spectra.  $N = 512$ .

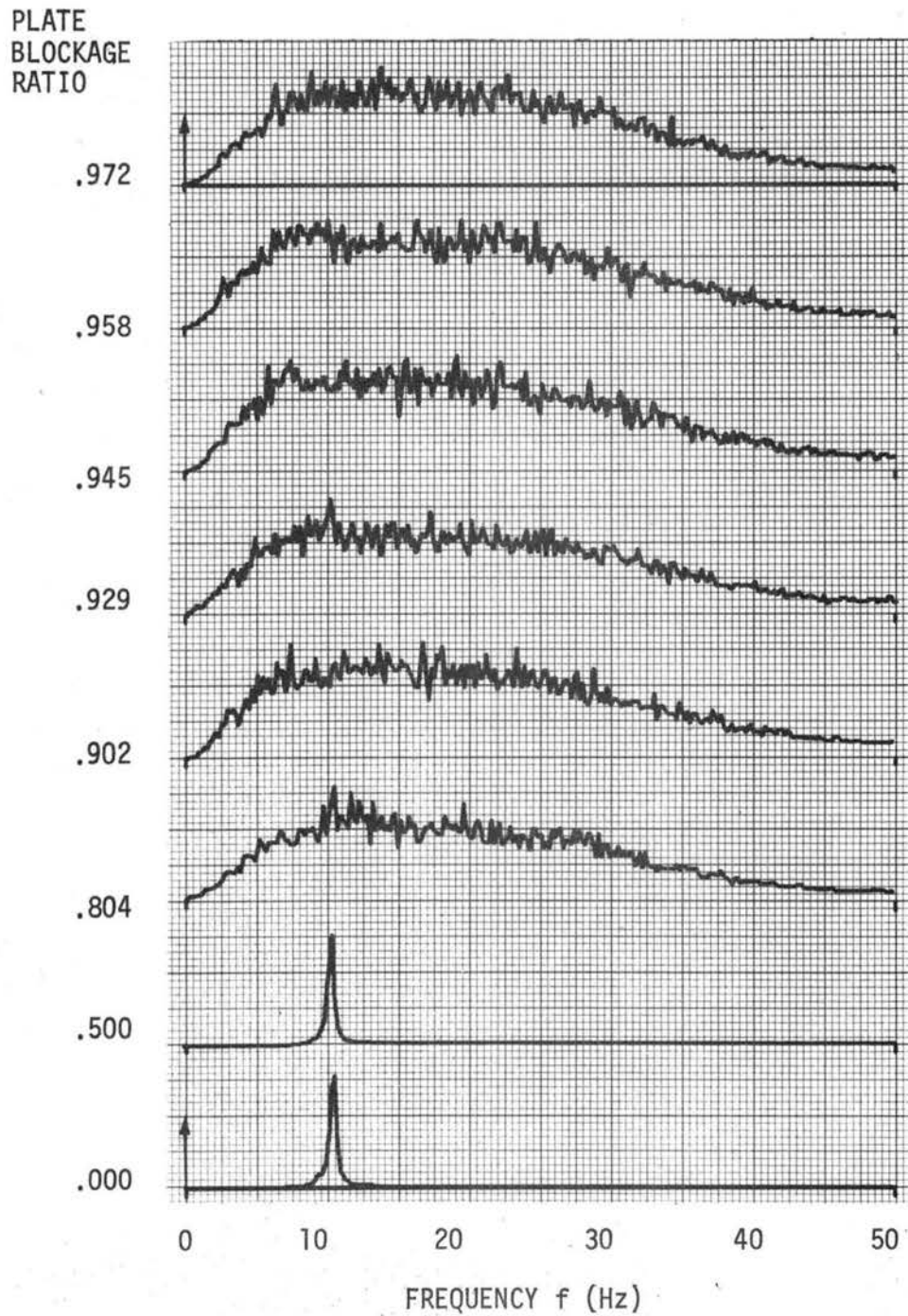
Pressure taps =  $\pm 150^\circ$ ;  $U \approx 18$  fps

Figure 14. Power spectra of vortex shedding frequencies by pressure transducer. 4.5" diameter cylinder. Mean of 60 spectra.  $N = 512$ .

4.5" cylinder

OPEN TUNNEL;  $U = 19.4$  fps

"A"

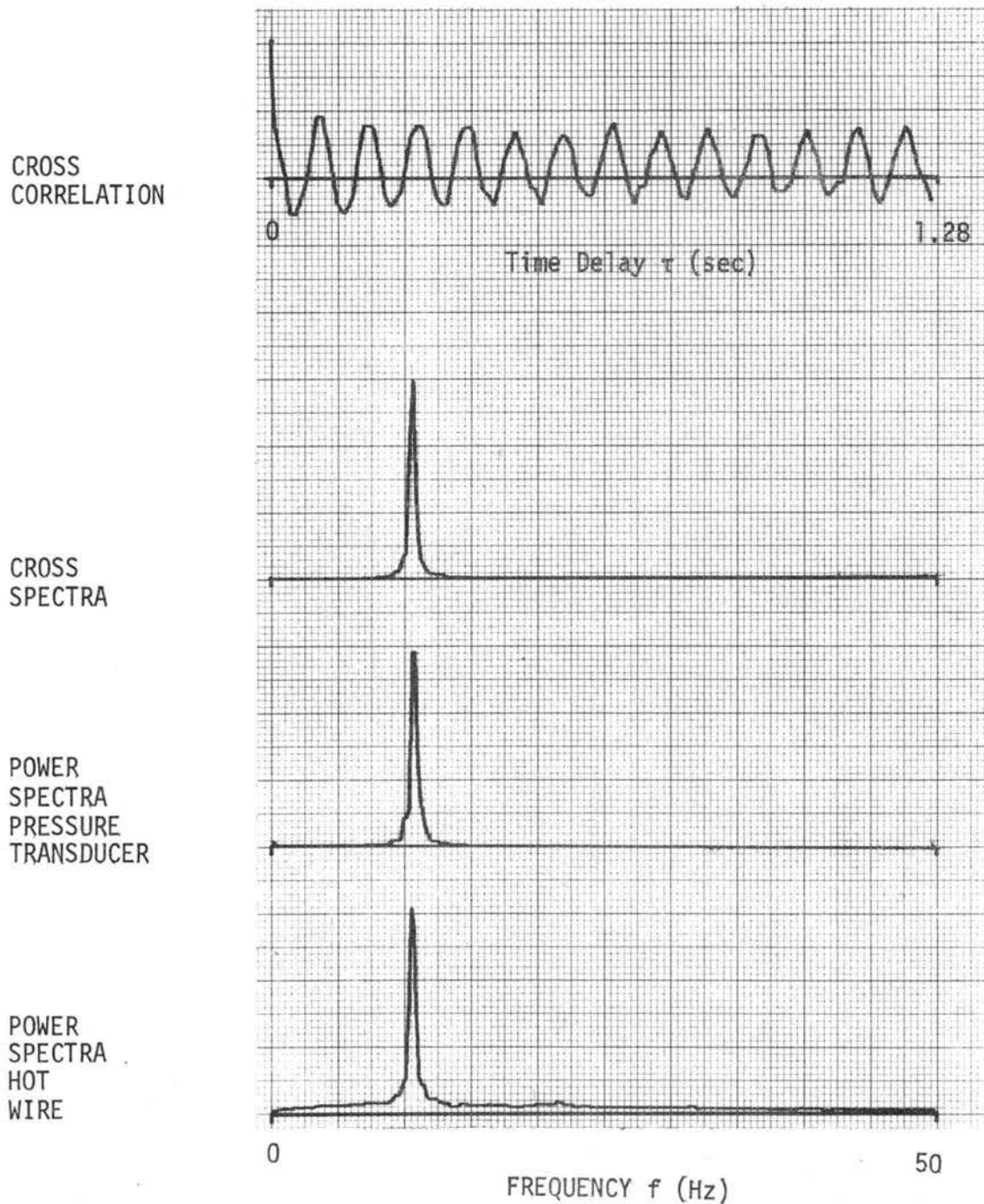
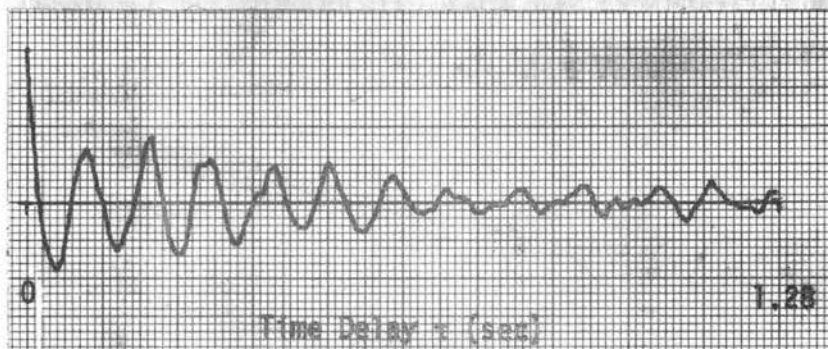
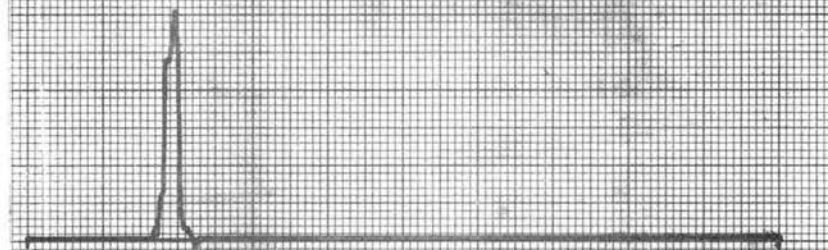
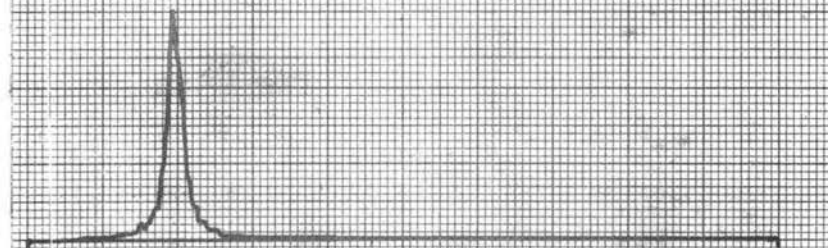
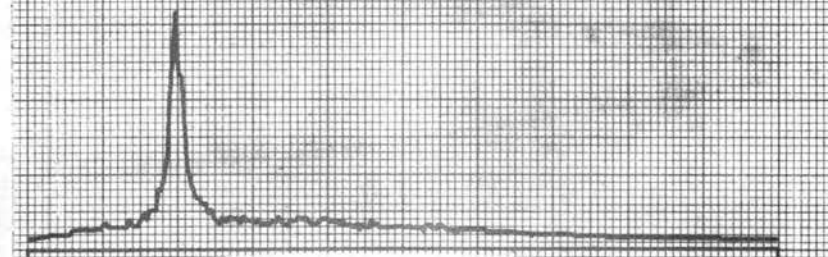


Figure 15. Frequency of vortex shedding observed simultaneously by hot wire and pressure transducer. Pressure taps  $\pm 130^\circ$ . Hot wire at  $x = 1.5D$ ;  $z = .5D$ .  $N = 512$ . Mean of 60 spectra or correlations.  $f = 10.6$ .  $St = .205$ .  $Re = 3.8 \times 10^4$ . Comparable to condition "A" in figure 1.  $\Delta f = .195$  Hz.

4.5" cylinder

PLATE .690;  $U = 17.4$  fps

"B"

CROSS  
CORRELATIONCROSS  
SPECTRAPOWER  
SPECTRA  
PRESSURE  
TRANSDUCERPOWER  
SPECTRA  
HOT  
WIRE

0

50

FREQUENCY  $f$  (Hz)

Figure 16. Frequency of vortex shedding observed simultaneously by hot wire and pressure transducer. Pressure taps  $\pm 90^\circ$ . Hot wire at  $x = 1.5D$ ;  $z = -.5D$ .  $N = 512$ . Mean of 60 spectra or correlations.  $f = 9.8$ .  $St = .211$   $Re = 3.4 \times 10^4$ . Comparable to condition "B" in figure 1.  $\Delta f = .195$  Hz.

2.75" cylinder

PLATE .748;  $U = 13.7$  fps

"B"

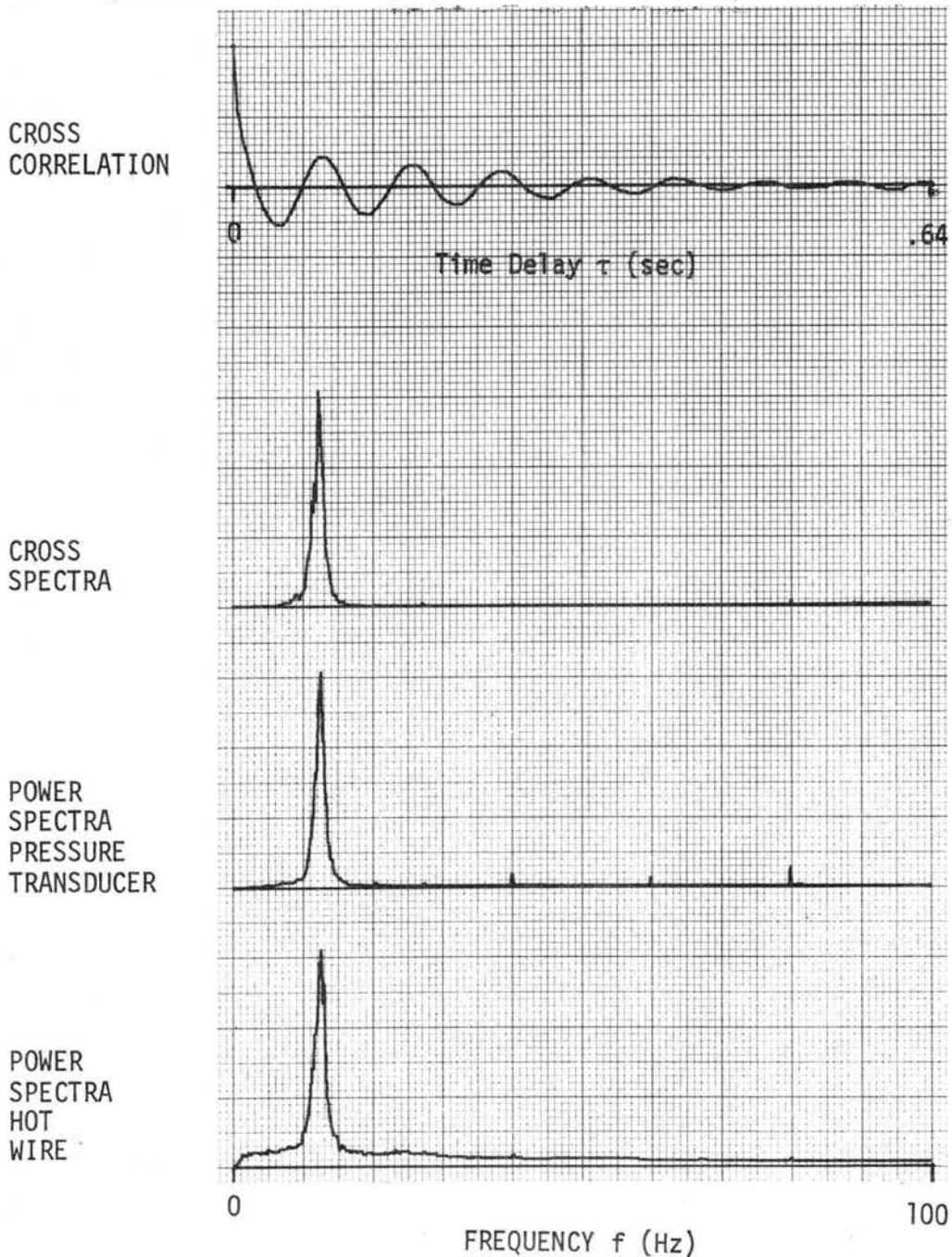


Figure 17. Frequency of vortex shedding observed simultaneously by hot wire and pressure transducer. Pressure taps  $\pm 130^\circ$ . Hot wire at  $x = 1.5D$ ;  $z = .5D$ .  $N = 512$ . Mean of 60 spectra or correlations.  $f = 12.3$ .  $St = .206$ .  $Re = 1.7 \times 10^4$ . Comparable to condition "B" in figure 1.  $\Delta f = .195$  Hz.

4.5" cylinder

PLATE .748;  $U = 16.9$  fps

"C"

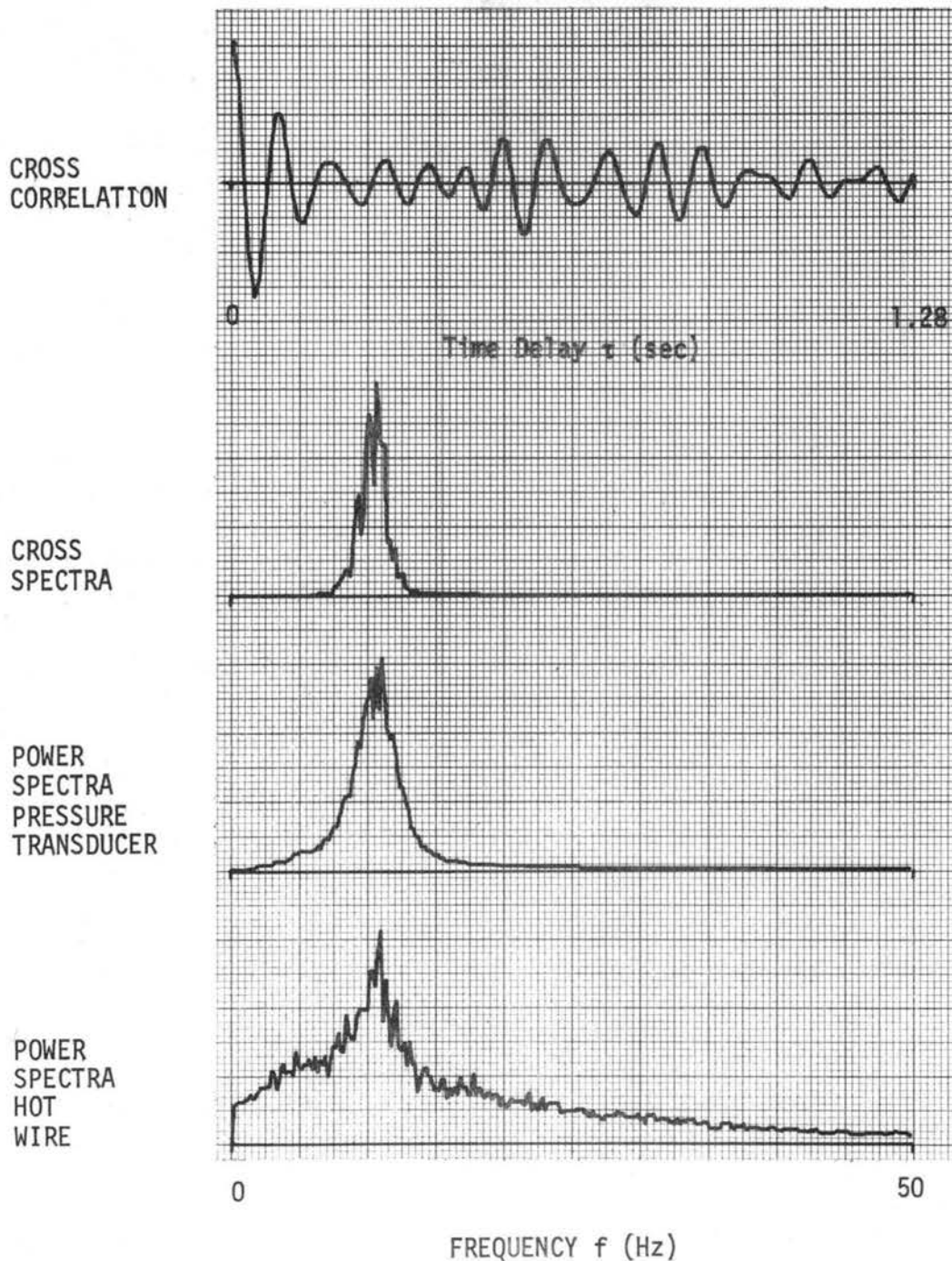


Figure 18. Frequency of vortex shedding observed simultaneously by hot wire and pressure transducer. Pressure taps  $\pm 90^\circ$ . Hot wire at  $x = 1.5D$ ;  $z = .5D$ .  $N = 512$ . Mean of 60 spectra or correlations.  $f = 11.2$ .  $St = .249$ .  $Re = 3.3 \times 10^4$ . Comparable to condition "C" in figure 1.  $\Delta f = .195$  Hz.

2.75" cylinder

PLATE 801;  $U = 16.4$  fps

"C"

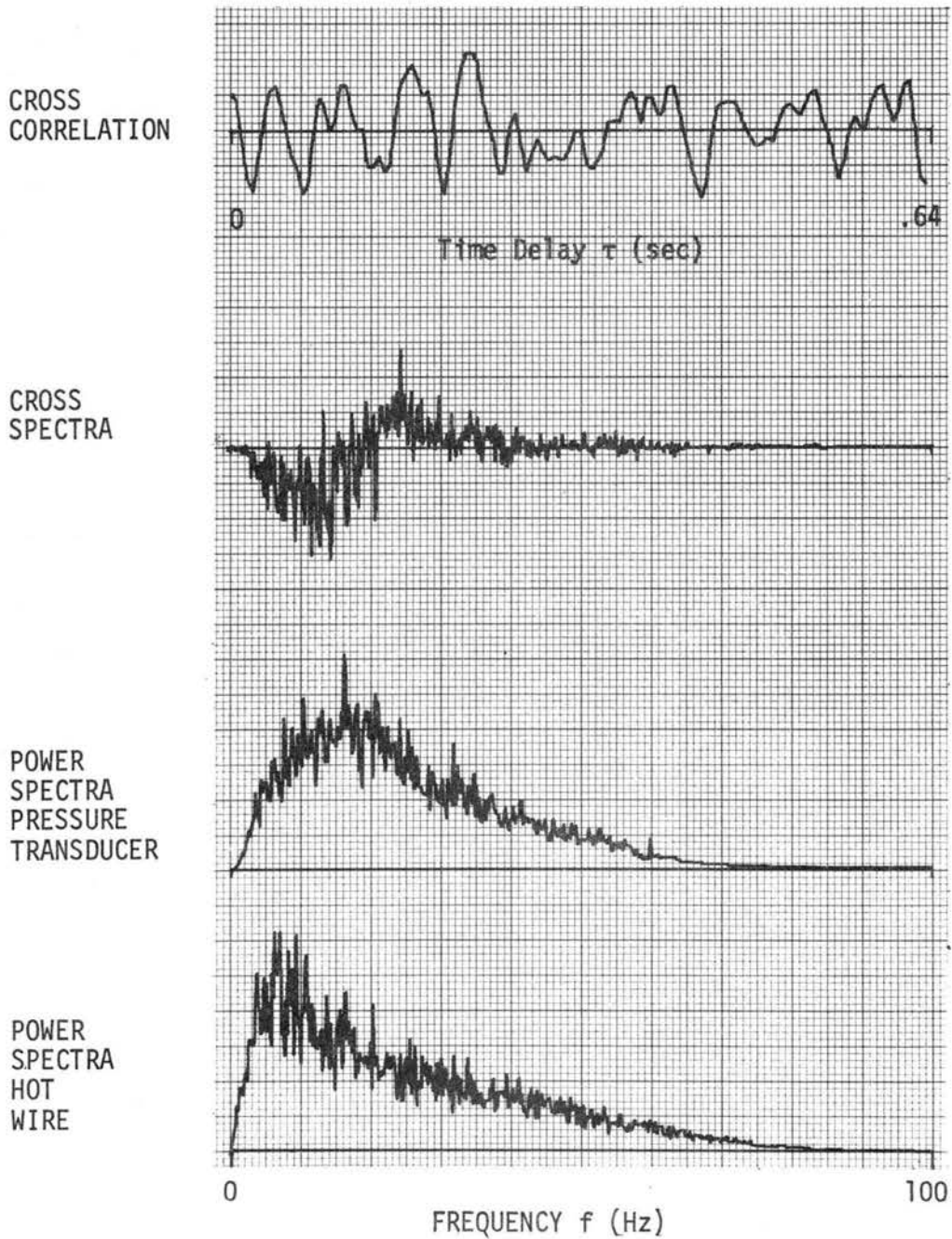


Figure 19. Frequency of vortex shedding observed simultaneously by hot wire and pressure transducer. Pressure taps  $\pm 150^\circ$ . Hot wire at  $x = 2.0D$ ;  $z = .3D$ .  $N = 1024$ . Mean of 60 spectra or correlations.  $f =$  undefined.  $St =$  undefined.  $Re = 2.0 \times 10^4$ . Comparable to condition "C" in figure 1.  $\Delta f = .195$  Hz.

4.5" cylinder

PLATE .804;  $U = 8.1$  fps

"D"

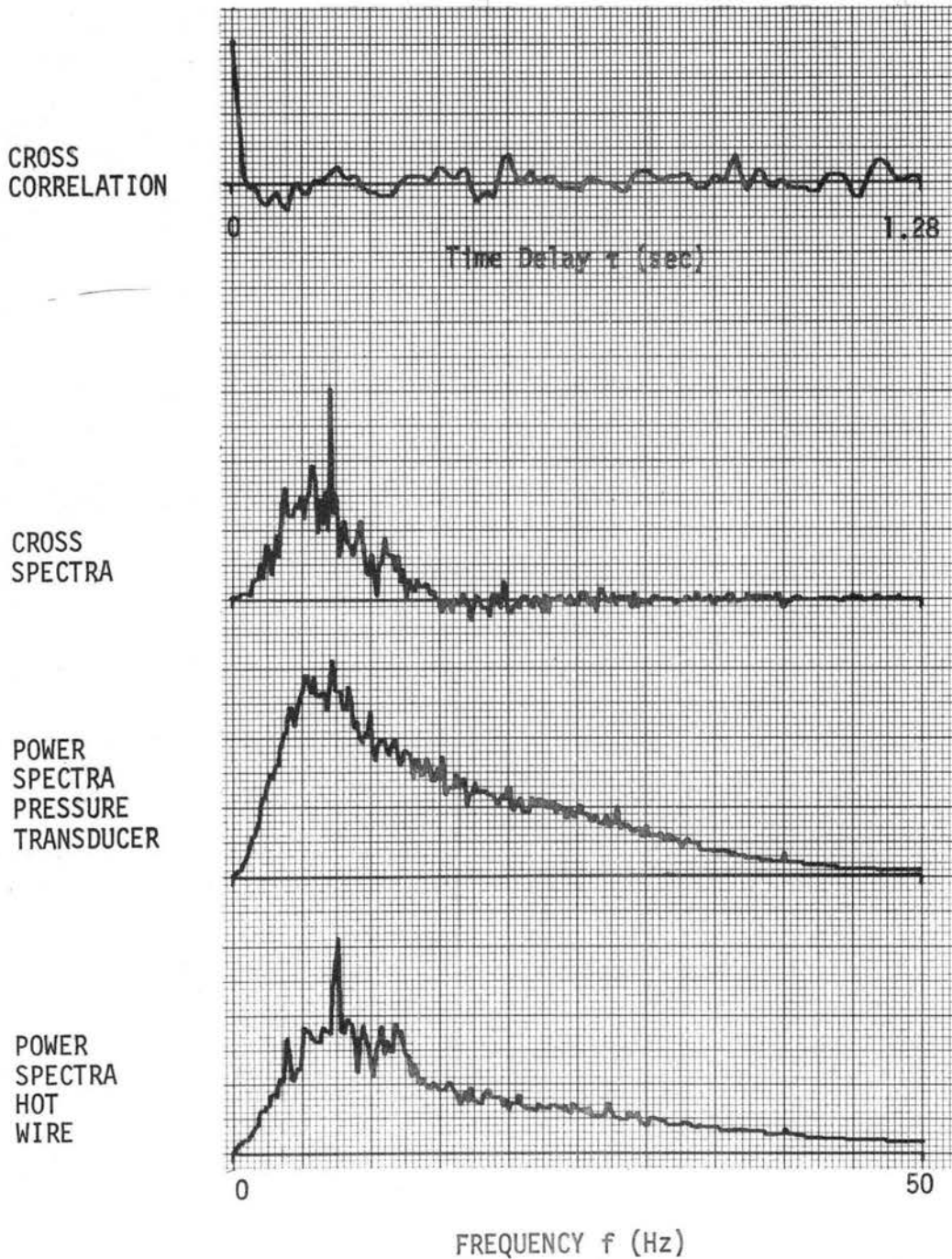


Figure 20. Frequency of vortex shedding observed simultaneously by hot wire and pressure transducer. Pressure taps  $\pm 150^\circ$ . Hot wire at  $x = 1.5D$ ;  $z = .5D$ .  $N = 512$ . Mean of 120 spectra or correlations.  $f = 7.1$ .  $St = .329$ .  $Re = 1.6 \times 10^4$ . Comparable to condition "D" in figure 1.  $\Delta f = .195$  Hz.

2.75" cylinder

PLATE .861;  $U = 7.1$  fps

"D"

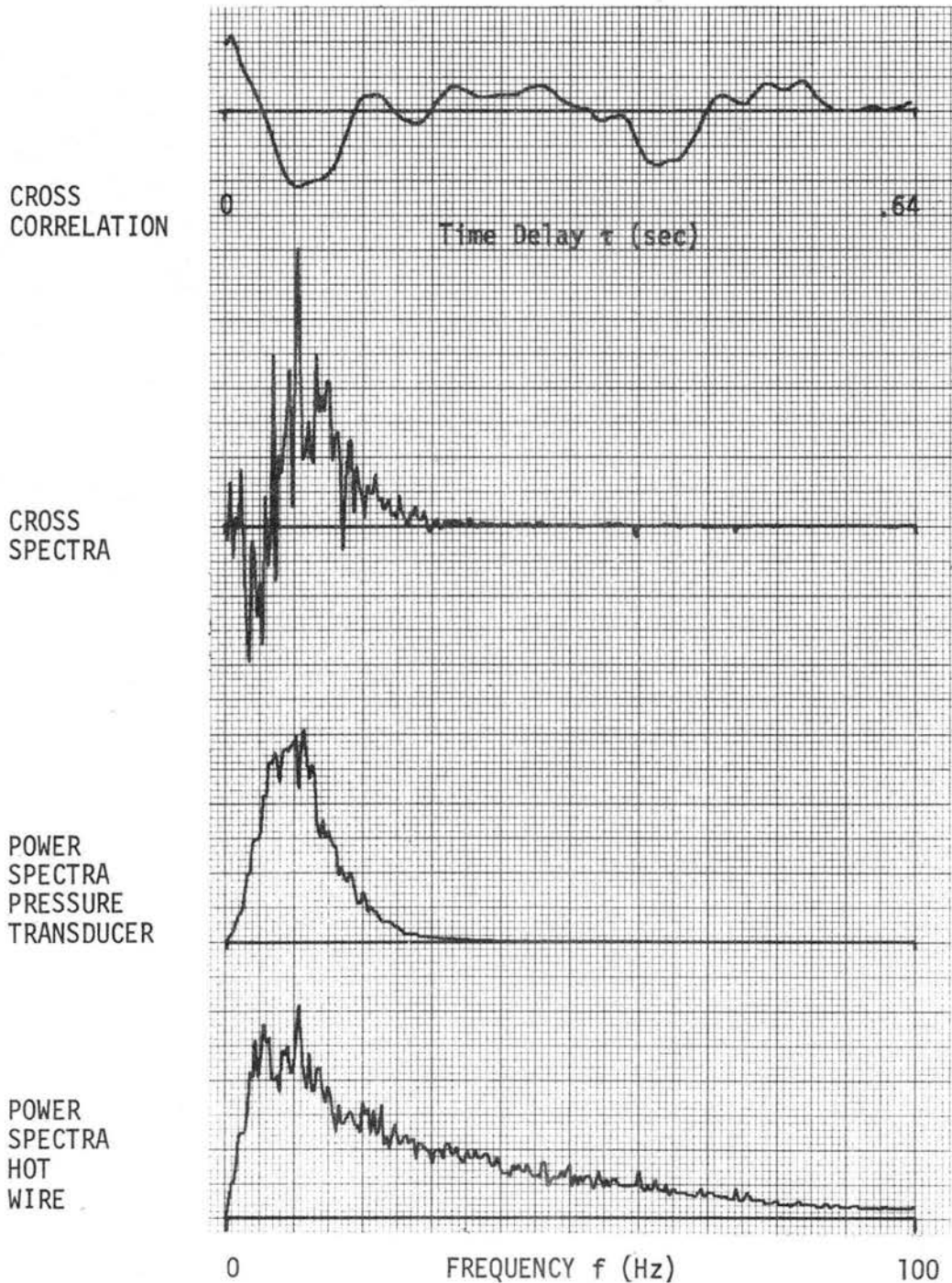


Figure 21. Frequency of vortex shedding observed simultaneously by hot wire and pressure transducer. Pressure taps  $\pm 150^\circ$ . Hot wire at  $x = 2.5D$ ;  $z = .4D$ .  $N = 512$ . Mean of 100 spectra or correlations.  $f = 10.5$  Hz.  $St = .339$ .  $Re = 8.6 \times 10^3$ . Comparable to condition "D" in figure 1.  $\Delta f = .391$  Hz.

4.5" cylinder

PLATE .945;  $U = 18.7$  fps

"E"

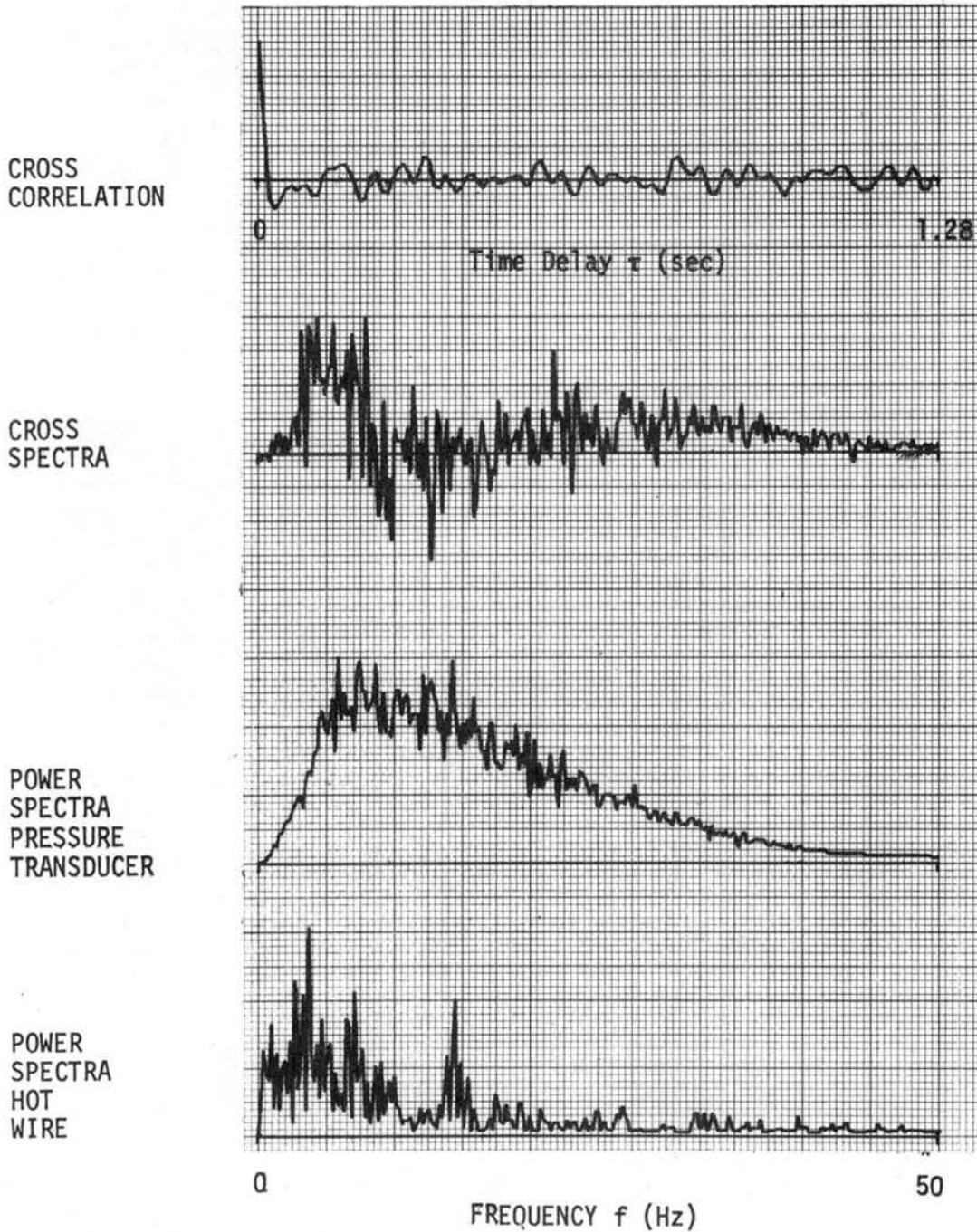


Figure 22. Frequency of vortex shedding observed simultaneously by hot wire and pressure transducer. Pressure taps  $\pm 90^\circ$ . Hot wire at  $x = .25D$ ;  $z = .5D$ .  $N = 512$ . Mean of 60 spectra or correlations.  $f =$  undefined.  $St =$  undefined.  $Re = 3.7 \times 10^4$ . Comparable to condition "E" in figure 1.  $\Delta f = .195$  Hz.

2.75" cylinder

PLATE .945;  $U = 20.9$  fps

"E"

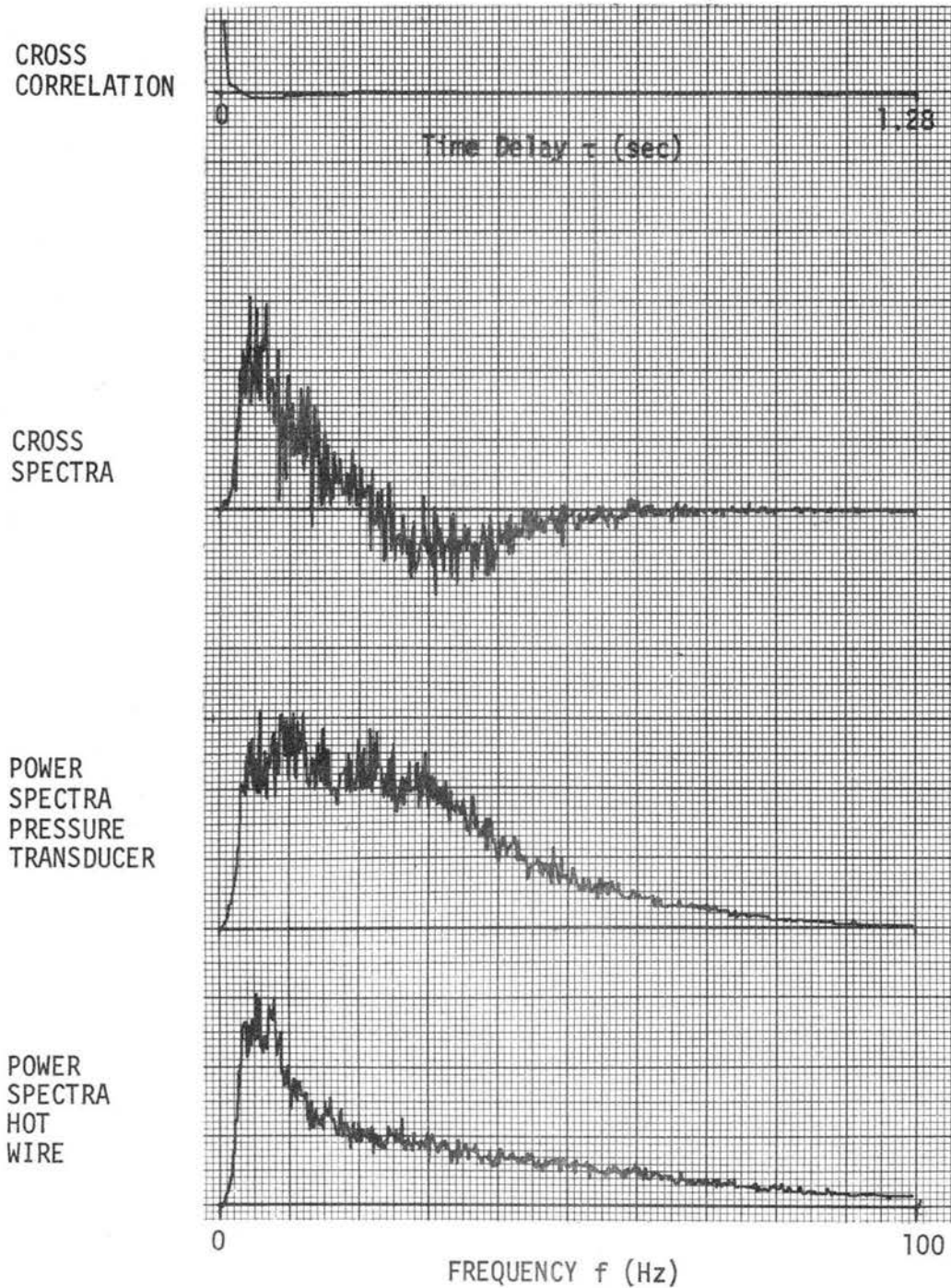


Figure 23, Frequency of vortex shedding observed simultaneously by hot wire and pressure transducer. Pressure taps  $\pm 90^\circ$ . Hot wire at  $x = 1.5D$ ;  $z = .5D$ .  $N = 1024$ . Mean of 75 spectra or correlations.  $f =$  undefined.  $St =$  undefined.  $Re = 2.5 \times 10^4$ . Comparable to condition "E" in figure 1.  $\Delta f = .195$  Hz.

4.5" cylinder

PLATE .972;  $U = 23.2$  fps

"F"

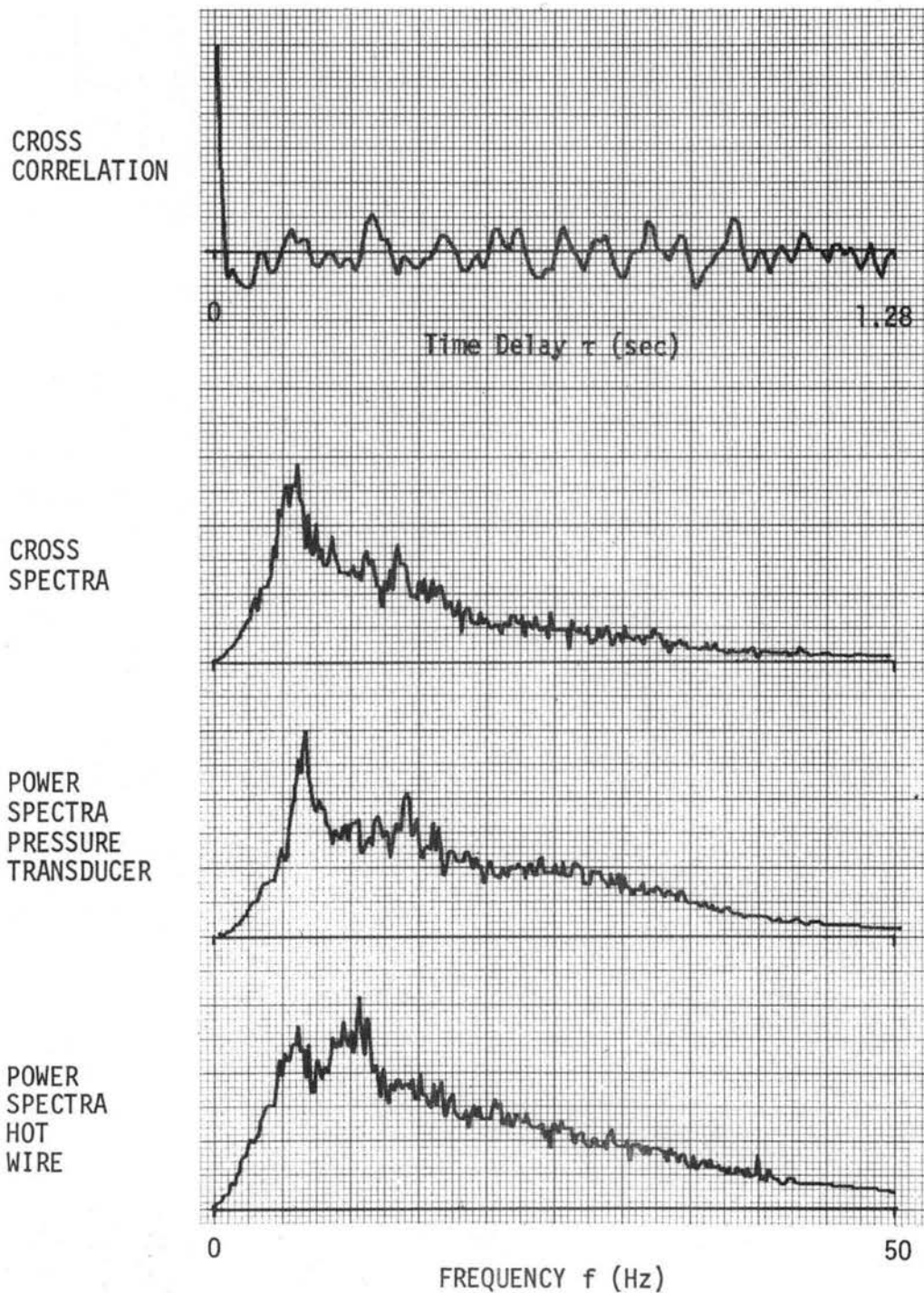


Figure 24. Frequency of vortex shedding observed simultaneously by hot wire and pressure transducer. Pressure taps  $\pm 130^\circ$ . Hot wire at  $x = 1.05D$ ;  $z = .5D$ .  $N = 512$ . Mean of 120 spectra or correlations.  $f = 6.2$ .  $St = .100$ ,  $Re = 4.6 \times 10^4$ . Comparable to condition "F" in figure 1.  $\Delta f = .195$  Hz.

4.5" cylinder

PLATE .972;  $U = 16.1$  fps

"F"

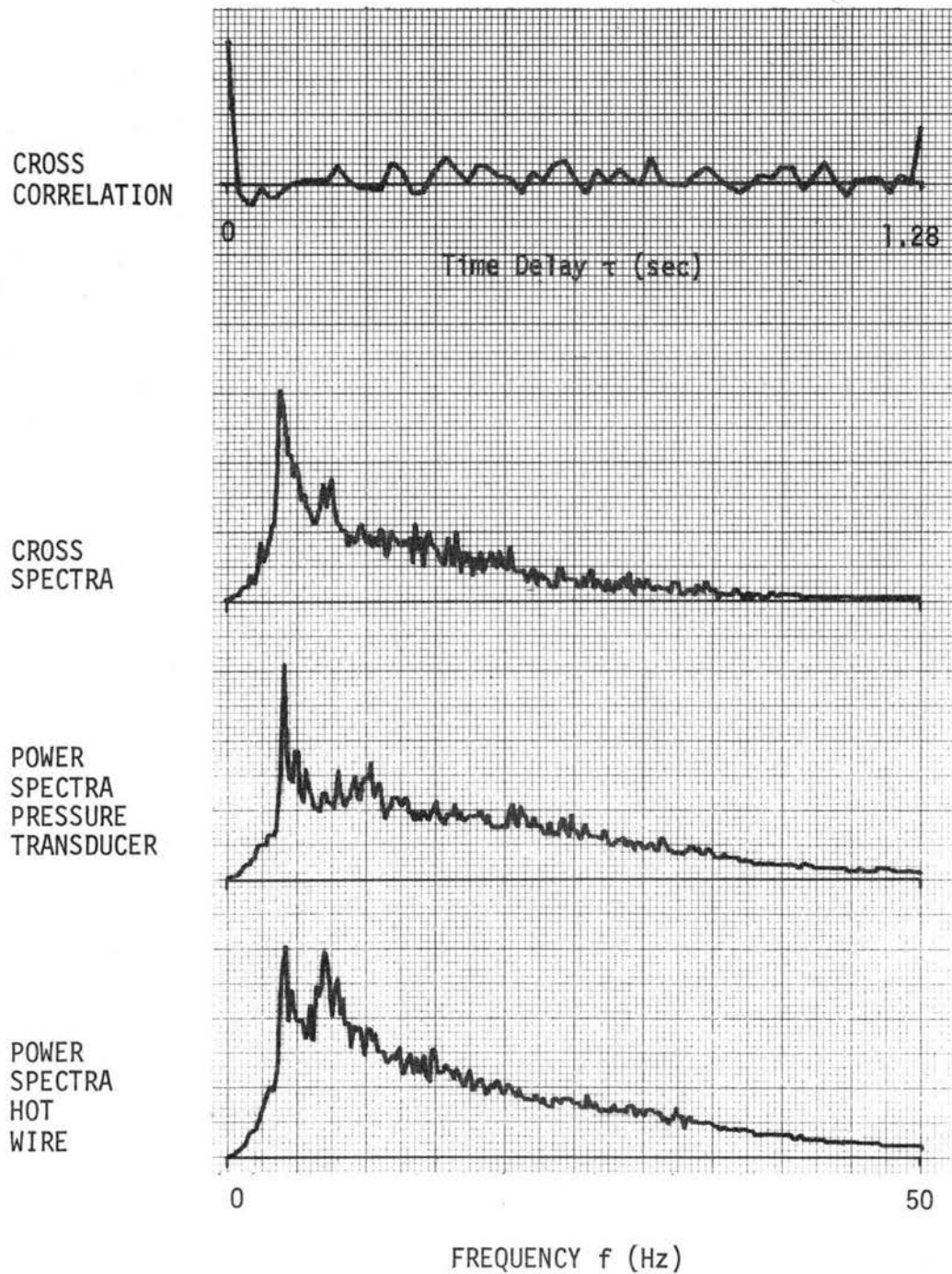


Figure 25. Frequency of vortex shedding observed simultaneously by hot wire and pressure transducer. Pressure taps  $\pm 130^\circ$ . Hot wire at  $.25D$  down from  $130^\circ$  tap.  $N = 512$ . Mean of 120 spectra or correlations.  $f = 4.0$ .  $St = .093$ .  $Re = 3.2 \times 10^4$ . Comparable to condition "F" in figure 1. Note best defined cross spectra.

4.5" cylinder

PLATE .972;  $u = 15.3$  fps

"F"

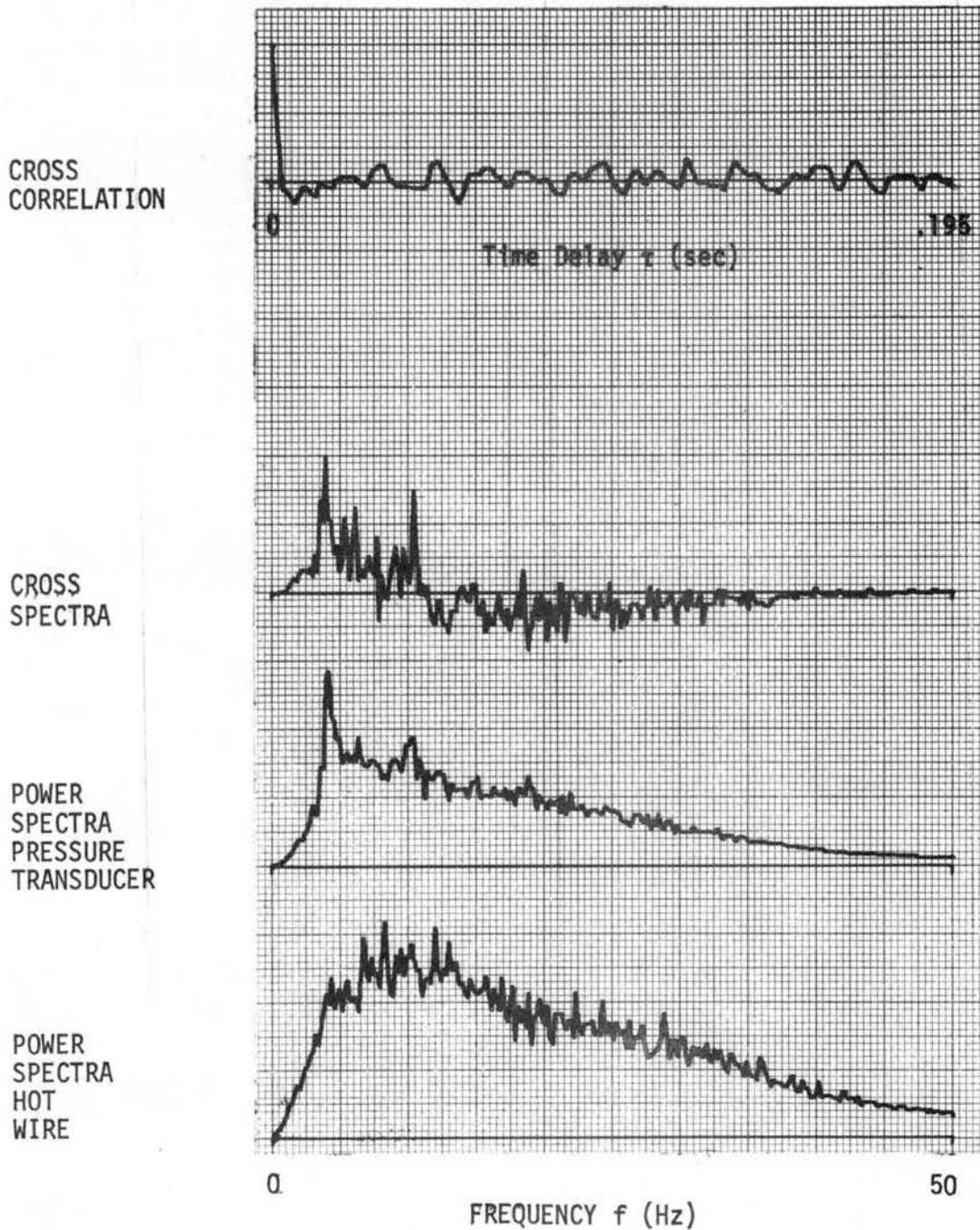


Figure 26. Frequency of vortex shedding observed simultaneously by hot wire and pressure transducer. Pressure taps  $\pm 130^\circ$ . Hot wire at  $x = 1.5D$ ,  $z = .5D$ .  $N = 512$ . Mean of 120 spectra or correlations.  $f = 3.9$ .  $St = .096$ .  $Re = 3.0 \times 10^4$ . Comparable to condition "F" in figure 1. Note poorly defined cross spectra.

2.75 "cylinder

PLATE .972;  $U = 23.3$  fps

"F"

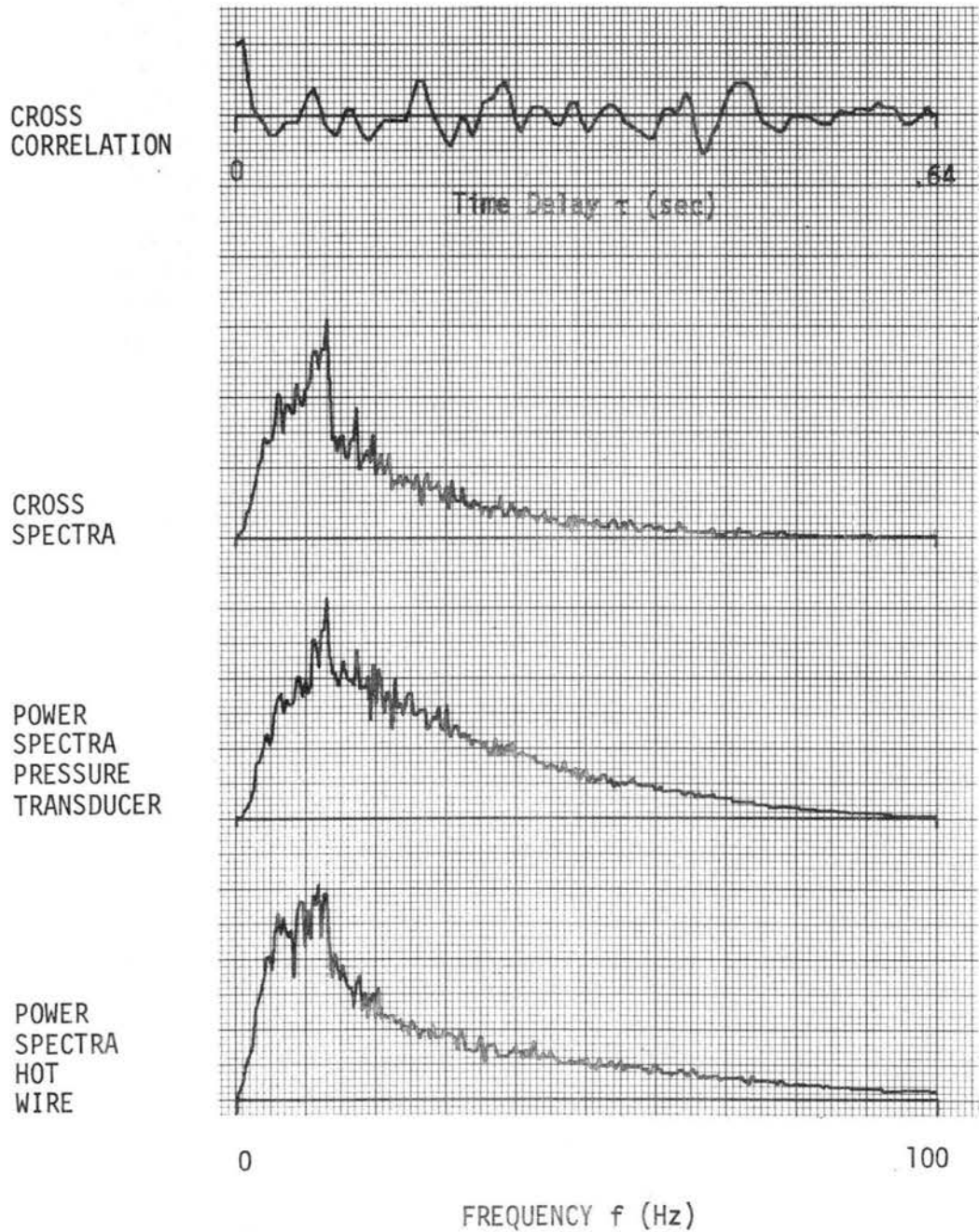


Figure 27. Frequency of vortex shedding observed simultaneously by hot wire and pressure transducer. Pressure taps  $\pm 90^\circ$ . Hot wire at  $x = .36D$ ,  $z = .5D$ .  $N = 512$ . Mean of 120 spectra or correlations.  $f = 13$ .  $St = .128$   $Re = 2.8 \times 10^4$ . Comparable to condition "F" in figure 1.  $\Delta f = .391$  Hz.

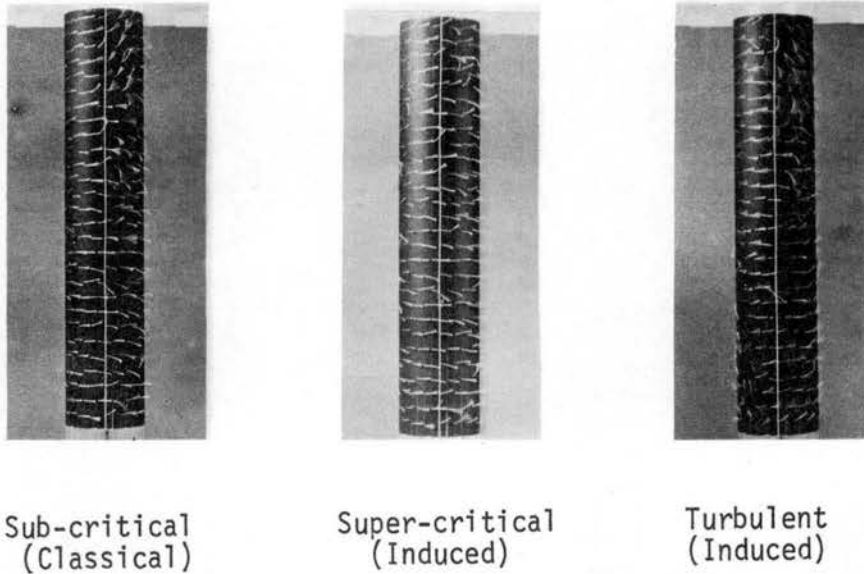


Figure 28. Flow Visualization of Boundary Layer and Separation Conditions.

The above three photographs show flow visualization by the motion of silk threads on a 2.75" diameter cylinder. They cover (longitudinally on the cylinder) the middle 14" of the cylinder in a 24" x 24" wind tunnel. The air motion is from left to right and the vertical white line is at 90° from the front stagnation point.

The sub-critical case is in an open tunnel,  $U = 28$  fps,  $Re = 4 \times 10^4$ ,  $Re(E) = 4 \times 10^4$ , and  $Ti = .3\%$ . A laminar boundary layer is apparent upstream from 90° and some indications of separation immediately downstream.

The induced super-critical case is behind plate .861,  $U = 6.5$  fps,  $Re = 8.8 \times 10^3$ ,  $Re(E) \approx 1 \times 10^6$ , and  $Ti \approx 8\%$ . There is little indication of separation. This is probably due to the low air speed. Ideally separation and quick re-attachment should be indicated near 120° along with final separation behind 140°.

The induced turbulent case is behind plate .972,  $U = 16$  fps,  $Re \approx 2.2 \times 10^4$ ,  $Re(E) \approx 3 \times 10^6$ , and  $Ti \approx 23\%$ . Turbulence is indicated in the boundary layer upstream and turbulent separation at about 110°. (Note the much greater turbulence than in the sub-critical case which has much higher air speed.)

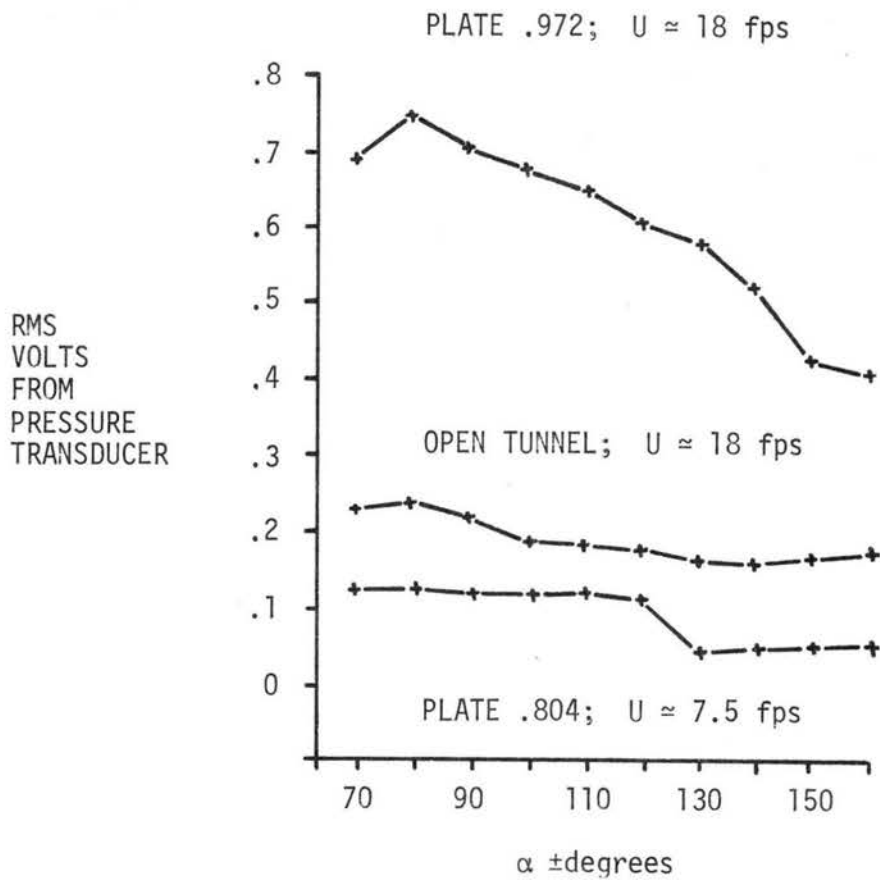


Figure 29. Variation of RMS voltage from pressure transducer as angle  $\alpha$  of pressure taps is changed. 4.5" cylinder.

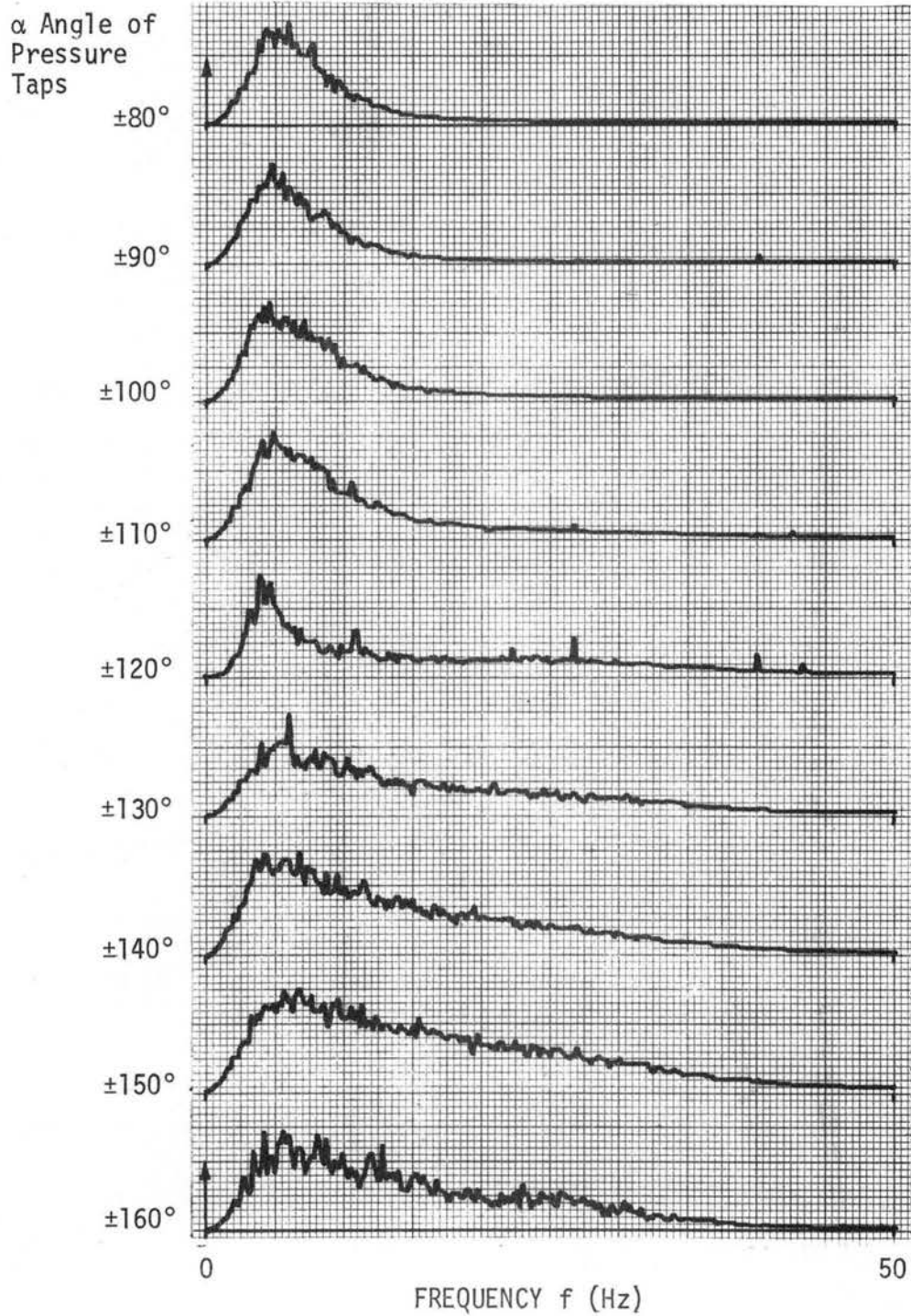
PLATE .804;  $U \approx 8$  fps

Figure 30. Change of spectra with  $\alpha$  angle of pressure taps. 4.5" cylinder. Mean of 60 spectra.  $\Delta f = .195$  Hz.

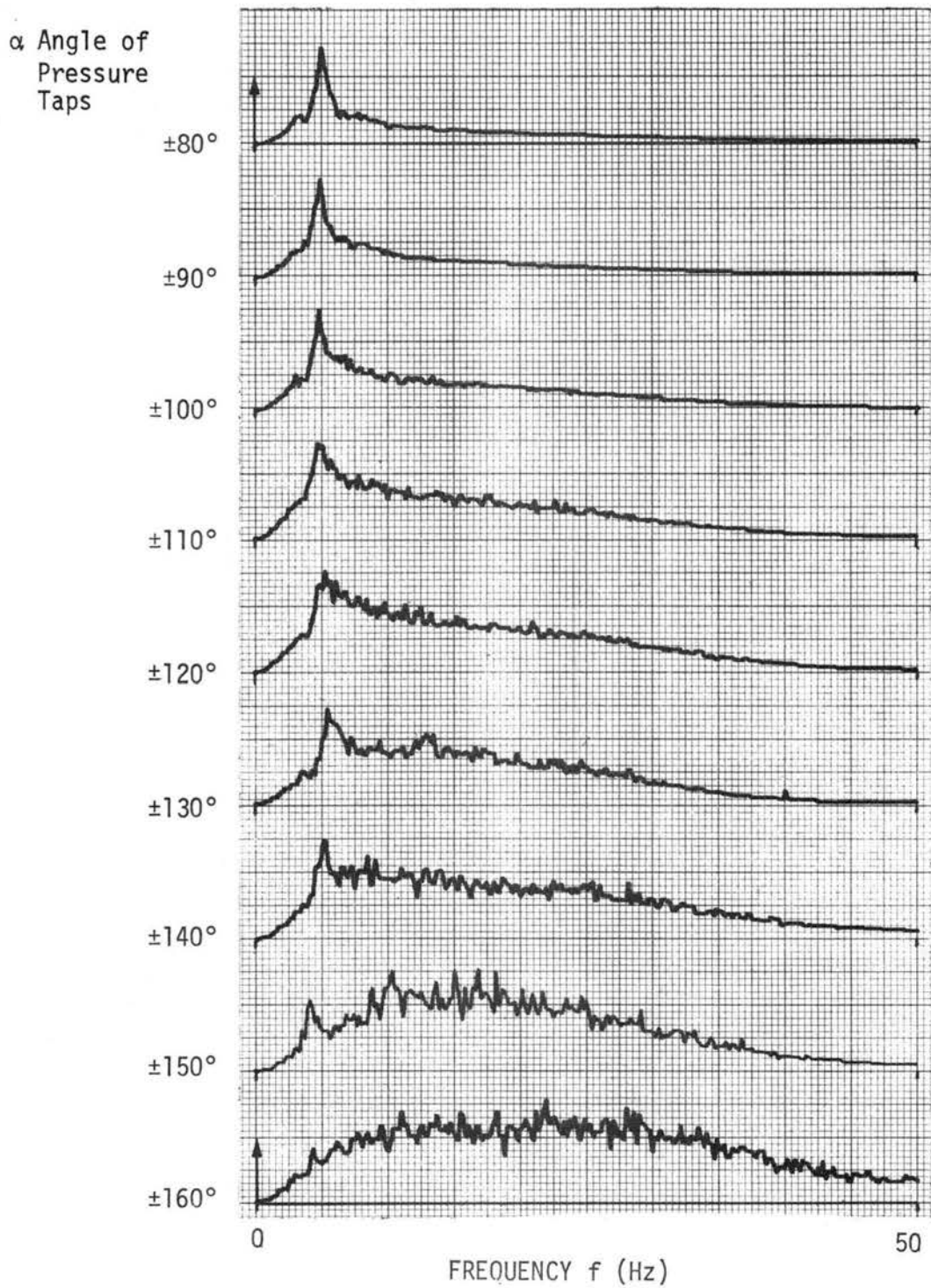
PLATE .972;  $U \approx 18$  fps

Figure 31. Change of spectra with  $\alpha$  angle of pressure taps. 4.5" cylinder. Mean of 60 spectra.  $\Delta f = .195$  Hz.

OBSERVATIONS OF TURBULENCE INTENSITY AND AIR SPEED DISTRIBUTIONS  
NEAR A CIRCULAR CYLINDER IN TWO DIFFERENT TURBULENT FLOW CONDITIONS

## DIAGRAM OF OBSERVATION POINTS

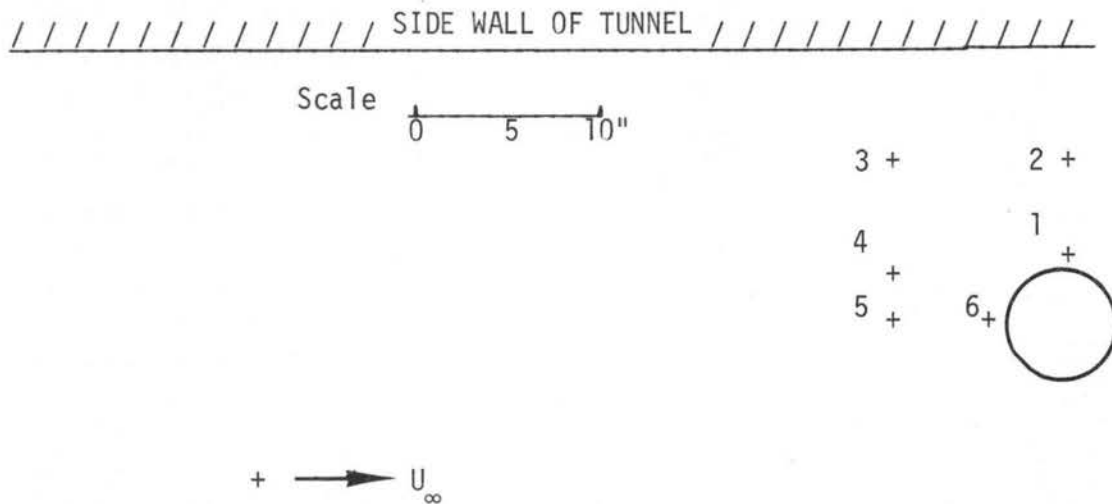


PLATE Br	POSITION	U fps	$U_{\infty}$ fps	$\frac{U}{U_{\infty}}$ *	Ti(1) %	Ti(2) %	$\frac{Ti(1)}{Ti(1)1}$ **
.36 Surry	1	28.0	19.0	1.47	8.6	8.6	1.00
	2	19.0	18.5	1.03	11.7	11.8	1.37
	3	16.6	18.1	.92	15.3	15.7	1.78
	4	15.0	17.8	.84	21.3	19.0	2.48
	5	15.8	18.1	.87	17.2	17.7	2.00
	6	5.0	18.0	.28	48.7	58.8	5.66
.972	1	34.0	16.2	2.10	24.7	24.2	1.00
	2	14.6	16.5	.88	41.8	43.3	1.69
	3	10.3	18.0	.57	46.0	49.1	1.86
	4	14.8	17.9	.83	26.0	26.8	1.05
	5	17.3	18.7	.93	25.0	25.6	1.01
	6	8.0	19.2	.42	51.9	57.3	2.10

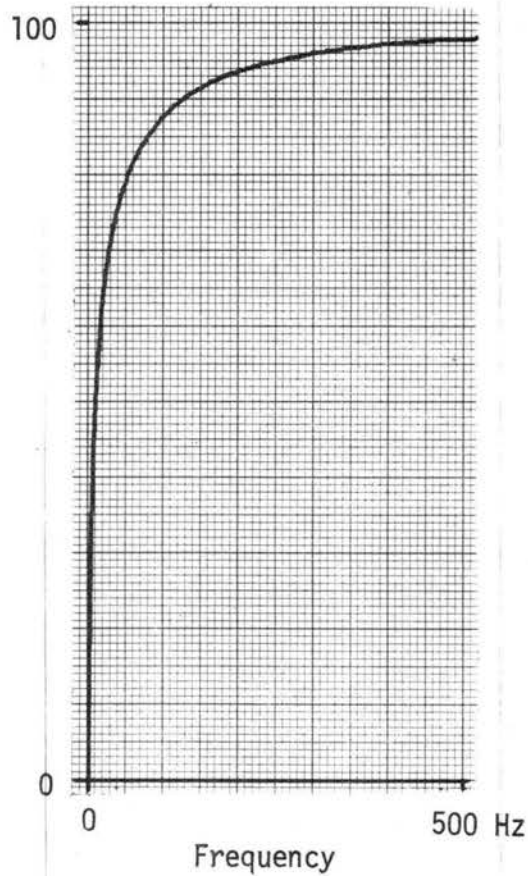
NOTES: Positions 1 and 6 are 1/4" from the cylinder.  
Ti(1) is calculated by King's Law with least squares A, B, C.  
Ti(2) is calculated by the intercept method.

\*Normalized velocity, using  $U_{\infty}$  to divide.

\*\*Normalized Ti, using Ti in position 1 to divide.

Figure 32. Turbulence and speed distributions.

Summation  
of  
Percent  
of  
Total Area  
Under  
 $G_{xx}(f)$   
0 to 5 KHz



Summation of  $G_{xx}(f)$  as calculated by Fourier Analyzer System.  $G_{xx}(f)$  was from a recording of  $e$  in flow behind plate .972,  $U \approx 22$  fps.

The same recorded voltage was sent through a low-pass filter and  $\overline{e^2}$  measured by a voltmeter. The following results were obtained for comparison with above curve.

$\overline{e^2}$ : 0 to 250 Hz = 96% of total for 0 to 5 kHz  
 0 to 100 Hz = 89%  
 0 to 50 Hz = 83%  
 0 to 25 Hz = 70%  
 0 to 15 Hz = 61%  
 0 to 10 Hz = 54%

Figure 33. Comparison of power spectra by Fourier Analyzer System and mean square voltage read with use of low-pass filter.

## TURBULENCE OBSERVATION #1

PLATE .690; U = 17.6 fps

"B"

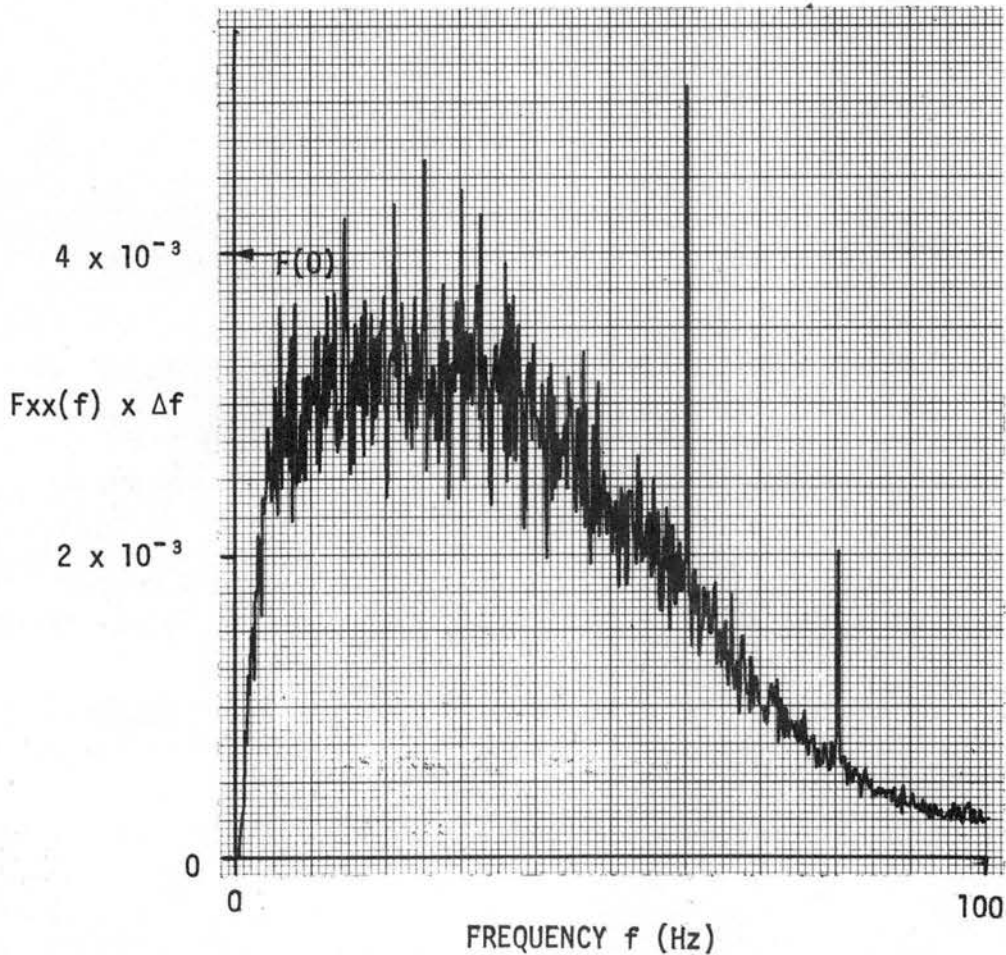


Figure 34. Power spectra of turbulent flow, at origin. No cylinder in tunnel. Mean of 60 spectra.  $\Delta f = .195$  Hz.  $F(0)$  estimated at  $4 \times 10^{-3}/\Delta f$  seconds, which gives  $L_x(F) = .0902$  ft. A 10% correction for harmonics makes  $L_x(F) = .0992$  ft.

## TURBULENCE OBSERVATION #1-1

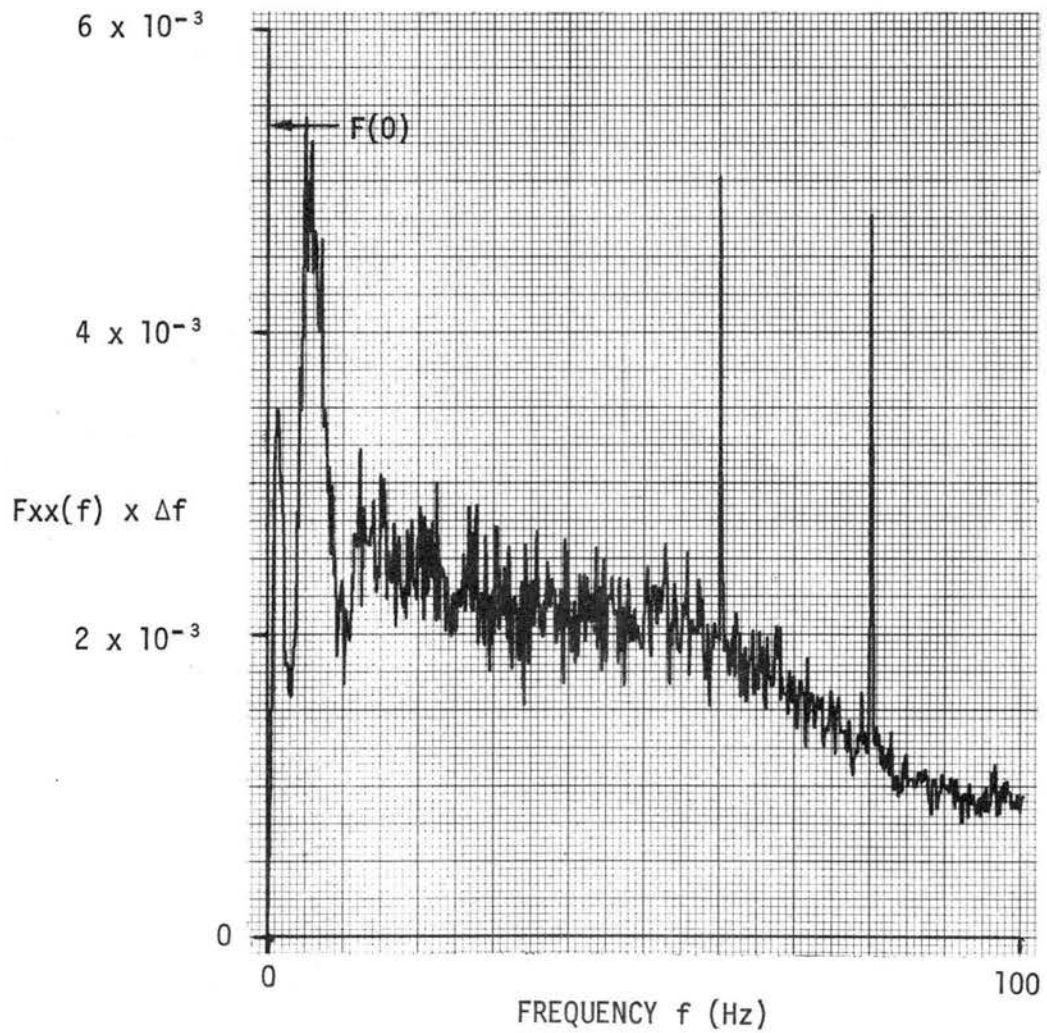
PLATE .690;  $U = 29.3$  fps

Figure 35. Power spectra of turbulent flow, at origin. No cylinder in tunnel. Mean of 100 spectra.  $\Delta f = .195$  Hz.  $F(0)$  estimated at  $5.4 \times 10^{-3}/\Delta f$  seconds, which gives  $L_x(F) = .2029$  ft. An 8% correction for harmonics makes  $L_x(F) = .2191$  ft.

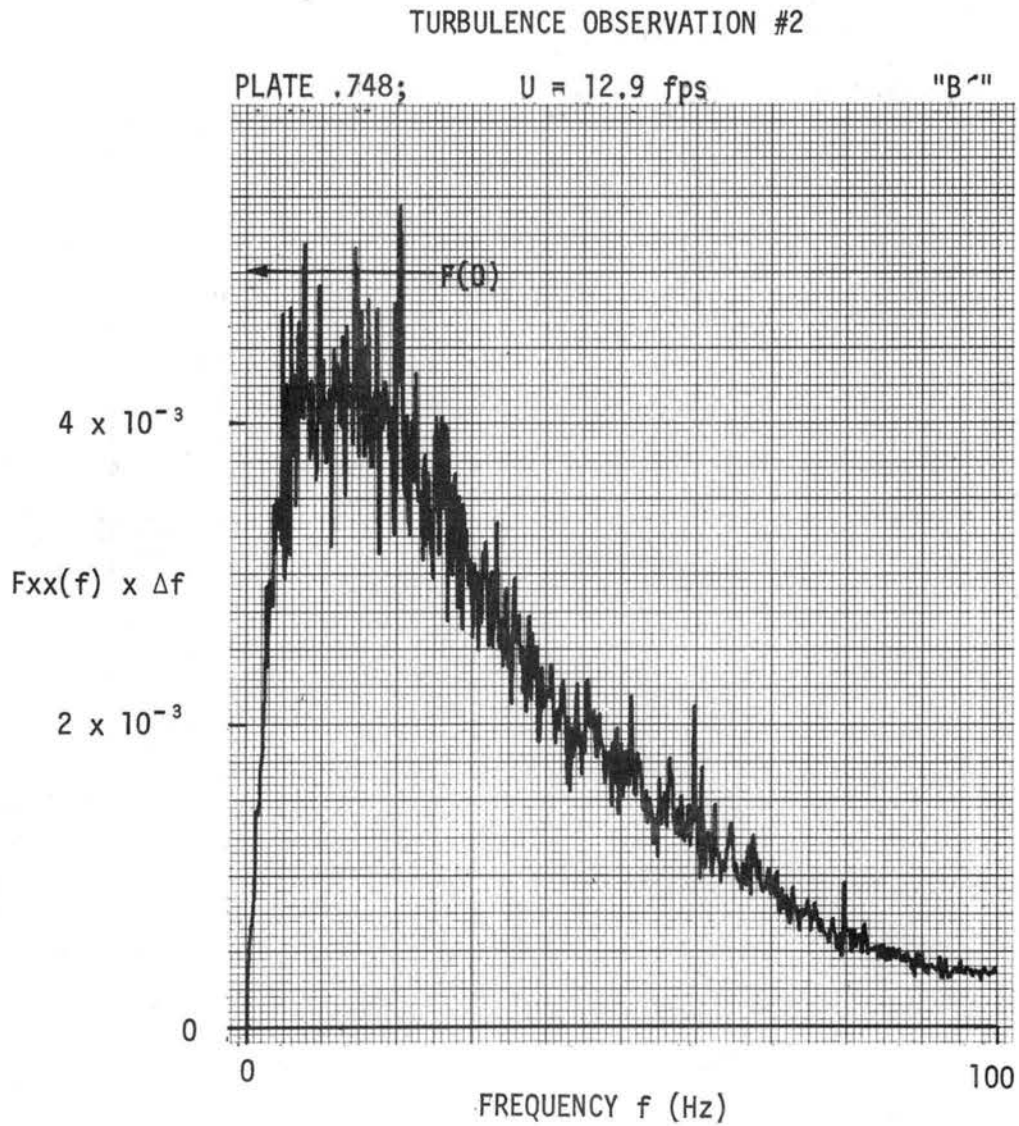


Figure 36. Normalized power spectra of turbulent flow, at origin. No cylinder in tunnel. Mean of 100 spectra.  $\Delta f = .195$  Hz. Arrow indicates estimated value of  $F(0) = .005/\Delta f$  sec, which gives  $L_x = .083$  ft. An 8% correction for harmonics makes  $L_x(F) = .089$  ft.

## TURBULENCE OBSERVATION #3

PLATE .748;  $U = 17.2$  fps

"C"

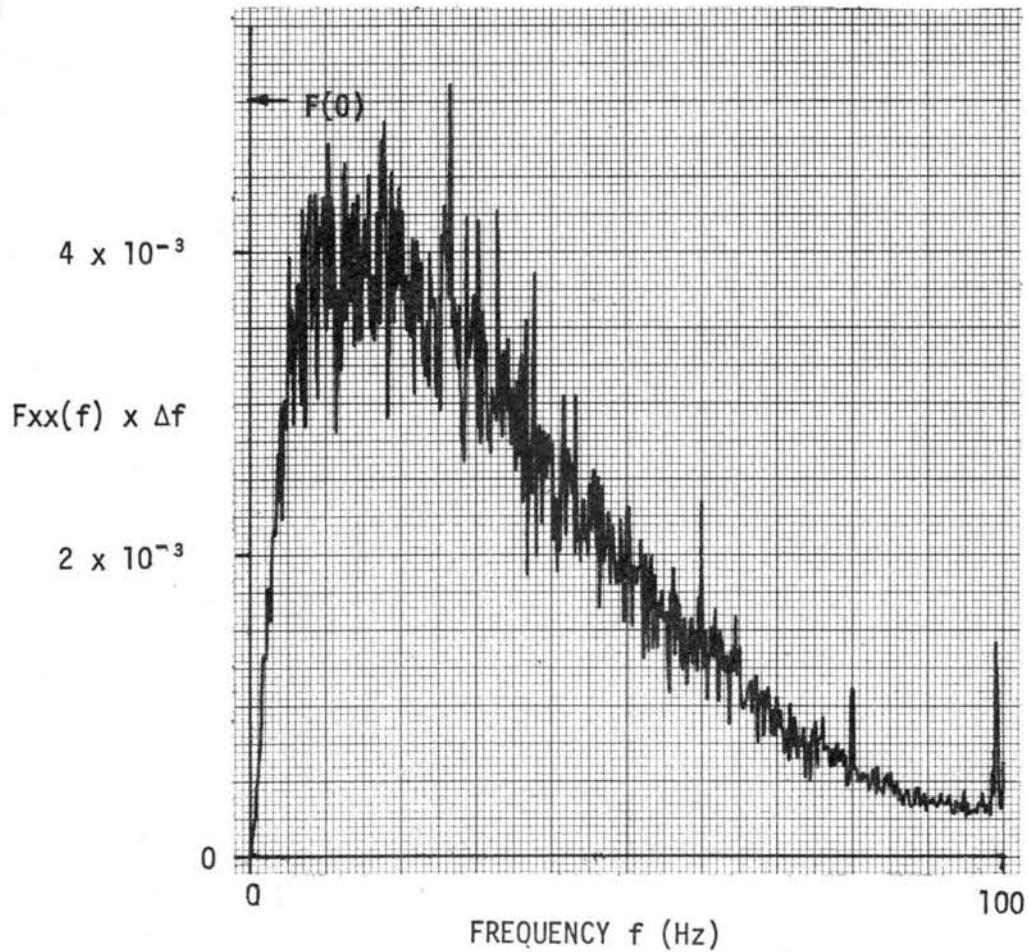


Figure 37. Power spectra of turbulent flow, at origin. No cylinder in tunnel. Mean of 72 spectra.  $\Delta f = .195$  Hz.  $F(0)$  estimated at  $5 \times 10^{-3}/\Delta f$  seconds, which gives  $L_x(F) = .1103$  ft. A 6% correction for harmonics makes  $L_x(F) = .1169$  ft.

## TURBULENCE OBSERVATION #4

PLATE .801;  $u = 15.9$  fps

"C"

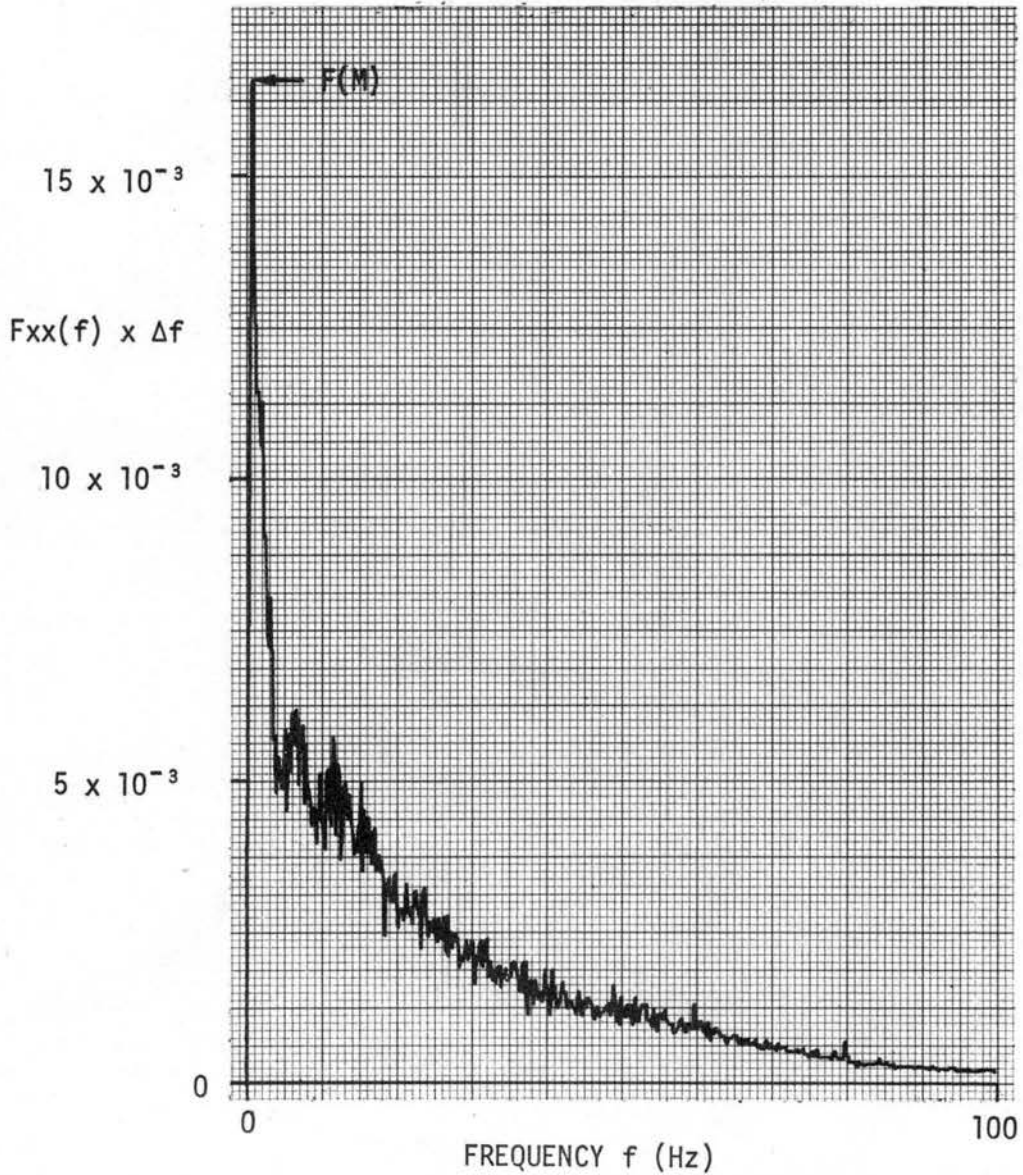


Figure 38. Normalized power spectra of turbulent flow, at origin. No cylinder in tunnel. Mean of 100 spectra.  $\Delta f = .195$  Hz. Arrow indicates value of  $F(M) = 16.57 \times 10^{-3} / \Delta f$  seconds, which gives  $L_x(F) = .34$  ft. A 5% correction for harmonics makes  $L_x(F) = .36$  ft.

## TURBULENCE OBSERVATION #5

PLATE .804;  $U = 9.7$  fps

"D"

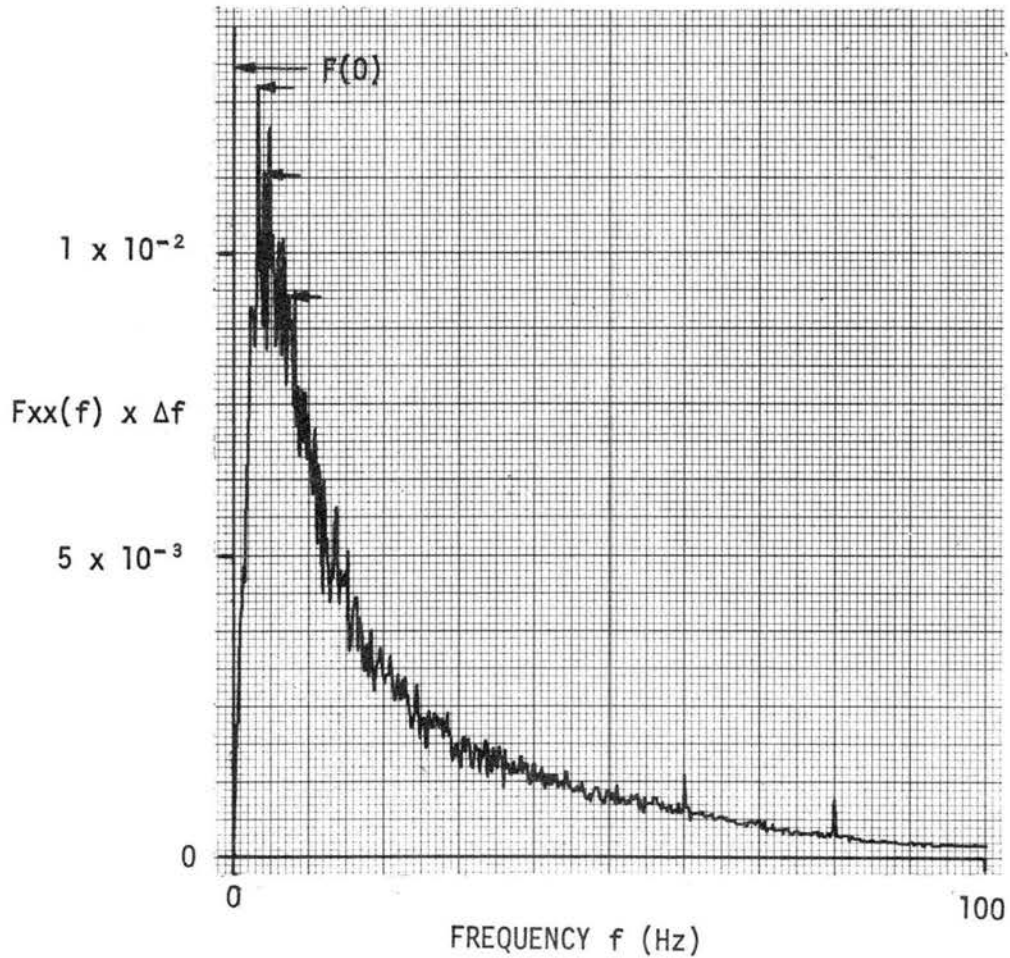


Figure 39. Power spectra of turbulent flow, at origin. No cylinder in tunnel. Mean of 100 spectra.  $\Delta f = .195$  Hz. Arrows indicate values used in calculating  $F(0)$  by least squares extrapolation.  $F(0) = 1.302 \times 10^{-2}/\Delta f$  seconds, which gives  $L_x(F) = .1617$  ft. A 4% correction for harmonics makes  $L_x(F) = .1682$  ft.

TURBULENCE OBSERVATION #6

PLATE .861;  $U = 8.7$  fps

"D"

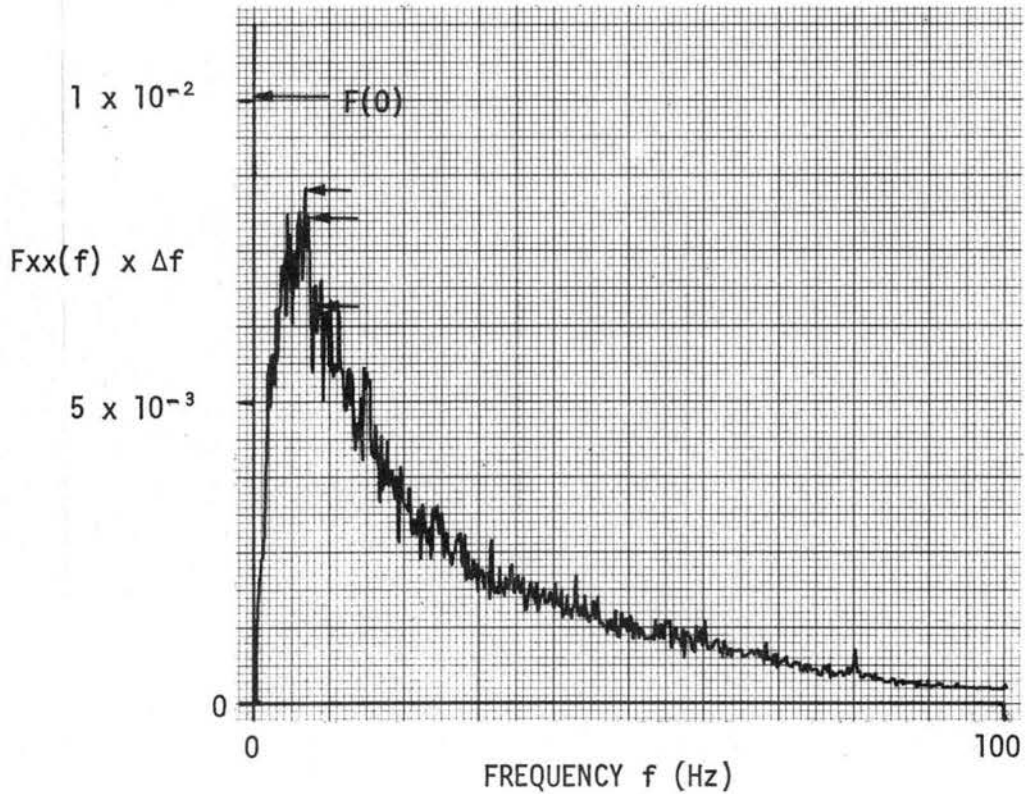


Figure 40. Power spectra of turbulent flow, at origin. No cylinder in tunnel. Mean of 100 spectra.  $\Delta f = .195$  Hz. Arrows indicate values used in calculating  $F(0)$  by least squares extrapolation.  $F(0) = 10.02 \times 10^{-2}/\Delta f$  seconds, which gives  $L_x(F) = .1116$  ft. A 1% correction for harmonics makes  $L_x(F) = .1127$  ft.

## TURBULENCE OBSERVATION #7

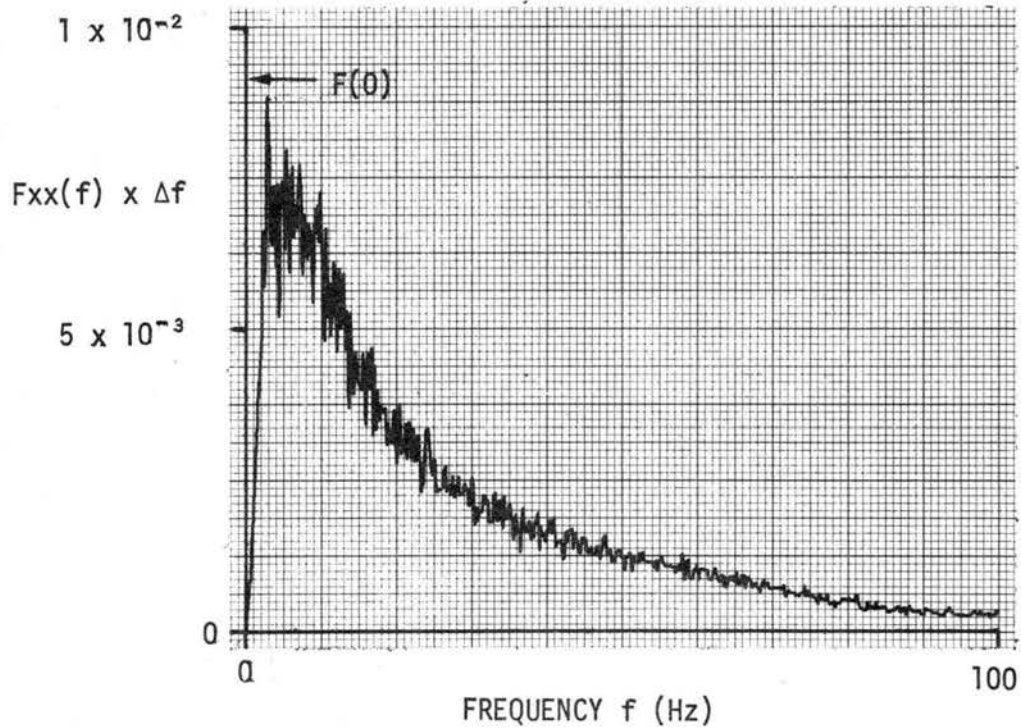
PLATE .945;  $U = 20.3$  fps "E"; "E'"

Figure 41. Power spectra of turbulent flow, at origin. No cylinder in tunnel. Mean of 100 spectra.  $\Delta f = .195$  Hz.  $F(0)$  estimated at  $9.125 \times 10^{-3}/\Delta f$  seconds, which gives  $L_x(F) = .237$  ft. No correction needed for harmonics.

## TURBULENCE OBSERVATION #8

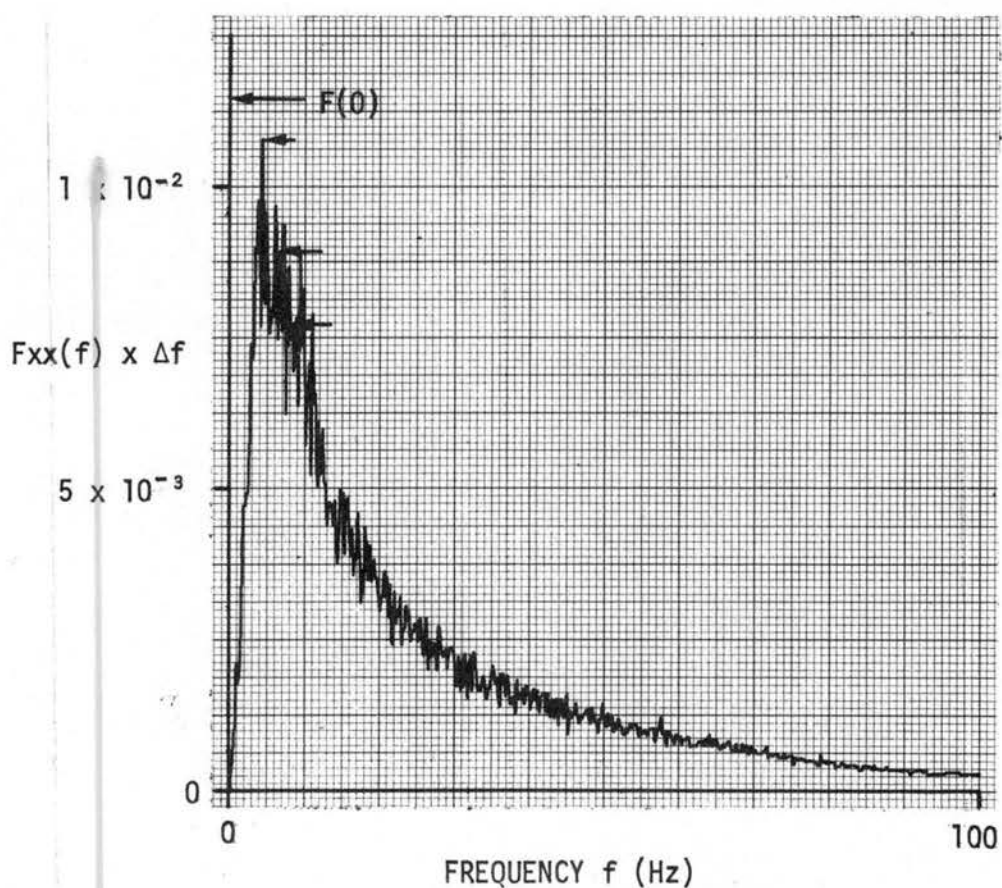
PLATE .972;  $U = 20.2$  fps "F" "F'"

Figure 42. Power spectra of turbulent flow, at origin. No cylinder in tunnel. Mean of 75 spectra.  $\Delta f = .195$  Hz. Arrows indicate values used in calculating  $F(0)$  by least squares extrapolation.  $F(0) = 1.141 \times 10^{-2}/\Delta f$  seconds, which gives  $L_x(F) = .295$  ft. No correction needed for harmonics.

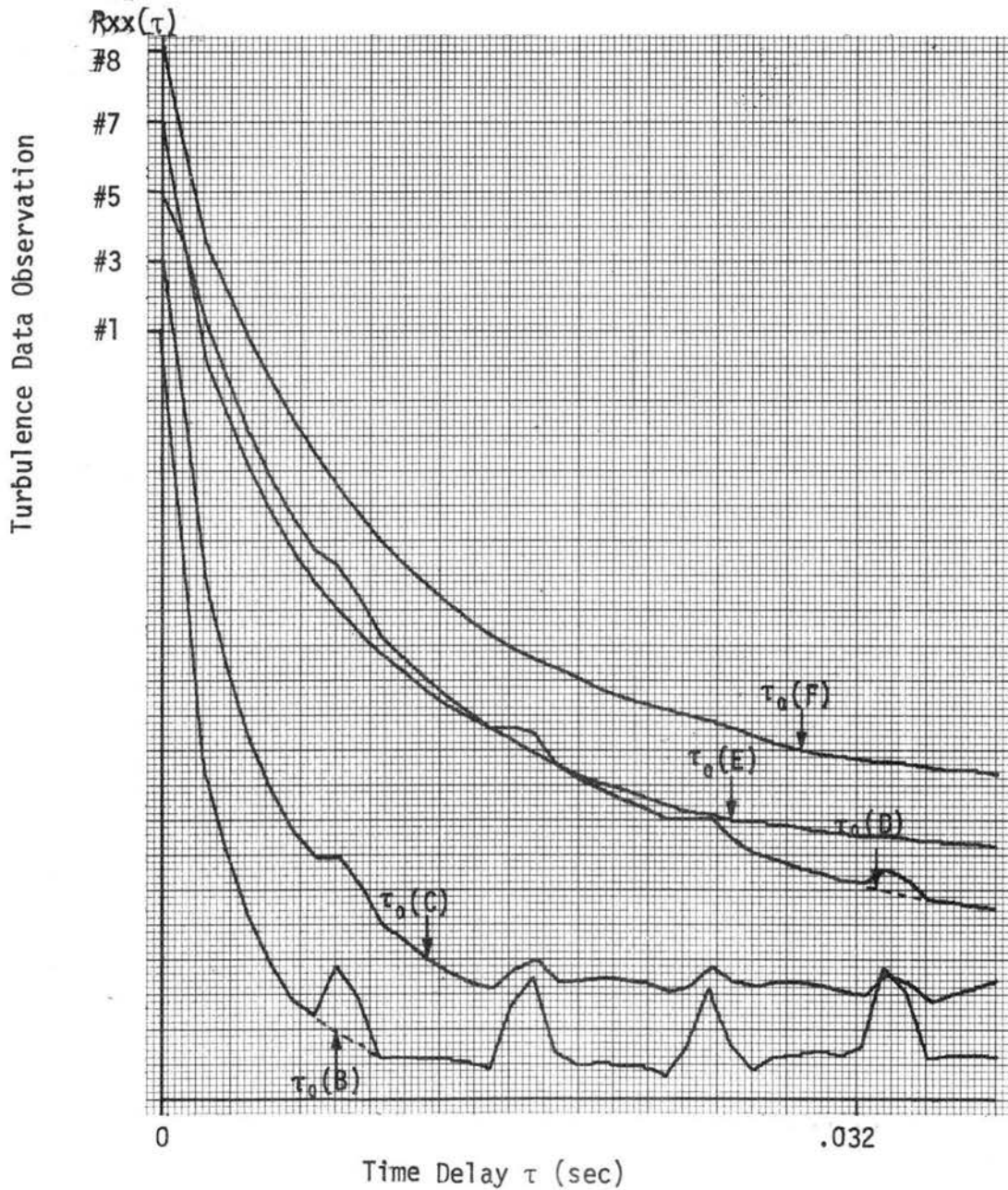


Figure 43.  $\tau_0$  observations by autocorrelation. For use with 4.5" cylinder vortex shedding data.  $\Delta t = .001$  sec.  $F_m = 500$  Hz. Mean of 50 autocorrelations.

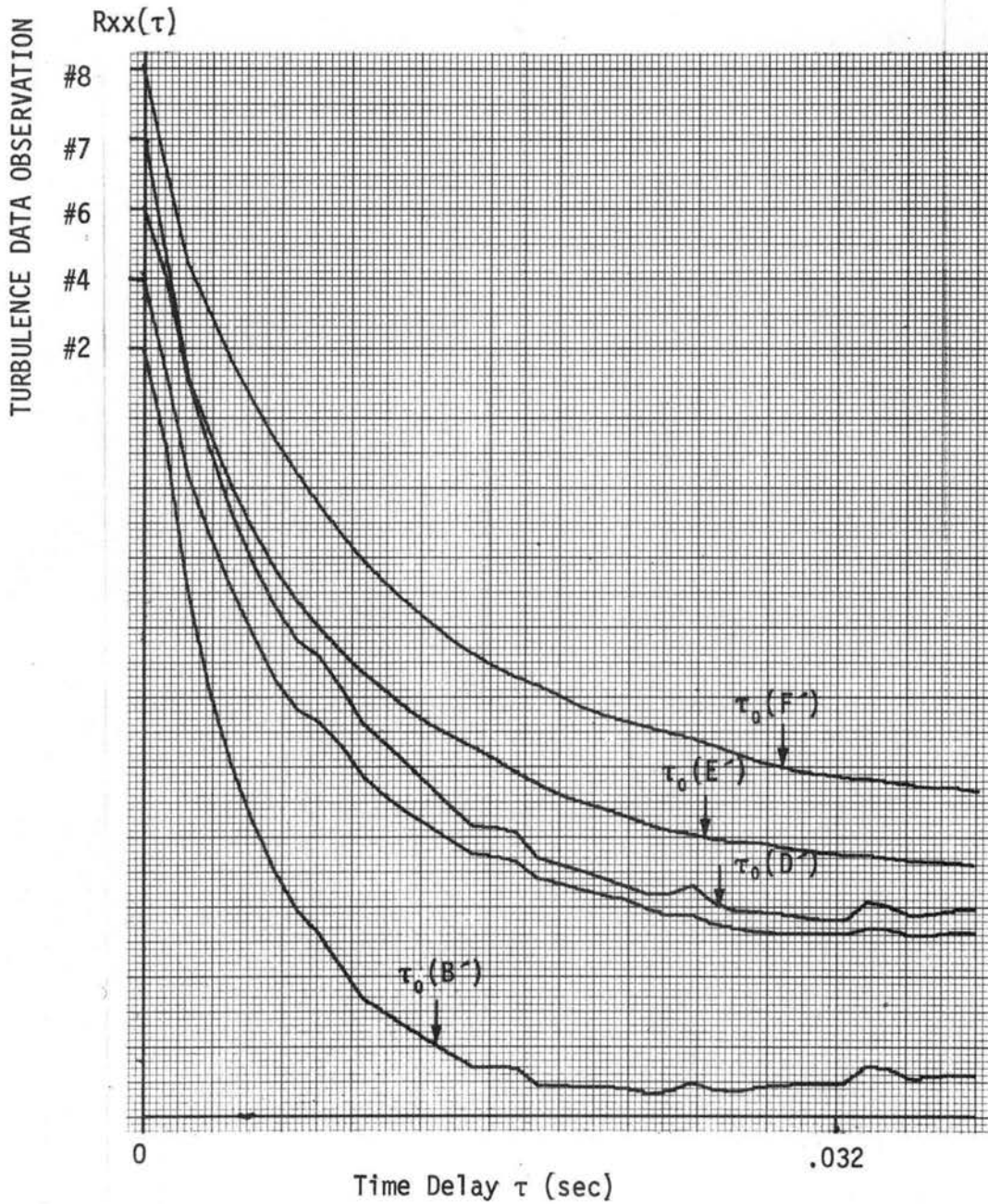


Figure 44.  $\tau_0$  observations by autocorrelation. For use with 2.75" cylinder vortex shedding data.  $\Delta t = .001$  sec.  $F_m = 500$  Hz. Mean of 50 autocorrelations.  $\tau_0(C)$  did not reach zero until approximately .3 sec.

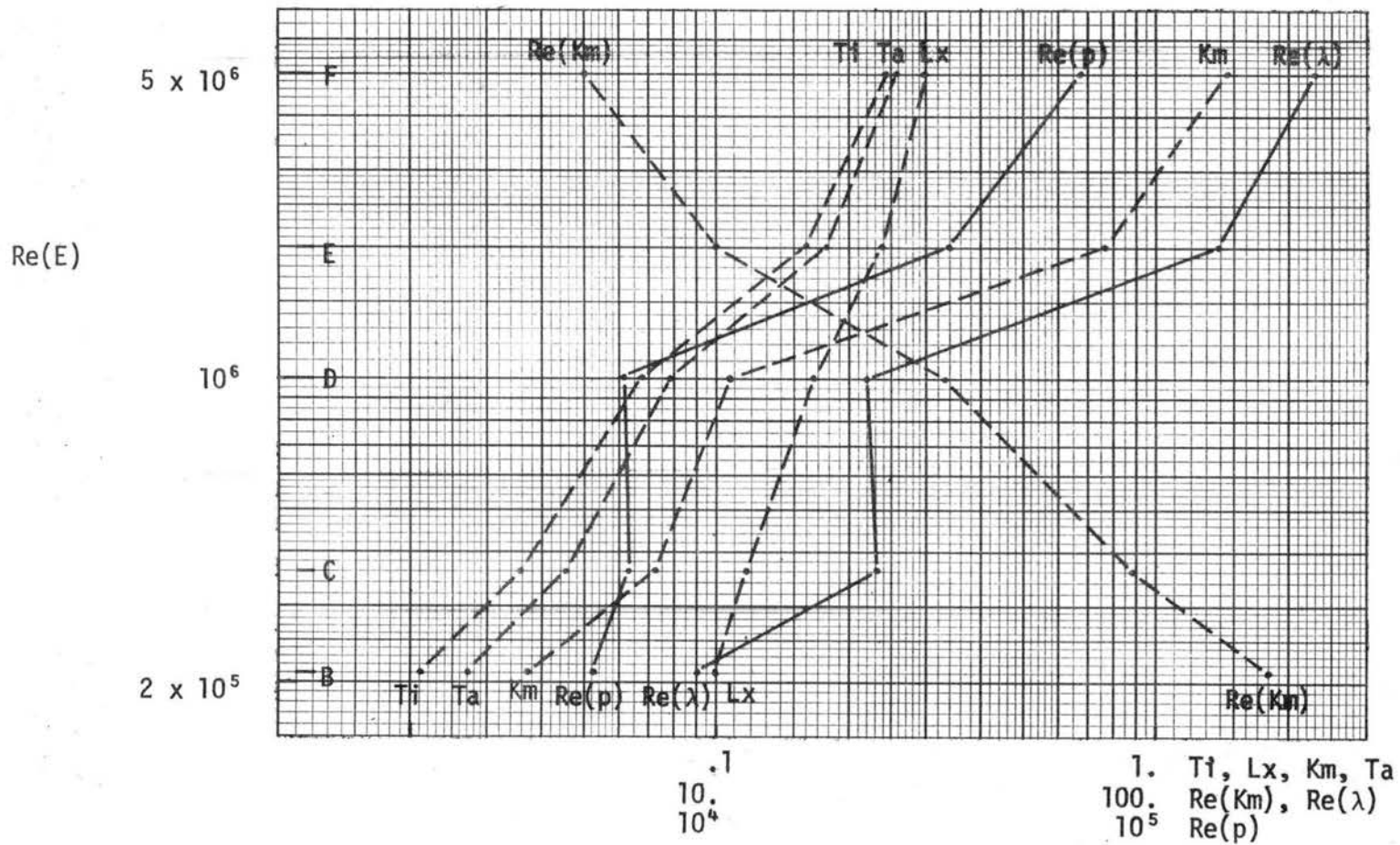


Figure 45A. Effective Reynolds number vs turbulence parameters, 4.5" cylinder, for induced vortex shedding conditions B, C, D, E, F. Data are in Table 3 (continued). Approximate functional expressions of curves are cases 1-7 in Table 6.

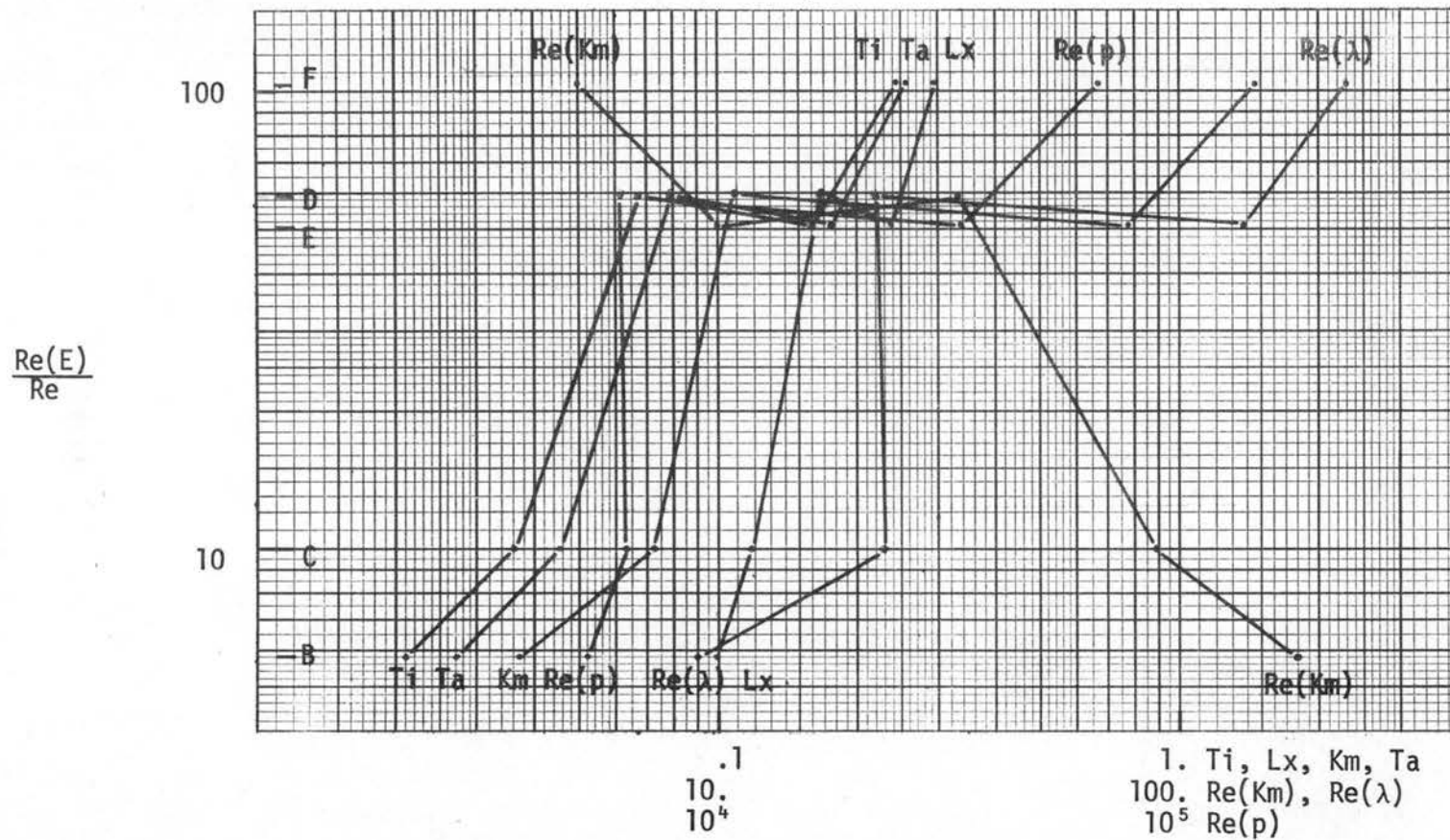


Figure 45B. Ratio of effective Reynolds number and Reynolds number vs turbulence parameters, 4.5" cylinder for induced vortex shedding conditions B, C, D, E, F. Data are in Table 3 (continued). Approximate functional expressions of curves are cases 8-14 in Table 6.

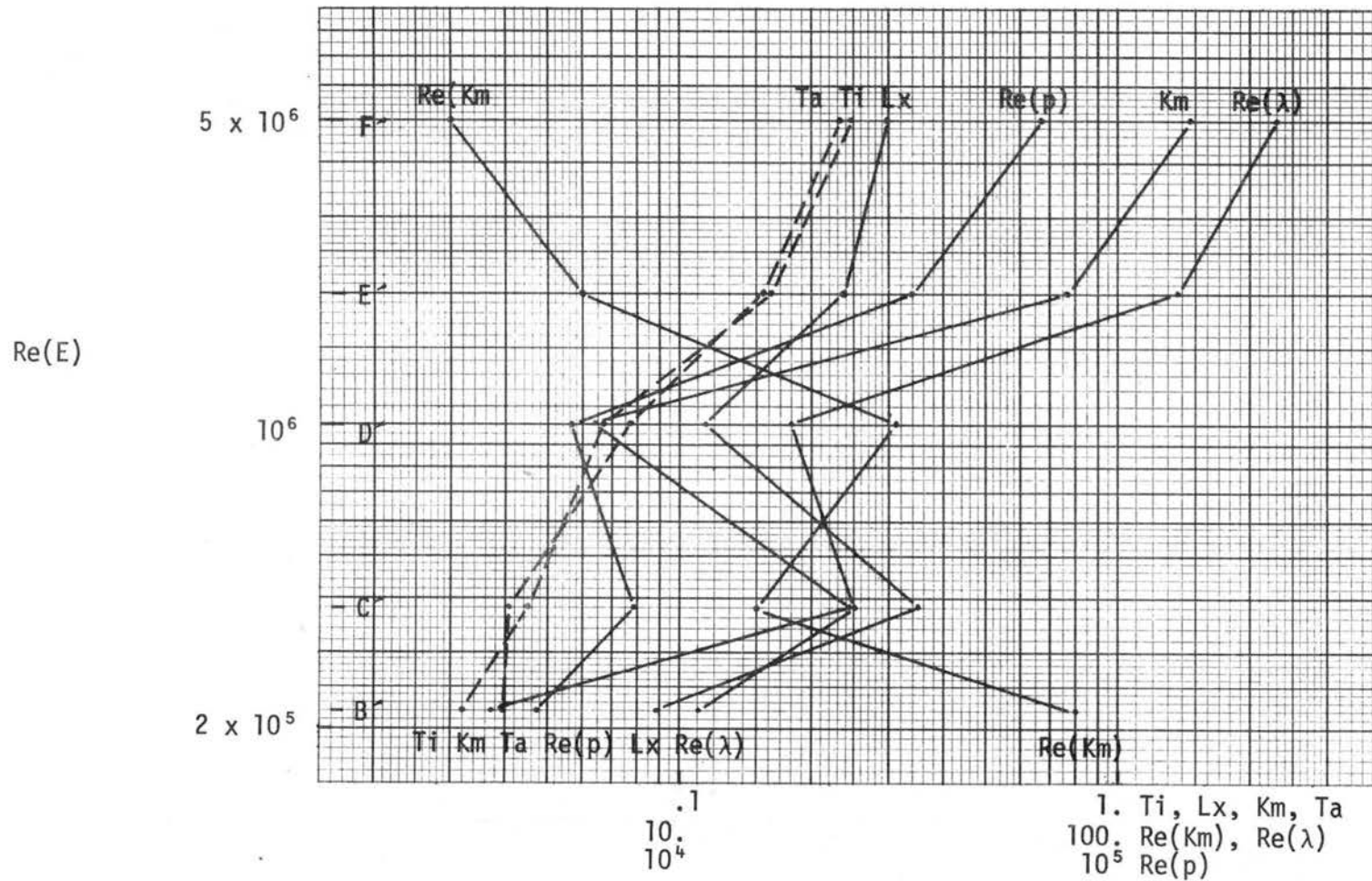


Figure 46A. Effective Reynolds number vs turbulence parameters, 2.75" cylinder. Approximate functional expressions of curves are cases 15-21 in Table 6.

$\frac{Re(E)}{Re}$

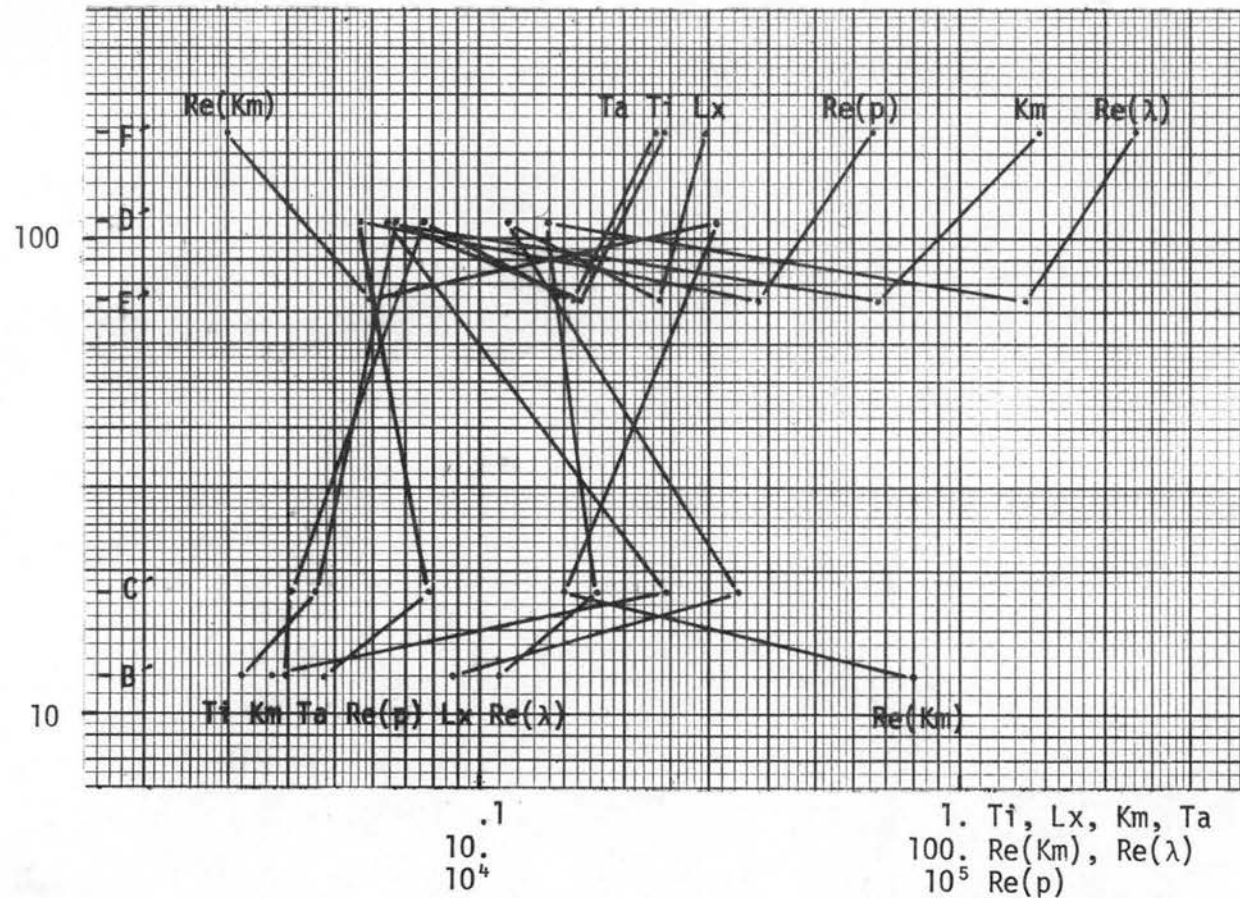
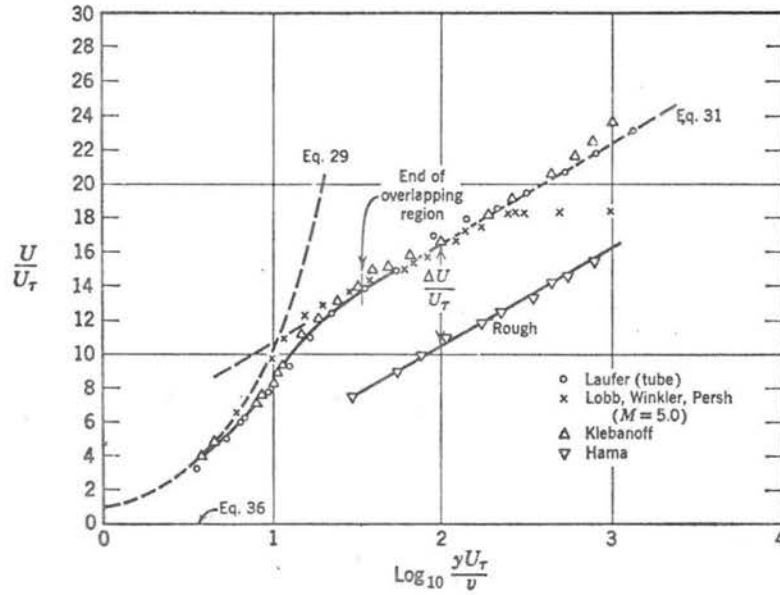


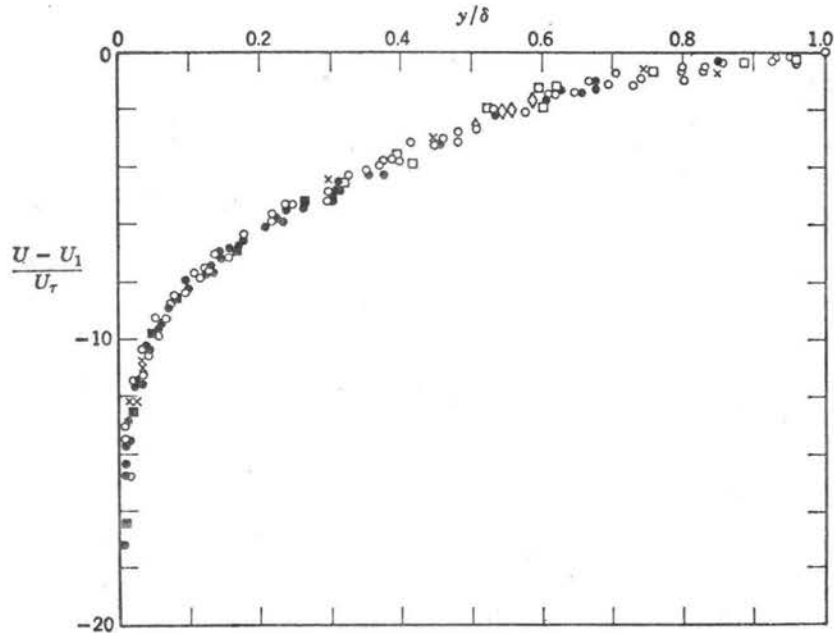
Figure 46B. Ratio of effective Reynolds number and Reynolds number vs turbulence parameters, 2.75" cylinder, for induced vortex shedding conditions B', C', D', E', F'. Data are in Table 3 (continued). Approximate functional expressions of curves are cases 22-28 in Table 6.

LAW OF THE WALL



Distribution of mean velocity near wall in turbulent flow. Effects of roughness and compressibility are shown. The Lobb et al. data are plotted using values of  $\rho$  and  $\mu$  at the wall.

VELOCITY DEFECT LAW



Turbulent boundary layer profiles on a flat plate. Incompressible flow, smooth and rough surfaces.

Figure 47. Turbulent boundary layer representation. From Kuethe and Schetzer (1961). Upper diagram is for inner and transition regions. Lower diagram is for the outer region.  $U_\tau$  is friction velocity,  $u_*$ .

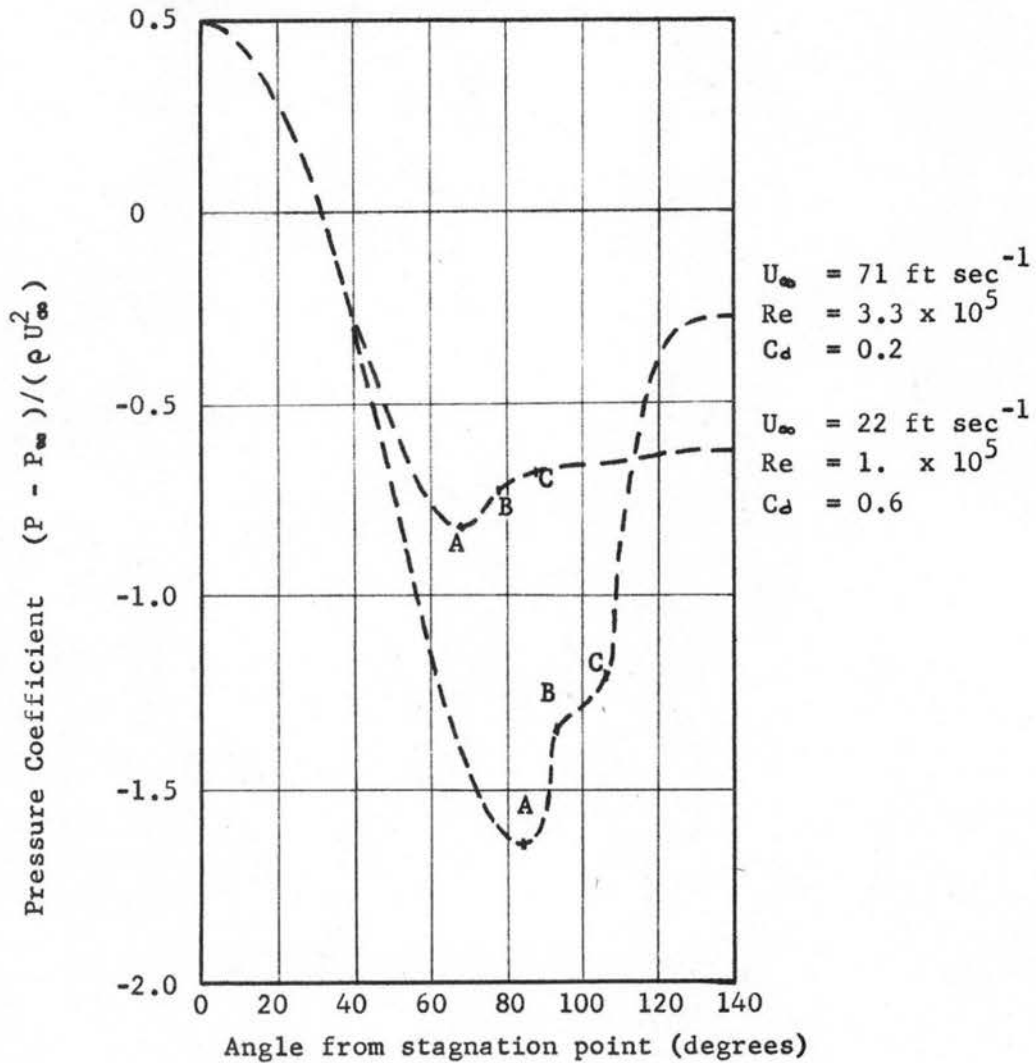


Figure 48. Pressure distribution around a circular cylinder for two flows encompassing the critical Reynolds Number. (Adapted from Fage, 1929) B is point where boundary layer separation starts. C is point where boundary layer separation fully exists. Transition occurs in region BC.

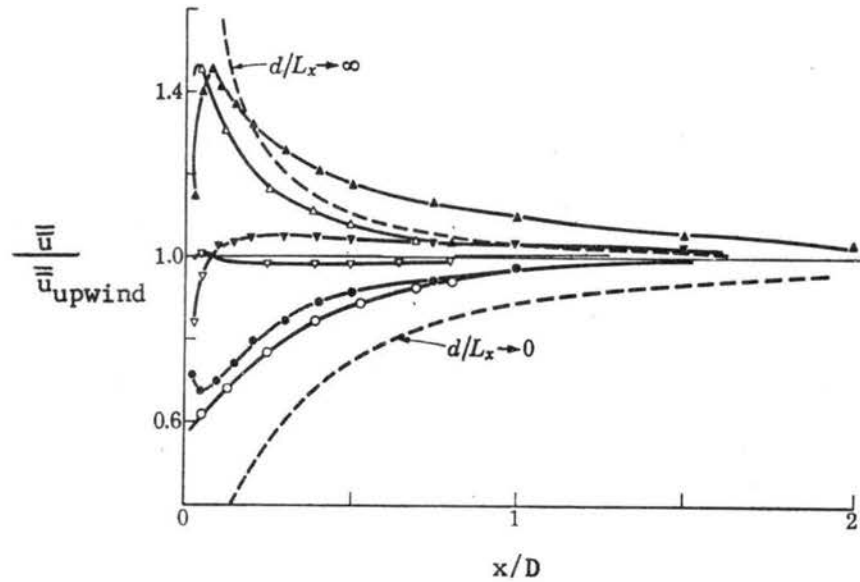


Figure 49. The change in turbulent fluctuations along the stagnation line for flow around a circular cylinder. Values of  $d/L_x$ : 0, ●, 0.26; △, ▲, 3.62. Solid symbols are experimental points, open symbols theoretical. Air is moving from right to left. (From Hunt, 1971)

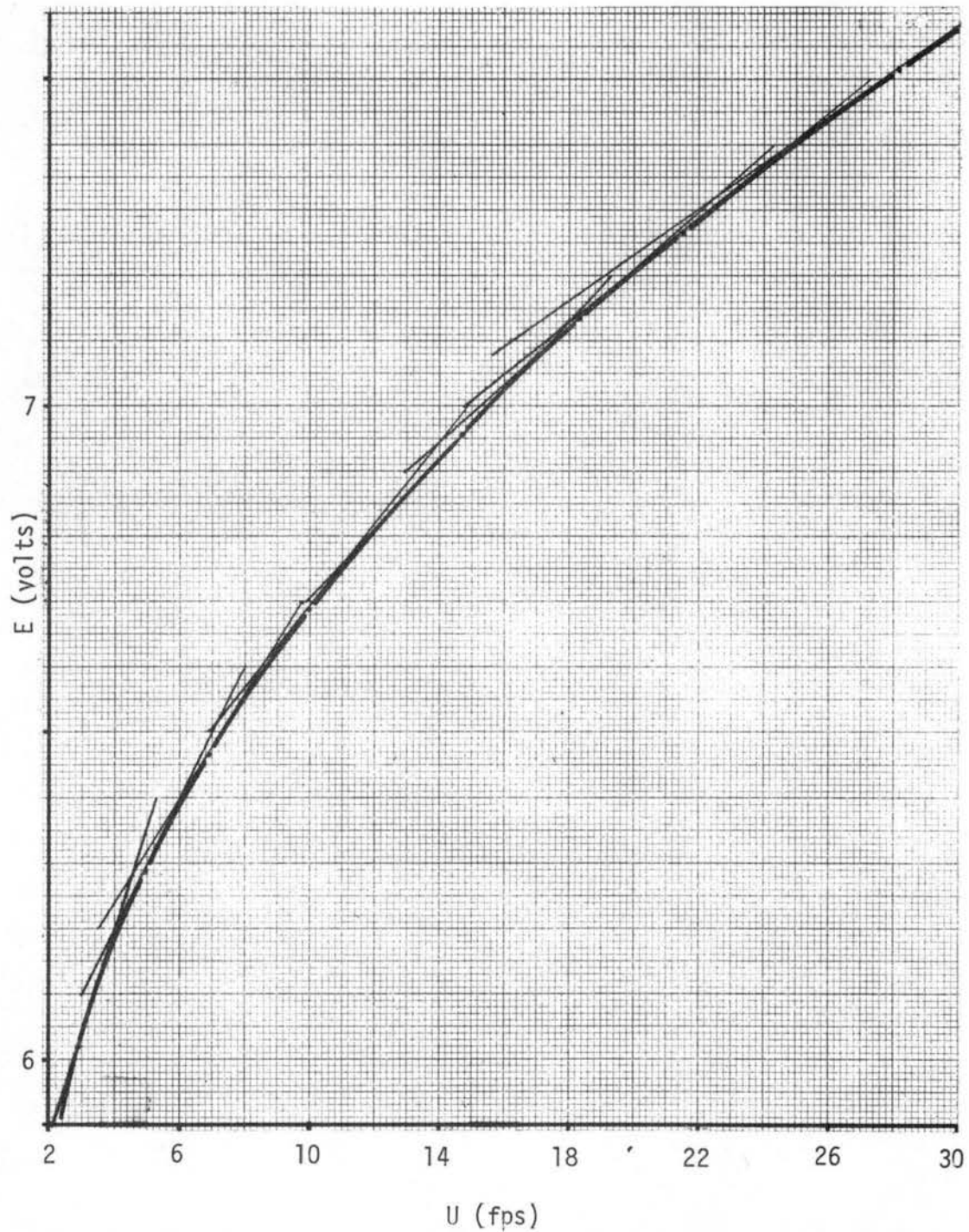
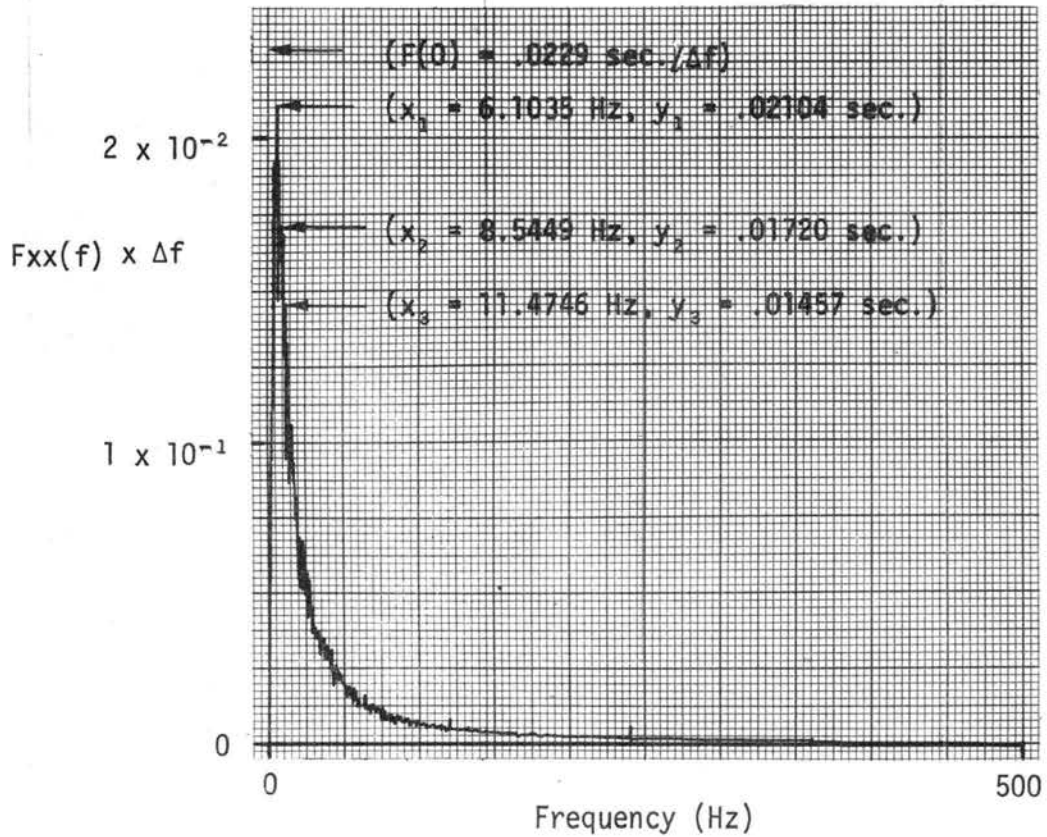


Figure 50. Calibration curve of DISA Hot Wire Sensor. Heavy line is calibration curve. Lighter lines, tangent to calibration data points are used to calculate  $\Delta E/\Delta U$ . This is used for comparing first derivative values  $dE/dU$  obtained analytically from King's Law calibration equation. See Table 4 for comparisons.



Above is the normalized power spectra for turbulence observation #7. (Plate .972,  $U = 22$  fps,  $F_m = 500$  Hz,  $N = 2048$ ,  $\Delta f = .488$  Hz.) The  $x_i, y_i$  values were printed out by teletype from Fourier Analyzer System.

$$F(0) = \frac{\sum y_i \sum x_i^4 - \sum x_i^2 \sum x_i^2 y_i}{3 \sum x_i^4 - \sum x_i^2 \sum x_i^2} = \frac{(0.05281)(24055) - (241.93)(3.9580)}{(3)(24055) - (241.93)(241.93)}$$

$$F(0) = \frac{.0229 \text{ sec.}}{\Delta f} = .0469 \text{ sec.}$$

Figure 51. Example of calculation of  $F(0)$ .

PLATE .958; U = 17.4 fps

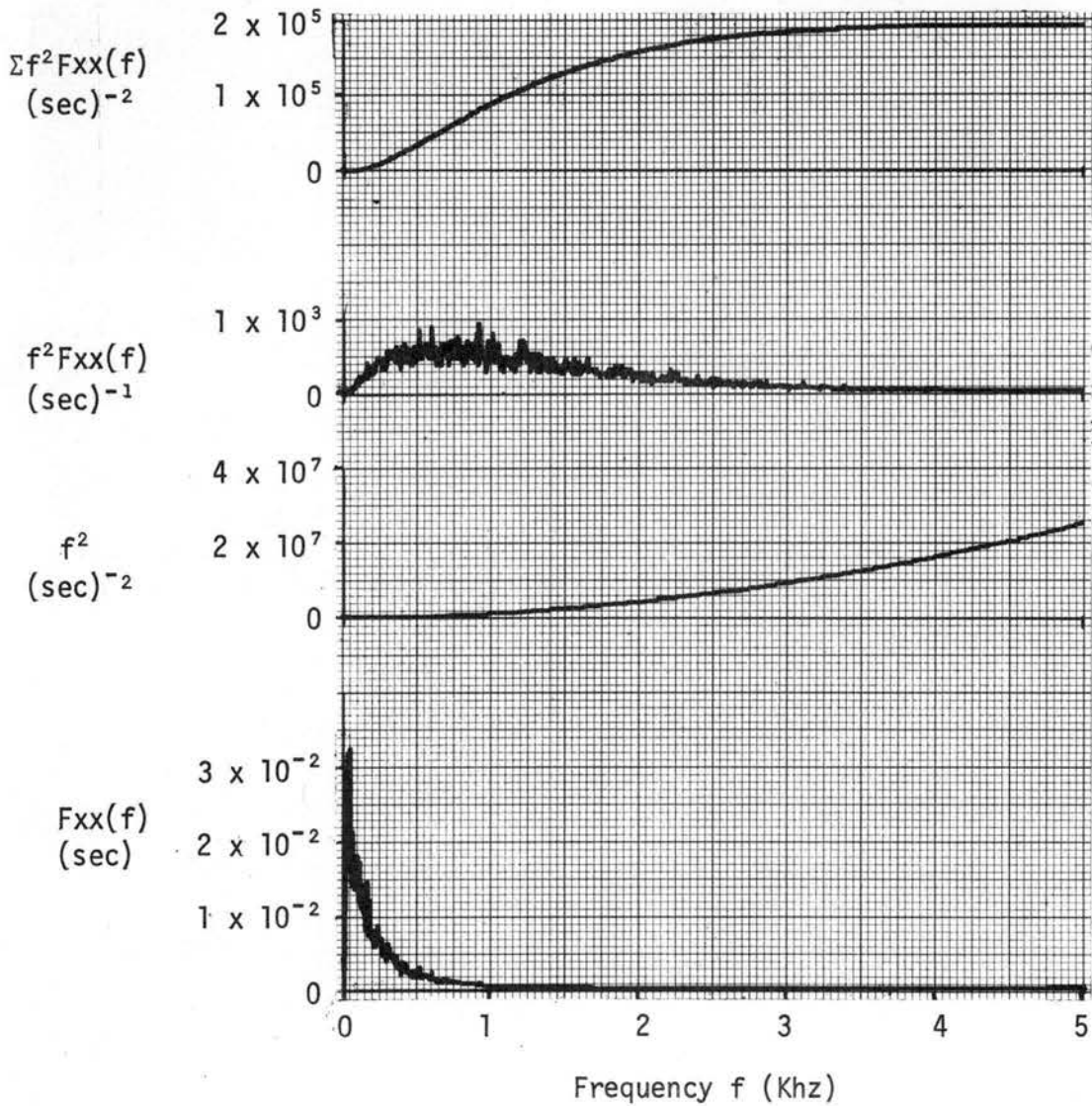
 $1.923 \times 10^5 \text{ sec}^{-2}$ 

Figure 52. Numerical FAS calculation of  $\int_0^{\infty} f^2 F_{xx}(f) df$  for micro-scale by Taylor's method. Turbulent flow 45" downstream from plate .958. Mean air speed 17.4 fps. Mean of 100 spectra;  $F_m = 5 \text{ KHz}$ ;  $N = 2048$ ;  $\Delta f = 4.88 \text{ Hz}$ ;  $\Delta t = 10^{-4} \text{ sec}$ ;  $T = .2048 \text{ sec}$ .

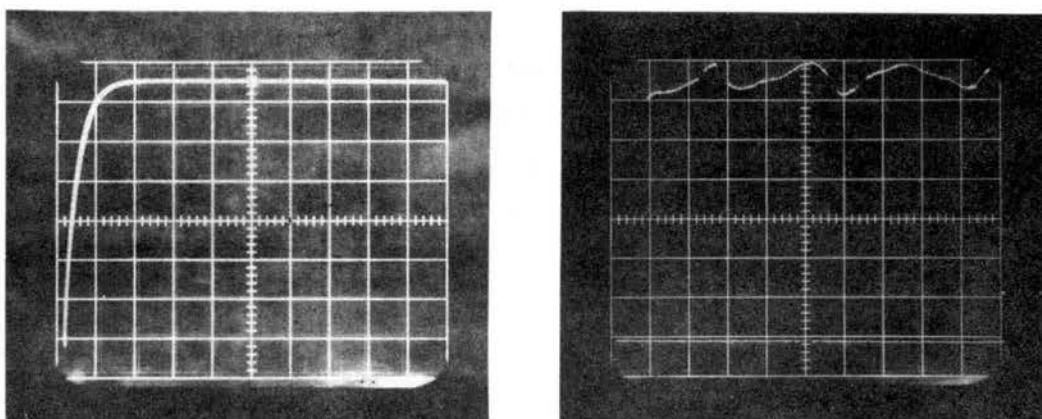


Figure 53. Calculation of hot wire time constant by response to a shock wave in an air pulse tube.

On the upper left is an oscilloscope trace representing an idealized response of a first order electrical system to an instantaneous step increase in voltage. This is done by an RC electrical circuit.

On the upper right is the trace of a DISA hot wire voltage response to a shock wave of air and a resulting steady air flow. The initial air flow was zero and its voltage is the horizontal trace at 0.9 units from the bottom. The hot wire voltage responds to the shock wave at the left end of this trace. The voltage increases so rapidly that it is not recorded until about  $40 \mu\text{s}$ . later in the upper left corner; where a continuous trace begins and extends across to the right as the air flow approaches a steady state. This upper beginning point is  $40 \mu\text{s}$ . and 6.1 divisions (3.05 volts) from the initial response. This leads to a time constant of  $\tau = 17.6 \mu\text{s}$ . for the hot wire, treating it as a first order system. This converts to a maximum frequency of 9.05 KHz that the wire can sense.

The assistance of Mr. Fred Brock, University of Oklahoma, in conducting this experiment at WSMR is gratefully acknowledged.

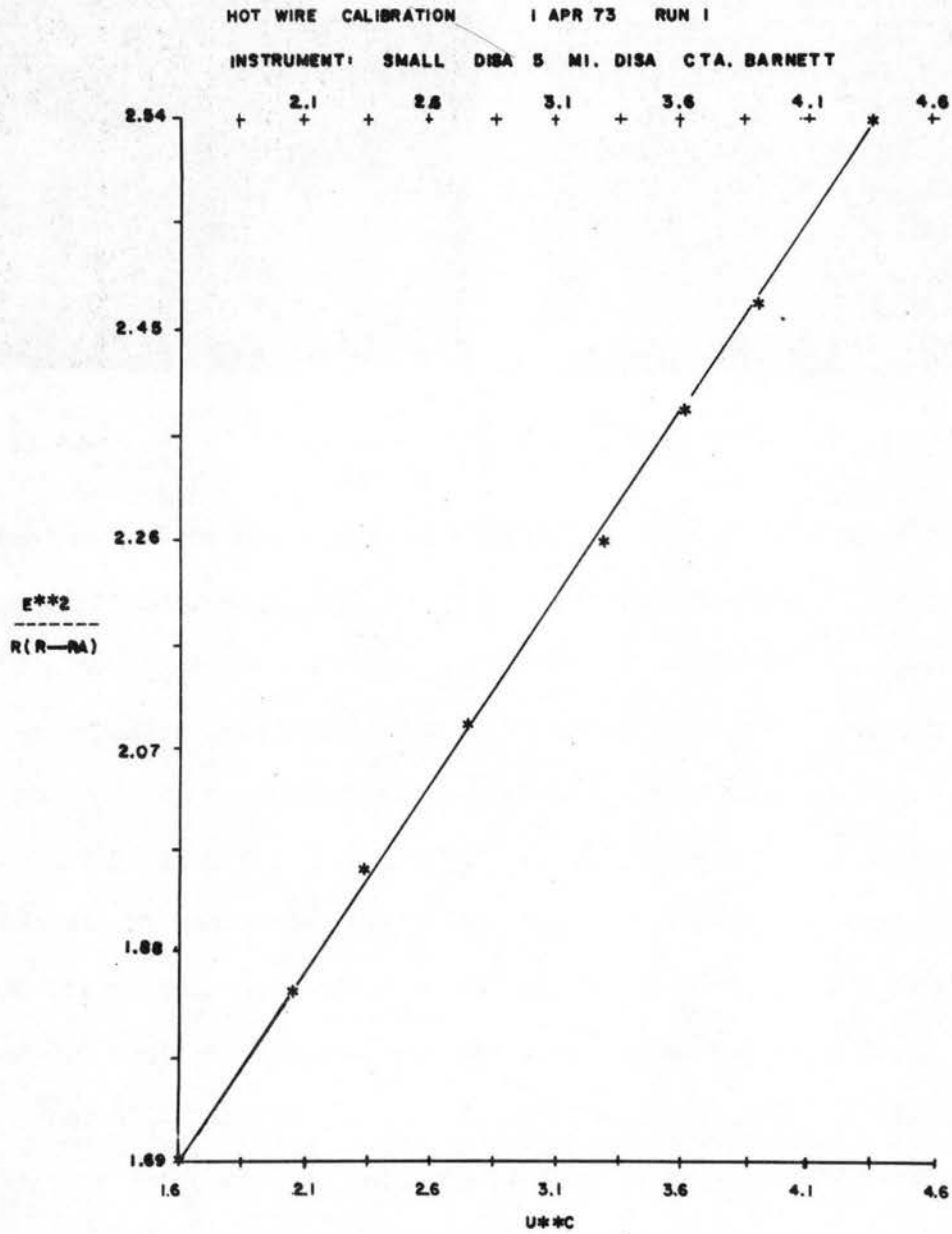


Figure 54. Check on hot wire calibration from Peterka's least squares solution of King's Equation. This is a reduced scale of print-out by computer. Linearity of equation is tested by drawing a line through calibration points.

HOT WIRE CALIBRATION 1 Apr 73 RUN 1

INSTRUMENT: SMALL DISA 5 MI, DISA CTA, BARNETT

TEMPERATURE = 79.0 F PRESSURE = 873.00 MBS

HOT RESISTANCE (OHMS) = 6.940

COLD RESISTANCE (OHMS) = 3.860

SOLUTION TO KINGS EQUATION

$$\frac{E^2}{R(R-RA)} = (1.153955) + (.3396657) U^{(.4419)}$$

N	CALIBRATION DATA		LEAST SQUARE'S SOLUTION		
	U (FPS)	E (VOLTS)	U**C	E**2/R(R-RA)	E
1	2.900	6.020	1.6008	1.6977	6.0240
2	5.000	6.282	2.0365	1.8457	6.2811
3	6.900	6.467	2.3480	1.9515	6.4586
4	10.000	6.689	2.7663	2.0936	6.6896
5	14.700	6.958	3.2798	2.2680	6.9627
6	18.280	7.132	3.6114	2.3806	7.1335
7	21.510	7.267	3.8806	2.4721	7.2692
8	28.140	7.513	4.3698	2.6382	7.5095

Figure 55. Least Square's Solution to Calibration of DISA Hot Wire, Using Peterka's Computer Program

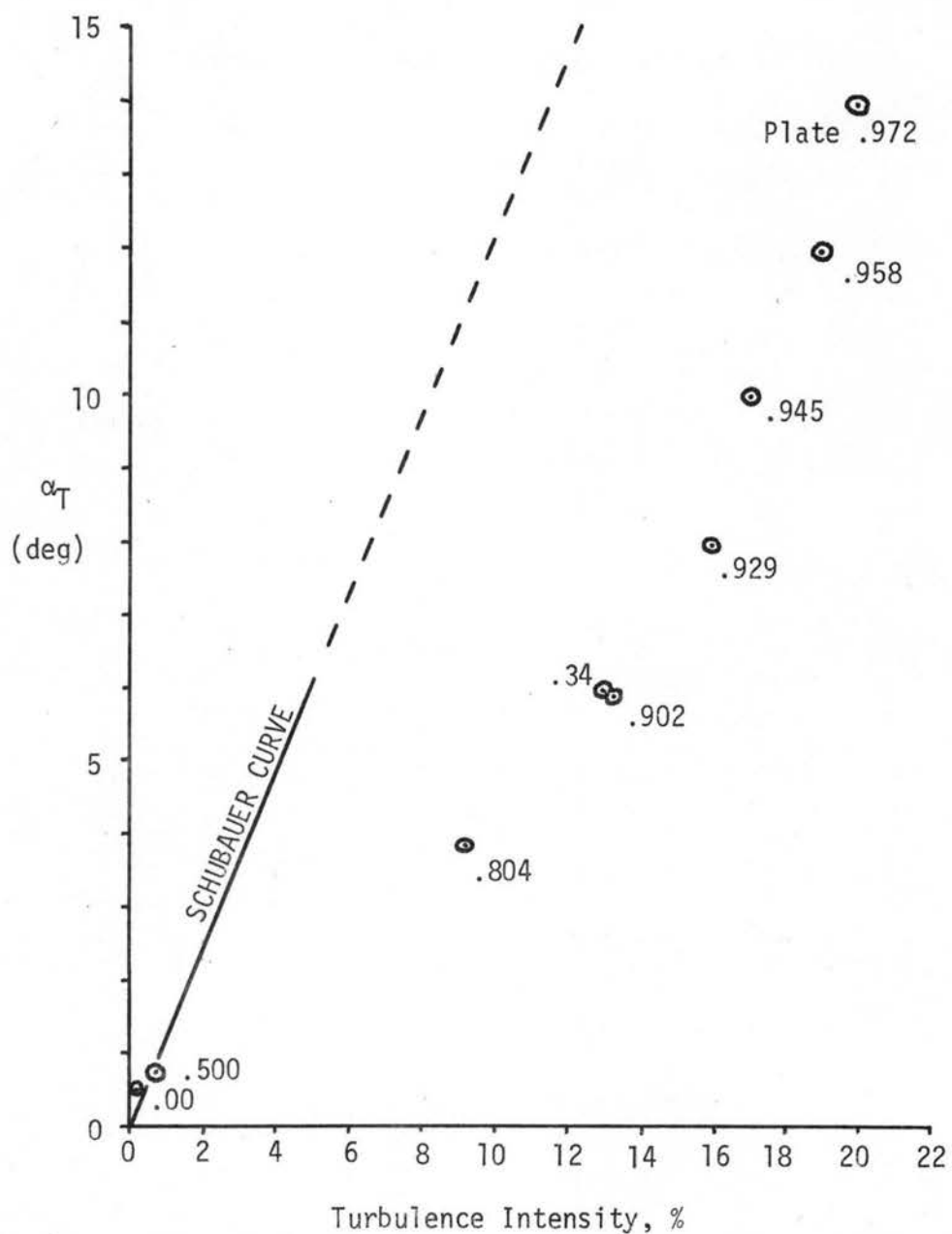


Figure 56. Comparison of turbulence intensity measured by Hot Wire techniques and by Schubauer's Heat Diffusion method. Data points  $\odot$  are identified by plate blockage ratio which produced turbulent flow.  $U \approx 18$  fps. Schubauer curve defines  $\bar{w}/U \times 100$ , and data points define  $\bar{u}/U \times 100$ .

DOCUMENT CONTROL DATA - R&D

(Security classification of title, body of abstract and indexing annotation must be entered when the overall report is classified)

1. ORIGINATING ACTIVITY (Corporate author) Fluid Dynamics and Diffusion Laboratory College of Engineering, Colorado State University Fort Collins, Colorado 80521		2a. REPORT SECURITY CLASSIFICATION unclassified	
		2b. GROUP	
3. REPORT TITLE Turbulence Induced Changes in Vortex Shedding from a Circular Cylinder			
4. DESCRIPTIVE NOTES (Type of report and inclusive dates) Technical Report			
5. AUTHOR(S) (Last name, first name, initial) Kenneth M. Barnett and J. E. Cermak			
6. REPORT DATE January 1974		7a. TOTAL NO. OF PAGES 238	7b. NO. OF REFS 81
8a. CONTRACT OR GRANT NO. N00014-68-A-0493-0001		9a. ORIGINATOR'S REPORT NUMBER(S) CER73-74KMB-JEC27	
b. PROJECT NO.		9b. OTHER REPORT NO(S) (Any other numbers that may be assigned this report) THEMIS Tech. Rept. No. 26	
c.			
d.			
10. AVAILABILITY/LIMITATION NOTICES Distribution of this report is unlimited.			
11. SUPPLEMENTARY NOTES		12. SPONSORING MILITARY ACTIVITY U.S. Department of Defense Office of Naval Research	
13. ABSTRACT Turbulence effects on vortex shedding from a circular cylinder were investigated in a wind tunnel. In this study, turbulence intensity, near the center of a wind tunnel, was increased from .3% to 25% by plates of similar geometry (many small holes) with blockage ratios from .50 to .97. The $Re$ of all flows was kept near $4 \times 10^4$ . Vortex shedding frequency $f$ was observed simultaneously by a pressure transducer (with sensors on cylinder surface) and a hot wire anemometer (immediately downstream). Means of 50 to 150 cross-spectra defined $f$ . Flow visualization, spectra and transducer output voltages with different $\alpha$ were utilized to estimate transition and separation. Six things were observed that have not been published, to the best of the author's knowledge: (a) analogous changes in vortex shedding processes can be obtained either by increasing the air speed (while holding the turbulence intensity very low) or by increasing the turbulence intensity (while holding the air speed approximately constant); (b) the frequency of the vortex shedding becomes relatively smaller, for the vortex shedding regime, as the turbulence intensity is increased; (c) an estimate of the turbulence induced changes in vortex shedding can be made from $Re$ of the flow, mean air speed, rms value of longitudinal speed fluctuations, integral scale of turbulence and cylinder diameter; (d) the "super critical" regime, associated with highest $\alpha$ and $St$ , can be disrupted by sufficient turbulence intensity; (e) the extent to which turbulence can induce changes in vortex shedding is limited.			

14. KEY WORDS	LINK A		LINK B		LINK C	
	ROLE	WT	ROLE	WT	ROLE	WT
turbulence, vortex shedding, pressure transducers, hot-wire anemometer, flow visualization turbulence intensity						

INSTRUCTIONS

1. **ORIGINATING ACTIVITY:** Enter the name and address of the contractor, subcontractor, grantee, Department of Defense activity or other organization (*corporate author*) issuing the report.

2a. **REPORT SECURITY CLASSIFICATION:** Enter the overall security classification of the report. Indicate whether "Restricted Data" is included. Marking is to be in accordance with appropriate security regulations.

2b. **GROUP:** Automatic downgrading is specified in DoD Directive 5200.10 and Armed Forces Industrial Manual. Enter the group number. Also, when applicable, show that optional markings have been used for Group 3 and Group 4 as authorized.

3. **REPORT TITLE:** Enter the complete report title in all capital letters. Titles in all cases should be unclassified. If a meaningful title cannot be selected without classification, show title classification in all capitals in parenthesis immediately following the title.

4. **DESCRIPTIVE NOTES:** If appropriate, enter the type of report, e.g., interim, progress, summary, annual, or final. Give the inclusive dates when a specific reporting period is covered.

5. **AUTHOR(S):** Enter the name(s) of author(s) as shown on or in the report. Enter last name, first name, middle initial. If military, show rank and branch of service. The name of the principal author is an absolute minimum requirement.

6. **REPORT DATE:** Enter the date of the report as day, month, year, or month, year. If more than one date appears on the report, use date of publication.

7a. **TOTAL NUMBER OF PAGES:** The total page count should follow normal pagination procedures, i.e., enter the number of pages containing information.

7b. **NUMBER OF REFERENCES:** Enter the total number of references cited in the report.

8a. **CONTRACT OR GRANT NUMBER:** If appropriate, enter the applicable number of the contract or grant under which the report was written.

8b, 8c, & 8d. **PROJECT NUMBER:** Enter the appropriate military department identification, such as project number, subproject number, system numbers, task number, etc.

9a. **ORIGINATOR'S REPORT NUMBER(S):** Enter the official report number by which the document will be identified and controlled by the originating activity. This number must be unique to this report.

9b. **OTHER REPORT NUMBER(S):** If the report has been assigned any other report numbers (*either by the originator or by the sponsor*), also enter this number(s).

10. **AVAILABILITY/LIMITATION NOTICES:** Enter any limitations on further dissemination of the report, other than those imposed by security classification, using standard statements such as:

- (1) "Qualified requesters may obtain copies of this report from DDC."
- (2) "Foreign announcement and dissemination of this report by DDC is not authorized."
- (3) "U. S. Government agencies may obtain copies of this report directly from DDC. Other qualified DDC users shall request through \_\_\_\_\_."
- (4) "U. S. military agencies may obtain copies of this report directly from DDC. Other qualified users shall request through \_\_\_\_\_."
- (5) "All distribution of this report is controlled. Qualified DDC users shall request through \_\_\_\_\_."

If the report has been furnished to the Office of Technical Services, Department of Commerce, for sale to the public, indicate this fact and enter the price, if known.

11. **SUPPLEMENTARY NOTES:** Use for additional explanatory notes.

12. **SPONSORING MILITARY ACTIVITY:** Enter the name of the departmental project office or laboratory sponsoring (*paying for*) the research and development. Include address.

13. **ABSTRACT:** Enter an abstract giving a brief and factual summary of the document indicative of the report, even though it may also appear elsewhere in the body of the technical report. If additional space is required, a continuation sheet shall be attached.

It is highly desirable that the abstract of classified reports be unclassified. Each paragraph of the abstract shall end with an indication of the military security classification of the information in the paragraph, represented as (TS), (S), (C), or (U).

There is no limitation on the length of the abstract. However, the suggested length is from 150 to 225 words.

14. **KEY WORDS:** Key words are technically meaningful terms or short phrases that characterize a report and may be used as index entries for cataloging the report. Key words must be selected so that no security classification is required. Identifiers, such as equipment model designation, trade name, military project code name, geographic location, may be used as key words but will be followed by an indication of technical context. The assignment of links, rules, and weights is optional.

All addressees receive one copy unless otherwise specified

Defense Documentation Center  
Cameron Station  
Alexandria, Virginia 22314 (12 copies)

Technical Library  
Naval Ship Research and  
Development Laboratory  
Annapolis, Maryland 21402

Professor Bruce Johnson  
Engineering Department  
Naval Academy  
Annapolis, Maryland 21402

Library  
Naval Academy  
Annapolis, Maryland 21402

Professor W. P. Graebel  
Department of Engineering Mechanics  
College of Engineering  
University of Michigan  
Ann Arbor, Michigan 48108

Professor T. Francis Ogilvie  
Department of Naval Architecture and  
Marine Engineering  
University of Michigan  
Ann Arbor, Michigan 48108

Professor W. W. Willmarth  
Department of Aerospace Engineering  
University of Michigan  
Ann Arbor, Michigan 48108

AFOSR (REM)  
1400 Wilson Boulevard  
Arlington, Virginia 22204

Professor S. Corrsin  
Department of Mechanics and  
Materials Science  
The Johns Hopkins University  
Baltimore, Maryland 21218

Professor R. B. Couch  
Department of Naval Architecture  
and Marine Engineering  
The University of Michigan  
Ann Arbor, Michigan 48105

Professor L. S. G. Kovaszny  
Department of Mechanics and  
Materials Science  
The Johns Hopkins University  
Baltimore, Maryland 21218

Professor O. M. Phillips  
Department of Mechanics and  
Materials Science  
The Johns Hopkins University  
Baltimore, Maryland 21218

Professor M. Holt  
Department of Mechanical Engineering  
University of California  
Berkeley, California 94720

Professor E. V. Laitone  
Department of Mechanical Engineering  
University of California  
Berkeley, California 94720

Librarian  
Department of Naval Architecture  
University of California  
Berkeley, California 94720

Professor P. Lieber  
Department of Mechanical Engineering  
Institute of Engineering Research  
Berkeley, California 94720

Professor J. R. Paulling  
Institute of Engineering Research  
Department of Naval Architecture  
University of California  
Berkeley, California 94720

Professor W. C. Webster  
College of Engineering  
Department of Naval Architecture  
University of California  
Berkeley, California 94720

Professor J. V. Wehausen  
Institute of Engineering Research  
Department of Naval Architecture  
University of California  
Berkeley, California 94720

Commander  
Boston Naval Shipyard  
Boston, Massachusetts 02129

Director  
Office of Naval Research Branch  
Office  
495 Summer Street  
Boston, Massachusetts 02210

Commander  
Puget Sound Naval Shipyard  
Bremerton, Washington 98314

Dr. Alfred Ritter  
Cornell Aeronautical Laboratory, Inc.  
P. O. Box 235  
Buffalo, New York 14221

Professor G. Birkhoff  
Department of Mathematics  
Harvard University  
Cambridge, Massachusetts 02138

Professor G. F. Carrier  
Division of Engineering and  
Applied Physics  
Harvard University  
Cambridge, Massachusetts 02139

Commanding Officer  
NROTC Naval Administrative Unit  
Massachusetts Institute of Technology  
Cambridge, Massachusetts 02139

Professor M. A. Abkowitz  
Department of Ocean Engineering  
Massachusetts Institute of Technology  
Cambridge, Massachusetts 02139

Professor A. T. Ippen  
Department of Civil Engineering  
Massachusetts Institute of Technology  
Cambridge, Massachusetts 02139

Professor Phillip Mandel  
Department of Ocean Engineering  
Massachusetts Institute of Technology  
Cambridge, Massachusetts 02139

Professor E. W. Merrill  
Department of Chemical Engineering  
Massachusetts Institute of Technology  
Cambridge, Massachusetts 02139

Professor E. Mollo-Christensen  
Department of Meteorology  
Room 54-1722  
Massachusetts Institute of Technology  
Cambridge, Massachusetts 02139

Professor J. Nicholas Newman  
Department of Ocean Engineering  
Room 5-324A  
Massachusetts Institute of Technology  
Cambridge, Massachusetts 02139

Commander  
Charleston Naval Shipyard  
Naval Base  
Charleston, South Carolina 29408

A. R. Kuhlthau, Director  
Research Laboratories for the  
Engineering Sciences  
Thorton Hall, University of Virginia  
Charlottesville, Virginia 22903

Director  
Office of Naval Research Branch Office  
536 South Clark Street  
Chicago, Illinois 60605

Library  
Naval Weapons Center  
China Lake, California 93555

Professor R. V. Edwards  
Division of Chemical Engineering  
Case Western Reserve University  
Cleveland, Ohio 44106

Professor J. M. Burgers  
Institute of Fluid Dynamics and  
Applied Mathematics  
University of Maryland  
College Park, Maryland 20742

Professor Pai  
Institute of Fluid Dynamics and  
Applied Mathematics  
University of Maryland  
College Park, Maryland 20742

Acquisition Director  
NASA Scientific and Technical Information  
P. O. Box 33  
College Park, Maryland 20742

Technical Library  
Naval Weapons Laboratory  
Dahlgren, Virginia 22448

Computation and Analyses Laboratory  
Naval Weapons Laboratory  
Dahlgren, Virginia 22448

Dr. R. H. Kraichnan  
Dublin, New Hampshire 03444

Commanding Officer  
Army Research Office  
Box CM, Duke Station  
Durham, North Carolina 27706

Dr. Martin H. Bloom  
Polytechnic Institute of Brooklyn  
Long Island Graduate Center  
Department of Aerospace Engineering and  
Applied Mechanics  
Farmingdale, New York 11735

Technical Documents Center  
Building 315  
U. S. Army Mobility Equipment Research and  
Development Center  
Fort Belvoir, Virginia 22060

Professor J. E. Cermak  
Department of Atmospheric Sciences  
Colorado State University  
Fort Collins, Colorado 80521

Professor O. H. Shemdin  
Coastal and Oceanographic Engineering  
Department  
University of Florida  
Gainesville, Florida 32601

Technical Library  
Webb Institute of Naval Architecture  
Glen Cove, Long Island, New York 11542

Professor E. V. Lewis  
Webb Institute of Naval Architecture  
Glen Cove, Long Island, New York 11542

Dr. J. P. Breslin  
Davidson Laboratory  
Stevens Institute of Technology  
Castle Point Station  
Hoboken, New Jersey 07030

Mr. C. H. Henry  
Stevens Institute of Technology  
Davidson Laboratory  
Castle Point Station  
Hoboken, New Jersey 07030

Dr. D. Savitsky  
Davidson Laboratory  
Stevens Institute of Technology  
Castle Point Station  
Hoboken, New Jersey 07030

Dr. A. Strumpf  
Davidson Laboratory  
Stevens Institute of Technology  
Castle Point Station  
Hoboken, New Jersey 07030

Dr. J. P. Craven  
University of Hawaii  
1801 University Avenue  
Honolulu, Hawaii 96822

Professor J. F. Kennedy, Director  
Iowa Institute of Hydraulic Research  
State University of Iowa  
Iowa City, Iowa 52240

Professor L. Landweber  
Iowa Institute of Hydraulic Research  
State University of Iowa  
Iowa City, Iowa 52240

Professor E. L. Resler  
Graduate School of Aeronautical Engineering  
Cornell University  
Ithaca, New York 14851

Dr. Y. H. Pao  
Flow Research, Inc.  
1819 South Central Avenue  
Suite 72  
Kent, Washington 98031

Dr. D. E. Ordway  
Sage Action, Incorporated  
P. O. Box 416  
Ithaca, New York 14850

Professor John Miles  
c/o I.G.P.P.  
University of California, San Diego  
La Jolla, California 92038

Director  
Scripps Institute of Oceanography  
University of California  
La Jolla, California 92037

Professor A. T. Ellis  
University of California, San Diego  
Department of Aerospace and  
Mechanical Engineering Science  
La Jolla, California 92037

Dr. Coda Pan  
Mechanical Technology Incorporated  
968 Albany-Shaker Road  
Latham, New York 12110

Mr. P. Eisenberg, President  
Hydronautics, Incorporated  
8210 Pindell School Road  
Laurel, Maryland 20810

Mr. M. P. Tulin  
Hydronautics, Incorporated  
8210 Pindell School Road  
Laurel, Maryland 20810

Commander  
Long Beach Naval Shipyard  
Long Beach, California 90802

Professor John Laufer  
Department of Aerospace Engineering  
University Park  
Los Angeles, California 90007

Dr. F. H. Harlow  
University of California  
Los Alamos Scientific Laboratory  
P. O. Box 1663  
Los Alamos, New Mexico 87544

Professor J. M. Killen  
St. Anthony Falls Hydraulic Laboratory  
University of Minnesota  
Minneapolis, Minnesota 55414

Lorenz G. Straub Library  
St. Anthony Falls Hydraulic Laboratory  
University of Minnesota  
Minneapolis, Minnesota 55414

Professor J. Ripkin  
St. Anthony Falls Hydraulic Laboratory  
University of Minnesota  
Minneapolis, Minnesota 55414

Dr. E. Silberman  
St. Anthony Falls Hydraulic Laboratory  
University of Minnesota  
Minneapolis, Minnesota 55414

Superintendent  
Naval Postgraduate School  
Attn: Library  
Monterey, California 93940

Professor A. B. Metzner  
Department of Chemical Engineering  
University of Delaware  
Newark, New Jersey 19711

Technical Library  
Naval Underwater Systems Center  
Newport, Rhode Island 02840

Office of Naval Research  
New York Area Office  
207 W. 24th Street  
New York, New York 10011

Professor V. Castelli  
Department of Mechanical Engineering  
Columbia University  
New York, New York 10027

Professor H. Elrod  
Department of Mechanical Engineering  
Columbia University  
New York, New York 10027

Engineering Societies Library  
345 E. 47th Street  
New York, New York 10017

Professor J. J. Stoker  
Institute of Mathematical Sciences  
New York University  
251 Mercer Street  
New York, New York 10003

Society of Naval Architects and  
Marine Engineers  
74 Trinity Place  
New York, New York 10006

Miss O. M. Leach, Librarian  
National Research Council  
Aeronautical Library  
Montreal Road  
Ottawa 7, Canada

Technical Library  
Naval Coastal System Laboratory  
Panama City, Florida 32401

Dr. J. W. Hoyt  
Naval Undersea R & D Center  
Pasadena Laboratory  
3202 E. Foothill Boulevard  
Pasadena, California 91107

Technical Library  
Naval Undersea R & D Center  
Pasadena Laboratory  
3203 E. Foothill Boulevard  
Pasadena, California 91107

Professor A. J. Acosta  
Department of Mechanical Engineering  
California Institute of Technology  
Pasadena, California 91109

Professor H. Liepmann  
Graduate Aeronautical Laboratory  
California Institute of Technology  
Pasadena, California 91109

Professor M. S. Plesset  
Department of Engineering Science  
California Institute of Technology  
Pasadena, California 91109

Professor A. Roshko  
California Institute of Technology  
Graduate Aeronautical Laboratories  
Pasadena, California 91109

Professor T. Y. Wu  
Department of Engineering Science  
California Institute of Technology  
Pasadena, California 91109

Director  
Office of Naval Research Branch Office  
1030 E. Green Street  
Pasadena, California 91106

Naval Ship Engineering Center  
Philadelphia Division  
Technical Library  
Philadelphia, Pennsylvania 19112

Technical Library  
Philadelphia Naval Shipyard  
Philadelphia, Pennsylvania 19112

Professor R. C. MacCamy  
Department of Mathematics  
Carnegie Institute of Technology  
Pittsburgh, Pennsylvania 15213

Dr. Paul Kaplan  
Oceanics, Inc.  
Technical Industrial Park  
Plainview, New York 11803

Technical Library  
Naval Missile Center  
Point Mugu, California 93441

Technical Library  
Naval Civil Engineering Laboratory  
Port Hueneme, California 93041

Commander  
Norfolk Naval Shipyard  
Portsmouth, Virginia 23709

Dr. H. N. Abramson  
Southwest Research Institute  
8500 Culebra Road  
San Antonio, Texas 78228

Editor  
Applied Mechanics Review  
Southwest Research Institute  
8500 Culebra Road  
San Antonio, Texas 78206

Dr. Andrew Fabula  
Code 600, Building 106  
Naval Undersea R & D Center  
San Diego, California 92132

Office of Naval Research  
San Francisco Area Office  
760 Market Street, Room 447  
San Francisco, California 94102

Library  
Pearl Harbor Naval Shipyard  
Box 400, FPO  
San Francisco, California 96610

Technical Library  
Hunters Point Naval Shipyard  
San Francisco, California 94135

Librarian  
Naval Ordnance Laboratory  
White Oak  
Silver Spring, Maryland 20910

Mr. J. Enig  
Room 3-252  
Naval Ordnance Laboratory  
White Oak  
Silver Spring, Maryland 20910

Fenton Kennedy Document Library  
The Johns Hopkins University  
Applied Physics Laboratory  
8621 Georgia Avenue  
Silver Spring, Maryland 20910

Professor E. Y. Hsu  
Department of Civil Engineering  
Stanford University  
Stanford, California 94305

Dr. Byrne Perry  
Department of Civil Engineering  
Stanford University  
Stanford, California 94305

Dr. R. L. Street  
Department of Civil Engineering  
Stanford University  
Stanford, California 94305

Professor R. C. Di Prima  
Department of Mathematics  
Rensselaer Polytechnic Institute  
Troy, New York 12181

Professor J. Lumley  
Department of Aerospace Engineering  
Pennsylvania State University  
University Park, Pennsylvania 16802

Dr. J. M. Robertson  
Department of Theoretical and  
Applied Mechanics  
University of Illinois  
Urbana, Illinois 61803

Technical Library  
Mare Island Naval Shipyard  
Vallejo, California 94592

Code 438  
Office of Naval Research  
Department of the Navy  
Arlington, Virginia 22217 (3 copies)

Code 461  
Office of Naval Research  
Department of the Navy  
Arlington, Virginia 22217

Code 463  
Office of Naval Research  
Department of the Navy  
Arlington, Virginia 22217

Code 466  
Office of Naval Research  
Department of the Navy  
Arlington, Virginia 22217

Code 468  
Office of Naval Research  
Department of the Navy  
Arlington, Virginia 22217

Code 473  
Office of Naval Research  
Department of the Navy  
Arlington, Virginia 22217

Code 481  
Office of Naval Research  
Department of the Navy  
Arlington, Virginia 22217

Code 2627  
Naval Research Laboratory  
Washington, D. C. 20390 (6 copies)

Library, Code 2629 (ONRL)  
Naval Research Laboratory  
Washington, D. C. 20390 (6 copies)

Code 6170  
Naval Research Laboratory  
Washington, D. C. 20390

Code 4000  
Director of Research  
Naval Research Laboratory  
Washington, D. C. 20390

Code 8030 (Maury Center)  
Naval Research Laboratory  
Washington, D. C. 20390

Code 8040  
Naval Research Laboratory  
Washington, D. C. 20390

Code 031  
Naval Ship Systems Command  
Washington, D. C. 20360

Code 0341  
Naval Ship Systems Command  
Washington, D. C. 20360

Code 0322 (L. Benen)  
Naval Ship Systems Command  
Washington, D. C. 20360

Code 0321 (J. Schuler)  
Naval Ship Systems Command  
Washington, D. C. 20360

Code 2052  
Naval Ship Systems Command  
Washington, D. C. 20360

Code 6034  
Naval Ship Engineering Center  
Center Building  
Prince George's Center  
Hyattsville, Maryland 20782

Code 6101E  
Naval Ship Engineering Center  
Center Building  
Prince George's Center  
Hyattsville, Maryland 20782

Code 6110  
Naval Ship Engineering Center  
Center Building  
Prince George's Center  
Hyattsville, Maryland 20782

Code 6114  
Naval Ship Engineering Center  
Center Building  
Prince George's Center  
Hyattsville, Maryland 20782

Code 6120E  
Naval Ship Engineering Center  
Center Building  
Prince George's Center  
Hyattsville, Maryland 20782

Code 6136  
Naval Ship Engineering Center  
Center Building  
Prince George's Center  
Hyattsville, Maryland 20782

Dr. A. Powell (Code 01)  
Naval Ship Research & Development Center  
Bethesda, Maryland 20034

Mr. W. M. Ellsworth (Code 11)  
Naval Ship Research & Development Center  
Bethesda, Maryland 20034

Dr. W. E. Cummins (Code 15)  
Naval Ship Research & Development Center  
Bethesda, Maryland 20034

Dr. H. R. Chaplin (Code 16)  
Naval Ship Research & Development Center  
Bethesda, Maryland 20034

Mr. G. H. Gleissner (Code 18)  
Naval Ship Research & Development Center  
Bethesda, Maryland 20034

Mr. R. Wermter (Code 152)  
Naval Ship Research & Development Center  
Bethesda, Maryland 20034

Dr. W. B. Morgan (Code 154)  
Naval Ship Research & Development Center  
Bethesda, Maryland 20034

Mr. J. B. Hadler (Code 156)  
Naval Ship Research & Development Center  
Bethesda, Maryland 20034

Library (Code 5641)  
Naval Ship Research & Development Center  
Bethesda, Maryland 20034

Mr. S. F. Crump (Code 1505)  
Naval Ship Research & Development Center  
Bethesda, Maryland 20034

Dr. P. Pien (Code 1521)  
Naval Ship Research & Development Center  
Bethesda, Maryland 20034

Mr. Paul Granville (Code 1541)  
Naval Ship Research & Development Center  
Bethesda, Maryland 20034

Mr. J. McCarthy (Code 1552)  
Naval Ship Research & Development Center  
Bethesda, Maryland 20034

Dr. Nils Salvesen (Code 1552)  
Naval Ship Research & Development Center  
Bethesda, Maryland 20034

Dr. M. Strasberg (Code 1901)  
Naval Ship Research & Development Center  
Bethesda, Maryland 20034

Code 03  
Naval Air Systems Command  
Department of the Navy  
Washington, D. C. 20360

AIR 5301  
Naval Air Systems Command  
Department of the Navy  
Washington, D. C. 20360

AIR 604  
Naval Air Systems Command  
Department of the Navy  
Washington, D. C. 20360

Code ORD 03  
Naval Ordnance Systems Command  
Department of the Navy  
Washington, D. C. 20360

Code ORD 035  
Naval Ordnance Systems Command  
Department of the Navy  
Washington, D. C. 20360

Code ORD 05413  
Naval Ordnance Systems Command  
Department of the Navy  
Washington, D. C. 20360

Code ORD 9132  
Naval Ordnance Systems Command  
Department of the Navy  
Washington, D. C. 20360

CNM PM-1  
Strategic Systems Project Office  
Department of the Navy  
Washington, D. C. 20360

Technical Division (CNM PM 11-20)  
Deep Submergence Systems Project Office  
Department of the Navy  
Washington, D. C. 20360

Oceanographer of the Navy  
Washington, D. C. 20390

Commander  
Naval Oceanographic Office  
Washington, D. C. 20390

Dr. A. L. Slafkosky  
Scientific Advisor  
Commandant of the Marine Corps (CODE AX)  
Washington, D. C. 20380

Librarian Station 5-2  
Coast Guard Headquarters  
NASSIF Building  
400 7th Street, S.W.  
Washington, D. C. 20591

Office of Research and Development  
Maritime Administration  
441 G Street, N.W.  
Washington, D. C. 20235

Division of Ship Design  
Maritime Administration  
441 G Street, N.W.  
Washington, D. C. 20235

National Science Foundation  
Engineering Division  
1800 G Street, N.W.  
Washington, D. C. 20550

Dr. G. Kulin  
National Bureau of Standards  
Washington, D. C. 20234

Science & Technology Division  
Library of Congress  
Washington, D. C. 20540

Chief of Research & Development  
Office of Chief of Staff  
Department of the Army  
Washington, D. C. 20310

Professor A. Thiruvengadam  
Department of Mechanical Engineering  
The Catholic University of America  
Washington, D. C. 20017

Dr. A. S. Iberall, President  
General Technical Services, Inc.  
451 Penn Street  
Yeadon, Pennsylvania 19050

Commander  
Portsmouth Naval Shipyard  
Portsmouth, New Hampshire 03801